STARS

2013

Ytterbium-doped Fiber-seeded Thin-disk Master Oscillator Power Amplifier Laser System

Christina Willis-Ott
University of Central Florida

Showcase of Text, Archives, Research & Scholarship

YTTERBIUM-DOPED FIBER-SEEDED THIN-DISK MASTER OSCILLATOR POWER AMPLIFIER LASER SYSTEM

by

CHRISTINA C. C. WILLIS
B.A. Wellesley College, 2006
M.S. University of Central Florida, 2009

A dissertation submitted in partial fulfillment of the requirements
for the degree of Doctor of Philosophy
in the College of Optics and Photonics
at the University of Central Florida
Orlando, Florida

Summer Term
2013

Major Professor: Martin C. Richardson

ABSTRACT

Lasers which operate at both high average power and energy are in demand for a wide range of applications such as materials processing, directed energy and EUV generation. Presented in this dissertation is a high-power 1 μm ytterbium-based hybrid laser system with temporally tailored pulse shaping capability and up to 62 mJ pulses, with the expectation the system can scale to higher pulse energies.

This hybrid system consists of a low power fiber seed and pre-amplifier, and a solid state thin-disk regenerative amplifier. This system has been designed to generate high power temporally tailored pulses on the nanosecond time scale. Temporal tailoring and spectral control are performed in the low power fiber portion of the system with the high pulse energy being generated in the regenerative amplifier. The seed system consists of a 1030 nm fiber-coupled diode, which is transmitted through a Mach-Zehnder-type modulator in order to temporally vary the pulse shape. Typical pulses are 20-30 ns in duration and have energies of ~0.2 nJ from the modulator. These are amplified in a fiber pre-amplifier stage to ~100 nJ before being used to seed the free-space Yb:YAG thin-disk regenerative amplifier. Output pulses have maximum demonstrated pulse energies of 62 mJ with 20 ns pulse after ~250 passes in the cavity.

The effects of thermal distortion in laser and passive optical materials are also. Generally the development of high power and high energy lasers is limited by thermal management strategies, as thermally-induced distortions can degrade laser performance and potentially cause catastrophic damage. Novel materials, such as optical ceramics, can be used to mitigate thermal distortions; however, thorough analysis is required to optimize their fabrication and minimize thermal distortions.

Using a Shack-Hartmann wavefront sensor (SHWFS), it is possible to analyze the distortion induced in passive and doped optical elements by high power lasers. For example, the thin-disk used in the regenerative amplifier is examined in-situ during CW operation (up to 2 kW CW pump power). Additionally, passive oxide-based optical materials and Yb:YAG optical ceramics are also examined by pumping at 2 and 1 μm respectively to induce thermal distortions which are analyzed with the SHWFS. This method has been developed as a diagnostic for the relative assessment of material quality, and to grade differences in ceramic laser materials associated with differences in manufacturing processes and/or the presence of impurities.

In summation, this dissertation presents a high energy 1 μm laser system which is novel in its combination of energy level and temporal tailoring, and an analysis of thermal distortions relevant to the development of high power laser systems.

For all the wonderful teachers whose presence I have been graced with,
starting with my parents, Nan & Jerry.

ACKNOWLEDGMENTS

TABLE OF CONTENTS

LIST OF FIGURES

LIST OF TABLES

LIST OF ACRONYMS

AR – Anti Reflection, refers to an optical element coating
BPF – Band Pass Filter
CCD – Charge Coupled Device
CW – Continuous Wave
EUV – Extreme Ultraviolet
FBG – Fiber Bragg Grating
GA – Genetic Algorithm
HR – High Reflectivity
HWP – Half-Wave Plate
LASER – Light Amplification by Stimulated Emission of Radiation
LIBS – Laser Induced Breakdown Spectroscopy
LIDAR – Light Detection And Ranging
LIFE – Laser Inertial Fusion Energy
LPL – Laser Plasma Laboratory
MOPA – Master Oscillator Power Amplifier
NA – Numerical Aperture
NIF – National Ignition Facility
PBC – Polarizing Beam Cube
PC – Pockels Cell (sometimes refers specifically to the PC used in the regenerative amplifier)
PCM – Particle Concentration Meter
PP – Pulse Picker (refers to the small Pockels cell)
PM – Polarization Maintaining
QD – Quantum Defect
ROC – Radius of Curvature
SHWFS – Shack-Hartmann Wavefront Sensing, or Shack-Hartmann Wavefront Sensor
SBS – Stimulated Brillouin Scattering
SRS – Stimulated Raman Scattering
SVR – Surface to Volume Ratio
TFP – Thin Film Polarizer
TLI – Townes Laser Institute
TATNAA – The Acronym That Never Appears Again
UAV – Unmanned Aerial Vehicle
VCSEL - Vertical Cavity Surface Emitting Lasers
WDM – Wavelength-Division Multiplexer
WFG – Waveform Generator

CHAPTER 1:   INTRODUCTION

This work is focused on two main aspects of high power laser development. The first focuses on the tailored development of lasers for specific desirable high power and high energy applications. The second portion addresses the thermal issues which are encountered in high power laser operation, the analysis thereof, and the application of high quality optical ceramics for the mitigation of these effects. This section serves as a general introduction to these concepts.

1.1. High Energy & High Power Lasers and Their Applications

High power and high energy lasers are versatile tools which have been used in many diverse applications. High power lasers, particularly CO_2 lasers, have long been the industry standard for metal cutting and welding processes [1-5]. Laser Wakefield accelerators based on high intensity laser pulses have been used to generate low-spread electron beams [6, 7]. High energy pulses can also be used to generate plasma which, for example, can be used as a source for extreme ultraviolet light (EUV) [8]. In addition to industrial and scientific applications, high power laser development is also the subject of various large military and government projects. Laser weapons have been developed in several different countries with output power ranges from 10 to 100 kW used to shoot down both missiles and UAVs [9-12]. The world's largest laser, the National Ignition Facility (NIF), which is operated by the National Nuclear Security Administration, can create two million joules of energy with the goal of creating Laser Inertial Fusion Energy (LIFE), and if harnessed, the energy results from such a reaction could be used to meet our expanding energy demands with a series of LIFE based power plants [13-15].

And the number of possible applications is growing. To meet the demands of scientific research and industry, development of high power and high energy lasers continues forward at a

rapid pace. In 2012, the worldwide commercial laser revenue was expected to exceed $7.5 billion, with typically high power applications such as materials processing and lithography constituting over a third of overall revenue [16]. Two large laser manufacturers, IPG and Trumpf, each reported total sales in the billions for the year 2012.

For each laser application there is a different set of criteria that the laser must meet; laser systems are often developed with a specific application in mind. In addition to high power and/or high energy, required laser output characteristics often include specifications on wavelengths, spectral widths, pulse shape/durations, and beam quality. The combination of these characteristics generally determines the blue print for the laser under development.

Two design characteristics that are central to deciding laser output characteristics are the gain medium/dopant and the architecture, and a multitude of different gain media and architectures exist. The first laser, demonstrated in 1960, used a rod-shaped ruby crystal ($Cr:Al_2O_3$) as its gain medium with silvered end faces to form the laser cavity [17]. Many other architectures and gain media followed. In the same year a gas-based laser, the Helium Neon laser, was demonstrated [18], and in 1961 the first fiber laser was built [19]. What has followed since are solid-state glass lasers [19], organic dye lasers [20], semi-conductor lasers [21], free electron lasers [22], vertical cavity surface emitting lasers (VCSEL) [23], slab and other waveguide lasers, thin-disk lasers [24], and many others, including advancements and improvements upon each type.

Each architecture and gain medium combination has its own set of costs and benefits which are considered during development. For example, the fiber laser architecture can create very stable, robust systems which have excellent thermal properties due to their surface-area-to-volume ratio [25]. However, because the energy in a fiber laser is confined in the core of the

fiber (typically microns in diameter), at high powers and intensities such systems are susceptible to non-linear effects which can degrade laser performance and damage thresholds which can be catastrophic. Conversely, solid state rod and slab systems are often used for high energy operation because of the higher damage thresholds that result from reduced intensity by distributing the energy over a larger area. However, these same systems also have trouble with thermal distortions due to inhomogeneous heating and temperature gradients that occur throughout their volume [26].

Laser development must address a variety of limitations created by scaling to higher powers and energies. Depending on the architecture of the laser in question, thermal distortions, runaway, non-linear effects, and damage thresholds must be addressed. Many creative solutions have been developed to solve problems posed by different gain media and architectures, which in turn can lead to the development of new architectures and devices. Fiber and thin-disk architectures are solutions to the thermal inhomogeneities seen in rod-type laser media: each creates a higher surface-area to volume ratio in order to ensure a more homogeneous temperature profile [27]. The slab-type geometry can also be used to employ side pumping and a zig-zag pattern of total internal reflection within the medium, which creates an averaging of the thermal distortions present at high power [28]. There are also many different cooling schemes including air, water and even cryogenics [29]. In fiber lasers, scaling up the core size diameter is required to raise both non-linear and damage thresholds, and although moving to longer wavelengths offers some benefits it can also be at the expense of overall efficiency [30]. One technique in particular for addressing system limitations is the Master Oscillator Power Amplifier (MOPA) which can be used to divide specific laser criteria into multiple laser stages [31].

The MOPA architecture is simply a "divide et imperia" strategy used to address high

power operation while maintaining control of other desirable output characteristics, be they spectral, temporal or otherwise. Because many optical components for creating and maintaining spectral and temporal aspects of a laser are delicate and do not possess high power and energy tolerances, the number of components that can be incorporated into a single cavity at high powers are limited. The MOPA architecture addresses this by taking the components for spectral, temporal and other characteristics, and incorporating them into a lower power Master Oscillator (MO). The output from the MO is then used to seed subsequent amplifier stages often including "pre-amplifiers" and concluding with a Power Amplifier (PA), which, as its name implies, boosts the power (as well as energy in the case of pulsed systems) of the seed signal through amplification. Because the amplifier is not a resonant cavity, it preserves the incoming spectral and temporal features to the extent that gain shaping and non-linear effects are absent, effects which can be mitigated with appropriate engineering. While the MOPA technique increases the complexity of the system, it offers a great deal of flexibility to tailor output characteristics and maximize performance in multiple aspects.

The first part of this dissertation discusses the development of a hybrid MOPA laser system which generates nanosecond (20-30 ns) high-energy pulses at 1031 nm with temporal shaping and good beam quality. The system consists of two stages, a Yb^{3+}-doped silica fiber stage and a free space stage including a Yb:YAG thin-disk regenerative amplifier. The fiber portion contains a continuous wave seed, a Mach-Zehnder type modulator for the carving of temporally tailored pulse shapes from the CW signal, and a single stage of pre-amplification. The solid-state regenerative amplifier acts as the PA, providing $7.8 \cdot 10^5$ amplification. The combination of architectures is chosen because of how the desired set of output characteristics plays to their respective strengths, and ytterbium is selected because of its high efficiency and the

maturity of the components available at 1 μm.

Interest in this combination of characteristics (high beam quality, near-infrared radiation, high energy and temporal pulse tailoring) comes from applications such as materials processing, EUV generation, and other light/matter interaction processes. On the ns time scale the temporal shape of an incoming pulse can change the effect that it has on a material because the heating effects and the pulse's shape are proportional. It is therefore possible to change and optimize the efficiency of the process or interaction by creating bursts of pulses, or by exploring different temporal pulse shapes. This has been demonstrated in both EUV experiments [32, 33], and various materials processing studies [34-38]. Through the unique combination of temporal pulse tailoring and high energy, greater efficiency of various light/matter interaction processes can be achieved through pulse-shape optimization.

1.2. Thermally Induced Distortions and Ceramic Materials

As described earlier, thermal distortions can wreak havoc on laser performance. Waste heat is produced in varying degrees by all laser gain media as a result of the quantum defect of the laser operation and other non-radiative decay processes. Heating of other elements in the system can occur due to small yet non-negligible absorption [39]. As heat accumulates in a laser system, which it can do very rapidly in a high power and/or high energy system, thermal expansion of optical materials and coatings occurs, which results in lensing and potential damage. These thermal expansions can cause distortions in the output beam quality and severely degrade operation efficiency. In terms of laser development and advancements in laser output goals such distortions represent an important area of study, specifically for high energy laser systems.

Thermal distortions have been addressed in a variety of ways such as devising better, more efficient cooling methods [40] and employing architectures, which more effectively dissipate heat [27]. For example, the move from the use of Nd (as a dopant ion for laser gain media) to Yb has largely been driven by the lower waste heat associated with the reduction in quantum defect, which was made accessible by the development of 9XX nm pump diodes. One approach explored in this dissertation is the application of novel host materials, specifically optical quality ceramics.

An optical quality ceramic (Figure 1) is a high purity and high density polycrystalline material consisting of many small crystalline grains which are randomly oriented and bonded together [41, 42] (Figure 2). The points at which the grains are bonded together are referred to as grain boundaries, and these boundaries are smaller than most applicable light wavelengths so do not cause scattering. Chemical and phase impurities, pores (Figure 3), and inclusions can cause light scatter in ceramics, making their fabrication a delicate and high precision process.
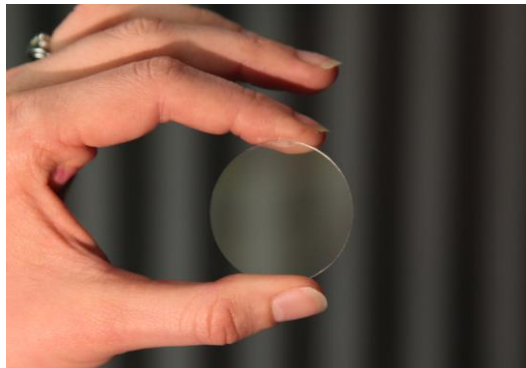
Figure 1: Transparent optical Yb:YAG ceramic material
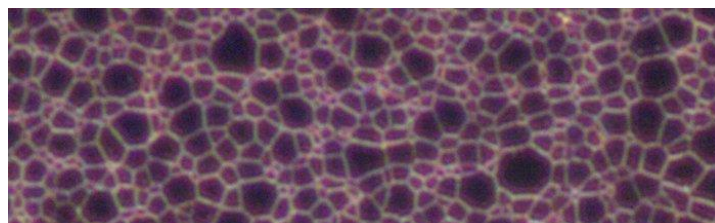
Figure 2: Optical microscope image of ceramic YAG. Image by Samuel Paul David and Romain Gaume, 2013.

6
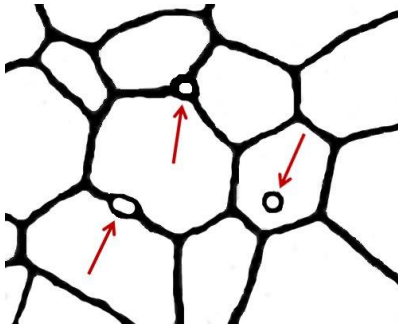
Figure 3: Illustration of ceramic grains with pores at grain boundaries and occluded in a grain, both of which are flaws that can cause light scatter

Transparent optical ceramics have been available since the 1960s; the first transparent ceramic (alumina) was fabricated in 1961 [43] and the first ceramic laser, CaF_2, was demonstrated in 1964 [44]. The first transparent ceramics were produced by Robert L. Coble, who discovered that the addition of magnesia, MgO, allowed ceramics to sinter to the point of theoretical density, which eliminated the sort of pores illustrated in Figure 3 [45]

The fabrication of an optical ceramic begins with crystalline powders. These powders are often combined with sintering aids and shaped into a compact known as a green body, or un-fired ceramic. The green body is then heat-treated (sintered), possibly with pre-sinter and/or post-sinter steps as part of the full sintering process. During the sintering process the ceramic achieves density commensurate to that of perfect theoretically density, eliminating nearly all pores in the material. Once sintering is complete, the ceramic may then be cut and polished according to its intended use.

Optical ceramics possess a number of advantages over traditional single-crystal gain media [46-49]. For example, while optical ceramics may be fabricated to arbitrary dimensions, with limitations imposed primarily by available equipment and the size of the sintering furnace; melt-grown single-crystals are limited by the size of the boule which can be grown, and typically a boule has to be cut down to a smaller size in order to remove portions which are non-uniform.

7

Ceramics can also employ host materials with melting points that would be prohibitively high for the single-crystal growth process [50]. They can be doped to higher concentrations than single-crystals because lattice distortions created by high levels of substitution in grains cannot propagate throughout the material. Further, due to the mixing process, ceramics have better dopant homogeneity. In addition, dopant gradients can be engineered into the ceramic to allow for better thermal management and gain-guiding schemes [41].

The same dopants which can be used in single crystal and glass gain media can be used to create active ceramic materials. Various rare earth ions have been incorporated successfully as dopants in transparent ceramics, including (but not limited to) neodymium, ytterbium and thulium [51-58]. Yb:YAG ceramic can be especially heavily doped (20 at.%) and has shown a slope efficiency of 52% at such high doping concentrations [53]. Another instance of high power ceramic gain media includes a diode-pumped Tm:YAG ceramic slab laser that was able to achieve 20% slope efficiency [57].

In order to exploit the unique features of optical ceramics to mitigate the effects of thermal distortions, a two-pronged approach is followed here. First, a general analysis of thermal distortions must be performed so that appropriate methods of compensation can be established. Second, the ceramics themselves, which can vary dramatically batch to batch, and manufacturer to manufacturer, must be assessed in terms of quality. In this work, in order to address both of these thrusts, Shack-Hartmann wave front sensing is employed.

The technique of Shack-Hartmann wavefront sensing, or Shack-Hartmann interferometry, allows all the Zernike polynomials of the incoming wavefront to be calculated from only one or two measurements. This analysis method was developed by Shack in the 1960's based upon the principle of Hartmann interferometry by replacing the Hartmann mask (an array of holes) with

an array of lenses [59]. A wavefront that is incident on the lenslet array is focused onto a detector (in modernity a CCD) as an array of spots (focal points) as shown in Figure 4. The location of the focal points is compared against the location of the points in a reference measurement or for an ideal wavefront. The displacement of the focal points is then used to create a 2D vector array (Figure 5).
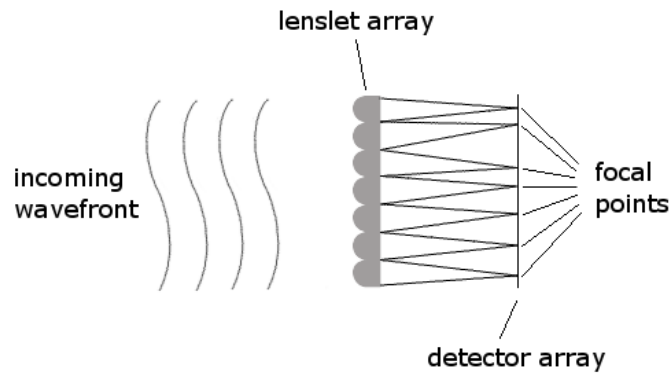
Figure 4: Principle of Shack-Hartmann wave front sensing and operation
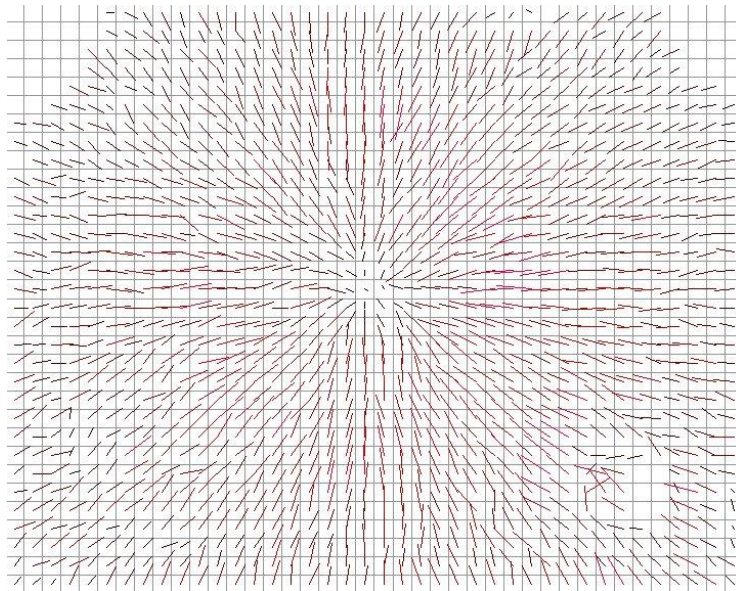
Figure 5: Vector array created by measuring the displacement of focal spots created by an aberrated wavefront, taken with Imagine Optic HASO First^{TM}3 WFS and HASOv3 software [60].

From the vector array, the Zernike polynomials of the incident wavefront can be calculated and all of the aberrations in the wavefront extracted. In this manner, either absolute

aberrations of a system can be measured, or the effects of most of the system's optics can be calibrated out with a reference measurement in order to focus on the effect of a single effect or element.

In this work, SHWFS is used to analyze thermal distortions in oxide-based passive materials, doped optical ceramics, and the Yb:YAG single-crystal thin-disk used the regenerative amplifier (described in the laser development portion of this work). Both the oxide and YAG samples are measured by transmitting an optical probe beam through the sample while the sample is heated by a pump source. For the oxide materials, a 2 μm pump source is used because of the higher absorption of the material at this wavelength thereby simulating irradiation at much higher powers at 1 μm wavelength. The doped ceramics are all Yb:YAG and are pumped on resonance at 940 nm to induce the maximum possible thermal distortion. The thin-disk is measured by reflecting the probe source off its face under lasing conditions. Through the measurements a more comprehensive picture of thermal distortions is built, and a diagnostic for the assessment of ceramic materials is established. In this matter the groundwork is laid for the application of ceramics for the mitigation of thermal distortions.

CHAPTER 2:   LASER DEVELOPMENT BACKGROUND

This chapter contains relevant background information concerning the development of the hybrid MOPA system. It provides a contextual picture of various issues, including the use of rare earth laser dopants, fiber laser and thin-disk architectures, the MOPA technique, and examples of laser systems similar to the laser described herein.

2.1. Laser Architectures

Laser architectures exist in many different forms and their structure is determined to some extent by the type of gain media used in the laser. In this work two different laser architectures are employed: fiber and thin-disk. Each of these architectures, their history, and their relative strengths and weaknesses will be discussed in this section, and, where relevant, comparisons will be drawn with the more traditional rod-type laser architecture.

2.1.1. Fiber Laser Architecture

The first fiber laser was demonstrated using flash-lamp pumping in 1964 [61], and the first silica-based fiber lasers were demonstrated in the 1970s [62]. Flash lamp pumping of fiber lasers generally yielded poor efficiencies, with only 10's of mW in peak output power available before 1990 [63]. But in 1990 a 4 W Er/Yb fiber laser was demonstrated, which represent a significant jump in available output power at the time [64]. This was possible because of two technological advancements: cladding-pumped fiber designs and the increased availability of high brightness laser diodes. With a commercial supply of cheap, highly efficient pump sources, the field of fiber lasers began to expand rapidly, first in telecommunications and later in the field of high power lasers [65-67]. Since 2000 there has been an explosion of development, with higher output energies and powers, greater efficiencies, and improved performance in both

pulsed and continuous wave regimes. As such, fiber lasers are taking the place of gas and free-space solid-state lasers in a variety of applications.

A primary feature of fiber laser systems is their excellent thermal properties, facilitated by their high surface-to-volume ratio (SVR) which dramatically facilitates heat removal [68, 69]. As a result many fiber lasers need no active cooling, and those that do need it can be wrapped on cooled mandrels or submerged directly in cooling fluid. Due to the fiber geometry, the output beam quality of fiber laser systems is effectively independent of the thermal loading, displaying nearly diffraction limited beam quality at powers of >1 kW and up to 10 kW [70, 71]. By way of comparison, a laser rod that is 5 mm in diameter and 50 mm long has a gain volume of 982 mm^3 and a SVR of 0.8 mm^{-1} (not including the area of the end faces). To have the same volume a single-mode fiber with a core diameter of 5 μm would need to be ~50 km long, and its SVR would be 800 mm^{-1}, giving a factor of 10^4 in the difference between SVR for these two geometries.
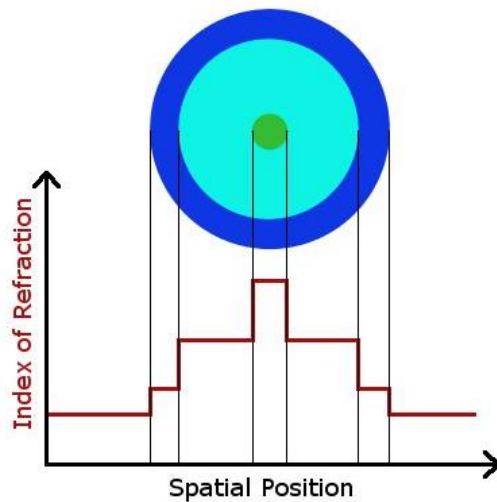
Figure 6: Cross-section and plot of index of refraction for double-clad optical fiber

Fiber lasers operate on the principle of total internal reflection, by which both pump and signal light are trapped and guided within the fiber. The most basic of optical fibers consists of a

12

core section which is of a higher index of refraction than the surrounding cladding material. Another common fiber type includes, in addition to the afore described structure, a secondary cladding layer, often made of a type of polymer, which has the lowest index of refraction of all three regions and can thereby guide and trap pump light propagating in the cladding region as well (Figure 6).

Due to the layers of decreasing index, light directed into the core of the fiber will be trapped and guided there, whereas light directed into the cladding will be trapped and guided within that region. Whether light becomes trapped in the core or the cladding is dependent upon its angle of incidence and the numerical aperture (NA) of the fiber. NA is defined in Equation 1, where n_{core} is the refractive index of the core region, and n_{clad} is the refractive index of the cladding.

$$NA = \sqrt{n_{core}^2 - n_{clad}^2} \tag{1}$$

Alternatively NA can be defined as in Equation 2, where n is the refractive index of the surrounding medium (in most cases this is air and n = 1), θ_{max} is the maximum acceptance angle, and θ_c is the critical angle for guiding in the fiber (Figure 7).

$$NA = n \sin \theta_{max} \tag{2}$$
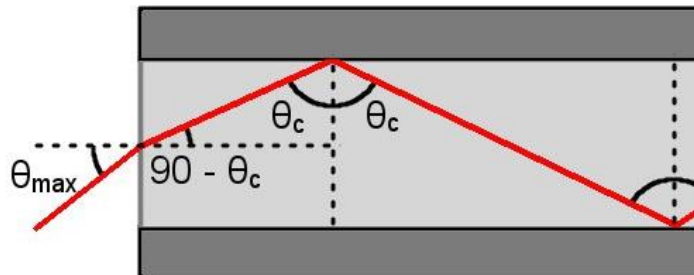
Figure 7: Light guided by total internal reflection in an optical fiber (θ_{max} - max. acceptance angle, θ_c - critical angle)

Thus the maximum acceptance angle for an optical fiber can be defined as in Equation 3.

$$\theta_{max} = sin^{-1}\left(\frac{\sqrt{n_{core}^2 - n_{clad}^2}}{n}\right) \qquad (3)$$

Related to the NA is a quantity defined as the V-parameter, which is defined for step index fiber in Equation (4. The V-parameter depends on the radius of the core a, and the index of the core and cladding respectively (due to the relationship with NA). This quantity describes the number of transverse modes which can be guided by the fiber. If the V-parameter (or fiber number) for a step-index fiber is less than 2.405 then the fiber will only support the propagation of a single transverse mode. As V increases beyond this value, more and more transverse modes can propagate within the fiber.

$$V = k_0 aNA = \frac{2\pi a}{\lambda}\sqrt{n_{core}^2 - n_{clad}^2} \qquad (4)$$

The value 2.405 comes from the first zero of the zero order Bessel function of the first kind ($J_0(2.405) = 0$). Bessel functions of the first and second kind are solutions to a particular differential equation shown in Equation 5, and are typically used to describe mode propagation in fibers and other cylindrical waveguides. Orders 0-5 of the Bessel function of the first kind are shown plotted in Figure 8.

$$x^2\frac{d^2y}{dx^2} + x\frac{dy}{dx} + (x^2 - n^2)y = 0 \qquad (5)$$

While the aspect ratio of length-to-diameter for optical fiber grants it benefits in terms of guiding and thermal handling, there are limitations that relate to both the potential long length of the fiber and its small cross-section. Limiting processes that scale with fiber length include non-linear processes, background loss and re-absorption effects (common for quasi-three level rare earth dopants). Because the signal light is tightly confined to the fiber core and the active

14

medium is long, non-linear effects can be observed even at moderate peak power levels [72].
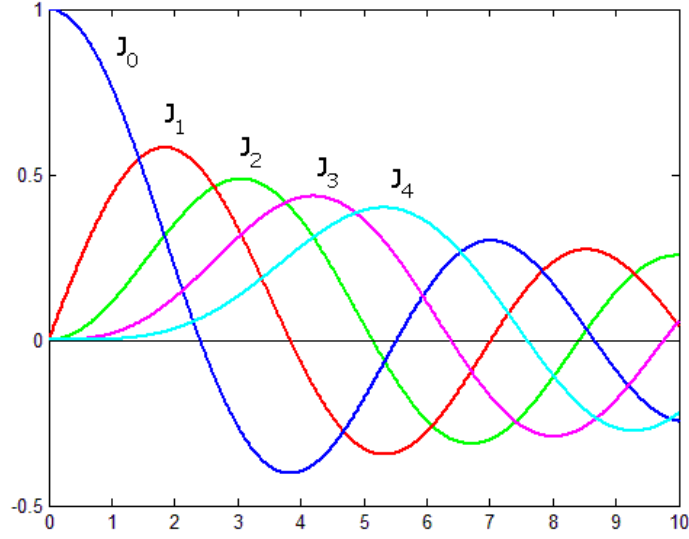
Figure 8: Bessel functions of the first kind used to describe propagation in optical fibers

The most prominent non-linear effects that plague fiber laser performance are stimulated Raman scattering (SRS), stimulated Brillouin scattering (SBS) and self-phase modulation (SPM) [68, 73]. The strengths of these effects are proportional to the peak power in the fiber and fiber length, and are inversely proportional to the fiber core area. Non-linear effects pose less of a problem for shorter fiber lengths because thresholds for the effects become higher.

$$P_{cr}^{B} \cong \frac{17 \, A_{eff}}{g_B L_{eff}} \qquad (6)$$

$$P_{cr}^{R} \cong \frac{16 \, A_{eff}}{g_R \, L_{eff}} \qquad (7)$$

These effects are proportional to the fiber area and length in the CW or Quasi-CW cases. Expressions for the thresholds of SBS and SRS are shown in Equations 6 and 7, where A_{eff} is the effective mode area, L_{eff} is the effective length, and g_B and g_R are Brillouin and Raman gain coefficient respectively [74]. Looking at Equation 6, and using typical values for fiber parameters (step index silica fiber with a 6 μm core diameter, $g_B \sim 5 \cdot 10^{-11}$ m/W - nearly-single

frequency linewidth), the SBS threshold for a 1 m single mode fiber is ~32 W [75]. SBS is especially troublesome for lasers with narrow spectral outputs, long fiber lengths, and small core diameters [73]. This is because g_B scales with the laser linewidth, achieving its peak value of $5 \cdot 10^{-11}$ m/W in silica fiber for narrow linewidths. At sufficiently large values of laser linewidth, g_B becomes small enough that SRS becomes the dominant effect, with peak g_R being $\sim 10^{-13}$ [72, 76]. These effects, SBS and SRS, represent a major limitation for fiber lasers with high peak power and narrow spectral width.

To describe the cumulative phase shift of a pulse due to all concurrent nonlinear processes in a fiber, a quantity called the B-Integral is used [77], shown in Equation (8). In this expression *I(z)* is the pulse peak intensity, the fiber length is *L*, and *n₂* is the nonlinear refractive index coefficient. In considering the B-integral, as long as it is less than π, the pulse is considered to be propagating linearly. In this way the B-integral is used to predict and plan for the overall effect of the non-linear processes.

$$B = \frac{2\pi}{\lambda} \int_0^L n_2 I(z) dz \qquad (8)$$

In terms of practical advantages, fiber lasers benefit from the wide array of fiberized components that are available in various different wavelength regimes. Items such as polarizers, splitters, couplers, combiners fiber-coupled pump diodes, circulators, modulators, isolators, fiber Bragg gratings, and beyond are all commercially available for many operating powers, energies, and wavelengths. Using fiberized components for construction of lasers it is possible to build systems which are all-fiber, containing no free-space components. By eliminating free space components, these systems can be extremely robust and generally insensitive to environmental factors. And by scaling to greater fiber core sizes or through the use of novel fiber structures, the onset of non-linear effects and thermal damage can be mitigated. All-fiber CW systems have

16

been demonstrated at multi-kW level and improvements continue to be made [67, 78].

In summation, the fiber laser architecture yields high beam quality which is maintained even at high output powers and energies due to the high SVR of the fiber architecture. Also, with many types of fiberized laser components available it is possible to create robust and compact all-fiber laser systems. The corresponding weakness of the fiber architecture lies in the onset of non-linear effects and facet damage particularly in the pulse regime. These effects can be mitigated by scaling to large core sizes and other more novel fiber types including photonic crystal fiber. This set of characteristics makes fiber an ideal architecture for the master oscillator of a MOPA system.

2.1.2. Thin-Disk Architecture

The precursor to the thin-disk laser is an architecture known as the active mirror. The first active mirror configurations were demonstrated in the 1960s, and the concept was patented in 1971 [79]. Though thin-disk lasers are occasionally referred to as active mirror lasers, there are important distinctions between the two concepts and as such the terms should not be used interchangeably. It wasn't until 1994 that the first truly thin-disk laser was demonstrated by Giesen et al. [24]. Today thin-disk lasers represent the current state-of-the-art in solid-state laser systems for high energy and high average power [80, 81].

The active mirror laser has an architecture much like it sounds. The "active" gain media is incorporated into a dichroic mirror which allows the transmission of pump light and reflects the signal light. By reducing the solid state gain media to a very thin slice, distortions created by thermal gradients are reduced because the temperature flow becomes one-dimensional (along the z-axis), and therefore the temperature distribution in the media is significantly homogenized with no radial temperature gradients. In contrast, the thin-disk laser does not transmit, but reflects

17

both pump and signal wavelengths. This allows for much more effective cooling by making it possible to bond the coated disk directly to a heat spreader and/or heat sink, further reducing the occurrence of thermal gradients.

The basic architecture of a thin-disk laser or amplifier (as seen in Figure 9) consists of a disk of active material with a thickness 100 to 200 μm. This disk is coated on both sides and mounted directly onto a heat sink or heat spreader. The mounted side of the disk is HR coated for both pump and signal wavelengths. Mounting is sometimes done by soldering, often consisting of heat-expansion matched indium-tin or indium-gold solder [80, 82], though other methods, such a diffusion bonding, exist [83]. The opposite face of the disk is AR coated at both the pump and signal wavelengths or bonded to a coated un-doped endcap for mechanical support and ASE suppression [84]. The reflecting surface is used as either an end or a folding mirror in the laser cavity [81], hence the similarity with active mirror systems. The heat sink is typically water-cooled via impingement, though some work has been done with cryogenic cooling [29].
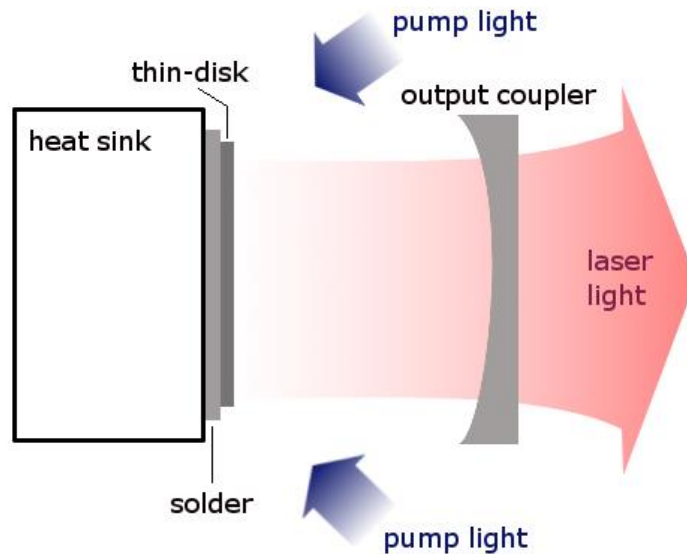
Figure 9: Anatomy of a basic thin-disk laser cavity

The design of the thin-disk system minimizes the thermal lensing and thermally induced birefringence problems that plague more traditional rod and slab shaped laser gain media [24, 82]. Both radial and end pumping configurations are common in conventional uniformly-doped rod-based laser systems, resulting in non-uniform thermal loading which leads to optical distortions in the gain media. The thin-disk architecture avoids most of these distortions because it distributes its heat over a thin (100 to 200 μm) medium with a relatively large cross-sectional diameter (5 to 20 mm), so that the heat flux is oriented collinearly with the direction of beam propagation [80, 85]. By comparison, heat-flow in rod-type systems is perpendicular to propagation (Figure 10) which generates much more significant distortion of the beam. For a thin-disk, the heat distribution is essentially one-dimensional, making it several orders of magnitude more resistant to thermal distortions than rod-type systems [86].
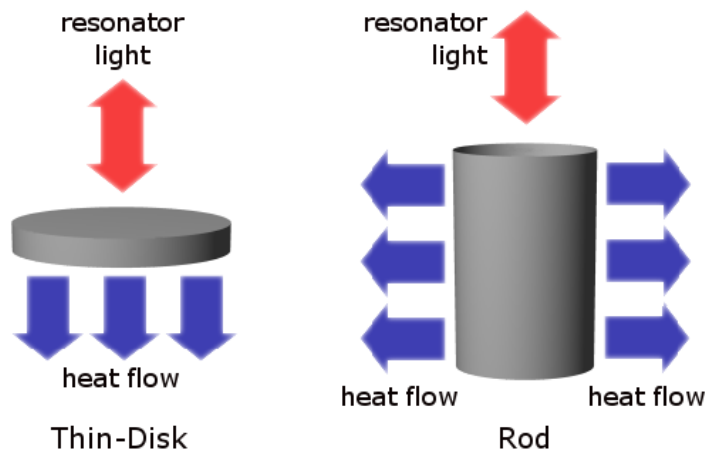
Figure 10: Comparison of heat flow in a thin-disk with a rod showing colinear heat flux

While significant gains are made in discouraging thermal distortion of the gain medium by making it so thin, it also results in a much reduced single-pass pump light absorption. In order to get adequate levels of pump absorption, it becomes necessary to recirculate the pump light in a separate "pump cavity". Often such pump cavities are designed to re-circulate the pump 16 times or more through the disk, enabling pump extraction of more than 90% [81].

19

Parabolic and folding mirrors are commonly used for pump recirculation, with one common scheme shown in Figure 11, with a relay pattern of the pump beam shown in Figure 12.
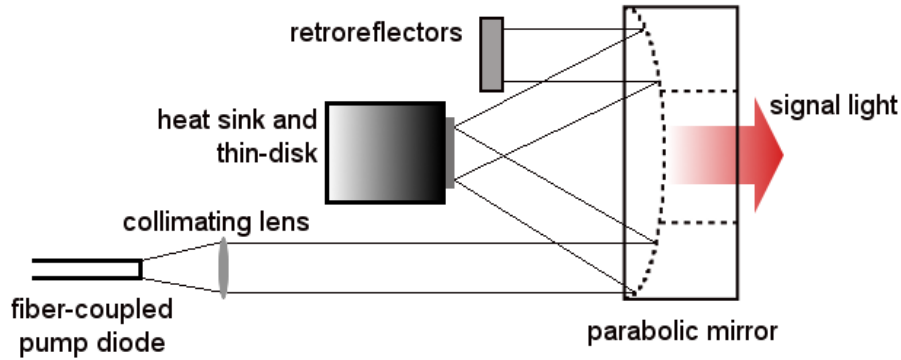
Figure 11: Side-view of a pump cavity for a thin-disk laser
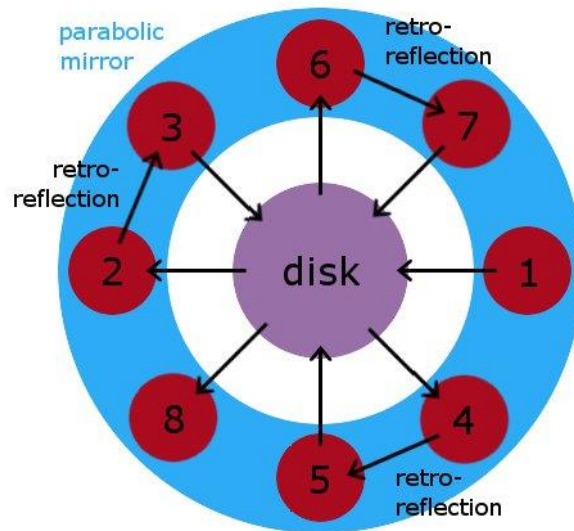
Figure 12: Retro-reflection relay pattern of parabolic mirror and thin-disk pump cavity

Ultimately the motivation behind the development of the thin-disk architecture was to improve beam quality and laser efficiency while operating at high powers and energies. Thin-disk lasers which can yield several kW of power from a single disk are currently available on the market [81]. To increase power further, scaling of thin-disk laser systems can be achieved one of two ways: incorporating multiple thin-disks in the same laser cavity (Figure 13), or by increasing the pump spot diameter while maintaining a constant pump density (Figure 14).
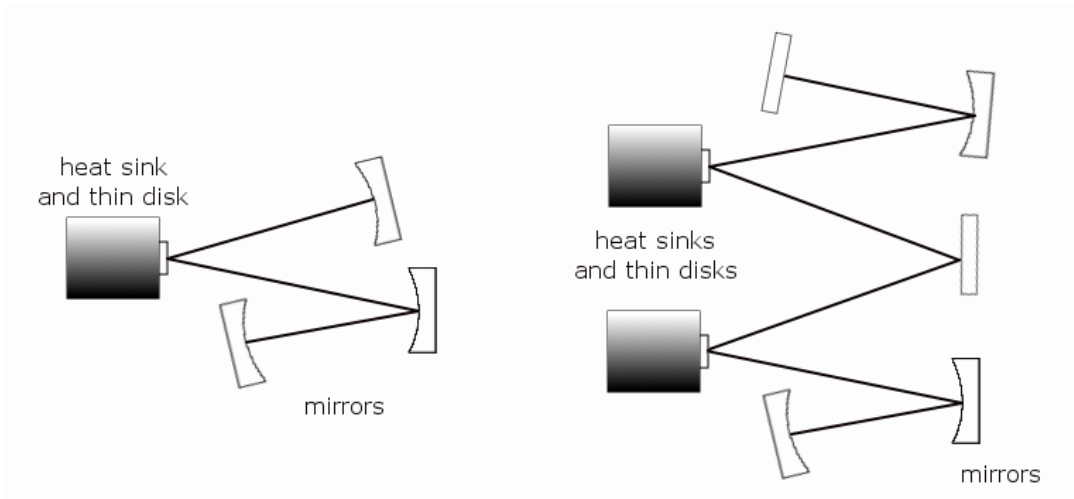
Figure 13: Multi-disk method of power scaling
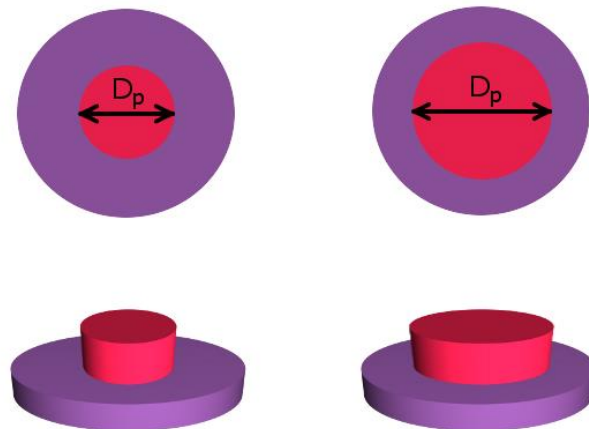
Figure 14: Power scaling by scaling pump spot size (D_p – pump diameter)

The average output power of a thin-disk laser is directly proportional to the overlap of the pumped gain area with the modal area of the beam [87]. Numerical calculations indicate that the theoretical limitations for power scaling with thin-disks extend up to hundreds of kilowatts [84]. Comparing similar cavities with 1, 2, 3 and 4 disks shows that each system has a nearly identical slope efficiency, the difference observed being in the laser threshold, which also scales proportionally to the pumped area [82]. While increasing the diameter of the pumped area is useful in scaling power, it becomes proportionally more difficult to manage thermally induced

distortions (maintain thermal homogeneity over a larger area) as the diameter of the disk increases.

Because the beam diameter of a thin-disk system is typically on the order of 1-2 cm or larger, even at high power operation (5 kW or more) thin-disk systems do not approach the damage threshold of the disk and other cavity elements (assuming similarly large mode size on all elements). Both the large beam diameter and the short length of the gain medium make a thin-disk laser relatively resistant to the non-linear effects that specifically limit fiber lasers systems. This makes a thin-disk system ideal for high peak and average power operation.

The weakness of the thin-disk geometry is that it can require large clear-aperture elements, a fact which conflated with its high power operating range, makes it difficult to incorporate components for spectral and temporal control elements directly into the cavity. Any component located in the cavity is subjected to very high intra-cavity operating powers (or energies), and so thermal lensing and distortion become a not insignificant obstacle. Further, due to the small single-pass gain of the disk medium, only very low loss components are acceptable.

As a result, while it is possible to incorporate various temporal and spectral control components into a thin-disk system, the large beam diameter and high powers can be a limitation for certain elements. By using the thin-disk as an amplifier stage it is possible to simplify some of the component requirements by incorporating them into a low power seed instead. While many different amplifier designs exist, the one of particular interest here is the regenerative amplifier, which is how the thin-disk is employed in this work. Amplifiers with a focus on regenerative amplifiers are discussed in the following sections.

2.2. Amplifiers & Amplifier Schemes

Amplifiers, which are very similar to lasers excepting that they have no feedback mechanism, exist in as many different architectures as do lasers. An amplifier is seeded by incoming light (which can make one or several passes depending on geometry) which depletes the population inversion in its gain medium, and is thereby amplified and boosted in power. For an amplifier to be able to boost the signal of the incoming light, the gain medium it contains must have an energy-level transition which can be stimulated by the seed light. Often times this means simply using the same pump wavelength and gain medium for both the oscillator and amplifier stages of the laser system, however it is possible to use different gain media or host materials so long as their emission wavelengths have appropriate overlap.

A variety of different amplifier schemes exist, some used more prevalently for certain laser architectures. These include the MOPA architecture, single and multi-pass amplifiers, regenerative amplifiers, and slave oscillators (the lattermost is an amplifier configuration which does include amplifier feedback). In addition to the level of gain necessary in the amplifier, other aspects such as the effect of the amplifier on the beam profile, potential for feedback into the oscillator, and the damage and non-linear thresholds of the amplifier itself must be considered. The sections which follow cover some standard amplifier designs with the goal of establishing a solid understanding of the MOPA technique and the regenerative amplifier type, both of which are used for the laser development portion of this work.

2.2.1. Master Oscillator Power Amplifier

A master oscillator power amplifier (MOPA) configuration is a common technique employed to provide multiple desirable output characteristics simultaneously. In this design type, a low power oscillator is used to create the desired spectral and temporal characteristics.

Control of these aspects is more easily performed at lower powers where more specialized and sensitive optical components and electronics can be used. After the desired characteristics are generated at low power in the master oscillator (MO), the output pulses can be used to seed an amplification stage which is crafted to maintain the desired input characteristics but increase the brightness of the seed signal.

The MOPA architecture is a commonly employed in high energy laser systems. NIF, as mentioned in Chapter 1, is itself an example of MOPA architecture which includes multiple stage of amplification [13]. This allows for a high level of control and parameter optimization compared to a single high power oscillator stage. However, while the MOPA system grants a significant advantage in terms of design flexibility, the exchange made for this is an increase in system complexity as this technique can significantly increase the overall number of optical components.

It is important to weigh the benefits of increased complexity and cost against the results achieved. Considering that many components either do not currently exist or cannot be built to withstand the sort of power levels generated in high energy, high average power systems, it can in many cases be the only option in terms of specific performance goals. This is currently the case with high resolution temporal shaping of laser pulses.

The MOPA architecture can be employed with amplifiers of many types, including single- and multi-pass amplifiers, as well as regenerative amplifiers. The following sections address these amplifier types.

2.2.2. Single and Multi-Pass Amplifiers

Amplifiers can be configured such that seed light passes through the amplifying gain medium one or many times based upon the power of the seed light and its ability to extract

energy from the gain medium. As the name implies, in single-pass amplifiers the seed light passes through the amplifying gain media once before exiting the amplifier stage. The ideal situation in which to use a single-pass amplifier is when there is enough power coming from the master oscillator such that a high level of energy extraction occurs in a single pass.

A trade-off exists between energy extraction and gain, as shown in Equation (9, where n is the inverted population density, σ is the stimulated emission cross-section, l is the effective length of the amplifier and a is proportional to the incoming photon flux. The higher incoming photon flux, the lower the overall gain of the output pulse, but the greater the depletion of the population inversion.

$$G = \frac{1}{a} ln[1 + e^{n\sigma l}(e^a - 1)] \tag{9}$$

Fiber lasers are often implemented as single-pass amplifiers due to the restricted geometry of the medium, and the simple nature of such a design. Such amplifiers can yield gain of as much as 30 dB, but can approach limits in terms of peak power and energy. An example of a single-pass fiber amplifier is shown in Figure 15, where the amplifier is used to boost the signal of a FBG-based linear oscillator.
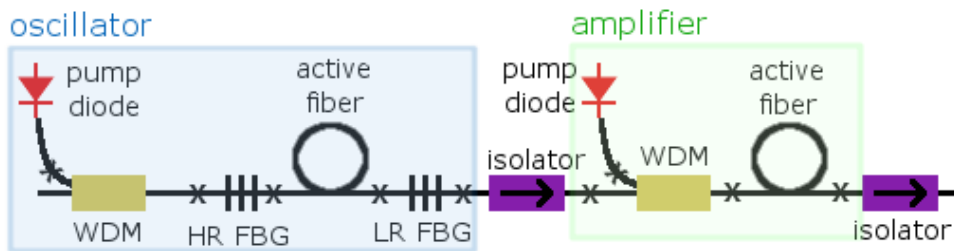
Figure 15: Fiber MOPA as example of a single-pass fiber amplifier

Multi-pass amplifiers are effectively the same as single-pass amplifiers, but allow the seed light to pass through the medium more than once before exiting the amplification stage. This is more common in solid-state lasers system where multiple mirrors can be used to walk the

beam through the gain medium more than once without retracing its path and creating parasitic feedback (Figure 16).
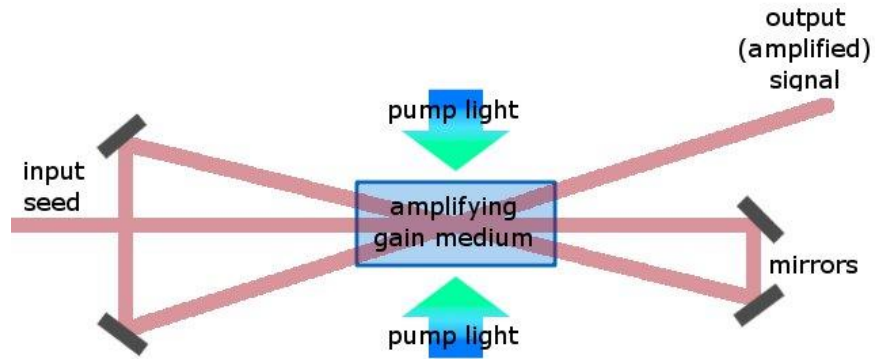
Figure 16: Basic schematic of a multi-pass (three pass) amplifier

In either case it is important to have isolation between the seed and amplifier stages in order to prevent any light from the amplifier from feeding back into the oscillator. If feedback occurs it can cause damage if the light is at a higher enough power and/or energy, or it can destabilize the spectral and temporal characteristics which have been specifically tailored in the oscillator. This is why it is particularly important that no parasitic lasing or feedback be permitted to occur between the seed and the amplifier.

Using a multi-pass amplifier allows for a higher energy extraction from the amplifier, creating greater flexibility in terms of the level of single-pass gain that is permissible with a given media. For example, because gain scales with the length of the amplifier gain medium (Equation (9), in a thin-disk amplifier the single pass gain is quite low due to the medium length of ~100's of μm. Accordingly, only a little of the energy stored in the gain medium is depleted on a single pass. However, if multiple passes can be used, the pulse increases exponentially with each pass until it begins to saturate the gain of the system. Ideally a pulse must achieve saturation fluence and deplete the gain to 1/e of its original value; otherwise the remaining un-used pump energy reduces the efficiency of operation.

26

It is possible to encounter design situations in which the saturation fluence of the gain medium exceeds its damage fluence or the damage fluence of other optics in the system, thus limiting the system efficiency. In such cases the use of multiple passes can help to increase operation efficiency without damaging the system because effective saturation fluence can be used, which is the saturation fluence reduced by a factor of N, which represents the total number of passes.

Ultimately, the use of multi-pass amplifiers broadens the range of possible gain media that can be employed in an amplifier while still maintaining a high level of amplification and good efficiency.

2.2.3. The Regenerative Amplifier

The regenerative amplifier is in a sense a multi-pass amplifier, but has a significant difference from the aforementioned geometries. In the previously discussed geometries all elements of the amplifier stage are passive except for the pumping of the gain medium and the signal travels a fixed number of times through the amplifying medium. The regenerative amplifier, however, contains active components which are able to trap the light in the amplification stage until such a time that the desired level of amplification is achieved. This allows the regenerative amplifier to achieve gain on the order to 10^6 [88]. The main purpose of a regenerative amplifier is to amplify very low energy pulses, typically on the order of nJ.

The term "regenerative amplifier" existed in electronics well before it was applied to describe what in the laser field is now known as a laser regenerative amplifier [89, 90]. The first demonstrations of optical regenerative amplifiers occurred in the 1960s [91], and has since become a common form of amplification for low-energy pulses [92-97]. The motive force

behind the development of the regenerative amplifier was a method by which to achieve high levels of amplification from low energy signals.

The active optical gate in many regenerative amplifiers is controlled by a Pockels cell (PC). The linearly-polarized pulse enters the cavity through an isolator composed of two thin-film polarizers flanking a rotator and half-wave plate (Figure 17). The pulse is initially horizontally polarized as it enters the cavity through the isolator. It then passes through the PC (which is off initially and has no effect) and is rotated by a quarter waveplate, then back through the waveplate and PC after reflecting off the HR end mirror. As a result the pulse is now vertically polarized, and it passes into the cavity by reflecting off the TFP that is included in the cavity.
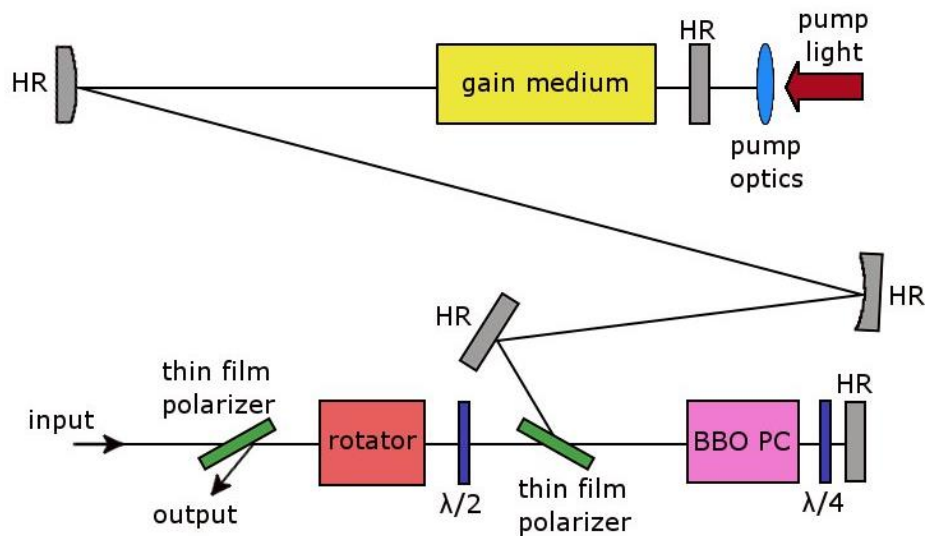
Figure 17: Generic regenerative amplifier layout (HR –high reflectivity mirror, λ/2 and λ/4 are half and quarter wave plates respectively)

The pulse travels through the rest of the cavity and is amplified by the gain medium, during which time the PC is switched on to quarter-wave voltage. When the pulse returns and passes through the PC (now on and optically active) and quarter wave plate again, it is still vertically polarized when it returns to the intra-cavity TFP, and is thereby trapped in the cavity as

long as the Pockels cell remains active. When the pulse has made the desired number of passes through the cavity, the Pockels cell is switched off, allowing the pulse to pass out of the system via the TFP.

By allowing the low-energy pulse to circulate many times through the cavity and the gain medium, the pulse is able to saturate the gain and achieve optimal energy extraction. However, the amount of amplification per pass is typically fairly low, sometimes less than 1 dB. Therefore for a regenerative amplifier to be effective, all the elements in the cavity, particularly the transmission elements, must be very low loss. Even a small amount of loss multiplied by tens of passes can severely reduce the efficiency of the amplifier.

2.3. Ytterbium and the Rare Earths

The rare earth metals are elements which include the scandium, yttrium and the lanthanide series of the periodical table. Rare earths are useful for a variety of applications because when they are alloyed with other metals they enhance the magnetic response and improve the high temperature tolerance of the material [98, 99]. These elements are also used extensively in today's electronics market, from computers and cell phones, to fluorescent light bulbs and high-power magnets in electric generators for items such as electric and hybrid cars [100]. They are considered a valuable commodity on the global market, so much so that there is considerable interest in how to recover them from disposed consumer electronics [101].

One application of rare earths that is of special significance is as dopants for laser gain media. In particular neodymium, erbium, holmium, thulium and ytterbium have been used extensively as dopant ions for various types of laser systems [102-108].   These ions typically operate as 3- or 4-level laser systems. As dopants in a crystal or ceramic they displace an ion of similar size and charge. A common example of this is Nd:YAG where the trivalent neodymium

29

ion replaces a trivalent yttrium ion in the crystal lattice. Yttrium itself is a rare earth, but not used for laser action. However, this means that it has a similar size and charge to other rare earths. YAG in particular is a common host media for doping with the rare earths, with other common materials including vanadates (such as YVO_4), tungstates and fluorides [109-111]. Typical doping concentrations are very low, with the doping ion displacing only a few percent of the total number of host ions in the material.

The energy level structure of each ion varies, making their pump and emission cross-sections and wavelengths different, as well as their efficiency and the applications for which they are useful. They were studied as fiber laser dopants starting in the 1960s but did not see much expansion until the 1980s and have since become a very substantial field and market [68]. While erbium, holmium and thulium all emit in the near to mid-infrared (mid-IR) region, ytterbium and neodymium are most commonly used at 1 μm. These key rare earth laser dopant ions will be discussed in the following sections comparing and contrasting their qualities and applications. This will give a contextual understanding for the selection of ytterbium as the dopant for the laser system presented herein. Ytterbium will subsequently be discussed in the fiber and thin-disk architectures.

2.3.1. Quantum Defect

During the discussion of the various rare earth dopants, a quantity called quantum defect (QD) is useful for the comparison of their efficiencies. QD is a quantitative value representing how much pump energy is lost in the conversion of light at the pump wavelength to output signal. The QD gives the highest theoretical efficiency possible as a function of the energy level structure, without accounting for parasitic effects that can also reduce laser efficiency, such as non-radiative transitions away from the upper laser level.

30

QD is defined in Equation 10, where ΔE is the energy difference between the upper state of the pump transition and the upper state of the signal transition, h is Planck's constant, v_p is the frequency of the pump light and v_s is the frequency of the signal light. Thus, QD is the ratio of the energy lost in the conversion of the light from pump to signal wavelength with the energy of the pump light (Figure 18).

$$QD = \frac{\Delta E}{E_{pump}} = \frac{hv_p - hv_s}{hv_p} \qquad (10)$$
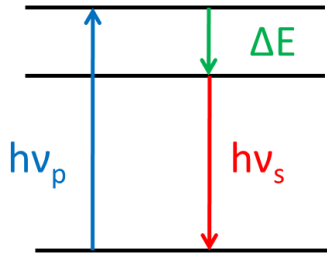
Figure 18: Energy levels and transitions of a generic laser system

A high QD does not guarantee a high efficiency operation of the laser system, but it does give an upper limit for possible efficiency. The QD will be referenced in the discussion of the following rare earth ions.

2.3.2. Neodymium

Neodymium is one of the most widely used rare earth elements in solid state laser systems. This was originally due to the absorption features it has, which are especially wide, with major peaks occurring at ~730 and ~800 nm [112]. This makes Nd-doped host material one of the more efficient media types for flash lamp pumping. In the early days of the laser, the flash lamp was the first and the most common method for pumping laser systems. A flash lamp effectively emits black body radiation, and the broad absorption features of Nd enable relatively efficient absorption.

As appropriate laser diode pump sources have become available, the use of flash lamp pumps has waned in use. However, because efficient diode pumping is also possible for neodymium, it is still a very common laser gain medium, and a market demand still exists for flash lamp pumped Nd systems. There are a variety of medical and industrial applications that utilize Nd-based lasers including: eye surgeries, hair removal, removal of fungal foot infections, and engraving, etching, marking and welding of plastics and metals [113-116]. In addition to diode pump sources, certain applications still exploit the broad nature of Nd's absorption features such as solar pumping [117, 118]. The absorption features of Nd create a good overlap with the emission wavelengths of the sun, making pumping possible.
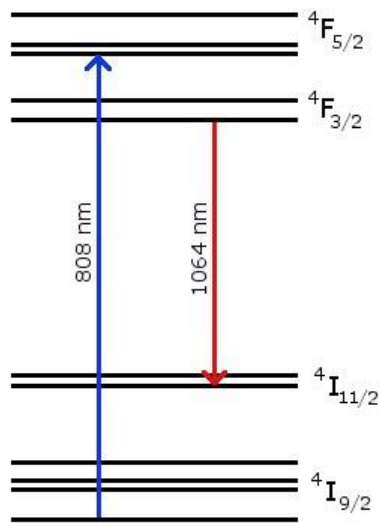
Figure 19: Energy level structure of Nd:YAG

The electronic transitions of Nd are shown in Figure 19. When diode pumping is employed, Nd:YAG is typically pumped at 808 nm with laser action occurring at 1064 nm, and a variety of high brightness diodes exist on the market at around ~800 nm. Other examples of host materials include Nd:YLF which can be pumped at 796 nm and emits at 1047 and 1053 nm [119], and Nd:YVO$_4$ which can also be pumped 808 nm and emits at 1064 and 1342 nm [120].

This transition sequence has a quantum defect of 24.1% (808 nm/1064 nm) in a YAG host [121], and has demonstrated a tuning range of 60 nm from 1057 to 1118 nm in silica fiber [68].

2.3.3. Erbium

Erbium is most typically used to generate signal light around 1.5 μm or 3 μm, dependent largely upon its host material. It can be tuned from 1.48 to 1.62 μm in silica fiber [122]. In silica fiber it is often used for telecommunications applications, particularly in erbium-doped fiber amplifiers [123]. Because silica is very low loss at 1.5 μm, operation at this wavelength enables very long propagation distances. In hosts such as YAG it can be used to generate signal near 3 μm [124] which is readily absorbed by water, making it common to be used for skin resurfacing and other laser skin treatments [125]. Er:YAG systems are also often used in dentistry for the ablation of enamel and can be used to cut bone in other medical procedures [126].
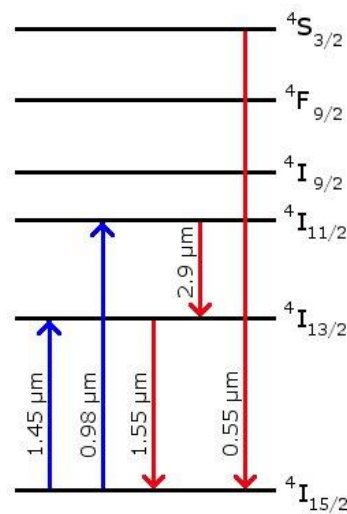
Figure 20: Energy level structure of Er:YAG

Erbium based lasers, however, typically lack high efficiencies and output powers [127]. This is due to a low absorption cross-section at the most potentially efficient pump wavelengths ($\sigma < 10^{-25}$ m^2 at 1480 nm in Ge:silicate and Al:Ge:silicate fibers [128]) and to large QD values

for other transitions which have better absorption. The absorption cross-section at 1480 nm (or 1450 nm depending on its host medium) is small enough such that 10's of meters are necessary for efficient pump absorption. In-band pumping of Er:silica fiber at 1480 nm can be performed to produce signal output at 1555 nm and has a QD of <5%. However, the 1480 nm pump light itself can create stimulated emission when it is not absorbed, and so the gain of such schemes can be limited a low level [129], though more recent developments are showing improvements in scalability, with demonstrated output exceeding 100 W [130].

When Er is pumped around 980 nm, it has a short non-radiative transfer time from the $^4I_{11/2}$ level to $^4I_{13/2}$ which prevents the pump light from causing much stimulated emission, and for Er:YAG produces emission at 1.55 µm [131]: a 37% QD (Figure 20). Flash lamp pumping of Er:YAG can also be performed to create emission at 2.94 µm, but yields efficiencies around 1%. Emission at 0.55 µm can be achieved through up conversion pumping as well [132] and can yield efficiencies in the high teens [133].

In order to achieve good efficiencies erbium is often co-doped with other rare-earth ions, particularly ytterbium [69]. Pumping is performed at an absorption wavelength appropriate for Yb, and energy is transferred from excited Yb ions to Er ions, which then emit to produce laser action (the efficiency of which can be reduced by various upconversion process). However, at high powers (around 300 W) parasitic lasing at a Yb ion transition overtakes the desired Er transition [70]. Co-doped media using Er/Yb or Er/Cr can also be pumped in a relatively efficient manner using flash-lamp pumping due to its broad absorption features. However, overall, the power levels attainable by Er-based lasers are limited, with the application of Er systems thus restricted to the low to mid power arena.

2.3.4. Holmium

Holmium has two prominent transmission regions, one near 2.1 μm, and the other at 2.9 μm, representing $^5I_7$ to $^5I_8$ and $^5I_6$ to $^5I_7$ energy level transitions respectively [134]. The strong absorption values of water at these wavelengths makes it useful for applications such as tissue cutting, skin resurfacing and dentistry as well as microwave applications [135-137].

Like erbium, holmium is hindered by a lack of high brightness pump sources, particularly diode sources, at the appropriate wavelengths. Direct pumping of holmium at 1.9 μm has been demonstrated, typically with thulium-based laser systems [102], but is limited in terms of power scaling. And because thulium can operate at 2 μm and beyond, when a Tm source is available for pumping a Ho system, it can be simpler to use the Tm source directly for the application and eliminate the additional step into pumping holmium. While holmium can emit at longer wavelengths than thulium, the transmission cut-off wavelength for silica fiber is very near to those emission wavelengths [138], limiting its utility in the fiber laser architecture.

As with erbium, holmium can be co-doped with ytterbium or thulium to improve absorption [139]. Excited ytterbium and thulium ions act as sensitizing ions which absorb pump light and transfer energy to holmium ions which then radiate. However power is limited due to problems with ASE and parasitic lasing at thulium and ytterbium wavelengths. In thulium co-doped systems the energy transfer between excited thulium and holmium ions is reversible, which along with up-conversion losses, impose additional limits on the maximum output power.

2.3.5. Thulium

Thulium's main transition of interest is centered around 2 μm. While all the rare earth dopants display a fairly large gain bandwidth in silica fiber [73], thulium's is the broadest with a range of ~300 nm from 1.86 – 2.09 μm [68, 140]. The wavelength and tunability of thulium

make it useful for long distance atmospheric propagation because of transmission windows present in the atmosphere which overlap well with thulium. It is also useful for medical applications, such as tissue ablation, which require strong absorption [141, 142].
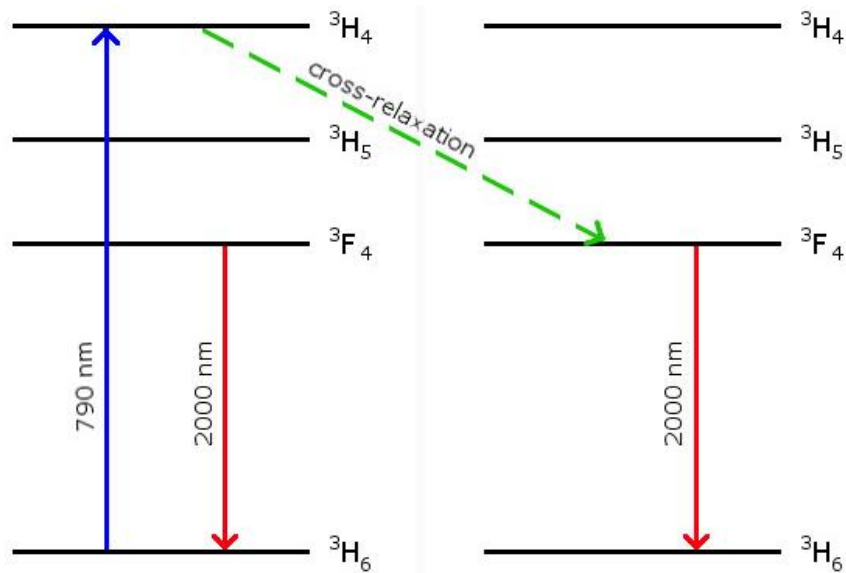
Figure 21: Cross-relaxation Between Two Adjacent Tm^{3+} Ions

Pumping at 790 nm with commercially available and inexpensive diode sources makes use of a cross-relaxation process which can double the theoretical efficiency of the laser system. The $^3F_4$, $^3H_4 \rightarrow {}^3H_6$, $^3H_6$ transition (Figure 21) is what is referred to as the cross-relaxation process. A 790 nm pump photon is absorbed by a Tm^{3+} ion causing an electron to transition to the $^3H_4$ state. Roughly half the energy from the excited ion is transferred to a neighboring ion in a ground state such that each ion has an electron in the $^3F_4$ state. From $^3F_4$ both ions relax and emit light at 2 μm. This process thus allows for two signal photons to be generated from a single absorbed pump photon and is often referred to as "2-for-1" process [143]. However, cross relaxation can only occur when the appropriate concentration of thulium is present, which can be as low as 1.3 wt.% [144, 145]. The quantum defect of thulium for this transition (790 nm pump,

~2000 nm emission) only allows for 40% efficiency, but the cross relaxation process can effectively double it to ~80% [138, 140].

In terms of overall efficiency Tm is not the best among the rare earths, but because of its tunability, the availability of efficient pump sources, and its eye-safe wavelength, it is an attractive source for the right applications. Comparing thulium to shorter wavelength sources, such as ytterbium-based systems, its longer wavelength allows it to operate single-mode in larger mode area fibers than is possible at shorter wavelengths. And because the radius of confinement affects various non-linear processes, the thresholds of these processes such as stimulated SRS and SBS are raised [146, 147].

2.3.6. Ytterbium

Ytterbium has a simpler energy level structure than other rare earth dopants, with only one excited state manifold directly accessible with available visible and mid-IR pump sources. The QD of ytterbium is consequently very small, as low as 3%. Various high brightness diode sources between 900 and 1000 nm have been developed to economically and efficiently pump Yb-based laser systems [148, 149], which combined with its low level of waste heat, makes it popular for high power operation in various architectures. High power ytterbium lasers are often used for industrial cutting, welding, and machining of various materials [150-152]. Its thermal properties and large absorption cross-section make it especially useful for the thin-disk architecture, and has been demonstrated in high power fiber laser systems as well [148].

Typically Yb-based lasers operate at 1 μm by way of a transfer process from $^4F_{5/2}$ to $^4F_{7/2}$ and pump wavelengths between 900 and 1000 nm. Depending on the host material, ytterbium can have a quantum defect of only 2.9% in crystalline $GdVO_4$ [153] and 5% in silica fiber [154]. Because of energy transfer processes that are possible between Yb and other rare-earth ions, it is

also often used as a sensitizing agent, facilitating absorption and excitation of the co-doped ions. However, these schemes are typically limited in output power due to parasitic lasing that begins to occur at ytterbium-related transitions.

The efficiency of ytterbium as a dopant, the low level of thermal waste it yields, and the ready availability of 1 μm components make it an excellent candidate for this work. In the following sections, the operation of Yb fiber and thin-disk architectures will be discussed, both in terms of operating principles and prior published works.

2.4. Ytterbium in Silica Fiber

Initial work with ytterbium in fiber lasers was primarily focused on its application as a sensitizer for other rare earth dopants [155], though it was first demonstrated as a glass dopant in 1962 [156]. Due to the narrowness of its main absorption band, pumping via flash lamp yielded low efficiencies, and it did not become a popular high-power dopant until the advent of diode pump sources and double-clad fiber structures. Currently the majority of high power fiber lasers are based on ytterbium-doped silica fiber [140], and they can even be purchased commercially at powers of up to 100 kW [157].
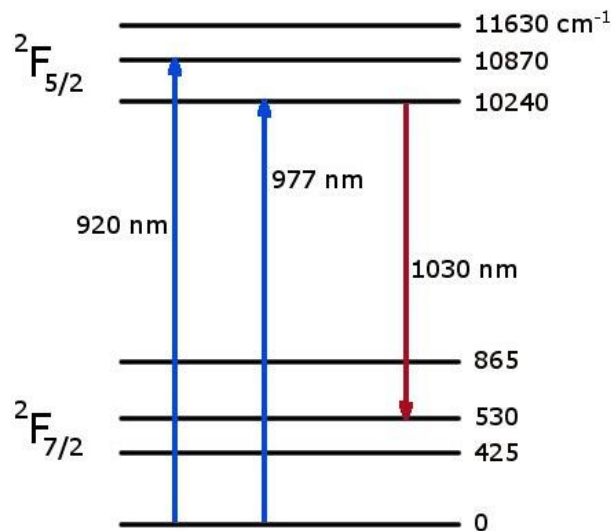
Figure 22: Energy levels and transitions of Yb:silica

38

When doped in silica fiber, ytterbium has a laser tuning range of 118 nm [56, 158]. It can be pumped directly with relatively inexpensive high power diodes emitting at 910 and 975 nm, and can emit at 1030 and 1080 nm [148, 149] with the transitions of interest occurring between the $^2F_{5/2}$ and $^2F_{7/2}$ energy levels (Figure 22).

Fiber lasers based on ytterbium are operated in many different temporal regimes, from CW to ultrafast operation with pulses of femtosecond duration. Ytterbium's broad emission enables it to produce very narrow temporal pulses, with its gain bandwidth supporting ~30 fs pulses [159]. It also possesses a long upper-state lifetime (~1 ms) which makes it well suited for longer Q-switched pulsing due to its large energy storage capacity in the upper level of the laser transition. Energy storage is defined in Equation (11, where J is stored energy, hv_s is the energy of a signal photon and n is the inversion population. The inversion population is proportional to the fluorescence lifetime of the upper level, so the longer the fluorescence lifetime the greater the capacity for energy storage. However the peak power that can be extracted is limited by non-linear effects when used in fiber geometry. In certain pulsed regimes the high peak powers that Yb can generate can be used for applications such as supercontinuum generation [160].

$$J = hv_s n \tag{11}$$

When the telecommunications industry took off in the 1980s and 1990s, the wavelength region between 1 and 1.5 μm was exploited because of the low-loss of silica fiber within this range. Extensive research and resources were put into developing this wavelength range in order to achieve better and more efficient transmission and component integration. The development of high average power Yb:fiber lasers rapidly accelerated in 2000 as a result of the transition of investment after the fall in the telecomm market.

Availability, combined with high efficiency, good thermal handling and architectural advantages make Yb³⁺-doped silica fiber lasers a good choice for master oscillator. While the ability of ytterbium to yield high power output will not be exploited in the fiber portion of this dissertation, the design capitalizes on the ready availability of various 1 μm components.

2.5. Yb:YAG Thin-Disk Lasers

The first demonstrated thin-disk laser was single-crystal Yb:YAG [24] and this remains the most common combination of dopant and host medium for the thin-disk architecture. The thin-disk architecture was specifically designed with InGaAs diode pumping of Yb:YAG in mind due to the convenience and efficiency of the associated transition, as stated in the 1994 publication by Giesen et al. [24].
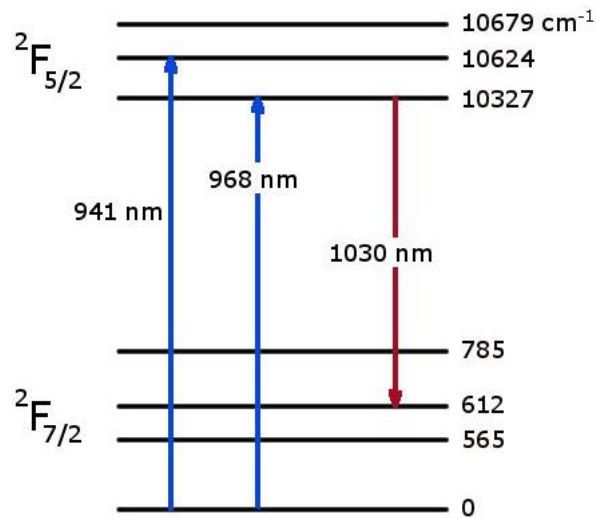
Figure 23: Energy level and transitions of Yb:YAG

Ytterbium's aforementioned small QD (8.6% in YAG) [102] enables a theoretical quantum efficiency of >91% in YAG when emitting at 1030 nm (Figure 23). This results in a low level of waste heat and a high potential laser slope efficiency. Due to simplicity of the energy level structure of Yb:YAG, with only one upper state manifold, there is effectively no upconversion or excited state absorption. The mechanical features of the material are also good,

with both a high thermal conductivity to aid the dissipation of waste heat, and good tensile strength which helps to reduce the fragility of the disks which are intentionally polished down to such narrow thicknesses.

The high absorption of Yb:YAG is also good for addressing the low single pass absorption characteristic of thin-disk lasers. For a thin-disk laser to achieve the superior thermal characteristics described above, it is requisite that the disk to be roughly ~200 μm or less. This allows for high operation efficiency and minimal waste heat, but conversely results in a very low single pass absorption. Because Yb:YAG has strong absorption features and can also be doped to relatively high concentrations, as much as 20% and up without destructive quenching effect or significant lattice distortions, the low single-pass absorption can be overcome. This makes it possible to create efficient Yb:YAG systems with crystals 200 μm thin or thinner, whereas other materials that have been explored, such as Tm:YAG [161] and Ho:YAG [162], can require a crystal thickness that leads very quickly to prohibitive levels of thermal distortion.

Yb is used as a dopant in YAG as well as other host materials such as YVO_4, YLF and various tungstate materials (including $KGd(WO_4)_2$, $KY(WO_4)_2$, $NaGd(WO_4)_2$, and $NaY(WO_4)_2$), and has several properties which make it especially useful for pulsed operation. These include a small emission cross-section (which allows for buildup of a large population inversion and high gain), a long upper-state radiative lifetime (~1 ms), and emission features which have enough bandwidth to enable pulses of a picosecond duration.

The drawback of Yb:YAG is that as a quasi-three-level laser system, it requires a low mean temperature in order to minimize the thermal population of the lower level of the laser transition. This results in a high pump density threshold, needing >1.5 kW/cm^2 at a temperature of 300 K [24]. Such a high pump density can result in large quantities of waste heat and thermal

distortions, and as such, the high level of thermal extraction that is possible in thin-disk architecture is particularly well-suited for quasi-three-level systems [163].

Yb:YAG thin-disks have been demonstrated in continuous wave, Q-switched, and ultra-short pulse operation, and can be configured as either oscillators or amplifiers. In the context of this work, the thin-disk employed is operated as a regenerative amplifier which can maintain a high input seed beam quality while dramatically increasing the power of the input seed signal. Thin disks have already been demonstrated as regenerative amplifiers, a configuration which has been shown to achieve gain levels of roughly 10^6 [88].

Successful demonstrations of high power Yb:YAG thin-disk regenerative amplifiers include a system demonstrated in 2009 was able to produce pulses at 3 kHz and 25 mJ with 1.6 ps duration [97, 164]. Another Yb:YAG thin-disk regenerative amplifier yielded pulse energies of 4.5 mJ at a repetition rate of 1 kHz with a 4.5 ps duration [94]. Similarly, a Yb:KYW thin-disk regenerative amplifier was seeded by a commercial Yb:Glass laser, and yielded 250 fs pulses at a 40 kHz repetition rate with 116 µJ of energy per pulse [96].

2.6. Fiber Seeded Thin-Disk MOPA System

The laser system developed herein is a fiber-seeded thin-disk MOPA laser system. The system is designed to generate high power temporally tailored pulses to improve the efficiency of various laser-material interactions. Producing high energy pulses with custom-designed pulse shapes in a single-stage system would prove difficult, as the desired energies would reach the damage thresholds of the more delicate components used for the temporal shaping and spectral control, which is why a MOPA scheme is employed. Ultimately the thin-disk regenerative amplifier provides a gain of $7.7 \cdot 10^5$ and yields pulse energies of up to 62 mJ with good beam quality.

CHAPTER 3:   LASER DEVELOPMENT: EXPERIMENTAL SETUP AND PERFORMANCE CHARACTERISTICS

In this chapter the design and characterization of the laser system is described in detail. First the fiber portion of the laser, various tailoring components, and the modulator for pulse shaping and pre-amplification are described. Subsequently the operation of the free-space portion of the laser including the thin-disk is described. Several different thin-disk system designs are explored, both non-seeded and seeded. Finally the overall system performance of the hybrid seeded system is presented along with modeling of the laser performance.

3.1. Fiber Seed

The "master oscillator" portion of the hybrid system consists of a 1030 nm seed diode with components for pulse carving, and a pre-amplification stage. The pulse carving is performed by a Mach-Zehnder type modulator in combination with a waveform generator in order to carve the temporal pulse shapes from the CW seed diode. These pulses then pass through a fiber pre-amplifier stage before being collimated in free space for pulse picking. This section describes the design and performance characteristics of these stages.

The fiber coupled Fabry-Perot seed diode (QPhotonics AFLD-1030-100S) is temperature tuned to a wavelength of 1030.5 nm at 34ºC (Figure 24) in order to match the preferred oscillating wavelength of the disk in the regenerative amplifier (1031 nm). In observing the spectrum of the seed diode, it was noted that the Fabry-Perot cavity which stabilizes the seed diode wavelength allows for several modes to oscillate simultaneously, resulting in a fluctuation in the output wavelength, though the main peak consistently presents at 1030.5 nm. This has a small effect on stability of the output power, which will be discussed in greater detail later. The seed diode has a slope value of 0.57 mW/mA with a maximum power of 100 mW (Figure 25).
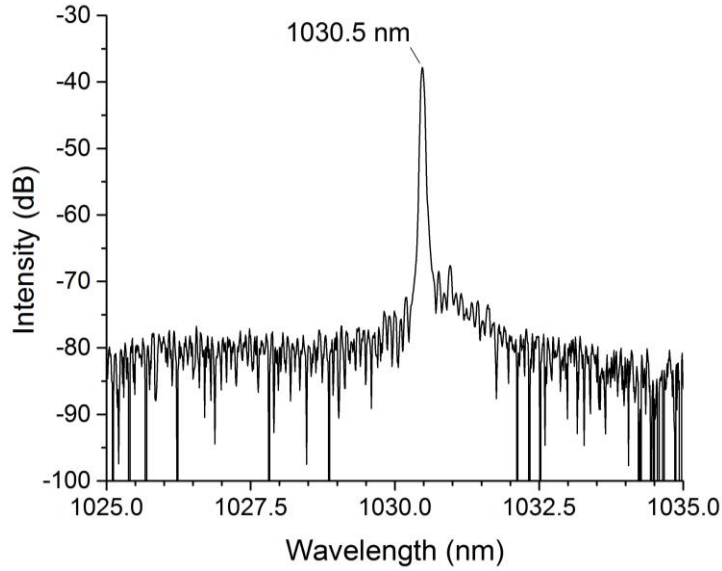
Figure 24: Output spectrum from seed diode
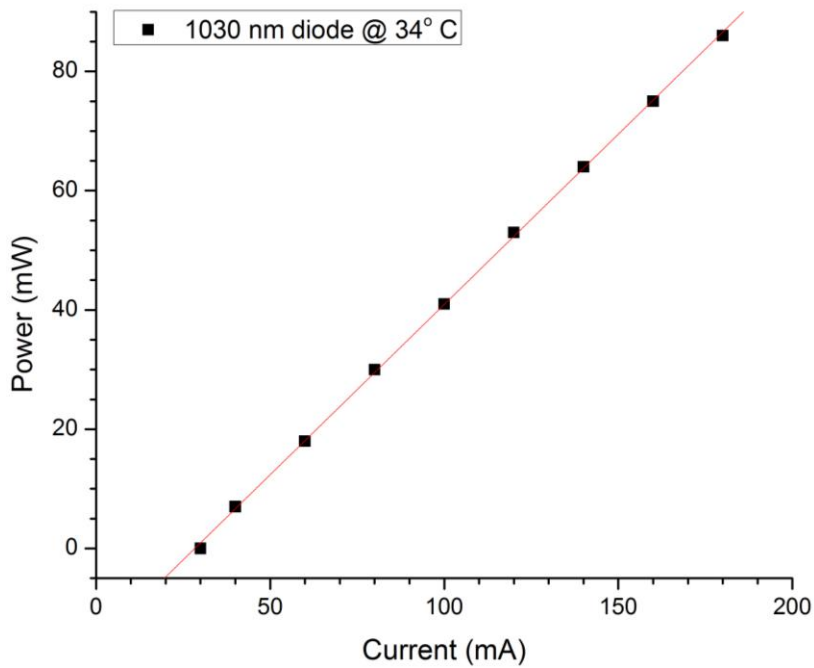
Figure 25: Slope of the seed diode

Output from the seed is isolated using a 1 W fiberized isolator (Oz Optics FOI-11-11-1030-6/125-P-50-XX-1-1-30-HP1). The seed diode output is linearly polarized, however the delivery fiber from the device is non-PM. Due to polarization instability and rotation in the delivery fiber there is polarization-induced loss when the light enters the 1 W isolator, which

44

transmits only light polarized along the slow-axis. While observing the total power output from the isolator the fiber was stressed and then secured in place with a loss of ~1.25 dB and a maximum output after the isolator of 74 mW.

The temporal stability of the isolator 1 output was examined on a longer timescale. Temporal variation of the seed will cause pulse-to-pulse variation of the carved pulses and ultimately in the output of the regenerative amplifier. The temporal variation was found to be ±12% of the output signal of the seed (Figure 26). This variation could be the result of some combination of spectral and polarization fluctuations of the seed diode output. However, this level of variation alone should not seriously limit the performance of the overall system.
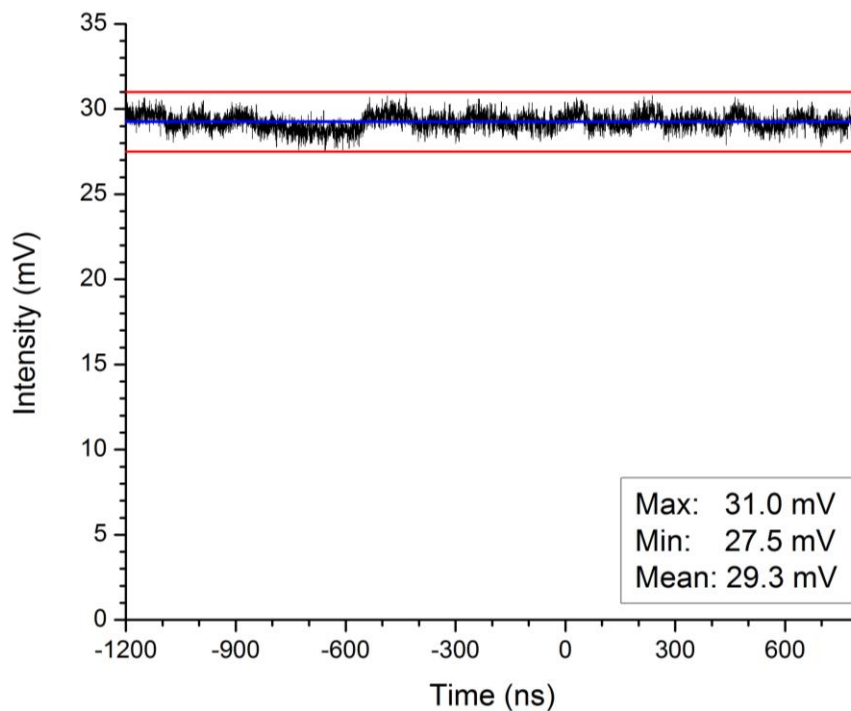
Figure 26: Temporal signal from the output of isolator 1 with the maximum (red), minimum (red) and mean (blue) of the signal marked

The output from the first isolator is sent through a 30 dB polarizer (AFW ILP-30-B-1-7-0-SA) in order to achieve the best possible modulation depth in the Mach-Zehnder device (Photline NIR-MX-LN-10-PD-P-P-00-00) and the output of the modulator is protected with

45

another isolator of the same type (Figure 27). The modulator has a loss of 6 dB, and as a result a maximum of 17 mW is transmitted through isolator 2 (Figure 28).
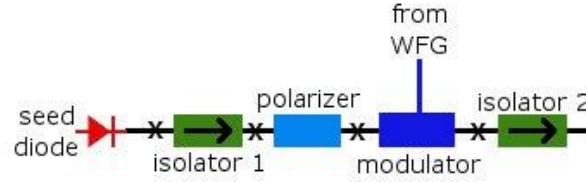
Figure 27: Front half of fiber seed from 1030 nm fiber system from seed diode to isolator 2 (WFG - waveform generator)
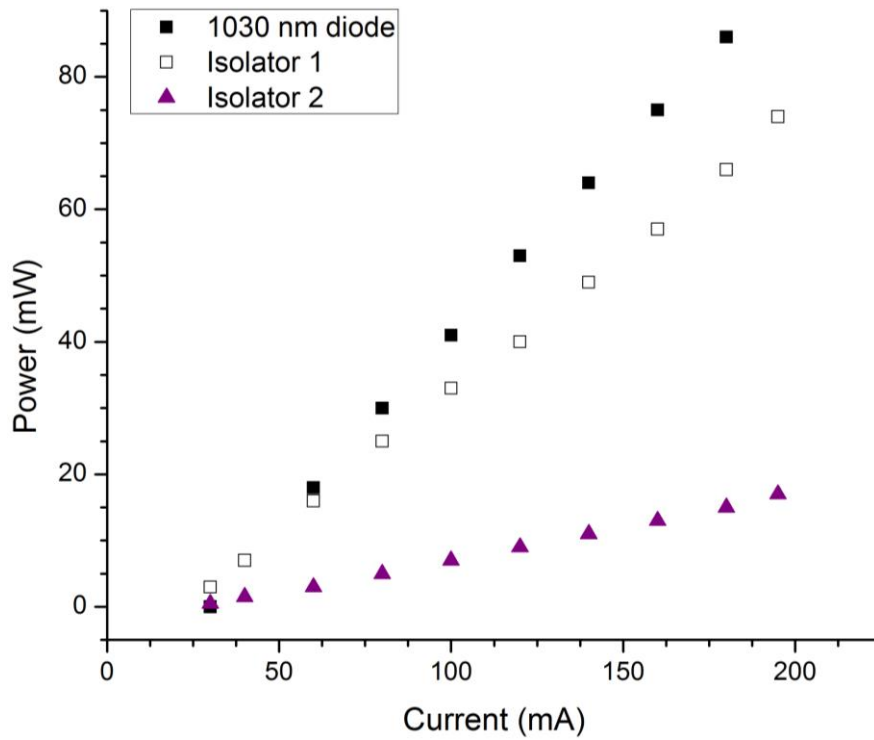
Figure 28: Total output power from the diode, and the first and second isolators as a function of seed diode current
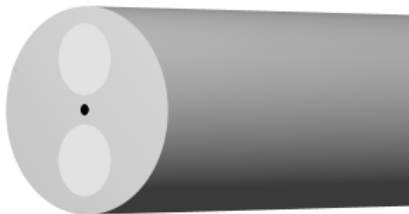
Figure 29: Panda-type PM fiber

46

All fiber used, excepting the delivery fiber of the seed diode, is panda-type polarization maintaining (PM) single mode fiber (Figure 29), which preserves the incoming linear polarization, and all devices have the fast-axis blocked on transmission.

3.2. Pulse Shaping

The purpose of the modulator is to create tailored pulse shapes which will ultimately be amplified to the mJ level. An Agilent 33521A arbitrary waveform generator (WFG) with programmable pulse shaping capabilities is used to drive the modulator. The modulator is an x-cut lithium niobate Mach-Zehnder type intensity modulator with an electro-optic bandwidth of >12 GHz. The WFG has a rise/fall time of 8 ns and a bandwidth of 30 MHz.

Using Agilent's BenchLink Waveform Builder Pro Software [165], arbitrary waveforms can be generated with a resolution of 16 ns (due to the 62.5 MSa/s maximum sampling rate of the device) with selected pulse durations ranging from 16 to 30 ns, and is operated at 1 MHz. The repetition rate of 1 MHz is discussed in the following section relating to the pre-amplification stage.

The required inputs and driving configuration for the intensity modulator include the optical signal, a tunable DC bias voltage (V_{bias}), and a driving RF signal which defines the shape of the pulses to be carved (Figure 30). The modulator operates best when driven with an RF signal that has a peak-to-peak voltage (V_{pp}) of 3 V or greater, which can be provided directly by the WFG. The V_{bias} level sets the phase delay between the two arms of the Mach-Zehnder interferometer, and for these experiments is tuned until the transmission is zero when the RF signal is zero.

In this configuration when the applied driving signal is non-zero it proportionally increases the transmission of the modulator. Because the transmission follows the shape of the

47

incoming RF signal, pulses of the same shape are carved from the input optical signal. This creates pulses of whatever desired shape that the WFG can create, but results in a significant drop in average power, with a peak power equivalent to the incoming CW signal power. The loss in power that results from the carving process is what necessitates the fiber pre-amplification stage in order to seed the thin disk amplifier.
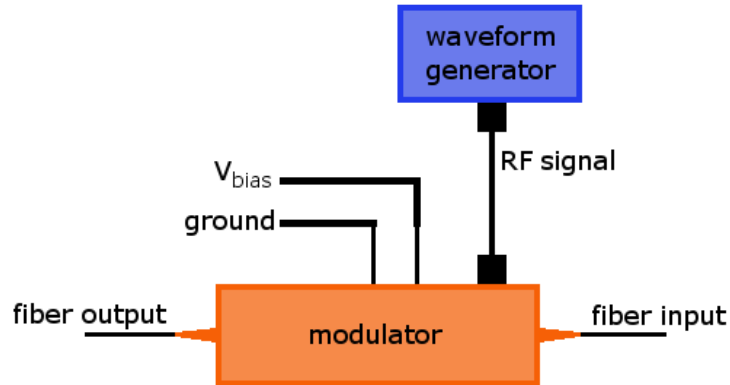
Figure 30: Inputs necessary for driving the intensity modulator

The performance of the modulator was first characterized using a stable low power ASE source (Figure 31). The ASE source consists of a ~1 m length of active fiber pumped by a 976 nm diode. This is followed by an isolator to prevent any feedback, then by a bandpass filter which reduces the ASE spectrum down to 8 nm, from 1026 to 1034 nm. A polarizer is used to ensure good carving contrast and the signal is sent into the modulator. This configuration gives the lowest possible noise level for the characterization of the device. Output from the modulator is measured using a fast photodiode with a 1 ns rise/fall time and an oscilloscope.

The necessary applied V_{bias} value for zero transmission between pulses depends on the V_{pp} of the driving signal in a linear fashion, with their respective values plotted in Figure 32. If the V_{pp} is changed but the V_{bias} is not appropriately adjusted, transmission through the modulator between pulses becomes non-zero. This effect is shown in Figure 33 where a square modulating

pulses is applied and the V_{pp} is varied. In this case the V_{bias} was optimized for $V_{pp} = 4$ V and then left fixed at this value (~6.5 V) while V_{pp} was tuned.
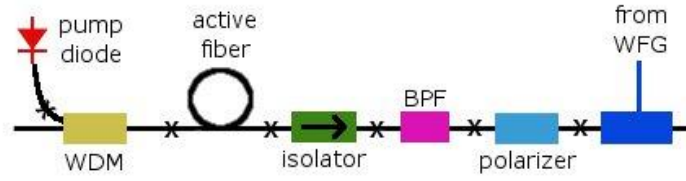
Figure 31: Schematic of ASE source used for initial characterization of modulator
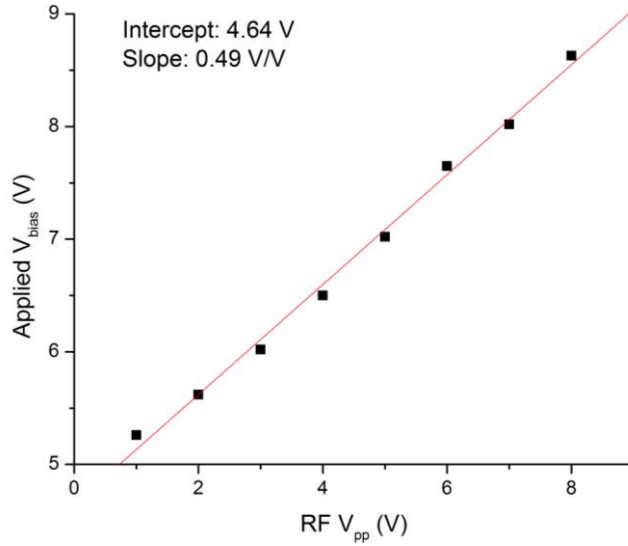
Figure 32: Linear relationship between the V_{pp} of the modulating RF signal and the V_{bias} level necessary for zero transmission between pulses (as measured for a square pulse)
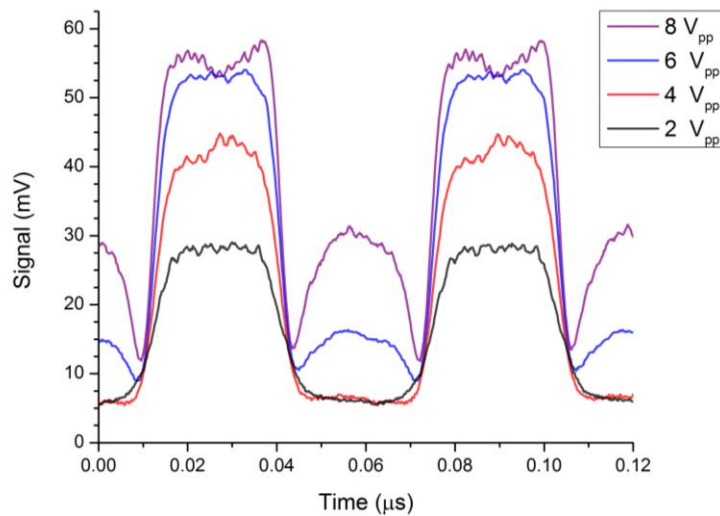
Figure 33: Leakage of signal between pulses when V_{bias} is a fixed value (optimized for $V_{pp}=4$ V) as different values of V_{pp} are applied

49

Using Agilent's software for creating custom waveforms, several custom shapes were created and loaded into the WFG. These signals were recorded twice: the electrical signal as measured directly by the oscilloscope and then again using the photodiode to monitor the optical signal output by the modulator while it was being driven. The signals showed a high level of fidelity and indicated that the modulator is performing as specified (Figure 34).
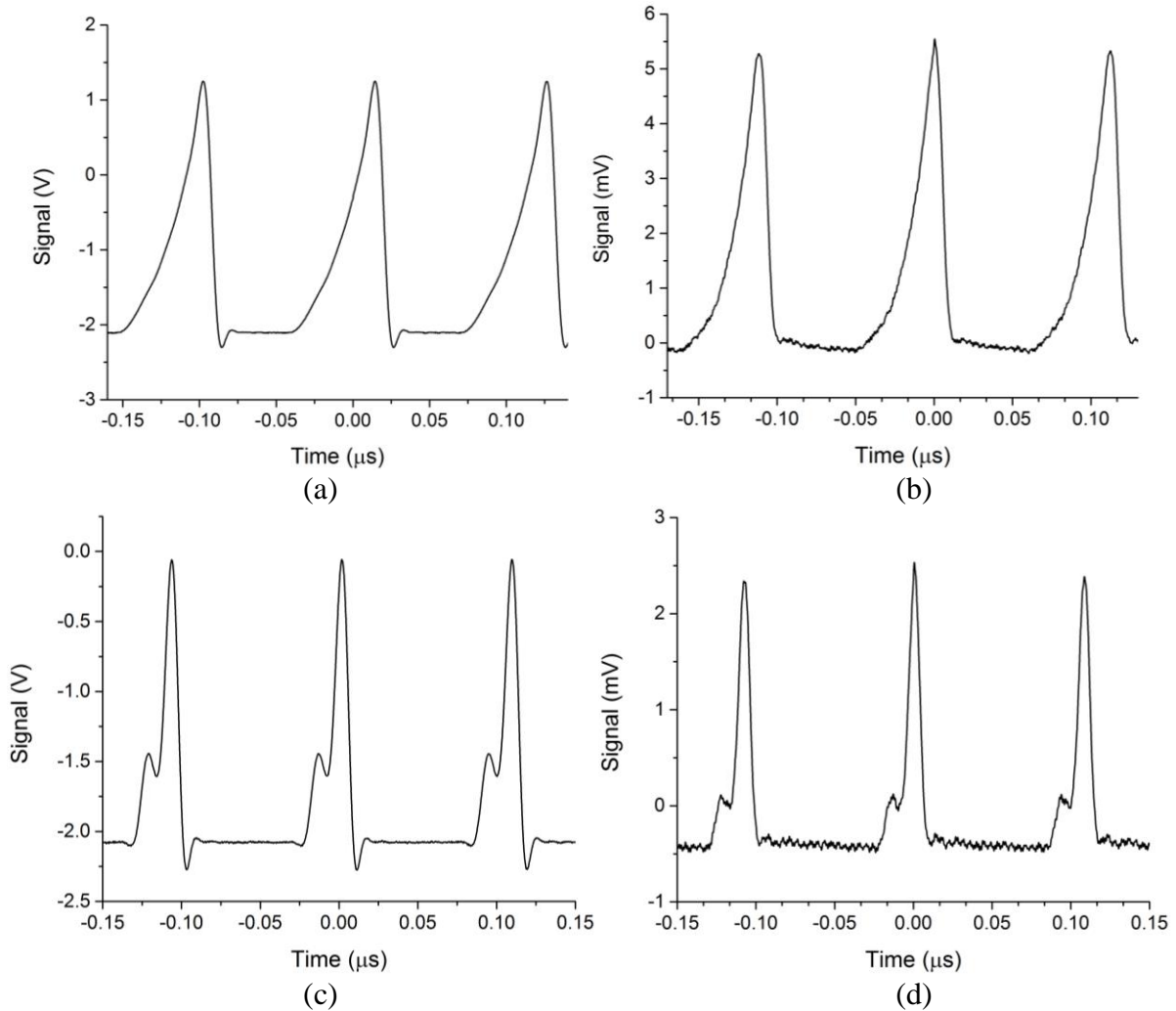
Figure 34: Pulse carving with WFG and modulator: a) and b) being the same shape as output from the WFG and the detected output from the modulator, with c) and d) being the same respectively for a second shape

Once the performance of modulator was confirmed, it was assembled into the system shown in Figure 31. These same pulse shapes were applied to the modulator with the diode seed

in place, and again good fidelity was observed (Figure 35). However, the noise as generated by the seed diode does result in a certain level of pulse-to-pulse variation, roughly ±2% about the mean (Figure 36).

(a)   (b)
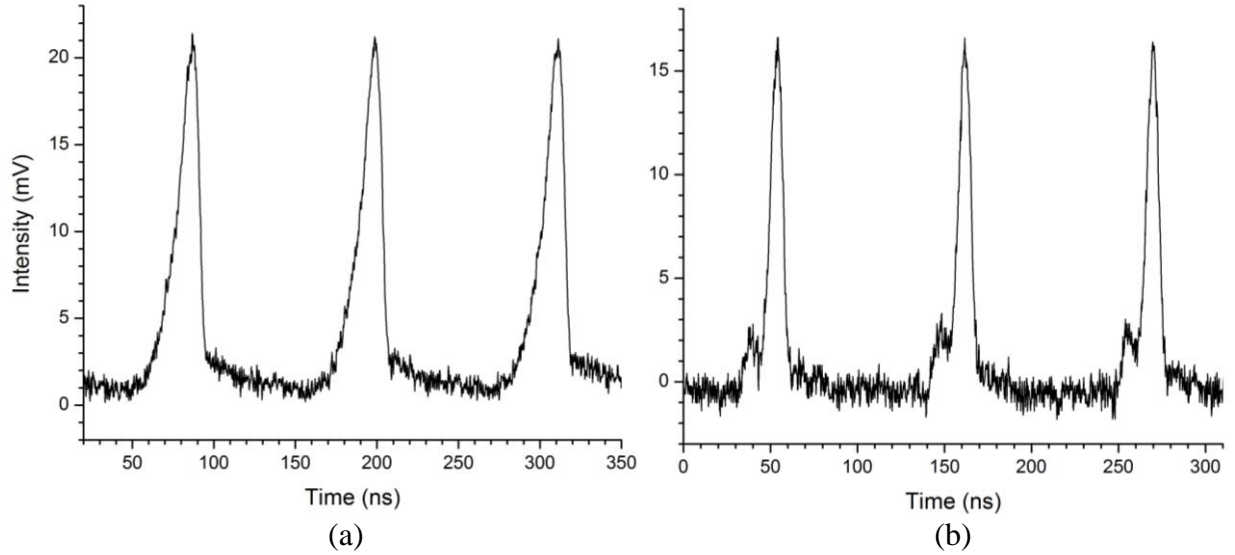
Figure 35: Photodiode detected pulse shapes out of the modulator using output of the seed diode
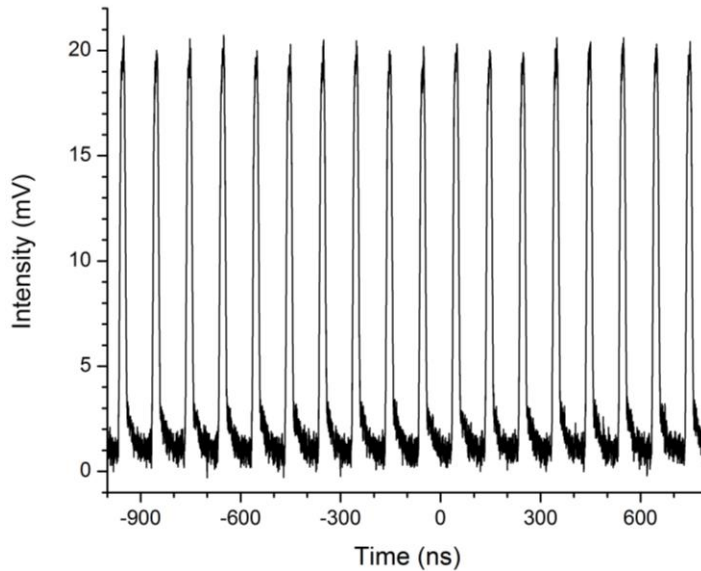
Figure 36: Pulse-to-pulse variation out of the modulator as caused by the noise of the seed diode

3.3. Pre-amplification & Pulse Picking

In to achieve the desired level of seed pulse energy (~100 nJ), the output of isolator 2 is spliced to the fiber pre-amplifier portion of the seed. Fiber pre-amplifier consists of a 974 nm

750 mW single-mode pump diode (Oclaro LC962UF74P-20R), a wavelength division multiplexer (WDM) (AFR PMFWDM-0398-N0B-Q) as the oscillator, Yb-doped active fiber, and a final isolator of the same type as the others, with an angle cleave on its output end (Figure 37). The length of the active fiber for the pre-amplifier was optimized experimentally to ~43 cm in order to maximize output power.
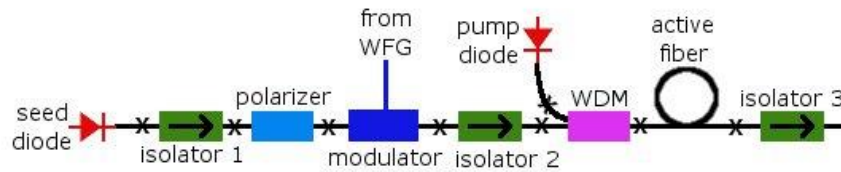
Figure 37: Schematic of full fiber front-end

The total output pulse energy and gain were examined as a function of pump power and repetition rate in order to establish the optimal repetition rate. This analysis was performed using a square seed pulse of 20 ns duration with a varying repetition rate and pump power, and using a fixed seed power for 0.2 nJ pulse energy out of the modulator.

The modulated square-pulse signal was selected arbitrarily and repetition rates of 100 kHz, 500 kHz, 1 MHz and 10 MHz were measured. At each repetition rate a slope of output power versus pump power was taken. At the repetition rate decreased a greater amount of ASE power was present between pulses, making the calculation of pulse energy based on the average power and repetition rate less accurate at lower rates. The pulse energy and gain was calculated for 500 kHz, 1 MHz and 10 MHz are shown in Figures Figure 38 and Figure 39. The lower limit on repetition rate relates to minimizing the amount of ASE present between pulses, and the upper limit relates to the amount of gain necessary to achieve the necessary amount of gain. The desired pulse energy for seeding the regenerative amplifier is around 100 nJ, and so the highest repetition rate which can achieve this pulse energy was selected (1 MHz) in order to satisfy both limitations.
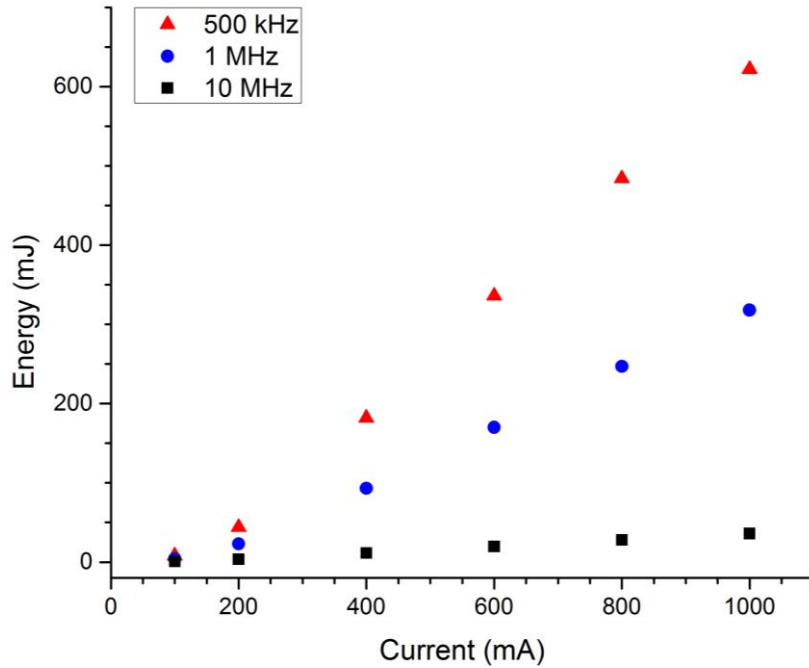
Figure 38: Pulse energy as a function of amplifier pump current (CW) for different repetition rates (seed pulse energy of 0.2 nJ)
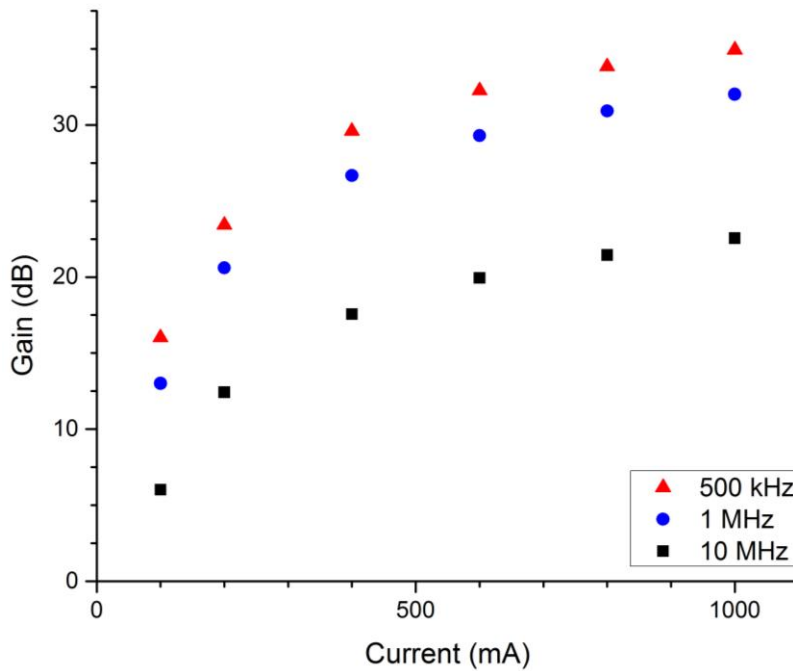
Figure 39: Gain at each rep. rate as a function of amplifier pump current (seed energy of 0.2 nJ)

The output temporal shapes from the pre-amplifier remained consistent with the shapes

output by the modulator directly, with the results of two different pulse shapes shown in Figures

53

Figure 40 and Figure 41. No significant level of gain shaping on the temporal shape of the pulse was noted.
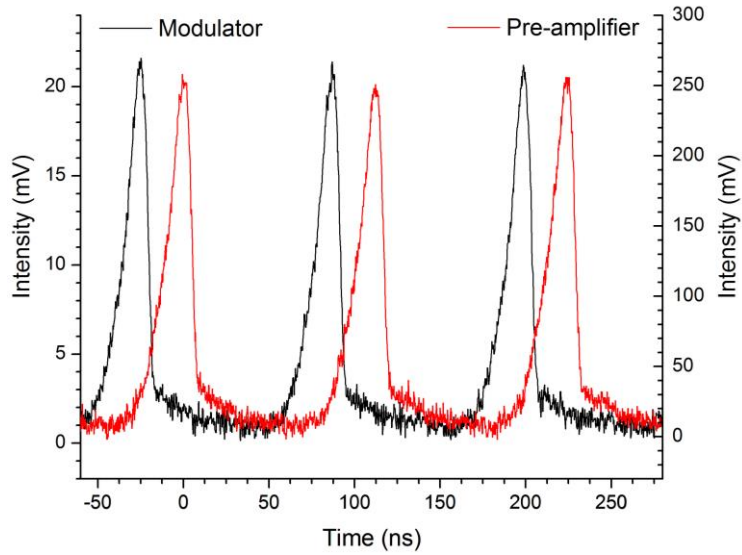
Figure 40: Example 1 of the pulse shape comparison for the output from the modulator and the fiber pre-amplifier
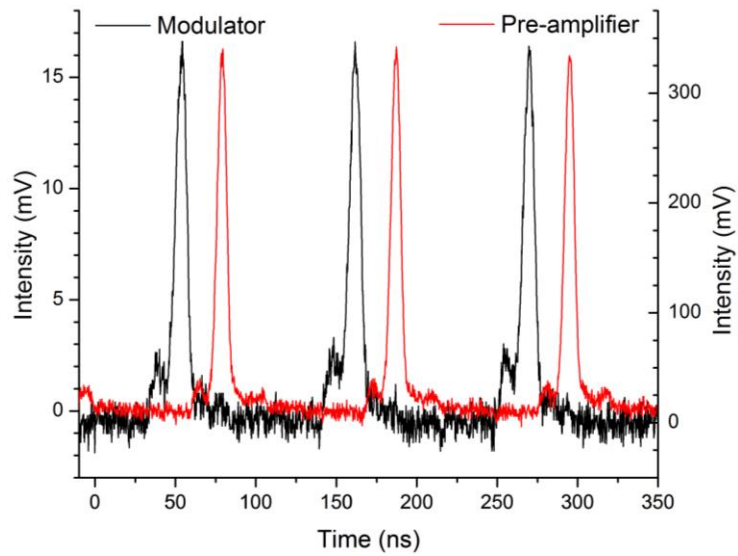
Figure 41: Example 2 of the pulse shape comparison for the output from the modulator and the fiber pre-amplifier

The pulse-to-pulse variation increased slightly out of the fiber pre-amplifier, with a measured variation of ±4% about the mean peak intensity of the pulses (Figure 42).

The entire fiber system thus fully assembled is housed in a plastic case which was fabricated in house (Figure 43). This case protects the system, and enables easy transport. Once the fiber system was fully assembled, it and all its associated electronics were moved to an optical table adjacent to the TruDisk 1000, from which the regenerative amplifier is constructed.
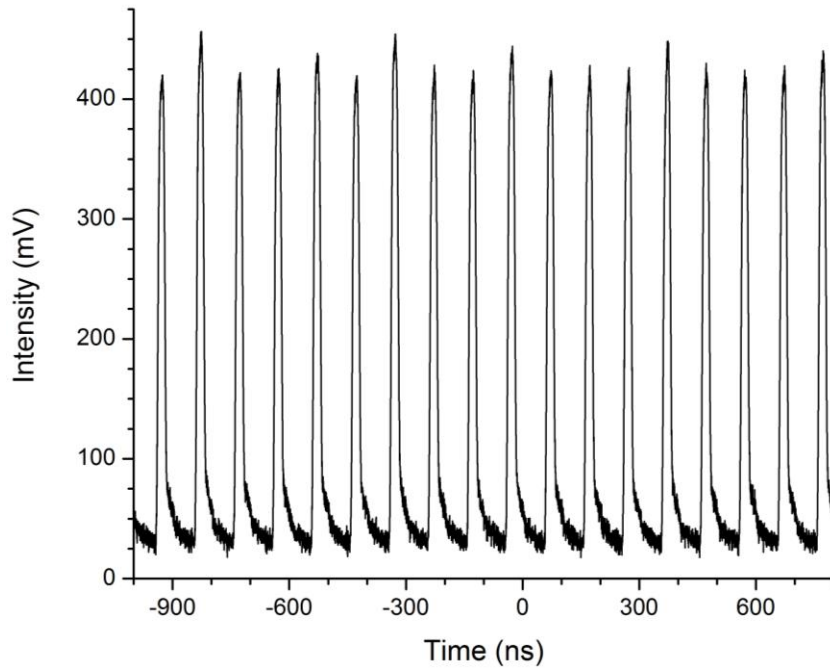
Figure 42: Pulse to pulse variation as observed at the output of the fiber pre-amplifier
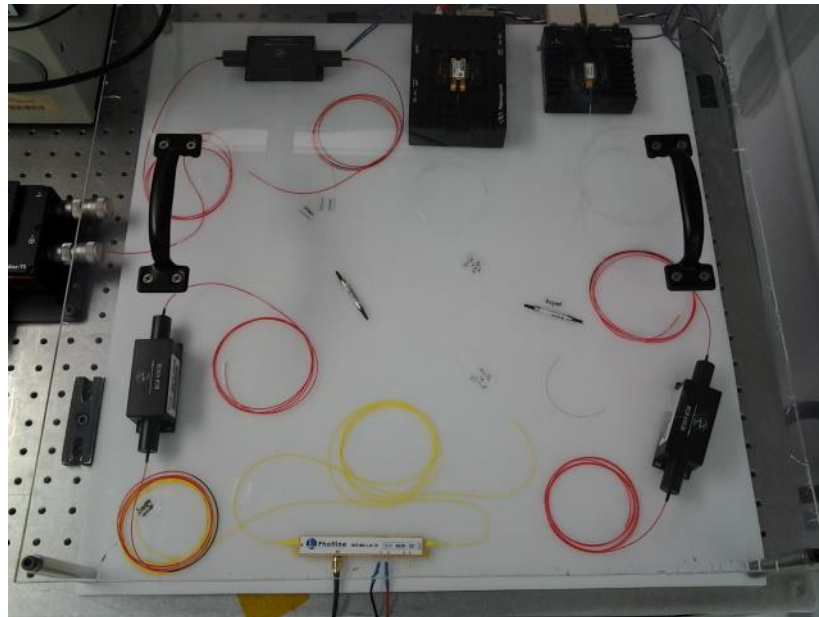
Figure 43: Fully-assembled fiber front end in case

As previously described, the higher repetition rate of the modulator helps to ensure a low inter-pulse power, however the maximum switching rate of the larger PC used in the regenerative amplifier is 10 kHz, necessitating a method for down-picking the pulses output from the fiber seed. To do this the output of the fiber pre-amplifier is collimated in free space and redirected through a series of polarization optics and a small Pockels cell (Starfire by QuantumTechnology, Inc.) for down-counting to the kHz range (Figure 44). Because two Pockels cells are used in this system, this PC which is used for pulse picking will be referenced as the PP, and the other PC which will be described later will be referred to as the PC.
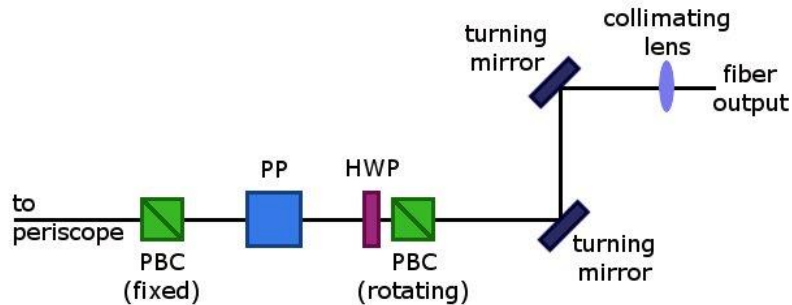
Figure 44: Schematic of optical elements used for pulse-picking, light traveling right to left as in experimental set-up (PBC - polarizing beam cube, HWP - half-wave plate, PP – pulse picker)

Two mirrors are used to redirect and level the beam to the height of the PP, with a polarizing beam cube (PBC) in a routing mount used to clean the linear polarization of the beam, and a rotating half-wave plate to match the rotation of the light's polarization to the PP. A second PBC is located after the PP and has with a fixed rotation. The HWP is rotated such that the light entering the PP is cross-polarized with respect to the orientation of the second PBC. While the PP is quiescent, the second PBC rejects the signal, and when it is switched on to half-wave voltage, a temporal pass window is created which allows pulses to be transmitted.

The pulses that pass through the second PBC travel to the end of the table where they are re-directed by a series of mirrors, including a periscope, to a level appropriate for the table of the

TruDisk 1000 (Figures Figure 45 and Figure 46). By using the synchronization output from the WFG to trigger the PP's driver, a specific window can be created to allow one or several pulses to pass through the PP (Figure 47). From the periscope these pulses enter the regenerative amplifier on the table of the TruDisk 1000, as described in the following section.
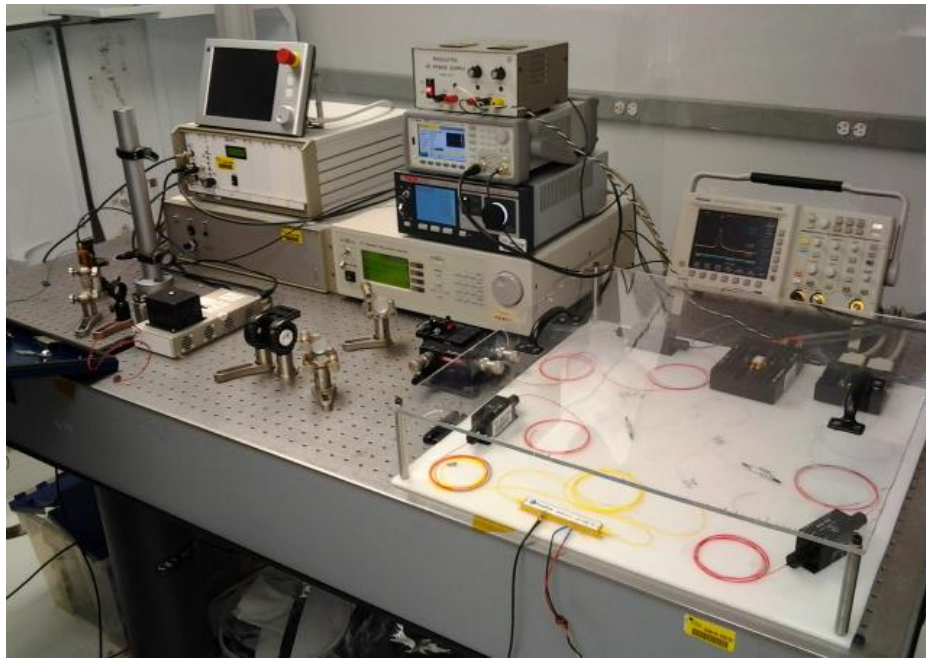
Figure 45: Photograph showing the fiber front end and its associated electronics along with free space elements for pulse picking and redirection into the TruDisk 1000 system

Figure 46: Alternate view of fiber oscillator and pulse picking set-up
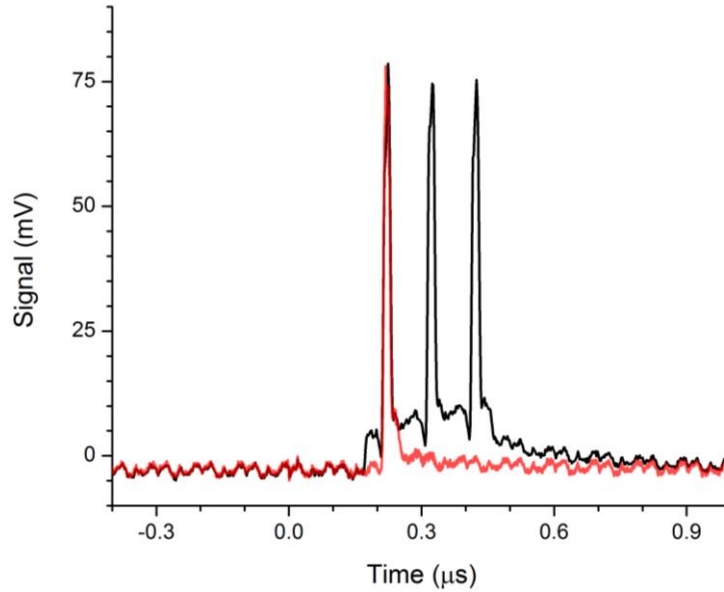
Figure 47: Square pulses at 10 MHz with 20 ns pulse duration picked down to 2 kHz with different gate times allowing through either one (red) or three (black) pulses at a time

As can be seen in Figure 47, inter-pulse ASE power is present. If the PP window is not closed down around the pulse preventing the passage of ASE, it is possible for this light to enter the regenerative amplifier and create spurious lasing. In order to ensure this does not occur the gate is always set to the bounds of the pulse using both fine and coarse adjustments of the PP on and off times.

3.4. Trumpf TruDisk 1000 and Modifications

As part of a collaboration between Trumpf Inc. and the Laser Plasma Laboratory at the Townes Laser Institute (TLI) and the College of Optics and Photonics, UCF, a commercial Trumpf thin-disk laser system was modified to create the regenerative amplifier portion of hybrid MOPA laser system.

The commercial system, a TruDisk 1000, is a Yb^{3+}:YAG thin-disk laser operating at 1030 nm in the CW regime with up to 1 kW of output power. It is a completely enclosed system (Figure 48) which contains its own cooling, monitoring and computer control system; and

requires only an external voltage supply (power connection) and a house water connection in order to operate. The primary advertised application for this commercial system is various types of industrial welding. In order to operate nearly continuously in an industrial setting, the system includes robust monitoring and control.

Figure 48: Trumpf TruDisk 1000: 1 kW CW thin-disk laser system

The laser cavity of the TruDisk 1000 consists of three mirrors and the disk itself arranged in a z-cavity configuration (Figure 49). **Error! Reference source not found.**It has a 90% reflective flat output coupler, a -4000 mm radius of curvature (ROC) turning mirror and a -500 mm ROC end mirror. The disk itself has a 2000 mm ROC in its quiescent state, but increases as the disk flattens at higher output powers (more in Chapter 4). Figure 50 shows the cavity in its original unmodified state with beam tubes and mechanical shutters in place.

The system is controlled by a touch screen computer interface (Figure 51) which allows the user to manipulate the system and access various diagnostic outputs. Under normal operating conditions the laser maintains a set output power by active monitoring of the real-time output

power and compensating the amount of voltage supplied to the diodes appropriately to match the
set point.
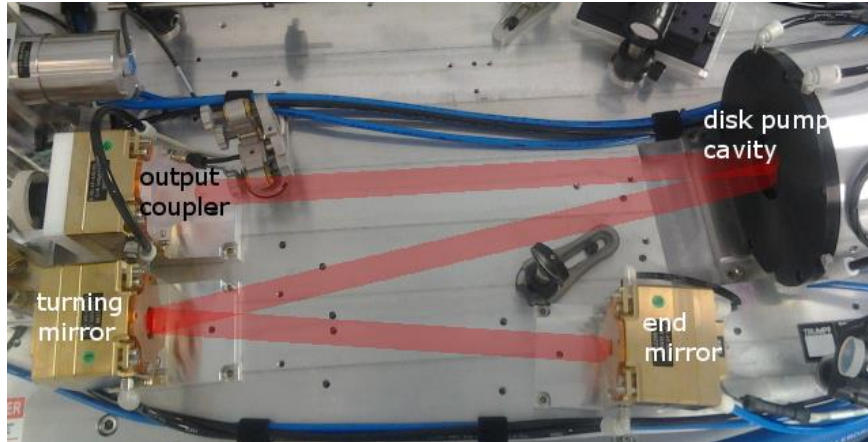
Figure 49: Photograph of unmodified TruDisk 1000 z-cavity

Figure 50: TruDisk 1000 laser cavity as factory installed

Figure 51: TruControl touchscreen showing diagnostic output for user

If the amount of necessary voltage supplied to the diodes to achieve a certain output power falls outside the acceptable range, the laser faults and turns off, providing the user with error information. Likewise, diagnostics such as the temperature of various elements, cooling water flow rates, and fluorescence are all monitored, with error messages and faults given when values fall outside of the acceptable range. Output from the system is monitored and controlled by a series of mirrors and switches (Figure 52) which can be manipulated through the laser's computer interface.
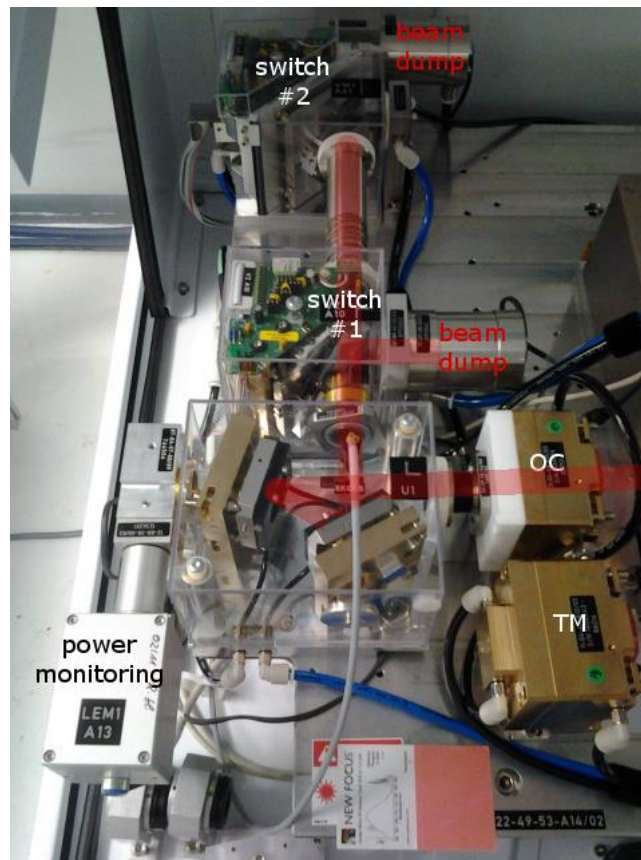
Figure 52: Output from the TruDisk 1000 laser cavity, the power monitoring unit (LEM), beam path switches, and beam dumps (TM - turning mirror, OC - output coupler)

The disk is pumped by two diode units which can yield 1.25 kW each at 940 nm (Figure 53). The spectrum of the pump light (no laser action) is shown in Figure 54 and the spectrum of the laser during oscillation is shown in Figure 55. Note that the spectrum shown in Figure 55

was not taken directly from the laser's output, but off-axis from the scattered light leaving the pump cavity, and therefore does not represent the relative presence of the various spectral lines shown in the laser's output power.
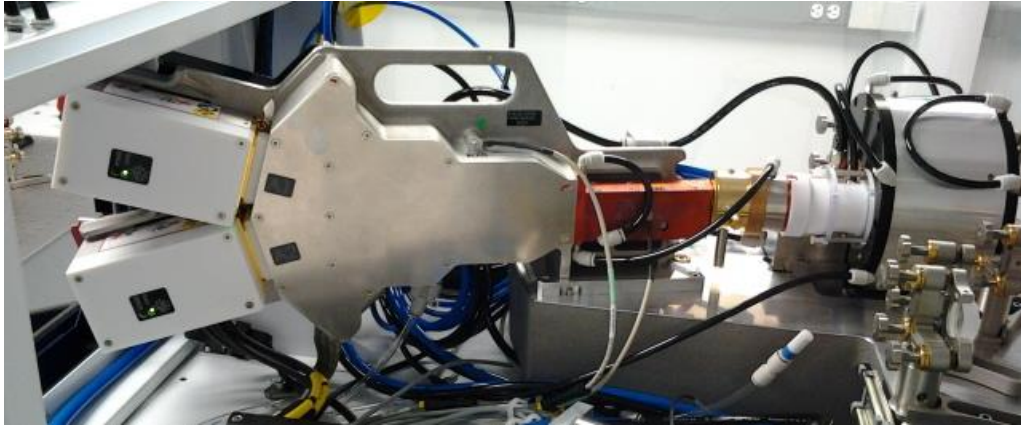
Figure 53: 1.25 kW 940 nm CW diodes for pumping of thin-disk propagated through homogenizing optics to pump cavity and thin-disk head
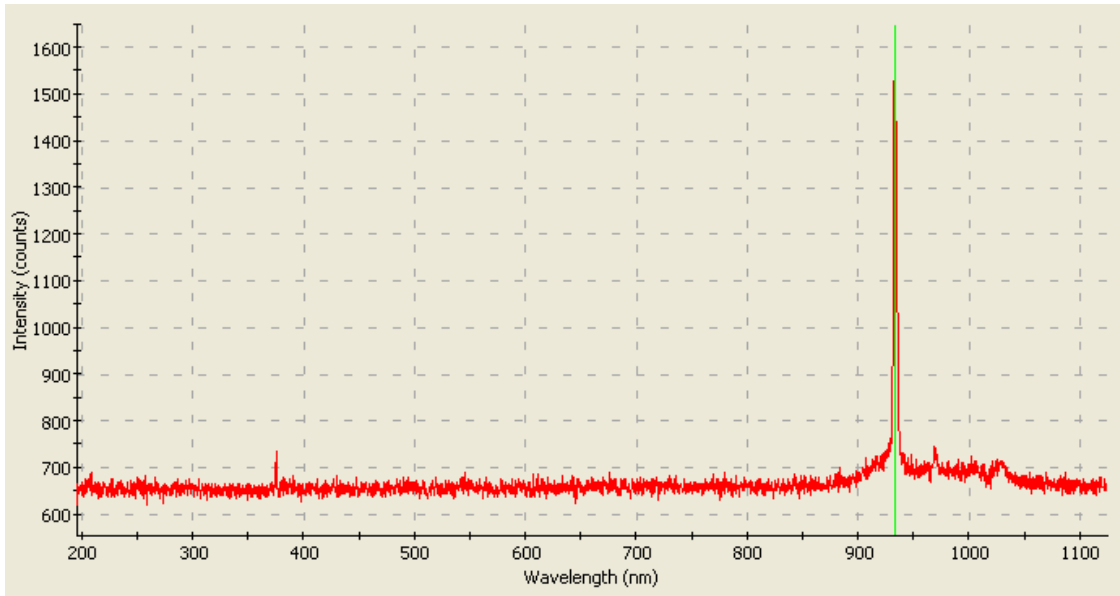
Figure 54: Spectrum of pump light on disk without laser oscillation, exhibiting some ASE

The light from the diodes is propagated through enclosed free-space homogenizing optics (Figure 56) which produce a uniform flat-top pump beam of 6.3 mm that is imaged onto the disk (Figure 57). A parabolic mirror and a series of retro-reflectors, as described in chapter 2, are

used to recirculate the pump power a total of 16 times in order to achieve a high level of pump absorption. In the standard CW cavity configuration, the overall system efficiency is ~54% with an output beam quality of 2 mm·mrad.
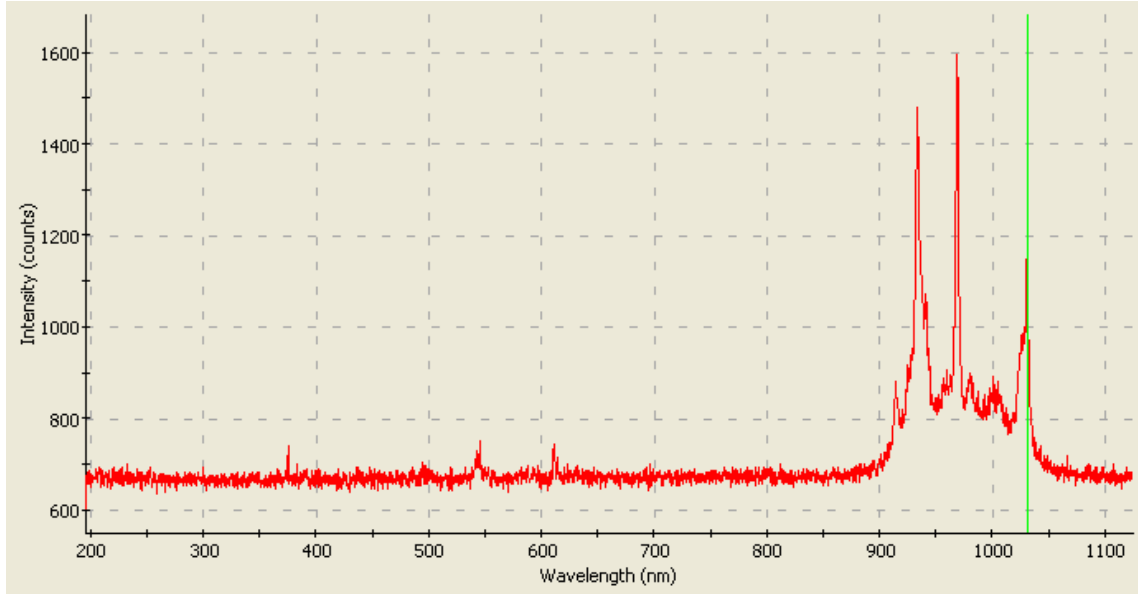
Figure 55: Laser output spectrum during oscillation

The Yb^{3+}:YAG thin-disk is 14 mm in diameter, with its exact thickness and dopant concentration values being proprietary to Trumpf Inc. The disk is bonded to a heat spreader, which is housed in a cold finger and water cooled from the back (Figure 58). The location of the cold finger in the back of the pump cavity can also be seen in Figure 56.

Figure 56: Pump light fed into the back of the pump cavity (disk assembly) via the homogenizer
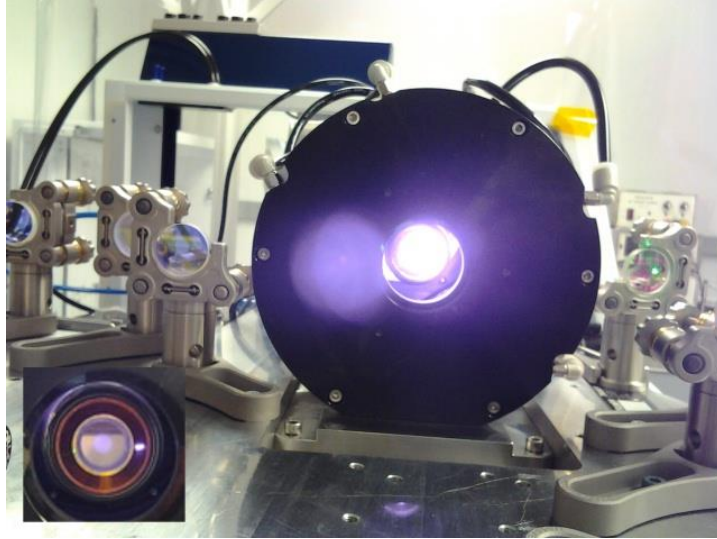
Figure 57: Pump spot on thin-disk as seen during laser oscillation (inset: disk during warm up)
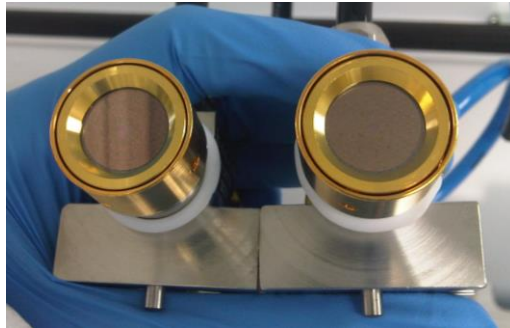
Figure 58: Two Trumpf Yb:YAG thin-disks mounted in a cold-finger assembly of the same type, one from TruDisk 1000 and one from a TruMicro 7050, are shown side-by-side.

In order to use the thin-disk in the TruDisk 1000 as the gain medium for the planned regenerative amplifier, a number of modifications were required. As described earlier, the TruDisk 1000 has a variety of monitoring systems and safety mechanisms which make it turn-key for a typical end user; it is not intended to be modified by the end user. All of the factory installed opto-mechanics, including the beam tubing, mirror mounts, switches and power monitoring unit required removal. Consequently various changes to the monitoring software, through both the front-end user interface, and the backend technician-level access were also required to compensate for the removal of various items. The current compensation for the pump diodes also needed to be deactivated, such that manual control of the pump diodes could

be exerted. Removal of the switches and various components is shown in Figures Figure 59-

Figure 61.
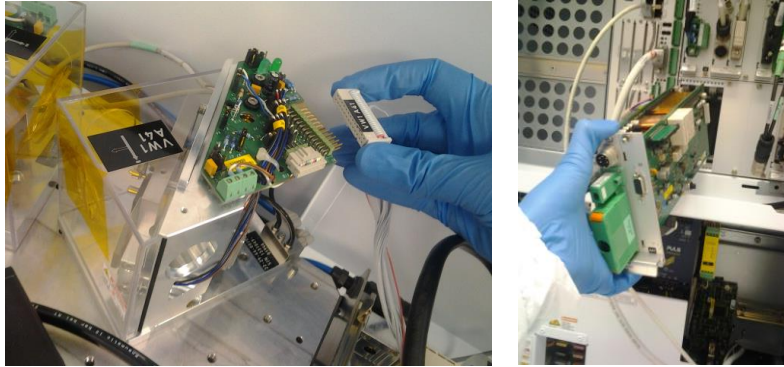
Figure 59: Removal of switch #2 and the electronics panel associated with it, removed in order to defeat the safety monitoring software
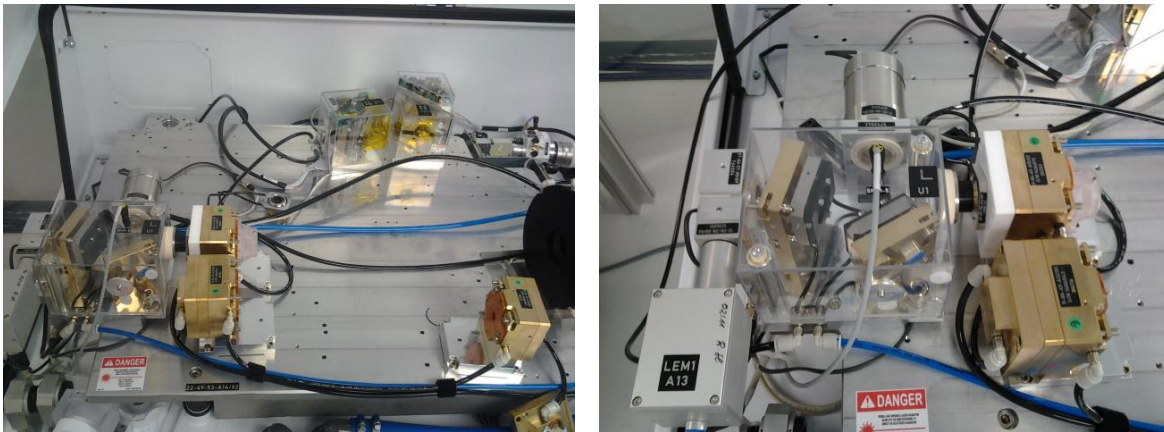
Figure 60: Relocation of switch #1, which must remain connected for the system to function
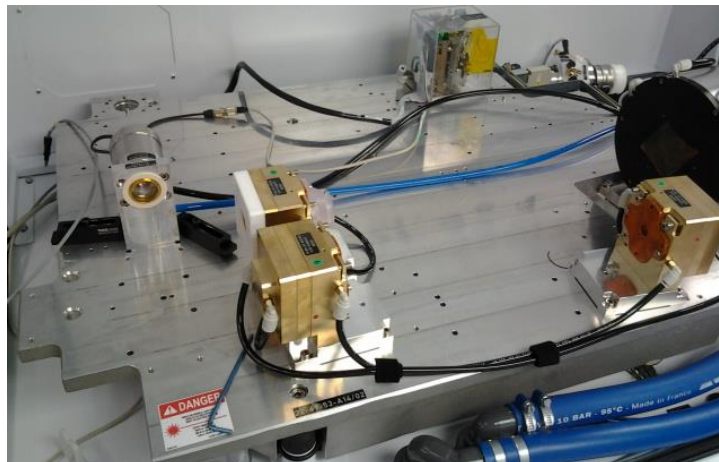
Figure 61: TruDisk 1000 system with both switches and the power monitoring unit (LEM) removed, with only opto-mechanics remaining

Because of the refitting of the cavity, the removal of the lid of the TruDisk 1000 became necessary in order to grant greater access and increase available space (Figure 62). This means the system and all its optics will be continuously exposed to open air. Operating at high powers in free space necessitates a high level of air quality in order to prevent dust from settling on the laser optics, as this can result in burning and damage. Trumpf specifies a Class 10,000 clean space to operate the laser system in open air.

Figure 62: TruDisk 1000 after removal of the factory installed opto-mechanics and container lid housed in the modular clean space

To meet these specifications regarding the air quality, a customized modular clean space designed and then assembled in the laboratory space where the TruDisk 1000 was installed (Figure 63). The clean space has seven HEPA filtration and fan units in its ceiling to create a positive laminar flow which helps to maintain the air quality.

Additionally, the laboratory space outside of the clean tent has been outfitted with various filtering and isolation devices in order to aid the air quality maintenance. Gowning procedures

are in place for entry into the lab space, and an air shower with interlocking doors and filtration units is the entry point for the lab space (Figure 64). The building air conditioning unit has been outfitted with a filter, and several HEPA air filtration units help to remove particulate from the air (Figure 65). Tacky mats are used at both the entrance and exit of the air shower, as well as at the entrance of the clean tent. Gowning procedures to enter the laboratory include a lab coat, hair net, and shoe covers. Further gowning procedures including a full-body Tyvek suit, face mask, gloves and a secondary pair of shoe covers are required to enter the clean tent in which the TruDisk 1000 is housed.

Figure 63: TruDisk 1000 Installed in Class 10,000 Cleanroom

Figure 64: Gowning area (left), and air shower (right) at entry way of laser clean space

Figure 65: HEPA aire filtration unit inside of clean space (left) and air-vent filter for building air (right)

Using a MetOne Particle Counting Meter (PCM) Model 228, the air quality was measured in the clean tent, the laboratory, and the external gowning area (Table 1). The device itself measures the number of particles per cubic foot, displaying the value every six seconds. The values taken represent an average of 20 or more measurements (2 min). It should also be noted that for the clean tent, when the PCM was left inside and the researcher remained outside,

it consistently registered a zero value. The value of 70 particles/ft^3 is a result of particles created by movement when the researcher was in the clean tent.

<p align="center">*Table 1: Measured values of particle concentration several areas*</p>

	Clean Tent	Laboratory	Gowning Area
Particles foot^{-3}	70	640	19,510
Particles·m^{-3}	2,470	22,600	682,850
Class	Class 10,000 (ISO 7)	Class 100,000 (ISO 8)	NA (ISO 9)

The device can only measure particles of 5 µm or larger, and measurements were only taken once, and so this does not provide an absolute metric for establishing the quality of the clean space. As such the classes specified for the various areas in Table 1 are only rough estimates; classification of cleanroom spaces requires a much more extensive set of measurements. However the relative values show that the measures taken to make the laboratory space in which the clean tent is located, and the clean tent itself, effectively reduce the particulate in the air by several orders of magnitude as compared to the gowning area which is in an unregulated laboratory space.

3.5. Design Considerations for the Regenerative Amplifier

One of the desired criteria of the output pulses from the regenerative amplifier is a temporal duration of 16 to 30 ns. This means that longest pulse (30 ns) that the cavity will need to accommodate is ~9 m in length spatially (according to $l = \tau \cdot c$). Additionally, the PC used as the switch for the regenerative amplifier has a finite rise and fall time, which adds to the necessary length of the cavity. This means that the distance that the pulse can travel in the time that it takes the PC to switch on must also be added to the total necessary cavity length. But because the pulse enters and exits the cavity through the same intra-cavity TFP, the total cavity

<p align="center">69</p>

length only needs to be half of the sum of the pulse length and the distance covered during the PC's rise time i.e. only the round trip time matters.

This means that a careful characterization of the PC's rise and fall time must performed in order to ensure that the appropriate cavity length is selected. The PC used is a LightGate 7 [166] water-cooled cell with a 7 mm clear aperture, designed and manufactured by Gooch & Housego Cleveland, formerly Cleveland Crystals (Figure 66). The high voltage driving electronics were designed by BME Bergmann Gmbh, and were specified to a 6 ns long 90/10 rise/fall time.

<div align="center">(a)   (b)</div>
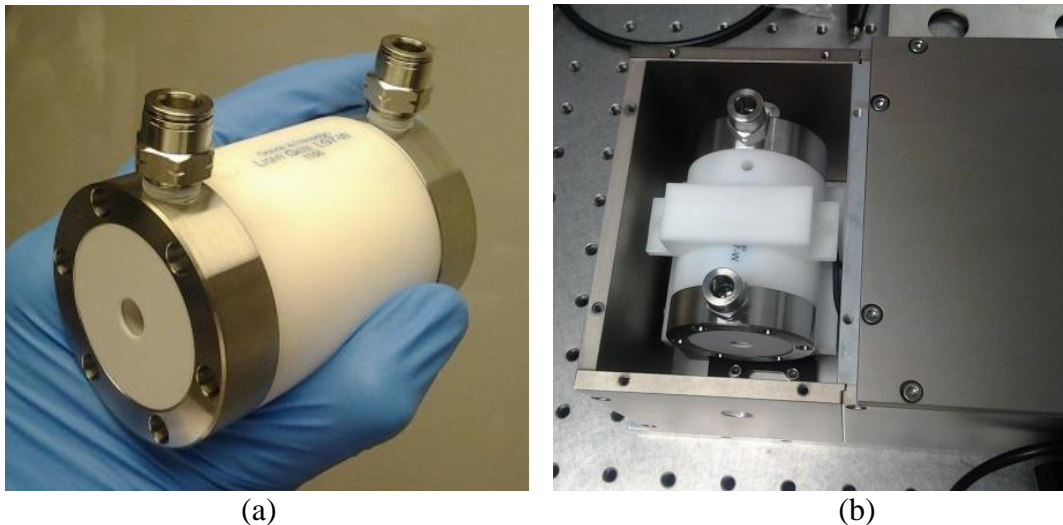
Figure 66: a) Shows the LightGate 7 watercooled PC, and b)is the PC mounted in the head of the driving electronics

As stated, a great advantage of the thin-disk laser system is its large diameter, raising the threshold of both non-linear and thermal damage effects. Due to the number of round trips that the pulse must make in the cavity (because of low single-pass gain), low-insertion loss and fast rise and fall times are imperative for the Pockels cell. However, these requirements must be satisfied in combination with a large clear aperture.

Because of the large clear aperture required, very few Pockels cells on the market (at the time of purchase) possessed all the required features without an impractically high driving

voltage. BBO was selected as the crystalline material because of its low absorption features as compared to other common Pockels cell materials for 1 μm, such as KD*P or RTP, as well as its resistance to RF ringing. For a BBO based Pockels cell, with the necessary low insertion loss and a 7 mm clear aperture, the quarter-wave voltage reaches up to ~12 kV. The best solution found was to use a dual-crystal Pockels cell, thus halving the voltage necessary for obtaining quarter wave rotation. The selected LG7W cell has a 5.4 kV quarter wave voltage.

The driving electronics consist of a unit which generates the high voltage, and a driving head in which the PC is mounted that switches the driving circuits (Figure 67). The driving head is controlled by software through a connection to the computer with SMA-to-BNC cables and an installed SDI card (Figure 68). The software sends two low voltage signals to the head, the first to switch the high voltage on and the second to switch it off. While the high voltage is on the PC is active and causes polarization rotation of light passing through it, but when the voltage is switched off the PC is optically neutral.
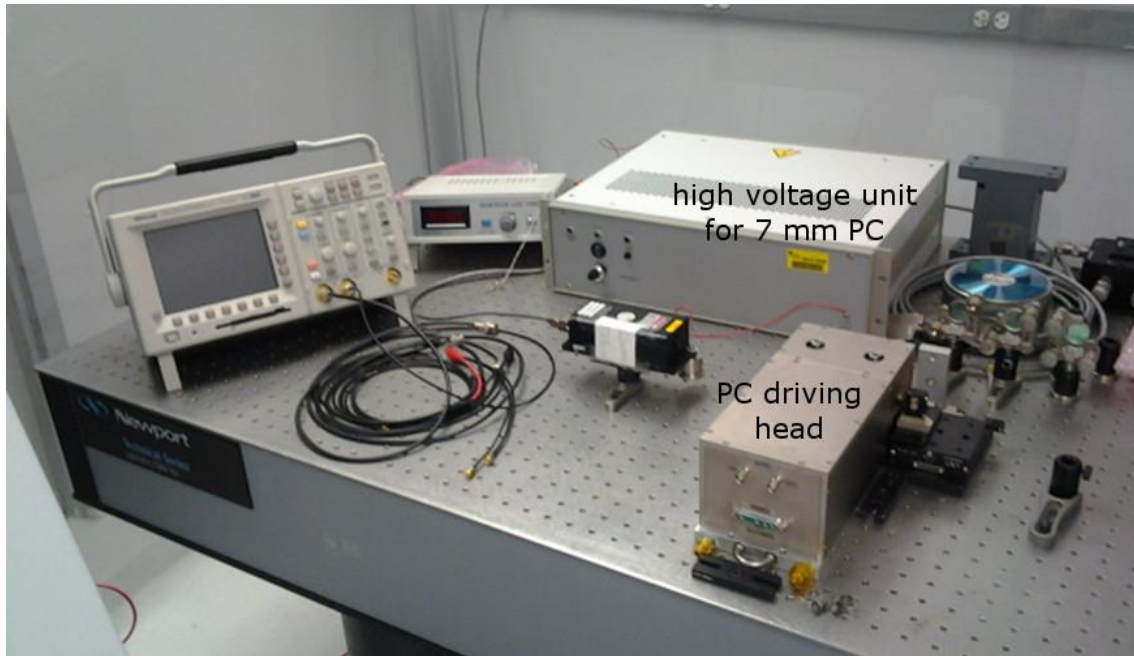
Figure 67: Test-set up for the PC characterization with driving electronics labeled
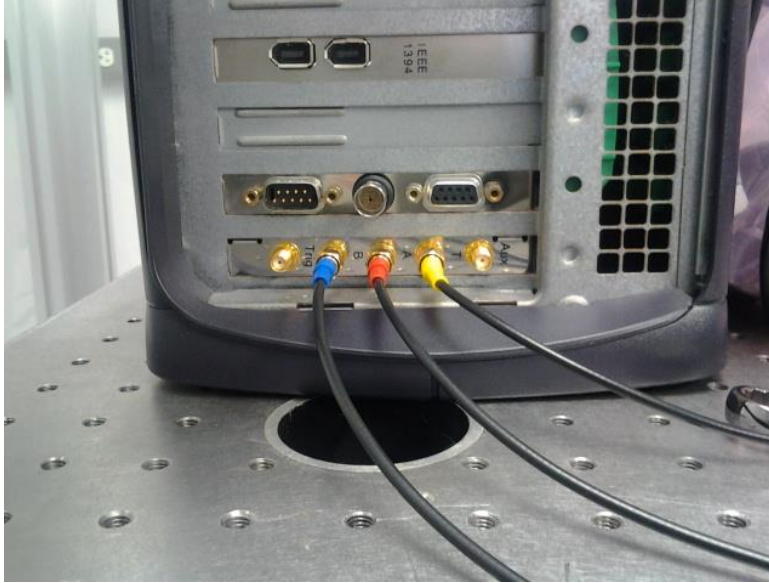
Figure 68: SDI card and connections from the computer to the PC driving head

Performance of the PC was experimentally verified using the test set up shown in Figure 67, the schematic of which is given in Figure 69. A 200 mW 1064 nm laser diode source (linearly polarized), a beam cube (used as a crossed polarizer), and a fast photodiode were used to read the throughput of the PC as it was driven. The PC was driven to quarter wave voltage for 1 μs at a 1 kHz repetition rate.
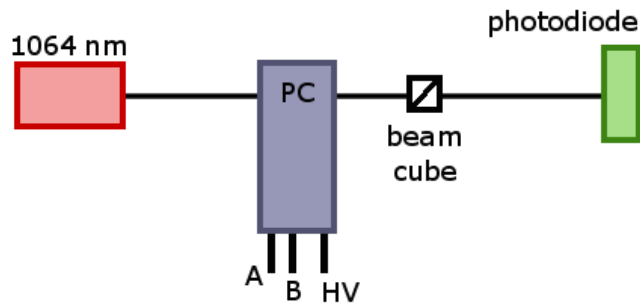
Figure 69: Schematic of the experimental testing setup for measuring the rise/fall time of the PC (connections labeled: A – on signal, B – off signal, HV – high voltage)

The photodiode and the trigger signal from the PC's driving electronics were connected to an oscilloscope and plots of the measured traces are shown in Figures Figure 70 and Figure 71. As the photodiode (Osram Photodiode, 720-sfh2701) was built in house and designed for

measuring femtosecond pulses, it shows an accurate reading at the initial rise of the pulse (the impulse response), but demonstrates an erroneous slow rise and fall after the initial changes, as seen in Figure 70. The slow rise across the length of the pulse can therefore be ignored, but the impulse response can be used to accurately measure the PC rise time.
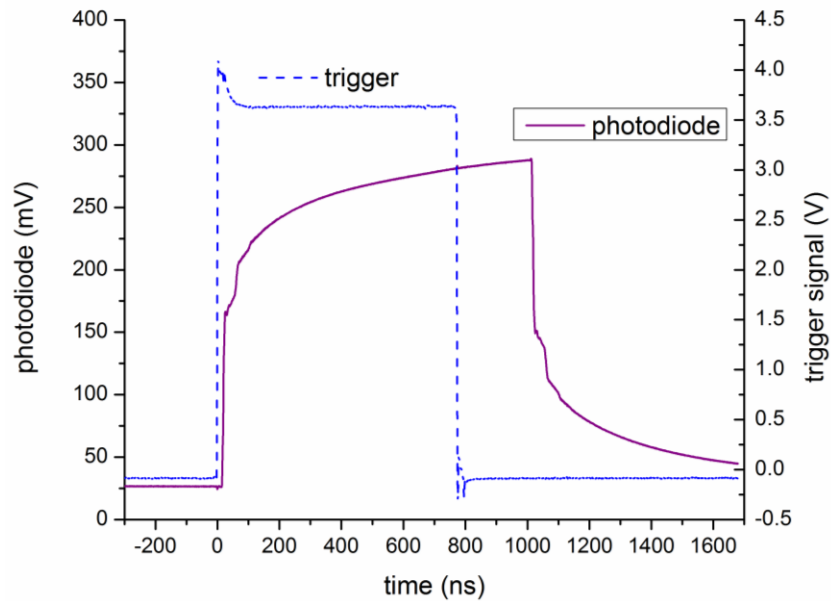
Figure 70: Plot of PC trigger signal and photodiode response

The rise time was calculated by taking a point at the bottom of the rise, and another at the top, denoting these values as 0% and 100%, from which 10% and 90% were determined. Because there was residual RF noise present in the signal even after shielding the photodiode, two points located on the slope of the rise were fit with a linear expression. Using the 10% and 90% values with the linear expression to solve for the rise time gave a value of 6.74 ns (Figure 71).

The rise time of the PC determined to be 6.74 ns equates to a distance of ~2 m, making the total round-trip length of the cavity from the PC onwards need to be 11 m, and thus a physical cavity length of 5.5 m. As such the design requirement for the cavity length will be 5.5 m or greater in order to ensure adequate space for the pulse.
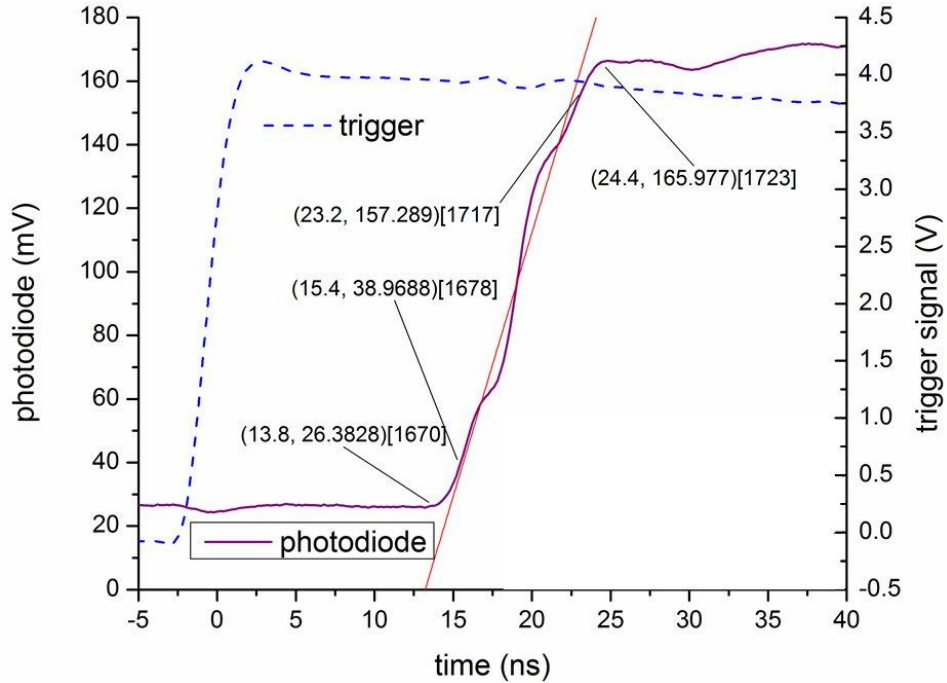
Figure 71: Response of Pockels cell

Damage thresholds of all the cavity elements are particularly important for the expected operating conditions: 1-10 kHz of up to ~50 mJ pulse energy. The disk, mirrors, and PC all have finite damage thresholds which must be honored, with the specific values for each shown in Table 2. Going by damage thresholds, the PC is the most vulnerable element in the cavity. From discussions with the manufacturer, over-filling the 7 mm aperture of the cell and clipping too much power on the cell creates the greatest risk of damage or failure for the PC. As stipulated by the manufacturer for these operating conditions, the cavity mode must be $\leq$ 3 mm in the PC. This gives upper and lower bounds to the cavity mode size for the region near the PC.

Table 2: Damage thresholds of intracavity optical elements

Element	HR mirrors	QWP	TFP	Pockels Cell	Disk
Damage threshold (J/cm^2)	30	10	30	10	5
Minimum spot size (mm^2)*	0.167	0.5	0.167	0.5	1
Minimum radius** (μm)	231	399	231	399	564
Spot size (mm^2)	1.17	1.18	1.23	1.20	20.52
Max incident energy (J/cm^2)*	0.43	0.42	0.41	0.42	0.02

* - for a 50 mJ pulse, ** - 1/e of a Gaussian beam with a 50 mJ pulse

74

Other design considerations which must be addressed include the mode quality, mode size at the disk, and collimation of the output beam. Additionally, the mode in the PC arm of the laser must be relatively collimated, such that expansion of the beam does not create clipping on the Faraday rotator through which the pulse must pass upon exiting the cavity.

The cavity of the regenerative amplifier was created with these aspects in mind using LASCAD and by cross-checking round-trip stability directly via ABCD matrices. These requirements also constitute the goal function for the cavity optimization code described in a later section. Figure 72 shows the regenerative amplifier cavity as it will be built first for CW operation, and then as a Q-switch before being seeded as an amplifier. Using LASCAD, various adjustments to length and curvature were made until all the above requirements were met. It also includes a minimum number of curved mirrors, which include the disk, a -700 mm ROC end mirror, a -4000 mm ROC and +2900 mm ROC turning mirror each, with most mirrors being flat folding mirrors. The total cavity length of the system is 5.85 m, with a round-trip cavity length PC being 11.7 m, allowing for a 30 ns pulses to be held in the cavity.
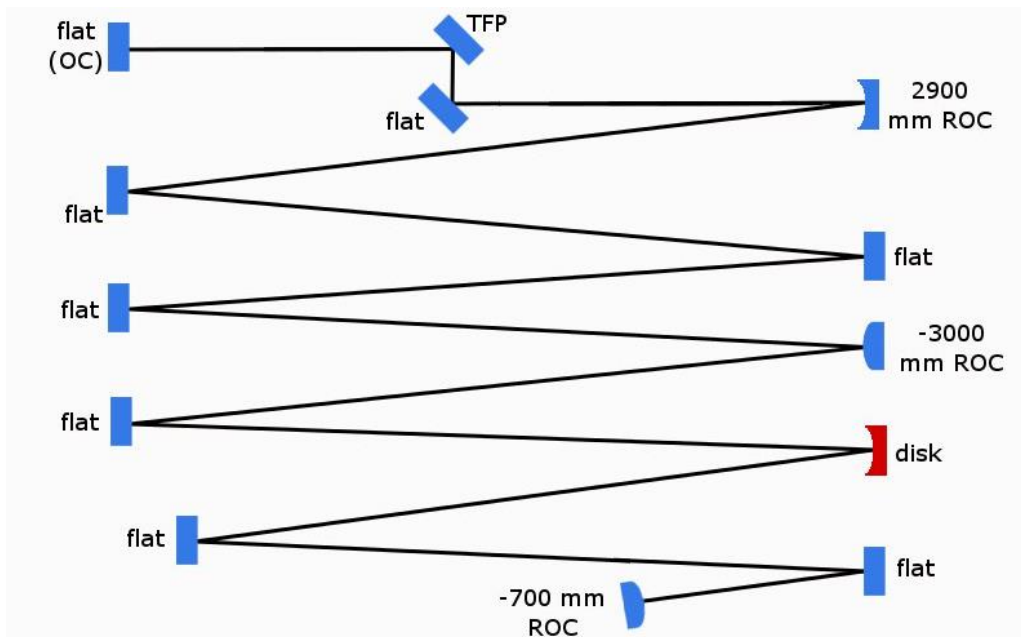
Figure 72: Cavity of the regenerative amplifier in a CW configuration

75

As will be described in the chapter on thermal behaviors, the disk itself flattens as it heats, changing the stability and modal sizes of the cavity with increasing power. Operating the TruDisk 1000 manually, the maximum pump current possible is 40 A or 576 W pump, which in its original CW configuration gives an output power of ~250 W. For the regenerative amplification process, the total amount of available pump power (>2 kW) will not be needed, so being limited to a maximum of 576 W is not limiting.
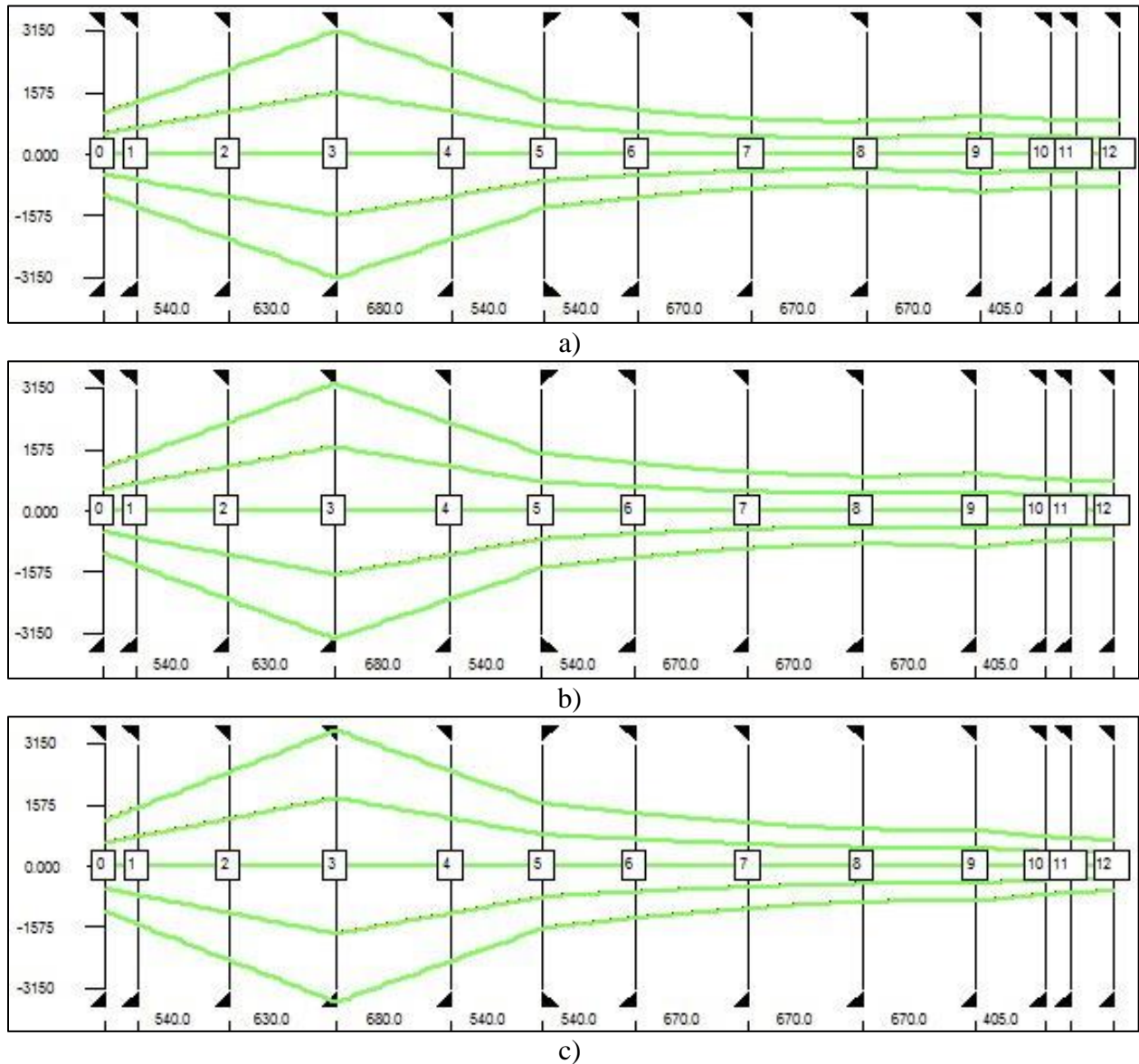
Figure 73: Mode plot of the x-plane of the regenerative amplifier cavity as created by LASCAD for disk ROC of a) 2080 mm, b) 2105 mm and c) 2130 mm

However, there are still a range of disk curvatures which need to be addressed by the model, ROC of 2080 mm at lower powers up to ROC of 2130 mm for higher powers. The design created in LASCAD was intended to accommodate this change while continuing to meet at the desired design parameters. The evolution of the cavity mode from low to high power is shown in Figure 73, and the cavity remains stable over the full range.

Mode quality of the designed cavity was calculated in LASCAD using an assumed aperture equivalent to the size of the pump spot on the disk (6.3 mm diameter). The mode was also designed such that it did not overfill the pump spot, which would create mode losses and prevent efficient operation. The cavity design yields a projected M^2 value of 1.5 for the x axis and 1.6 for the y-axis. While this is higher than the desired diffraction-limited M^2 value, a compromise had to be struck in terms of available mirror curvatures and existing damage thresholds. These projected values will be compared to the measured output beam quality in a later section.

In sum, this constitutes the design considerations for the regenerative amplifier cavity, and the subsequent sections describe the modeling of the cavity, and its assembly and characterization process.

3.6. Modeling & Optimization of the Regenerative Amplifier Cavity

Alongside the development of the regenerative amplifier cavity, an optimization code was created to design cavity according the desired operation characteristics. While the cavity designed in LASCAD and built in the laboratory meets these criteria, by creating a mathematical model to complement the physical construction of the cavity, better cavity designs can be discovered. Potential improvements of an optimized cavity include better stability, better beam

quality, and higher efficiency. Once complete, such a model can be used to improve the design of this system, and will also be useful for a variety of other cavity design applications.

The following list includes all the criteria which must be met by the laser cavity, as outlined in detail in the preceding section on design considerations. This set of requirements is used to develop a goal function which the optimization code uses to gravitate towards an optimal cavity design. The criteria which the cavity must meet are as follows:

- The cavity must be stable.

- The cavity must remain stable over a variety of disk curvatures.

- Damage thresholds of all optics must not be exceeded.

- The mode quality of the cavity should be as close to $M^2 = 1$ as possible.

- The cavity mode must match as closely as possible to the pump spot at the disk.

- The cavity mode must be 3 mm or less in the PC.

- The cavity mode must not diverge significantly in the PC or the Faraday rotator.

The majority of cavity design described in this work was performed using LASCAD, including the regenerative amplifier cavity which is built and described in the subsequent sections. LASCAD is a software package for LASer Cavity Analysis and Design which is sold by LAS-CAD GmbH, first published in 1996 [167]. Based on finite element analysis, LASCAD can be used to perform thermal analysis of laser gain media with temporal resolution as well as Gaussian propagation calculations and more. To design a cavity in LASCAD a user can define both the cavity elements and gain medium parameters, and when compiled the software yields a variety of cavity mode and output characteristics.

However, for the purposes of optimization, LASCAD cannot be used directly. The software itself will only offer results for a given set of parameters provided by the user, such that

78

if optimization were to be performed in LASCAD it would have to be by brute force entry of various parameter permutations. In order to perform an optimization it is necessary to develop an algorithm which not only accepts cavity parameters and returns various output characteristics, but can also use this information to incrementally improve the cavity design towards a specified set of criteria.

In order to develop such an optimization scheme, we collaborated with Dr. Matthias Wohlmuth, who had previously worked on the development of LASCAD. The approach we took uses both C++ based code developed by Dr. Wohlmuth, which can be called from and interface with MATLAB, and code that is written in MATLAB and takes advantage of MATLAB's Global Optimization Toolbox. The combination of these allows the user to input a set of cavity parameter values which can be compiled to find the cavity stability and mode properties within the cavity, and then to iteratively explore many different permutations of these same cavity parameters in order to find an optimal cavity arrangement. The optimization algorithm created in MATLAB is used to compare various cavity configurations against the specified goal function, and finally returns an optimal cavity arrangement based on this analysis.

MATLAB is a well-established software package that is used for many different scientific applications [168], and it has a variety of fully-developed optimization functions available. To any committee member who reads this sentence, I will offer $20 if it is mentioned on the day of my defense. Part of the reason the C++ code was designed to interface with MATLAB was to gain access to its optimization routines and thereby obviate the need to create a brand-new optimization algorithm from scratch. This is particularly helpful given that this optimization problem is discontinuous, non-differentiable, and non-linear, making it impossible to use standard gradient-based optimization techniques. Additionally, there are likely to be

many possible solutions which approximate to our set of criteria, and therefore there exists the possibility of being trapped in a local minimum. In order to find a true global optimum within this particular parameter space, while avoiding processing-expensive brute-force approaches, the appropriate optimization algorithm must be selected, and for this purpose the Genetic Algorithm (GA) was selected from MATLAB's Global Optimization Toolbox.

The operating principles of the GA are based upon the principles of evolutionary biology. Initially it produces a random population within the specified parameter space, represented by a vector. It then evaluates and ranks each individual in the population according to an objective fitness function, what we refer to as the goal function. The algorithm then randomly selects a subset of the better performing individuals which are used to create the next population. From this subset of individuals it creates the next generation by a) retaining some of these highest performing individuals without modification called the elite children, b) creating new individuals by cross-over of two individuals through random combination of their vectors, emulating reproduction, and c) randomly mutating some of the selected individuals to produce mutant children. For example, it can be specified that the population consists of 100 individuals, from which the 10 best individuals be taken as the elite, with a cross-over fraction of 0.25, meaning that 25% of the remaining population (total population less the elite) e.g. 23 individuals, will be created by cross-over, and the remaining 67 by mutation. This new population is then reassessed and the next generation created by the same refinement process, as shown in the flow chart in Figure 74.

As a starting point for simulations, a four mirror cavity is used to create the optimization code, with plans to expand to the full cavity. This allows for a shorter processing time while the code is written and de-bugged. For the 4 mirror cavity problem, a subset of the criteria from the

list given above is used as the goal function, which is applied to cavity permutations in two stages. The first stage of the analysis is done to ensure that the cavity is stable, that any excessively wide angles (>20°) and any non-physical arrangements are eliminated, as well as any mode sizes which violate the element damage thresholds. Cavities which fail these tests are assigned a failing goal value, and passing cavities are assessed for a goal value based on the fill factor of the mode on the pump spot of the disk, with an 80% fill factor being considered ideal.
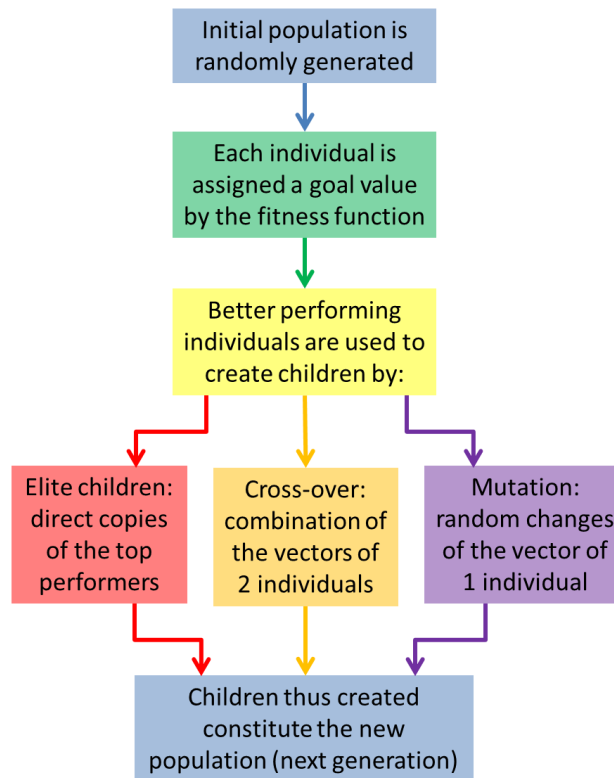
Figure 74: Flow chart depicting the behavior of the genetic algorithm

The optimization algorithm is set up to minimize the assigned goal value, with zero being a perfect match. As such the cavities which do not pass are assigned an arbitrarily large value (10^9) to indicate failure. Non-failing goal values are calculated as shown in Equation 12, where r_o is the radius for the optimal fill factor (r_o = 2.817 mm), and w_y and w_z are the mode radii in each transverse axis. The goal value is therefore an assessment of how closely the mode comes to matching the specified optimal radius value.

81

$$g = \frac{|r_o - w_y|}{r_o} + \frac{|r_o - w_z|}{r_o} \qquad (12)$$

The stability of the cavity must also be examined as the ROC of the thin-disk changes. The values used for the disk curvature are 2080 mm ROC for low power (cold cavity) and 2130 mm ROC for high power (hot cavity). The secondary analysis stage takes an input cavity and creates two cavities from it by changing the disk curvature to each the hot and cold values. Each cavity (hot and cold) is then assessed based on the tests described in the first stage of analysis, and each is assigned a goal value. If the goal value of each cavity is non-failing, it then returns the average of the two passing goal values as the new goal value for this particular configuration. This is referred to as the fitness function, which is called by the GA to assess each individual cavity solution. A flow chart of the cavity assessment process via the fitness function is shown in Figure 75.
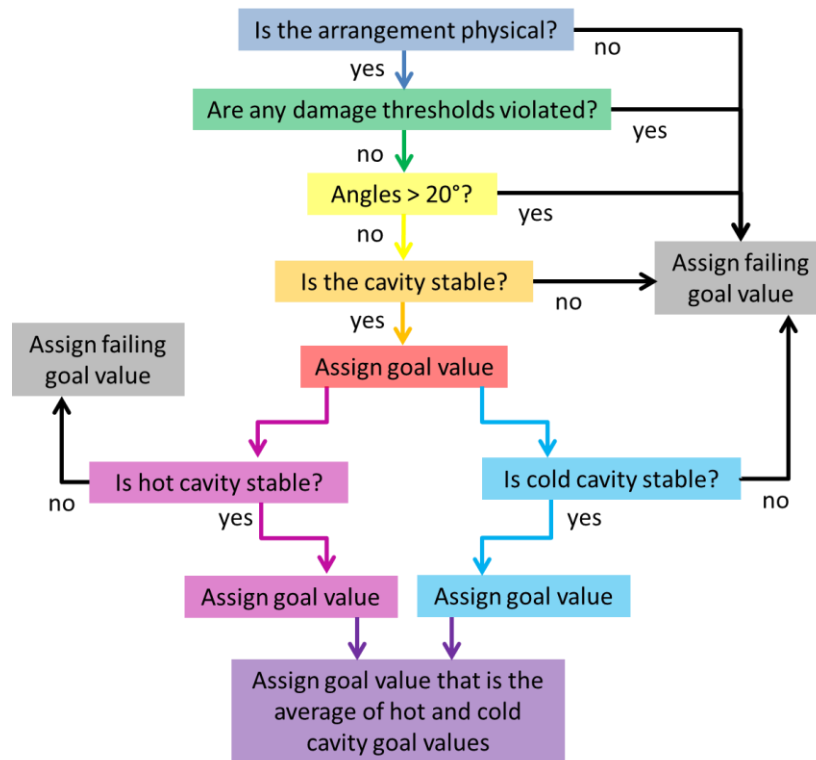
Figure 75: Flow chart showing the assessment process of an individual cavity solution using the fitness function

82

When the optimization process runs, the GA starts by generating an initial population of 1000 individuals. Each individual consists of a 1 x 12 array that contains an x-position, y-position, and a ROC for each of the 4 mirrors in the cavity. The ranges for each of these parameters are defined by the user, and in this case the positions of each mirror are limited to a sub-quadrant of a square 2D space that is 600 x 600 mm, with the specific ranges for each parameter shown in Table 3. The disk alone is held at a fixed position with a fixed curvature because the fitness function itself is responsible for examining the different curvatures of the disk.

Table 3: Specified bounds of the mirror positions and curvatures used by the genetic algorithm

Bounds (mm)	Mirror 1	Mirror 2	Disk	Mirror 3
Upper X	300	0	250	0
Lower X	0	-300	250	-300
Upper Y	0	0	250	300
Lower Y	-300	-300	250	0
Upper Curvature	10^5	10^5	2080	10^5
Lower Curvature	-10^5	-10^5	2080	-10^5

Each member of the initial 1000 member population is analyzed by calling the fitness function to assign it a goal value. The next generation is then created, consisting of 500 individuals (and 500 for every subsequent generation) by taking the best 90 performers as the elite children, and a 0.4 cross-over fraction, which means that 164 individuals are created by cross-over and 246 are created by mutation. The GA then continues to spawn new generations, looking for smaller and smaller goal values until it reaches the specified value for acceptance, chosen to be 0.05 which corresponds to a 95% percent match with the ideal fill factor. When a value of 0.05 or smaller is found, the code stops iterating and saves the goal value and the corresponding cavity arrangement. Alternately, the code terminates if the goal value does not advance for a specified number of iterations.

The optimizer is then run repeatedly. It typically succeeds in finding a solution which meets the specified goal value 93 out of every 100 final configurations generated. An arbitrary selection of 100 of these cavities, all with goal values < 0.05, is shown plotted spatially in Figure 76. As can be seen the disk remains spatially fixed at (250, 250). Mirrors 1 and 2 (lower two quadrants) are roughly confined within a smaller sub-space of each quadrant, while mirror 3 tends to range about much more dramatically spatially, indicating a lower dependence upon its location.
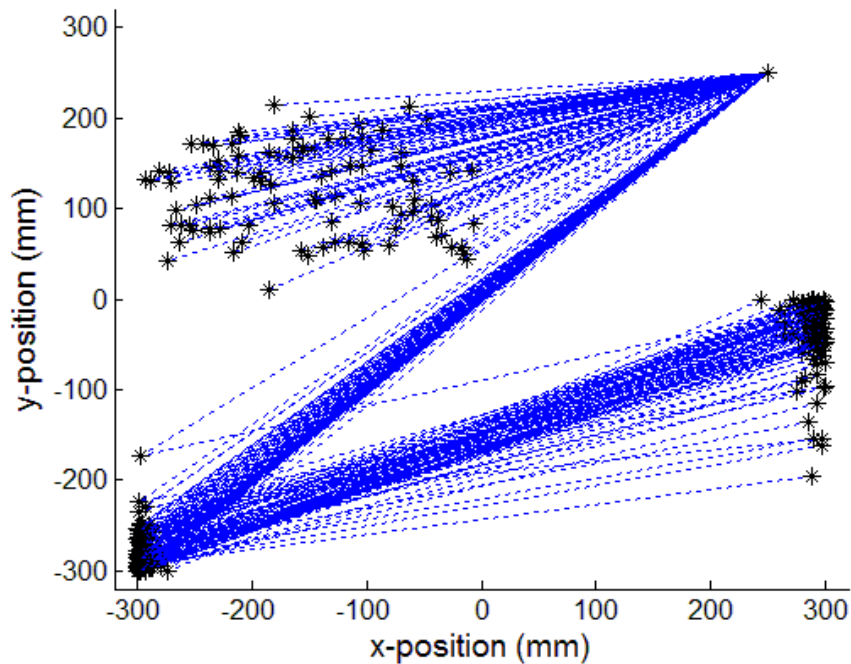
Figure 76: Spatial plot of the results 100 runs of the cavity optimization routine for a 4 mirror cavity

The best cavity produced out of these 100 runs has a goal value of 0.0328, and is plotted in Figure 77 along with the next four best cavities found, having goal values of 0.0402, 0.0418, 0.0427, and 0.0428 respectively. The parameters of the best cavity configuration are shown in Table 4. The ROC of mirrors 1 and 3 are very large and therefore approach flat mirror surfaces. The actual range of curvatures examined by the optimizer is from -10^5 to 10^5. A full range of curvatures which would include a closer approximation of a flat mirror also creates a very large

parameter space within which optimizer has difficultly locating stable solutions. This is why the curvature ranges were limited to -10^5 to 10^5. When this is considered, the best design as determined by the optimizer includes two flat end mirrors and a negatively curved mirror matched against the curvature of the disk.
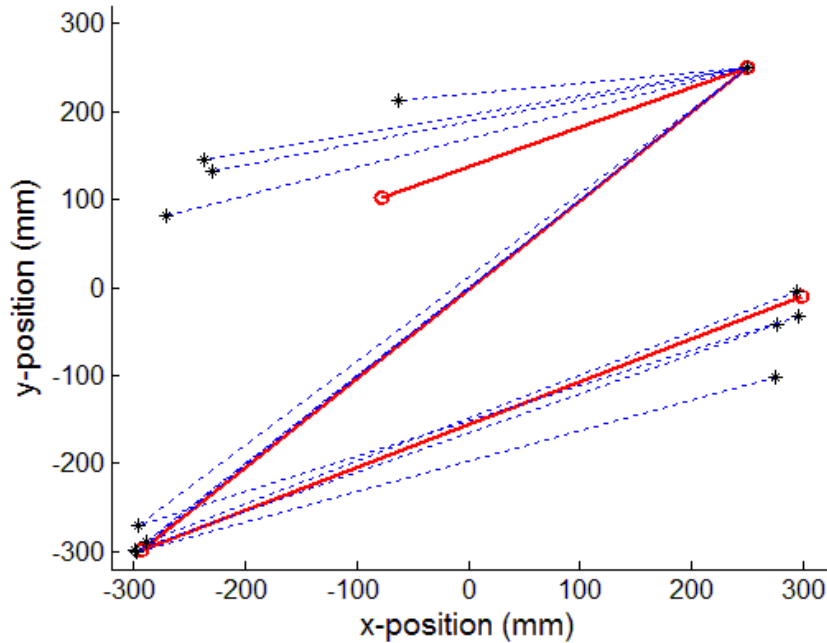
Figure 77: Five best 4-mirror cavity optimization results, with best value cavity (0.0328) shown in red.

Table 4: Optimized cavity results for a goal value of 0.0328

Parameter (mm)	Mirror 1	Mirror 2	Disk	Mirror 3
X position	299	-292	250	-78
Y position	-10	-298	250	102
ROC	73445	-598	2080/2130	91685

The mode plot of the best cavity solution as created by LASCAD is shown in Figure 78 for the 2080 mm ROC value for the disk. The mode size is smallest at mirror 1, but closely fills the pump spot on the disk. In comparison, for the original cavity design of the TruDisk 1000, a -500 mm ROC mirror is used as the end mirror, with flat mirrors adjacent to the disk as the turning and end mirrors (Figure 79).
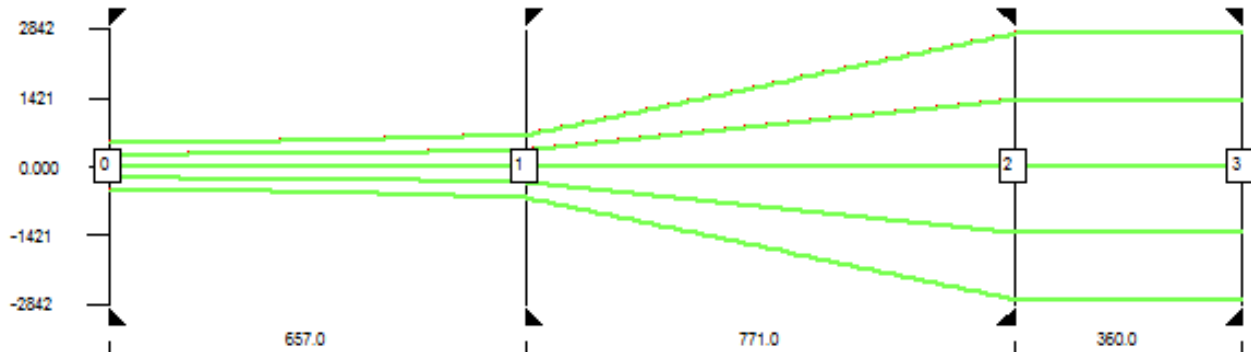
Figure 78: Cavity mode plot from LASCAD of the best optimized cavity results, showing 96.7% fill factor of the ideal radius for the disk (element 0 – flat end mirror, element 1 – negatively curved turning mirror, element 2 – thin-disk, element 3 – flat end mirror)
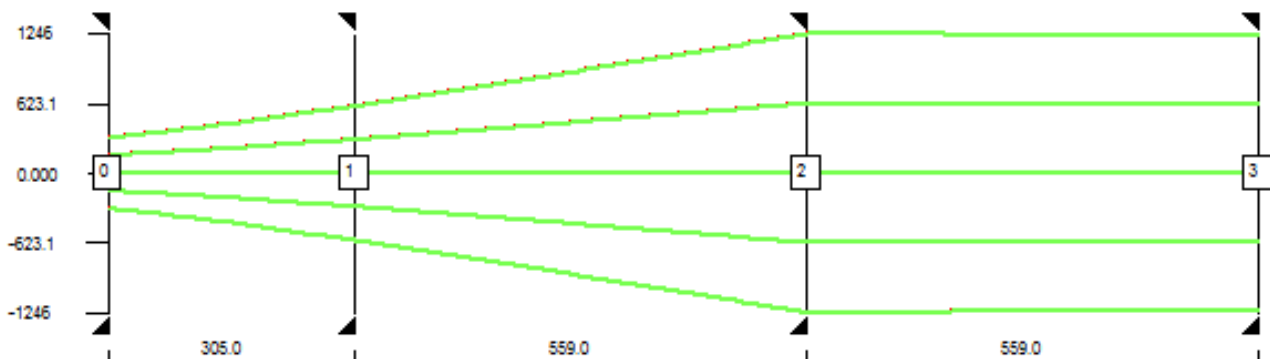
Figure 79: Mode plot of the fundamental mode in the original TruDisk 1000 cavity (element 0 – negatively curved end mirror, element 1 – negatively curved turning mirror, element 2 – thin-disk, element 3 – flat end mirror)

The optimizer code operates on the assumption that the cavity mode is TEM_{00}. However in LASCAD apertures can be used to calculate the modal content that the cavity can support, and give a projection of the output beam's M^2 value. Using an aperture of 3.15 mm radius at the disk (corresponding to the size of the pump spot), the estimated beam quality for the optimized cavity result is $M^2_x = 1.32$ and $M^2_y = 1.24$, whereas these same values for the original TruDisk cavity are $M^2_x = 6.42$ and $M^2_y = 6.39$. This indicates that while the optimizer code is not explicitly calculating and sorting for lower M^2 values, it is still achieving close to fundamental mode solutions via the 80% fill-factor criterion.

86

The spot sizes for the optimized cavity result as determined by LASCAD and the optimizer code are shown in Table 5. However, the optimizer code does not address astigmatism in the cavity that is specifically caused by non-zero angles of incidence on the mirrors i.e. the angular arrangement does not have an effect on the optimizer's goal value assessment. So for a more complete comparison the optimal cavity is also analyzed in LASCAD with a specified 0° incidence for all mirrors. Thus the cavity mode spot sizes are examined for three modeling cases: 1) the optimized cavity as entered into LASCAD with varying angles of incidence, 2) the values for spot sizes as produced by the optimizer code directly (identical in x and y), and 3) the optimized cavity entered into LASCAD with 0° incidence (also identical in x and y).

While the trend in the spot sizes from left to right is consistent across the different calculation methods, there is a significant difference in the numerical values, even when 0° incidence is applied in LASCAD in order to more closely approximate the optimizer code. It should also be noted that the initial results of the optimizer code yielded configurations which were deemed unstable when entered into LASCAD. The source of this error and the discrepancy between the spot sizes is most likely interrelated. While the stability issue was resolved by inserting an additional ABCD-matrix-based stability assessment as a MATLAB-based function, the spot size discrepancy has not yet been resolved, a subject which is currently under discussion with our collaborator.

Table 5: Spot size calculated values for the optimized cavity result via various programs

Parameter (µm)	Mirror 1	Mirror 2	Disk	Mirror 3
LASCAD spot size x	491	655	2739	2749
LASCAD spot size y	693	754	2831	2842
C++ spot size x	501	657	2729	2739
0º LASCAD spot size x	582	685	2707	2717

In considering the expansion from 4 to 13 mirrors (in order to model and optimize the full regenerative amplifier cavity), several issues must be examined as the requirements of the code

change. First, going from 4 to 13 mirrors dramatically increases the parameter space that must examined. For each mirror there are up to 3 parameters (x position, y position, and radius of curvature), and if all are varied this would produce a parameter space consists of 39 variables. In addition to the amount of processing power needed, this also presents a potential issue as to the increasingly low probability of randomly selecting a stable cavity out of such a large space. In order to reduce both the needed processing power and the parameter space, the final model will only optimize a sub-set of curvatures, and the positions of the mirrors will be restricted to smaller sub-domains of the full 2D area utilized. However, before further progress towards cavity expansion can continue, it is important to address and resolve the source of the spot size and stability discrepancies.

In its current state the optimizer code can find a configuration which optimally suited to the desired characteristics as outlined in the goal function and fitness assessment. As the discrepancy issues between the optimizer code and LASCAD are corrected, the accuracy of the model's final results is expected to improve, and then a full 13 mirror cavity optimization can be completed.

3.7. Continuous Wave Assembly of the Regenerative Amplifier Cavity

In order to assemble the full regenerative amplifier, the first step was construction of the cavity in the CW regime. In order to assemble the cavity in methodical fashion a plan for construction was created based on adding one mirror at a time. Using 4 intra-cavity irises and a visible alignment beam, the full system was assembled and characterized. One modification to the design that was employed in order to build the system was the use of a 90% reflective flat output coupler (OC). As the final cavity uses the TFP as the OC, building the final design without making a substitution for the OC would yield an all-HR mirror cavity, yielding very high

intra-cavity powers and only a leak from the TFP to be used to characterize the system. As such the OC was employed as a turning mirror during various stages of the construction, and finally as the flat end mirror in the PC arm (Figure 80).

The slope of this configuration is 38.6% (Figure 81) measured up to 104 W of output power. In the current configuration the operating software of the laser limits the maximum current to 40 A of pump current, which according to the measured slope would yield a maximum of ~179 W. The lower output power and slope efficiency is due to a lower level of energy extraction of the more fundamental beam than the previously more top-hat higher order operation. The power of the system fluctuated, most likely due to the presence of some higher order modes, this fluctuation range being shown as error bars. It was decided not to approach the maximum pump current in the CW configuration due to the level of fluctuation observed.
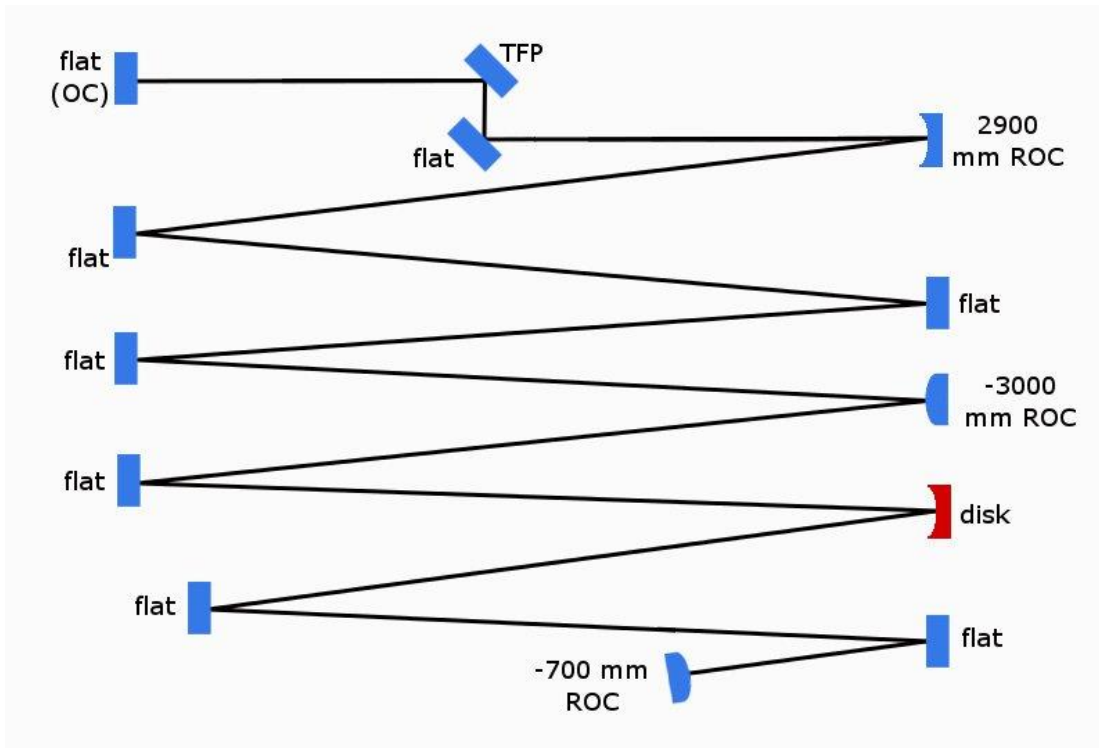
Figure 80: Cavity of the regenerative amplifier in CW configuration (TFP – thin film polarizer. All mirrors labeled "flat" are HR except when noted otherwise)

89
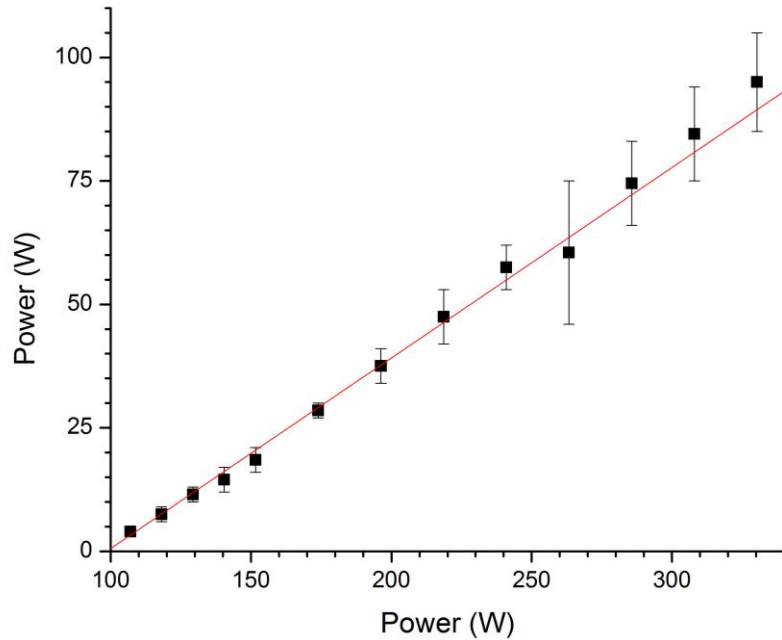
Figure 81: Slope of regenerative amplifier cavity operating CW

It was noted during the assembly of a prior design that the cavity mode appeared larger than was projected by the LASCAD design. The exact source of this discrepancy is unclear (as discussed in Section 3.6.1), but may be due to the propagation of higher order modes outside of the pumped region on the disk, which was observed with an IR viewer. However, given the importance of the mode size in the PC, the design was revised to its final state and measurements were taken to ensure that the mode size in the PC would not exceed 3 mm over the full range of curvatures of the disk. These mode measurements were performed by inserting an iris into the cavity near the ultimate location of the PC. With the aperture fully open a slope was taken. Then with the iris set to a diameter of 3 mm, the same slope was taken a second time. Both slopes are plotted in Figure 82.

By assuming a Gaussian beam, a model was created which could estimate the 1/e mode size. This model took the percent loss as measured and compared it to the ratio of two Gaussians, one clipped by an aperture and the other not, as shown in Equation 13, where P_a is

the power measured from the laser with the aperture set to 3 mm, P_0 is the power measured with the iris fully open, r is the radius of the aperture (1.5 mm) and w is the 1/e value of the Gaussian at the aperture. By finding the value of w for which this equation holds true, the mode size of the cavity was determined.

$$\frac{P_a}{P_0} = \frac{\int_{-r}^{+r} e^{-\frac{x}{w}} dx}{\int_{-\infty}^{+\infty} e^{-\frac{x}{w}} dx}$$ (13)
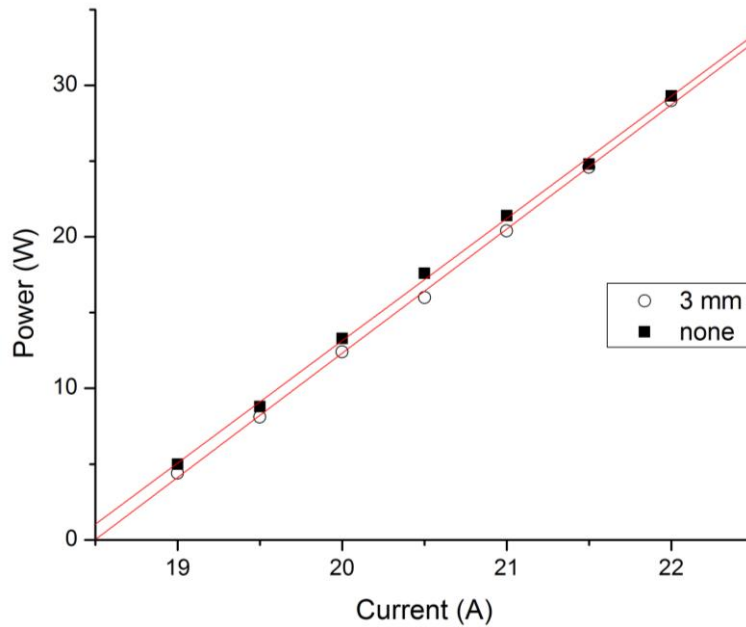
Figure 82: Slopes in W/A of the cavity with no constriction alongside the slope of the cavity with a 3 mm aperture constricting the cavity mode. Note that less power loss is induced as the current increases.

These waist values found with this model are shown in Figure 83. Because the curvature of the disk reduces as the temperature (i.e. pump power) increases, and the mode size in the PC arm is expected to decrease proportionally with the changes in the disk curvature. It is therefore possible to project the mode size at higher powers, in order to check that the mode size will not exceed the damage threshold limit of the PC. The values taken all occur between 0 and 30 W of output power, a portion of the ROC behavior which also exhibits linear behavior. The projection

of waist size was done in steps by measuring the change in slope between subsequent values of

disk curvature, and applying those changes proportionally to the calculated mode sizes.
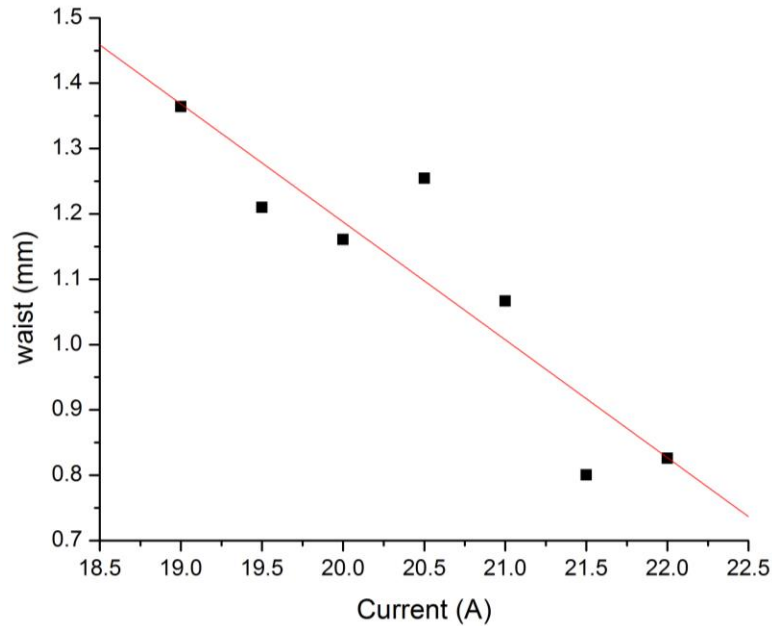
Figure 83: Mode size as calculated from measured power loss using a Gaussian model and a 3 mm aperture
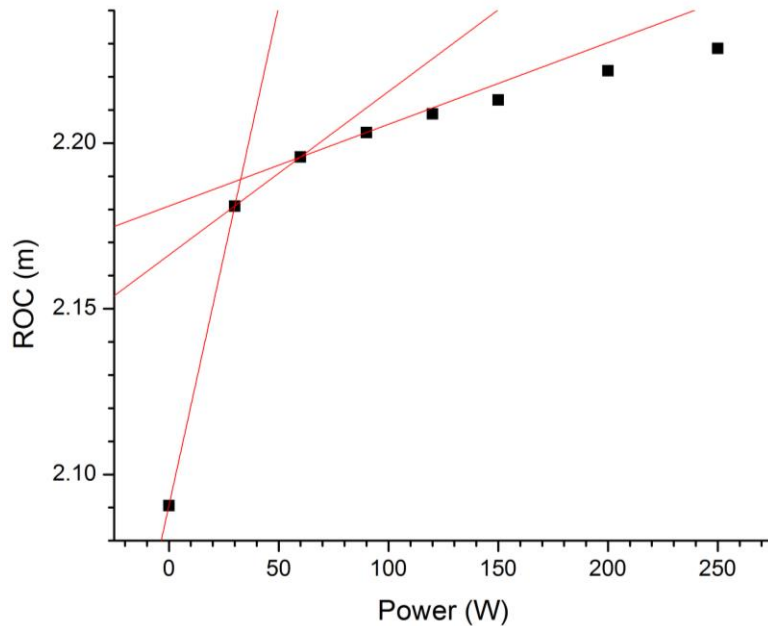
Figure 84: Disk ROC as a function of output power with the slopes created by sequential pairs of values plotted for the first four points (three lines). The changes in these slopes was used to proportionally project the expected waist values

For example, a line was fit to the first two values of the disk curvature measurement, and then a second line was fit between the second and third values (Figure 84). The percent change in slope of these two lines was calculated (%$_C$). Using the waist values at 0 and 30 W and fitting them with a line, the third waist value is projected by using %$_C$ to create the second line, which would connect waist values 2 and 3. This is iterated at various output powers up to ~200 W projected output power. The resulting projection is shown in Figure 85. For a pulse energy of 50 mJ, the minimum possible spot size is 0.4 mm (50 mJ with a limit of 10 J·cm^{-2}) and the value calculated for 40 A (~576 W pump) is 0.5 mm which is equivalent to 6.4 J·cm^{-2}. This confirms that the damage threshold of the PC will be honored over the full potential range of operating powers.
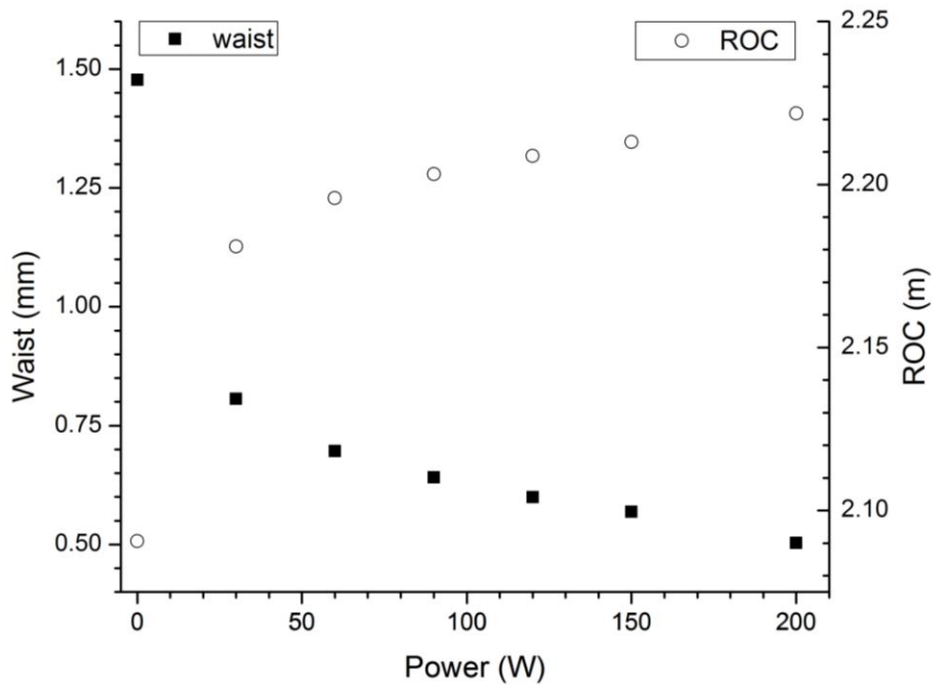
Figure 85: Projected waist values as a function of power, modeled off the changes in the ROC of the disk for the same powers. This indicates that the mode size will not exceed the PC damage threshold at the maximum output power.

As the PC is required not to be used as the limiting aperture in the cavity, apertures were inserted into the cavity which imposed greater restrictions on the cavity than the PC. Modeling

of the diffraction effects created by the apertures was performed using a numerical method published by Campbell and DeShazer 1967 in their paper "Near Fields of Truncated-Gaussian Apertures" [169]. The model was created in MATLAB using numerical integration as shown in the paper.

The code agrees with the authors' values when the same parameters are entered, as is shown in Figure 86. However, while the authors state that the model is accurate for lengths of "several" aperture diameter multiples up to D^2/λ distance (where λ is the wavelength), none of the results presented in the paper include distances of < 100 times the aperture diameter. The code used here appears to present un-physical results at distances of 10 or less multiples of the aperture diameter, so to ensure accurate results, only a multiple of 100 or more will be used here.
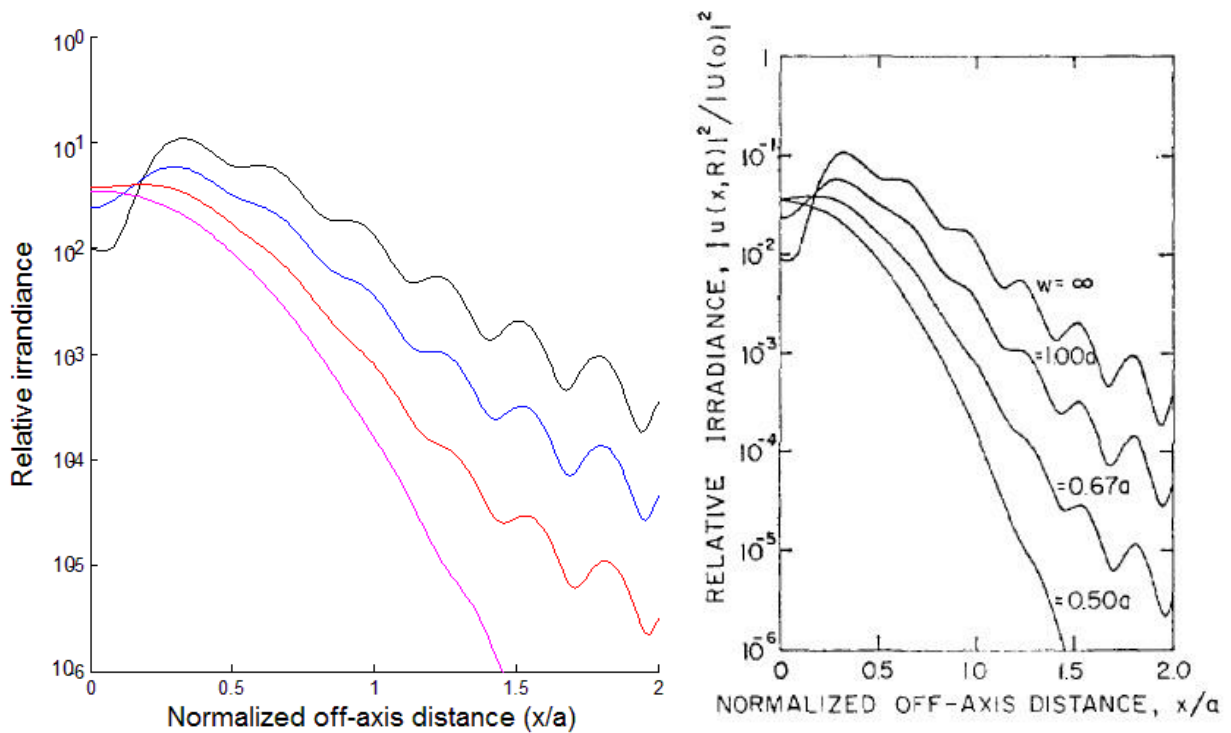
Figure 86: Verification and comparison of model results with results published by Campbell and DeShazer (right image by Campbell and DeShazer 1967 [169])

Several ceramic apertures of diameters of 4, 5, and 7 mm of the same kind as those used in the PC were acquired, and are assessed for use in the cavity as they are less reflective and are

less conductive than metal apertures. Using these aperture values as the radii for testing the model along with the calculated mode size, different distances from the PC were tested in order to determine acceptable locations for the apertures within the cavity. Acceptability was determined by the extent of the diffraction effects generated, specifically hot spots at the center of the mode.

It was determined that the amount of clipping and power loss caused by the 4 mm aperture at any location in the cavity generated diffraction effects with enough power to be of concern, and so only the 5 and 7 mm apertures were used. These were inserted at distances of 190, 960, and 2300 mm from the expected location of PC (Figure 87).
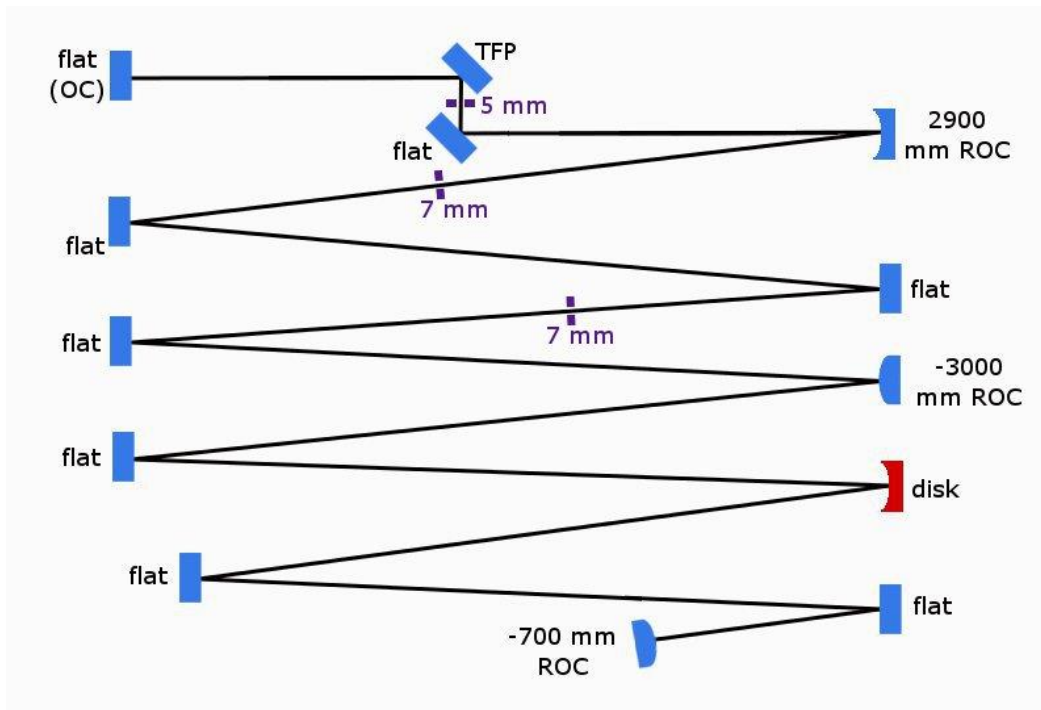
Figure 87: Regenerative amplifier cavity in CW configuration with apertures inserted

Examples of the diffraction effects created by these apertures as predicted by the model are given in Figure 88. In all cases the peak of the first diffraction ring is 1.8 dB down from the main peak, and none of the diffraction effects of the apertures will be able to enter the aperture of the PC, which is important in order protect the inside of the cell from off-axis damage.
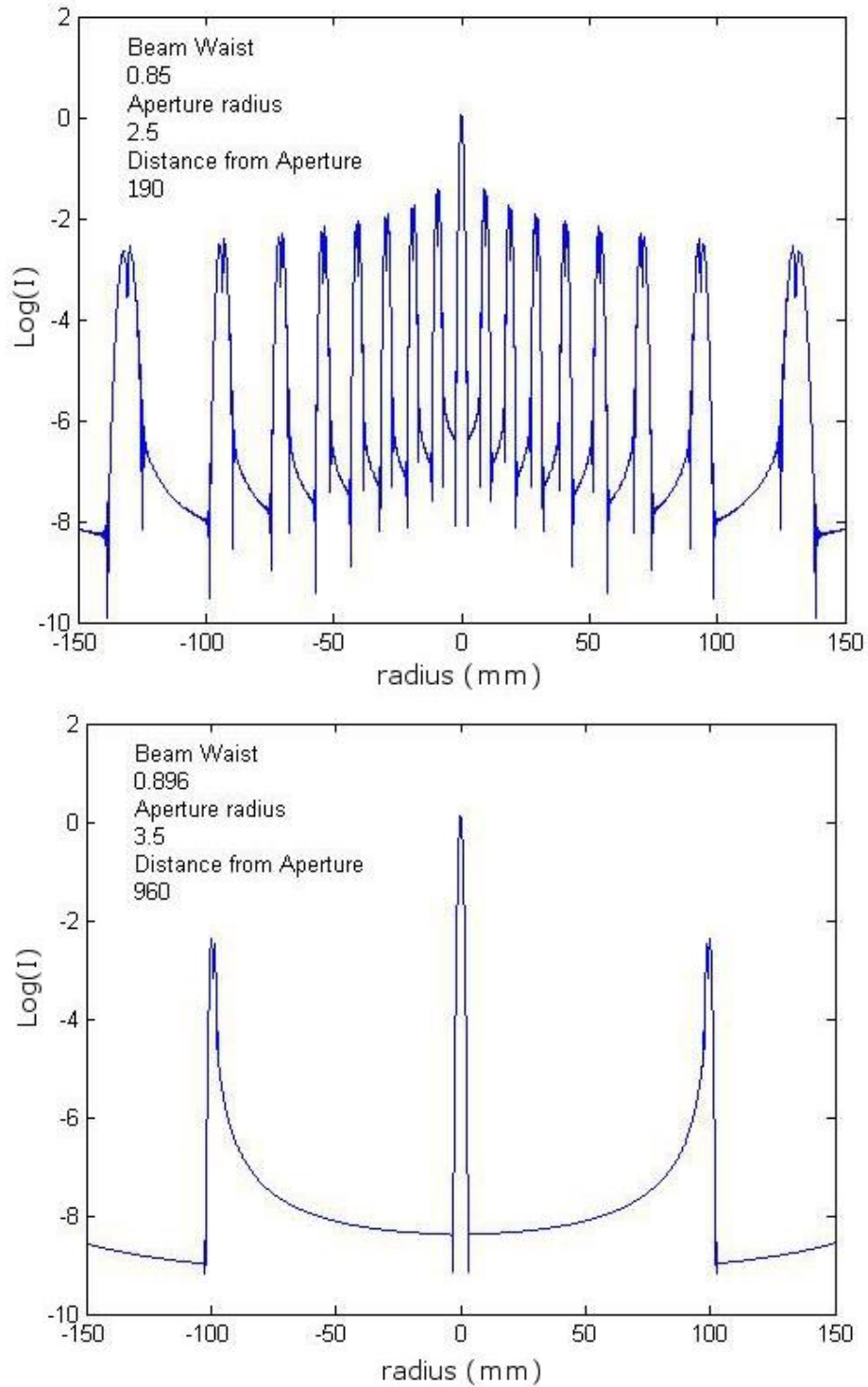
Figure 88: Diffraction effects of the intra-cavity apertures as modeled using the numerical integration method. Each uses the mode size calculated at the cavity location of the aperture for an output power of 30 W. The upper plot is for a 5 mm aperture place near the TFP and the lower for a 7 mm aperture placed after the 2900 mm ROC mirror.

The secondary purpose of the apertures is to ensure that no caustics may propagate in the cavity. It was observed in previous experiments that the PC, even when aligned correctly, generated some stray spots, which if amplified could cause damage to the PC or other parts of the cavity. Observing the apertures with an IR Viewer the spots are visible on the apertures, and all spots are accounted for and blocked by the apertures.

After insertion of the apertures another slope was taken to ensure that no notable loss is observed in the output, the result of which is shown in Figure 89. The slope taken after the insertion of the apertures has a higher slope efficiency (40.7%) compared to the previous value of 38.6% before the aperture insertion, however this difference may be due purely to the uncertainty created by the level of fluctuation in the output power.
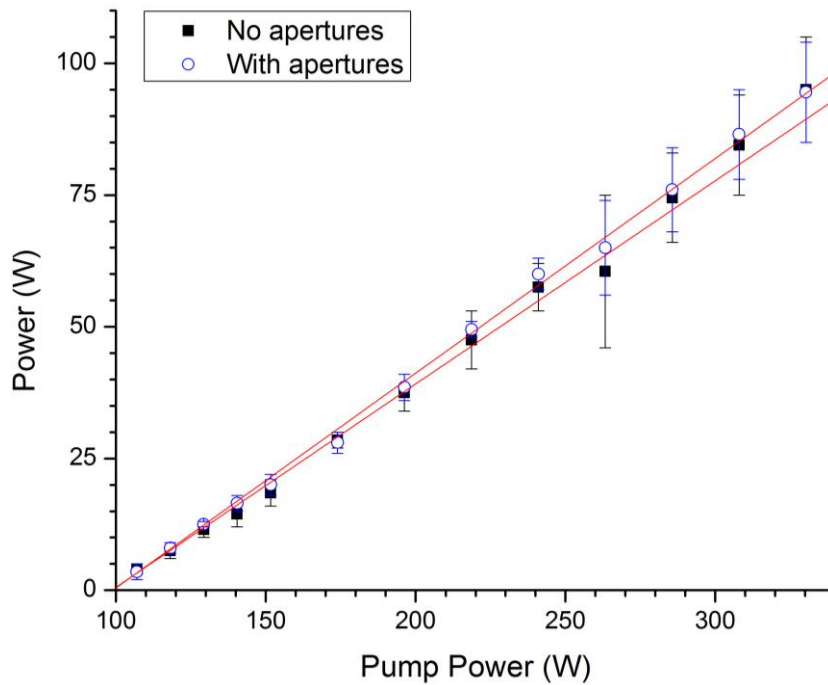
Figure 89: Slope of the regenerative amplifier cavity in CW configuration before and after the insertion of 5 and 7 mm apertures.

3.8. Q-Switched Operation

In order to begin Q-switch operation of the cavity, the PC and a QWP were inserted (Figure 90). The purposed of Q-switching it to optimize the alignment of the QWP and PC as well as optimize the voltage applied to the PC in preparation for regenerative operation. The goal is to establish operation such that lasing occurs while the PC is on, and lasing is blocked while the PC is off. Alignment of the PC is important both in terms of centration of the mode on the aperture, and in terms of pitch and yaw of the cell, and to optimize its contrast ratio. Once these alignments are accomplished insertion of the QWP and optimization of its rotation angle is performed, along with optimization of the PC voltage.
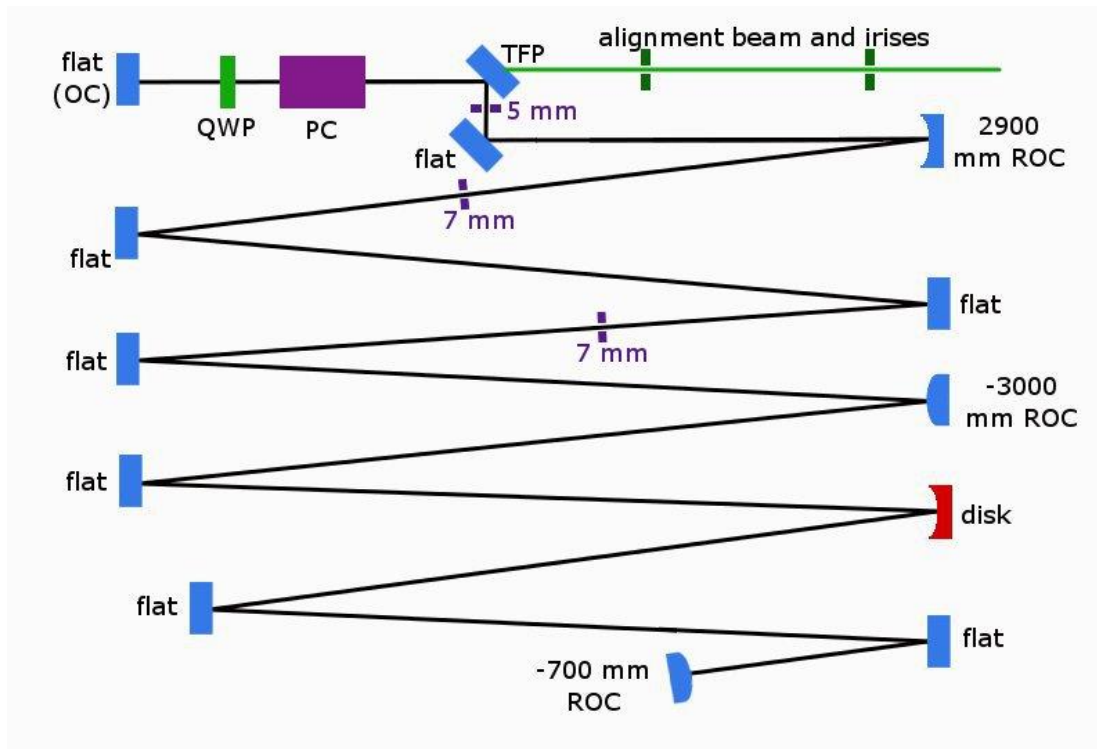
Figure 90: Cavity of the regenerative amplifier with PC and QWP inserted for q-switched operation (all mirrors labeled "flat" are HR)

The OC is left in place so that its cavity loss keeps the intra-cavity powers low. This adds operational safety margin while alignment is optimized. Once the full alignment and optimization is completed the OC will be replaced with an HR mirror.

In order to align the cell, an alignment beam was matched to the cavity mode in the PC arm. This was done by centering two irises on the light leaked from the TFP. These irises were centered at the same height as all the cavity optics, 70 mm, and some alignment of the TFP and end mirror was necessary in order to level the leaked light to match the height of both irises. This is especially important for the isolator when it will be installed. The tip and tilt of the TFP was then locked, and the alignment beam matched to the center of the irises.

Rough alignment of the PC mount was then performed using a dummy PC. The dummy cell consisted of an aluminum cylinder with the same length and diameter as the PC (Figure 91). At each end brass clips were fitted to the face of the cylinder and a shallow counter bore with the outer diameter of 1" was made so that the 4 mm ceramic apertures could be fitted to the faces of the cell. The driving electronics for the cell were set in the cavity, and the dummy cell place in the PC mount. The mount for the cell was then adjusted to match the alignment beam, and then the laser was turned on at low power, and the centration of the cavity mode (matched with the alignment beam) was confirmed by inspection with an IR viewer.

(a)   (b)
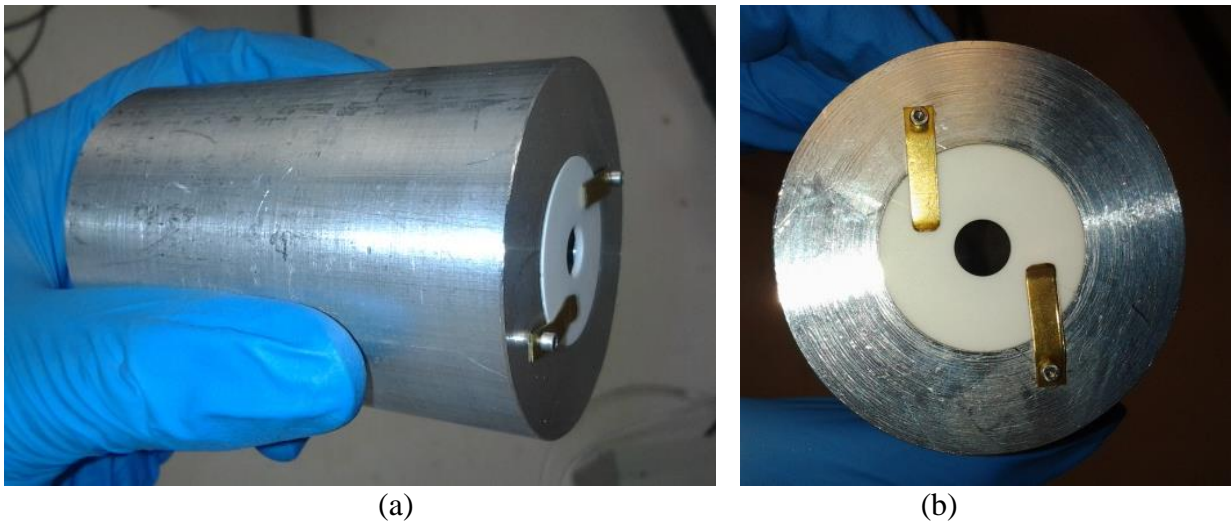
Figure 91: Dummy PC filled with ceramic apertures (7 mm shown) for rough alignment of the PC mount

With the rough alignment performed, the real PC was connected to the driving electronics and inserted into the mount. Using the visible alignment beam, the standard alignment setup of a diffuser and cross-polarizers was used in order to center the produced Isogyre or Maltese cross pattern (Figure 92). Once the pattern was centered and the centration of the beam on the apertures was checked, the laser was turned on with the PC passive, and the alignment of the end mirror adjusted for power.

<center>(a)   (b)</center>
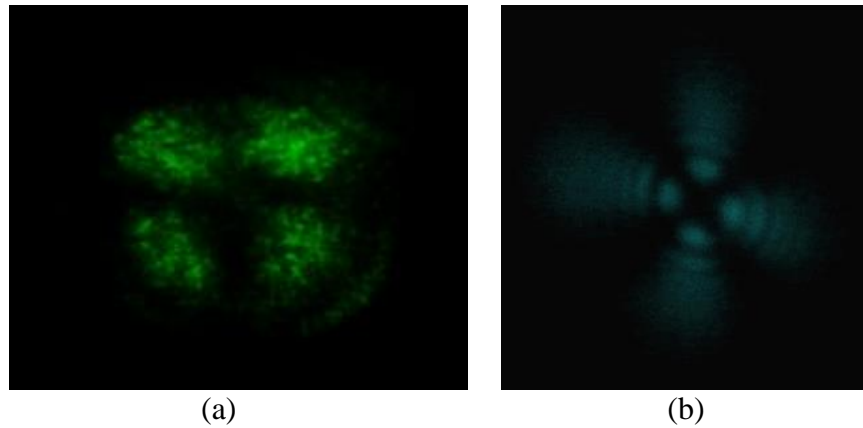
Figure 92: a) Green alignment beam used to produce Isogyre pattern from PC for regenerative amplifier, and b) a white light source for the same (color manipulated for contrast)

The QWP was inserted into the cavity in order to enable Q-switched operation. Output power was observed while the QWP was rotated, and the angle was set such that lasing was obstructed. Because the light in the cavity is s-polarized by reflection off of the TFP, the angle where lasing is obstructed is at 45º to the s-polarized light. This circularly polarizes the light, which is then converted to p-polarized light after reflecting off the end mirror and passing back through the QWP. Then when it encounters the TFP it is transmitted, and therefore lasing in the cavity is frustrated.

The PC requires a duty cycle of 5% or less for safe operation, so in order to operate in the Q-switched the system (which requires longer PC on-times than for regenerative operation) it was operated at lower repetition rates (hundreds of Hz) than it will for seeded operation. When

the PC turns on to quarter wave voltage, it also acts as a QWP, such that by passing through both the PC and then back again, it remains s-polarized and can feedback into the cavity by reflecting off the TFP. The PC circularly polarizes the s-polarized light, the QWP converts it to p-polarized light, which returns p-polarized to the QWP, which circularly polarizes it, and then is changed back to s-polarized light by the PC. Thus the cavity is only able to lase during the PC on time.

The Q-switched configuration was used primarily as a stepping stone towards seeded operation. The voltage applied to the PC and the rotation angle of the QWP were iteratively optimized until the highest output power was found. Once this was accomplished the first study of the Q-switch operation was a study of the gate time of the PC at a set pump power of 117 W. Output powers were observed through the OC, and the pulses that exit the cavity were measured temporally using a photodiode. Looking at the output power as a function of PC on time, the power increases linearly from 40 to 70 µs with a slope of 93 mW/µs, then levels off with an average output power 2.43 W (Figure 93).
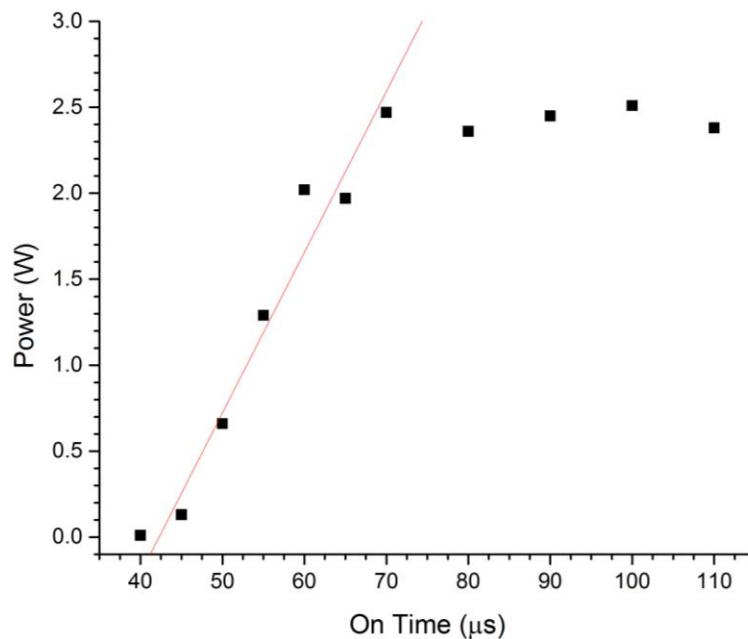
Figure 93: Output power through OC as a function of PC on-time

In terms of temporal behavior, the point in Figure 93 where the output power stops increases represents the onset of parasitic lasing as the PC remains on for longer periods of time. The output pulse varied in shape from shot to shot and is of durations from 370 to 410 ns as the gate time increases from 40 to 100 µs (Figure 94).
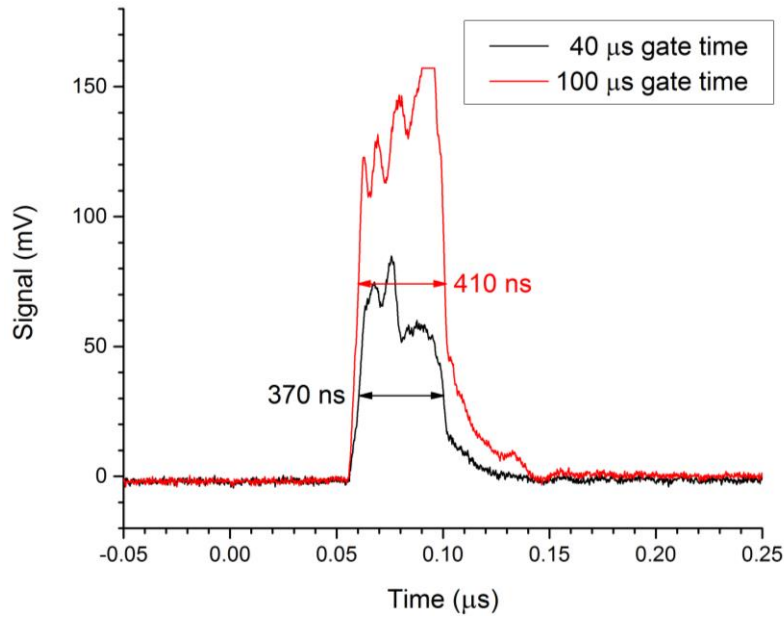
Figure 94: Output pulse at 40 and 100 µs gate times
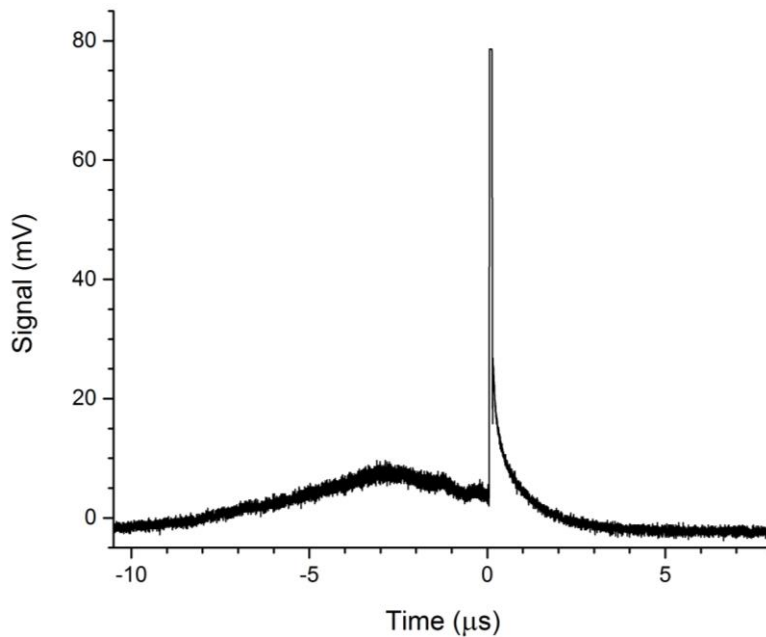
Figure 95: Output pulse for a gate time of 60 µs showing onset of parasitic lasing (photodiode)

For shorter gate times no parasitic lasing is apparent with the output pulse being the dominant feature, but as the gate time increases to 60 μs, leakage through the TFP from parasitic lasing becomes visible in the temporal domain (Figure 95). The hump in the temporal signal preceding the output pulse represents power leaked from the TFP as the cavity begins to lase continuously due to the long PC on-time. Starting at 70 μs the parasitic lasing begins to dominate and the output power levels off.
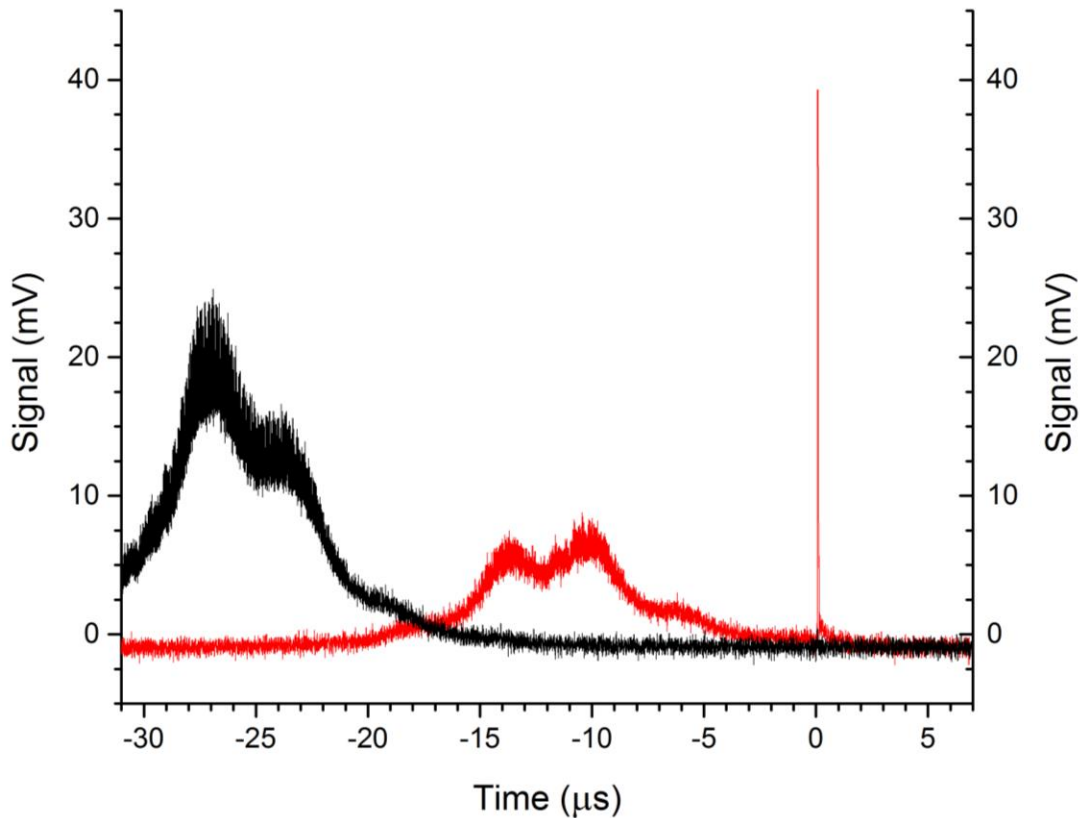
Figure 96: Temporal output of the Q-switched cavity at a gate time of 80 μs showing two different shots which demonstrate the variation in the output

However, there is an on-going competition between the parasitic lasing and the output pulse, which is most likely related to the power instabilities observed in the purely CW case. One possible cause of this is variation in the level of gain experienced by the pulse. Observing the temporal output at 80 μs, sometimes only leaked parasitic lasing is visible, and at other times

both leaked power and an output pulse are visible (Figure 96). In Figure 96 both shots are triggered by a signal which is synchronized with the off-signal of the PC voltage. In the case where no output pulse is visible, the onset of parasitic lasing occurs 13 μs sooner (black) than when an output pulse can be observed (red). The former case most likely results when the pulse experiences higher gain.

Next, looking only at the temporal signal, measurements were taken in order to establish the gate time which yields the highest pulse power for this repetition rate (250 Hz) and pump power (117 W). To measure this, the shot-to-shot variation was averaged using the oscilloscope and the amplitude of the average was taken. As gate time increased power increased linearly until the maximum value (57.5 μs) and then decreased linearly above that point (Figure 97).
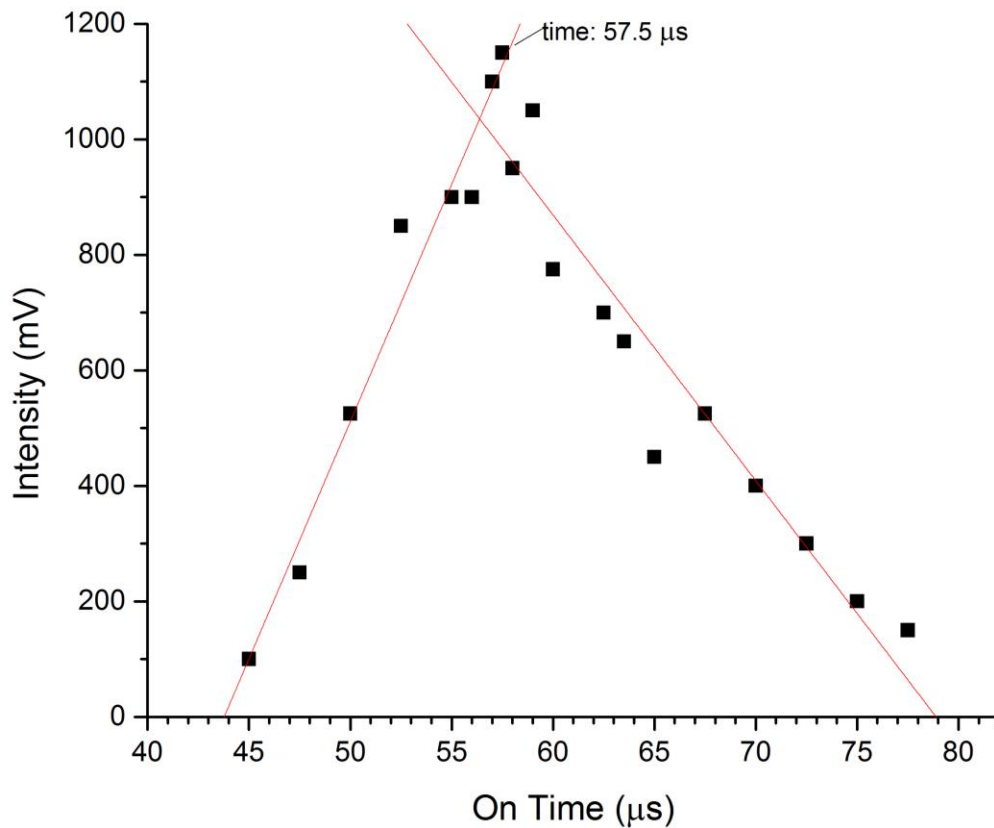
Figure 97: Intensity of output pulses as a function of gate time with 57.5 μs being the optimal time for a repetition rate of 250 Hz at 117 W of pump power

Finally an analysis of pulse energy was performed by fixing the gate time at 57 µs with the same pump power, while the repetition rate was varied. Repetition rates ranging from 250 to 870 Hz were examined. Average power was taken at the OC and used to calculate the average pulse energy of the pulses at each repetition rate. As the repetition rate increased the pulse energy decreased at a rate of 7 µJ/Hz (Figure 98). This indicates that the optimal repetition rate for this system as a Q-switch is lower than the range that has been tested.
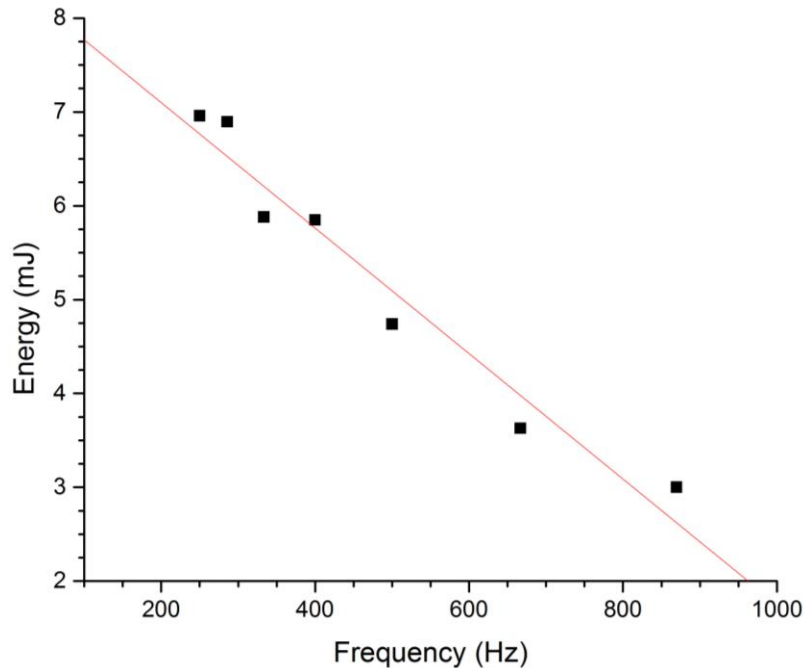
Figure 98: Calculate average pulse energy of q-switched cavity as a function of PC repetition rate, showing a decrease in pulse energy with increasing repetition rate

3.9. Seeded Operation of the Regenerative Amplifier

With Q-switching measurements completed the system was ready for conversion to seeded operation. The irises which had been installed for the alignment of the PC were removed, and the remaining parts needed to form the isolator were assembled (Figure 99). These elements included the Faraday rotator, half-wave plate (HWP) and the second TFP. The alignment was performed using the small percent of light leaked from the intra-cavity TFP (Figure 100) and optimized such that a minimum of light was transmitted through the second TFP.
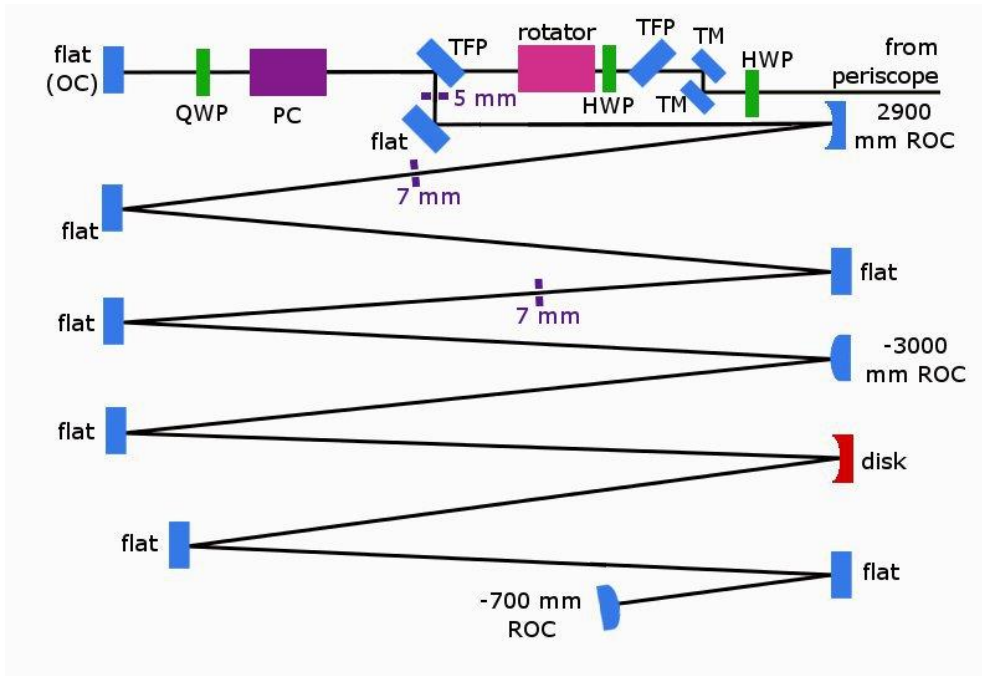
Figure 99: Thin-disk regenerative amplifier and other associated optics for conditioning and redirecting the seed pulses (all mirrors labeled "flat" are high power HR mirrors, TM is for the low power turning mirrors)
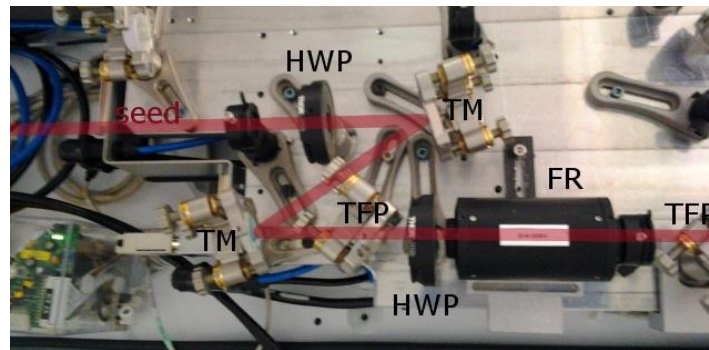
Figure 100: Free space isolator through which the seed enters the regenerative amplifier (HWP - half wave plate, TM - turning mirror, TFP - thin film polarizer, FR - Faraday rotator)

In order to establish alignment of the seed beam with the cavity, two turning mirrors and a HWP were used to align the leaked light from the free-space cavity to a pair of irises. One iris was set between the pulse-picker and the periscope on the seed table, and the other was set on the TruDisk table before the turning mirror and HWP (Figure 101). The seed beam was aligned to these irises and then fixed in place. Then the two turning mirrors on the TruDisk table were used

to bring the small percent of light leaked from the isolator into alignment with the irises, which allowed the seed pulses to oscillate in the regenerative amplifier cavity.
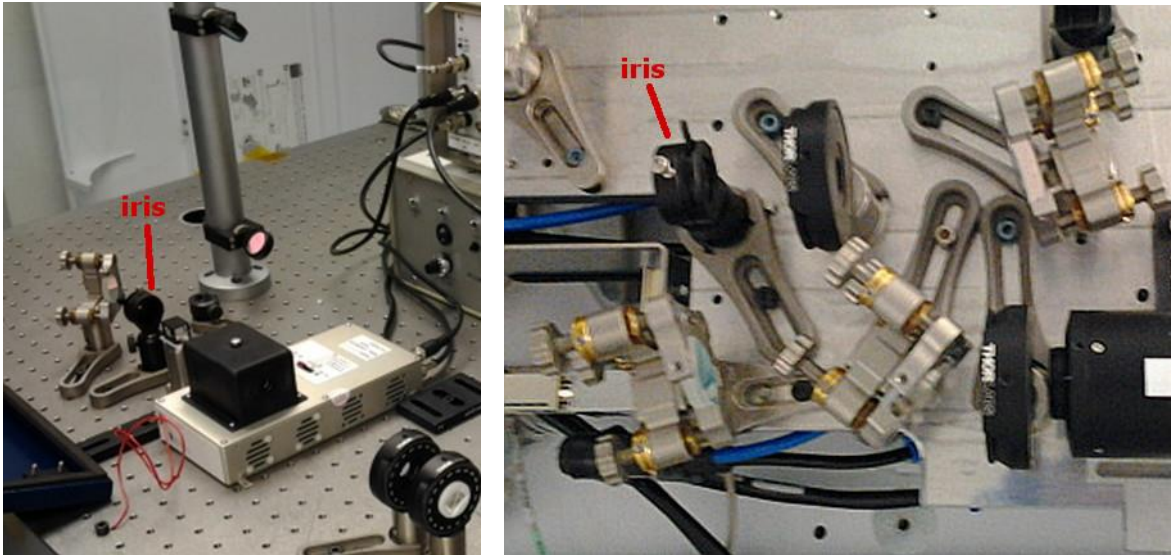
Figure 101: Irises used for the alignment of the seed to the regenerative amplifier cavity

A diagnostics table was set up next to the TruDisk system with a second periscope to capture the light exiting the amplifier. All regenerative amplifier characterization measurements were taken on this this table (Figure 102). With the seed aligned to the cavity and both the PC and TruDisk 1000 off, a pulse train was observed by the photodiode as the pulses passed into the cavity, made one transit of the cavity and then passed back into the isolator which redirects the light to the diagnostics table. This confirmed that the seed light was well-aligned to the cavity.

Next the OC was replaced with an HR mirror. Alignment of the HR mirror was done using the green alignment beam and the photodiode. Rough alignment was performed using the green alignment beam and an intra-cavity iris. This brought the mirror into close enough alignment such that pulses from the fiber seed were observable by the photodiode on the diagnostics table. Fine alignment was then performed with the oscilloscope to ensure that the signal received by the photodiode was optimized. Finally the end mirror knobs were locked in place, which completed all necessary mechanical alignment for the system (Figure 103).
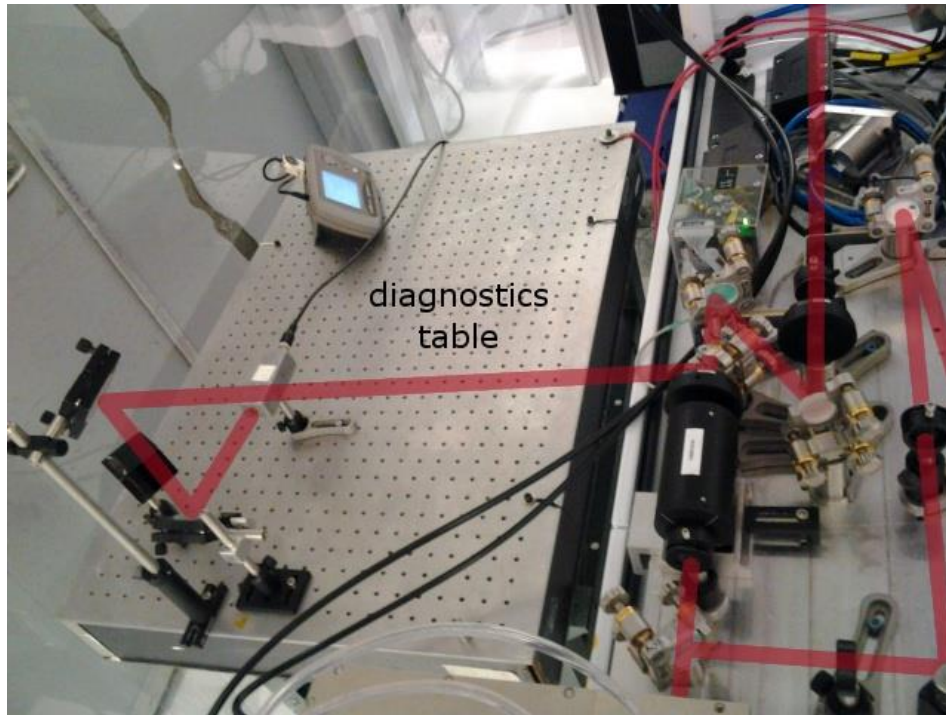
Figure 102: Output of the regenerative amplifier as sent to the diagnostics table by the isolator
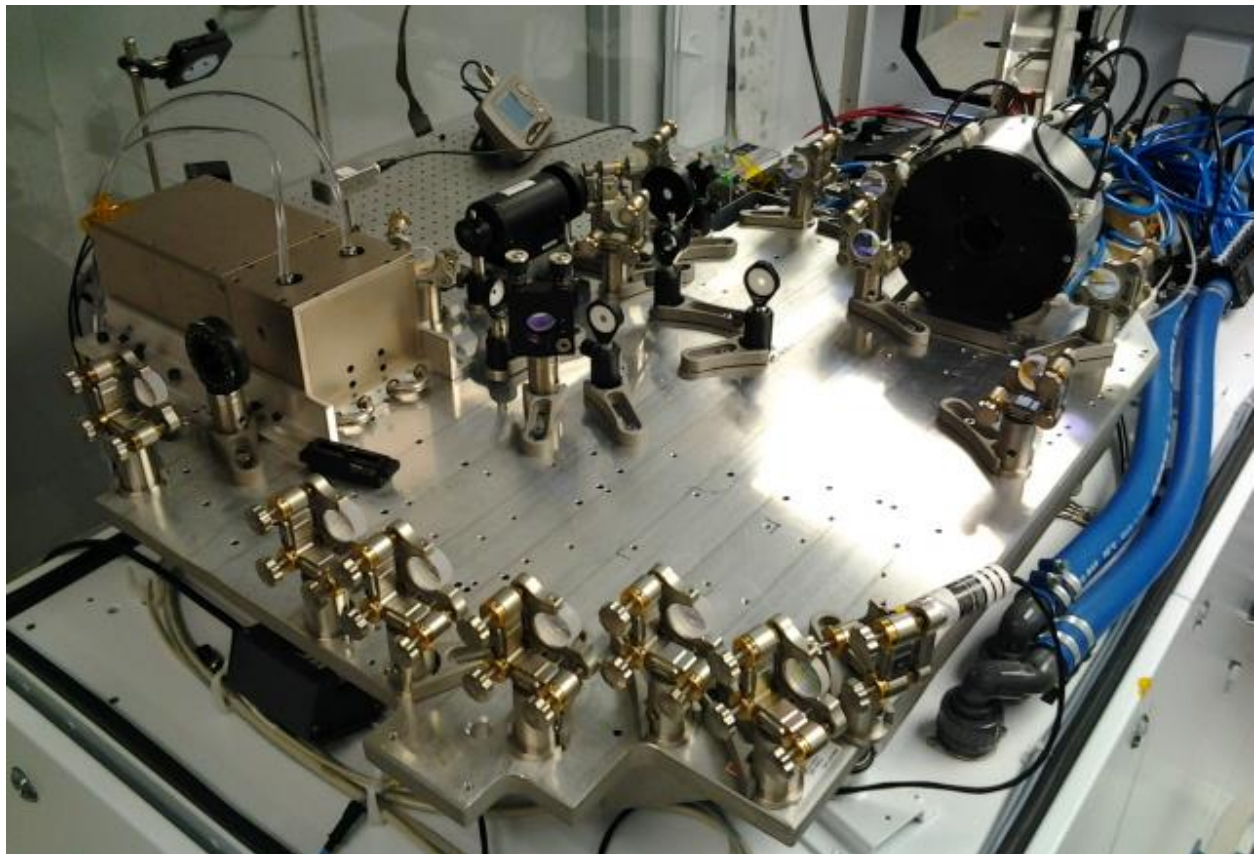
Figure 103: Fully assembled regenerative amplifier cavity

Next temporal alignment of the system was performed such that the correct relative timing between the incoming seed pulses and the operation of the PC could be determined. The seed pulses need to enter the cavity while the PC is off, and once the pulse has entered the cavity the PC must turn on before the pulse makes a complete transit through the cavity in order to trap the pulse. If the pulse enters too early and returns to the PC before it has switched on, it will make a single transit through the cavity and then be rejected by the cavity. If the pulse enters too late and the PC is already on, it will only be able to pass through the PC arm and be p-polarized when it returns to the TFP, such that it passes out of the cavity.

To establish the correct relative timing, the PC was triggered externally using the advanced output from the PP delay generator. In its final state the global timing scheme triggers the PP with sync output from the WFG, and the output from the PP delay generator triggers the PC. For diagnostic purposes a synchronization output from the PC controller is used to trigger the oscilloscope in order to observe the temporal output behavior. For the Q-switching arrangement the PC was triggered via its own internal clock, but seeded operation required a move to external triggering.

For the initial timing assessment, the pulse picker gating was set such that several pulses were allowed through in a burst. The delay of the PC was then triggered off the PP delay generator such that some of these pulses arrived before the PC was switched on, and rest after it has switched on. The PC on-time was set to a duration that was shorter than the period between pulses (1 µs period/1 MHz seed repetition rate), arbitrary value of 200 ns. While observing the pulses as they exited the cavity using the oscilloscope and photodiode, the phase applied to the waveform was tuned continuously. This shifted the pulses temporally within the window created by the PP, and relative to the point at which the PC turns on. As the phase was tuned, when the

pulse entered the cavity and became trapped by the PC, the temporal position of the pulse "jumps" temporally by the amount of the PC on-time (200 ns). Once this behavior was observed, the gate of the PP was closed down to exclude all pulses but the one that was being trapped.

A study of the effect of vibrations on the system output was performed. Vibrations are suspect for two reasons. First, in order to be amplified and analyzed, the seed pulses have to travel from the table where the fiber seed is located, to the TruDisk 1000 table where they were amplified, and then finally to a third separate table for analysis. Second, the TruDisk 1000 optical table is seated on top of its own electronics and cooling system. In order to assess the effect of vibrations on the system, pulse variation was observed as seen from the diagnostics table after each pulse makes 5 passes through the regenerative amplifier cavity. Four cases were examined: 1) with the TruDisk 1000 was shut off entirely and only the PC running in order to trap the pulses in the cavity, 2) with only the electronics of the TruDisk 1000 powered on, but the cooling system shut off and no pump light on the disk, 3) with the system on and the cooling system running, but again without any pump light on the disk, and 4) with the TruDisk 1000 system powered on and with 117 W of pump power on the disk. In all cases the PC on time is 195 ns, corresponding to 5 passes taking 39 ns for each pass.

The results of this test are shown in Figure 104. Each measurement is the envelope created by a total of 512 pulses overlaid on each other. It is also notable that the total pulse variation is lowest when the laser system is off completely (case 1), with a total variation of ±16% about the mean. For cases 2 and 3, where the electronics of the TruDisk 1000 are running, but no pump power is applied, the variation is ±40% and ±42% about the mean (respectively), indicating that vibrations caused by the electronics of the TruDisk are increase the noise by ~2.5

times, but that the cooling system is not a significant contributor of noise. However there is a very significant increase in variation with the application of pump power, increasing to ±74% about the mean, or a factor of >4.5 times higher than the first case. As has been seen in other modes of operation, this indicates the presence of a temporally variable loss in the system.
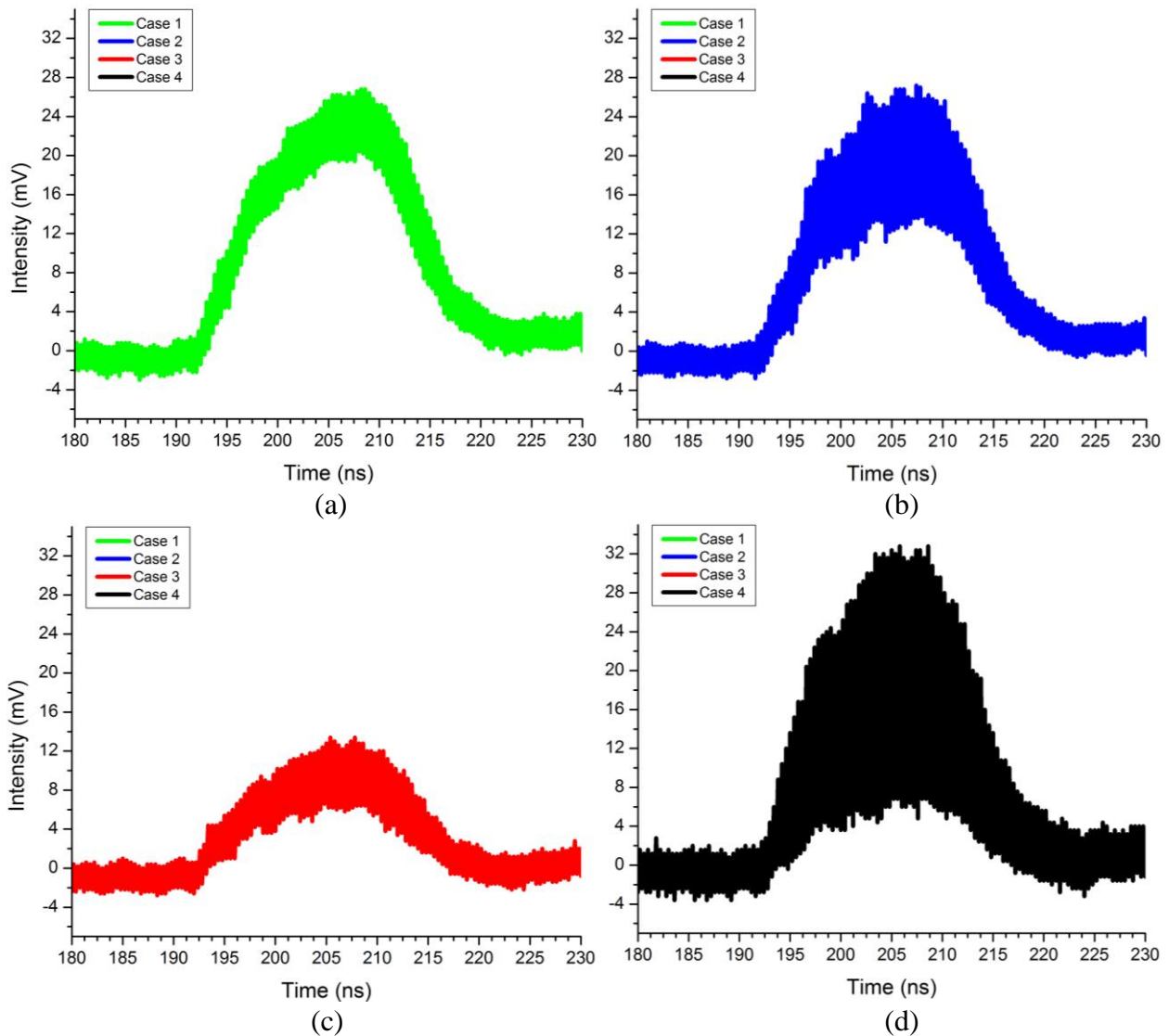
Figure 104: Vibration analysis for four cases: a) TruDisk 1000 off, b) TruDisk 1000 on only, c) TruDisk 1000 on and the cooling system running, and d) TruDisk 1000 on, the cooling system on and 117 W of pump light applied to disk. Each measurement is an envelope created by the overlay of 512 pulse measurements.

Something unexpected to note is that the amplitude of the pulse is dramatically affected when cooling system is switched on. The cooling system may be operated by depressing a

button on a hand switch, a feature included to test the system for leaks (the system will not normally operate the cooling system without pump light applied to the disk). Thus the cooling system, which cools all the optics including the disk, may be turned on without the application of pump power (conversely though it is not possible or advisable to turn the pump light on without the cooling system operating). When the system is running and the hand switch is operated, the pulse amplitude dropped with the onset of cooling, and returned immediately when the cooling system is switched off. This is most likely due a change in curvature of the disk affected by the cooling water, possibly causing modal losses.

Because the sample rate of the WFG is 62.5 MSa/s there is a limited level of resolution when creating arbitrary pulse shapes (only 16 ns/Sa). As such, only 2 non-zero points can be manipulated to create a pulse that is under 30 ns in duration. Operating within this constraint, three different pulse shapes were used for seeded operation. The first is a 20 ns long square pulse which is a built-in function of the WFG. The two other functions were drawn using the arbitrary waveform software purchased with the WFF, and are mirror images of each other. Shape 1 rises from 0 to 4 V in 16 ns, from 4 to 1 V in the next 16 ns, and from 1 to 0 V in another 16 ns. Shape 2 is shape 1 mirror opposite, rising from 0 to 1 V, 1 to 4 V, and dropping from 4 to 0 V. This gives shape 1 a leading edge which is sharper than its falling edge, and gives shape 2 a falling edge which is steeper than its leading edge. The shapes as output by the fiber pre-amplifier are shown in Figure 105. While not dramatic in shape variation, the arbitrary waveforms are adequately distinguishable for a demonstration of pulse shape retention.

The evolution of each shape 1 and 2 was examined as a function of the amount of time the pulse spends in the regenerative amplifier cavity i.e. the number of passes the pulse makes. At a low number of passes the shape maintains a high level of shape integrity. As the number of

passes increases an element of noise is introduced which increases with each pass until the output pulse shape mostly dominated by noise. This root cause of this is likely linked to the cause of the power fluctuations in the CW case and the variation observed in the Q-switching case.
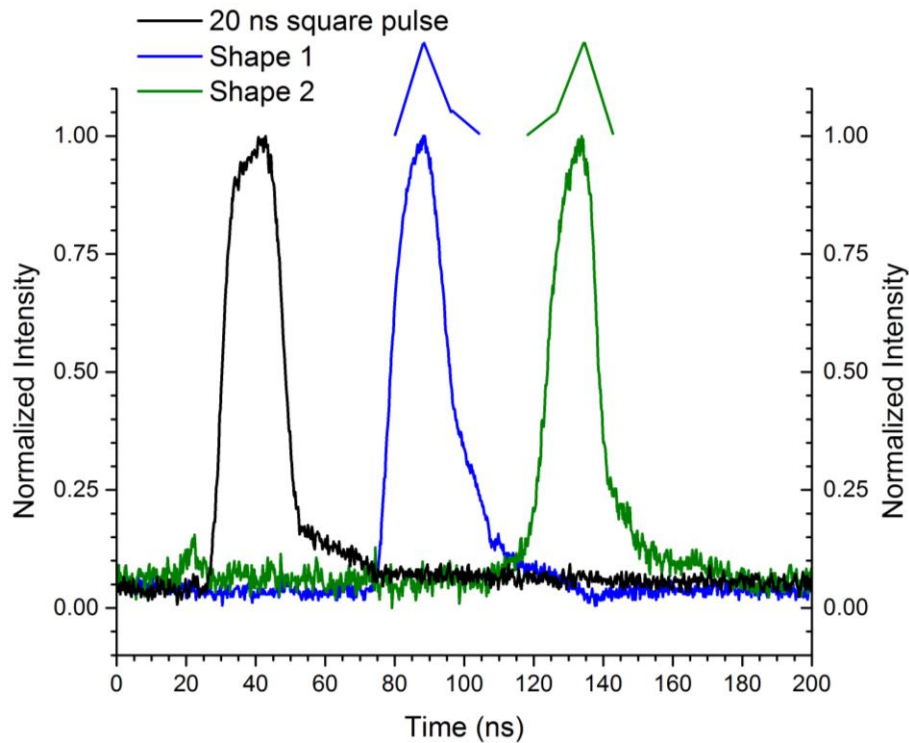
Figure 105: The three pulse shapes used in the operation of the regenerative amplifier

However, though the noise increases dramatically with the number of passes, when observed shot-to-shot it is apparent that the original pulse shape is retained in some instances. The evolution of pulse shapes 1 and 2 is observed for an increasing number of passes, and the overall shape is retained for up to hundreds of passes (Figures Figure 106 and Figure 108). However, as the noise is proportional to the number of passes, shots which have a strong resemblance to the original pulse shape become fewer and farther between. Gain shaping is particularly evident the longer the pulse remains in the cavity (Figure 108), but the original pulse shape is not entirely lost. Note that the offsets shown between the pulses in the following figures

demonstrating the pulse shape evolution is a matter of differing trigger times only, and does not represent a material difference or delay between the pulses.
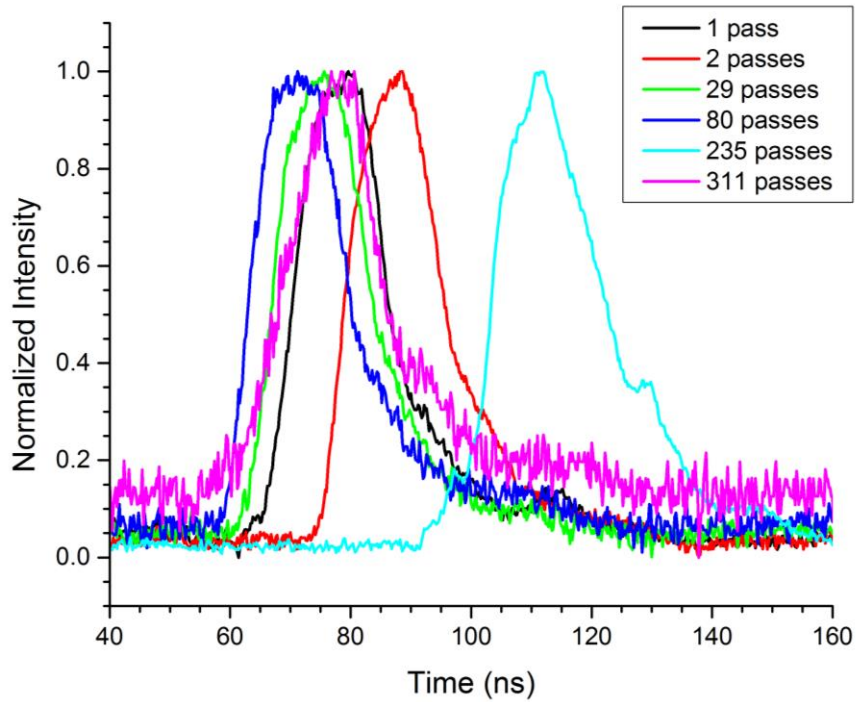
Figure 106: Evolution of pulse shape 1 as the number of cavity passes increases
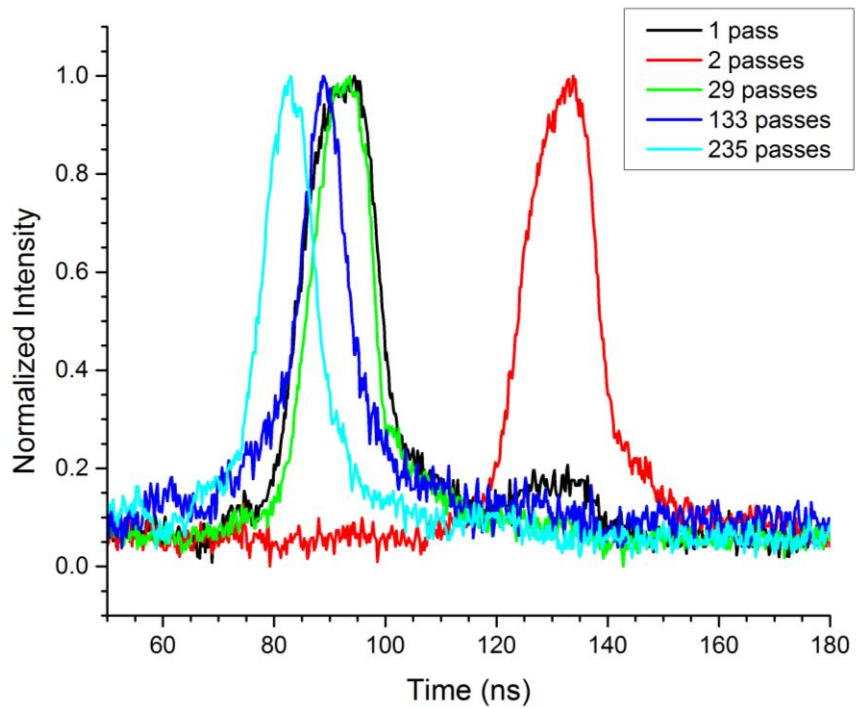
Figure 107: Evolution of pulse shape 2 as the number of cavity passes increases

114
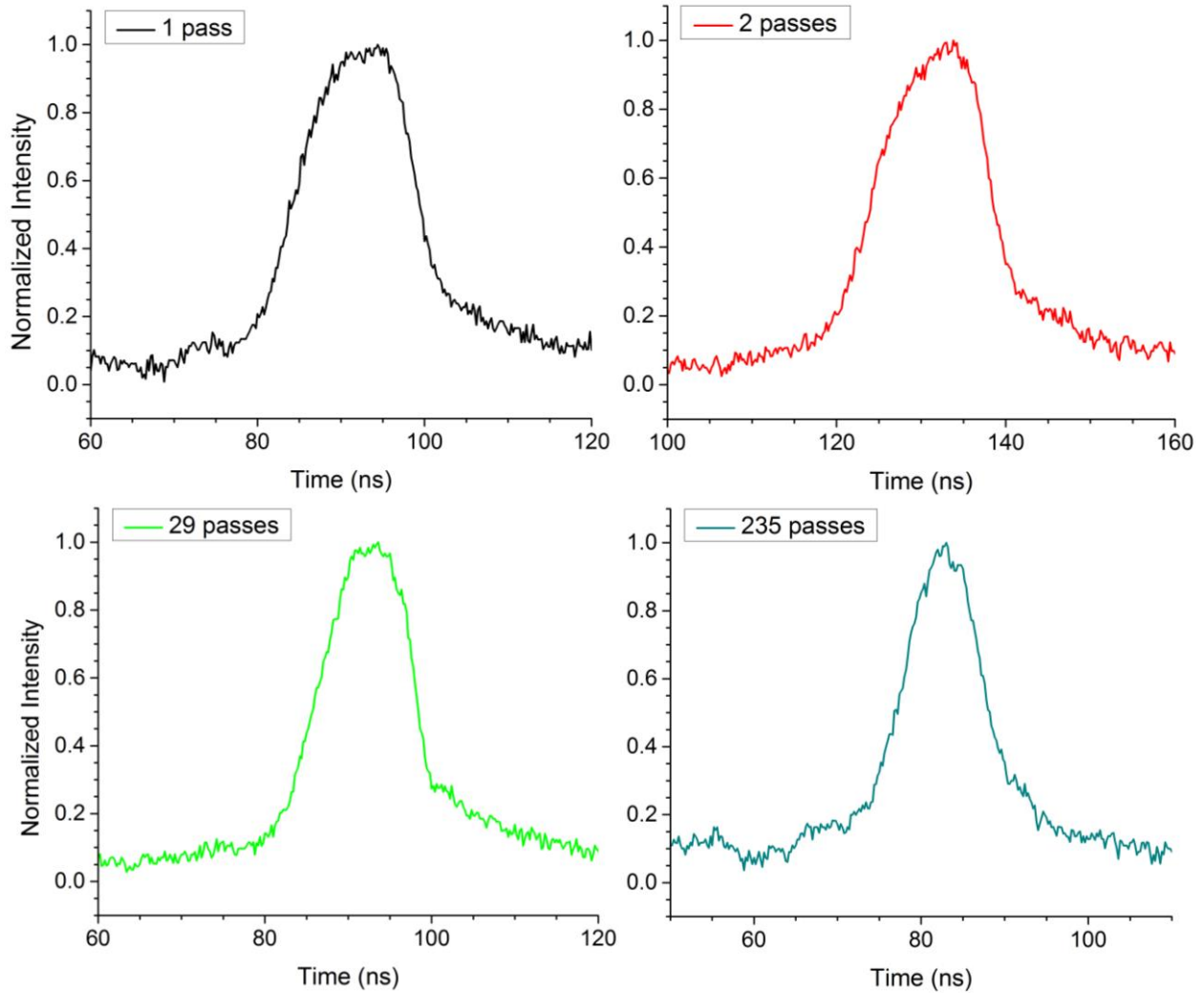
Figure 108: Evolution of pulse shape 2 shown for an increasing number of passes

The pulse build up was examined with a photodiode which was placed behind one of the HR cavity mirrors to catch the small percent (<0.001% of intra-cavity power) of light leaked through the mirror. With this photodiode monitoring the intra-cavity power, and the other photodiode measuring pulses exiting the cavity, a complete picture of pulse build up could be taken (Figure 109). The periodicity of the buildup can clearly be seen in the temporal shape of the pulse, and corresponds directly to the shape of the pulse which is output from the cavity (Figure 110).
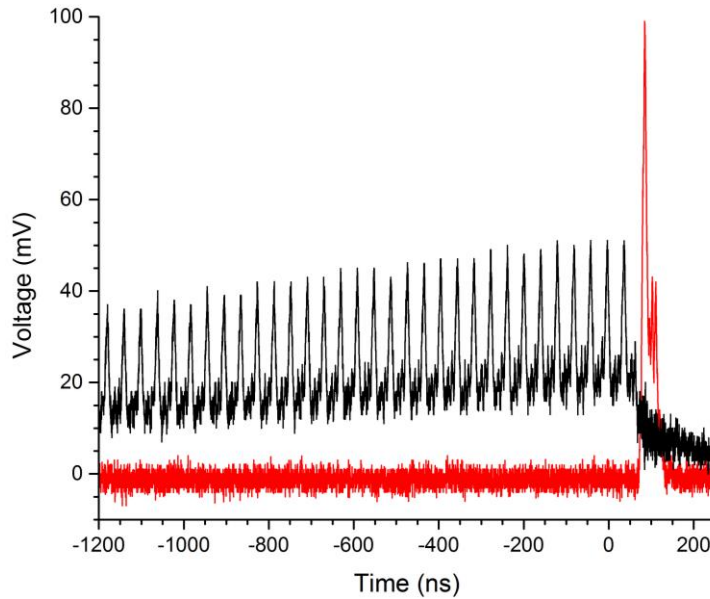
Figure 109: Pulse and intra-cavity buildup as observed using two photodiodes
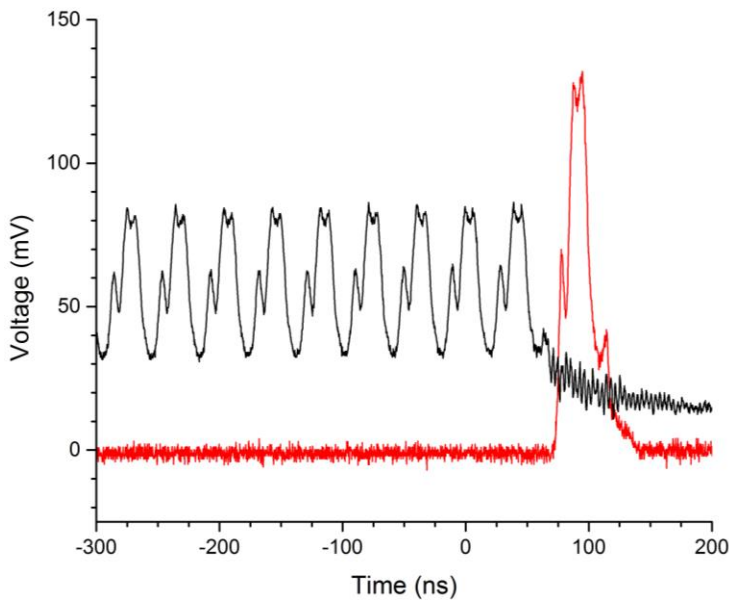
Figure 110: Buildup of pulse and final output pulse showing periodicity and temporal shape

However, the noise which is present in the output power and temporal pulse shape is also readily apparent when watching the intra-cavity pulse buildup time. Using a fixed gate time and taking single shots of the buildup, it becomes apparent that the presence of a temporally dependent loss is affecting the buildup time of the pulse. This changes pulse-to-pulse the number of passes needed to saturate the gain in the cavity. For a gate time of 34.175 µs,

corresponding to 876 passes in the cavity, it can be seen that sometime pulse saturate the gain, and its energy is decaying by the time the PC switches off and releases the pulse, and at other times the pulse is released at the peak of the build, or even before it reaches the peak (Figure 111).
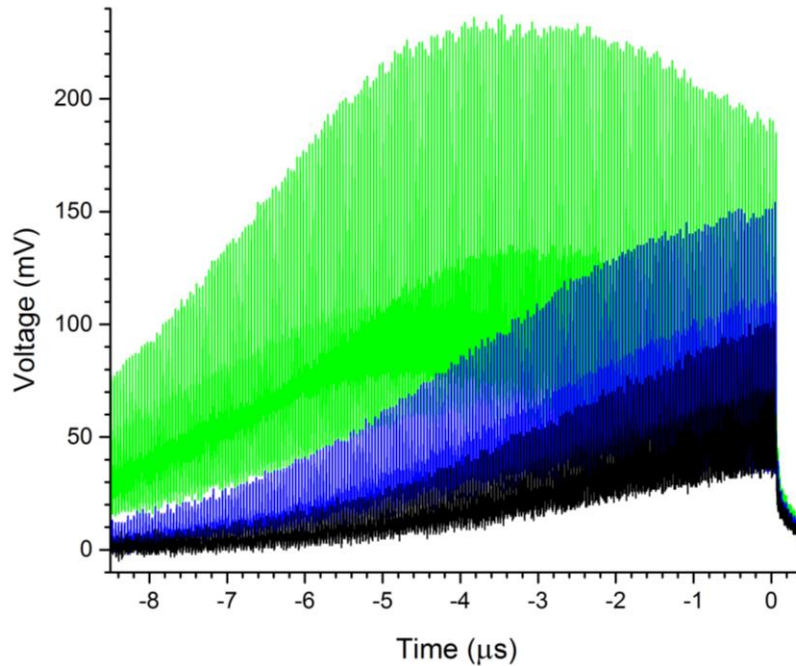
Figure 111: Three cases of pulse buildup at a fixed pump power and gate time, showing the variation in the number of passes needed to saturate the gain in the disk

The vibrational analysis assessment earlier demonstrated that when the TruDisk 1000 electronics are running there is an increase in noise and pulse variation, and there was a significant level of variation in output power when the system was operated in the CW regime before the PC was inserted. Other possible sources of pulse variation are fluctuations in pump power, which would directly affect the gain of the system, and the possibility that the regenerative amplifier is not being seeded with high enough pulse energy.

However, when scattered pump light was measured using a photodiode placed on the TruDisk 1000 table, no significant level of variation was noted. Likewise, the fiber pre-amplifier pump power was increased from 100 nJ up to as much as 252 nJ without any reduction in noise.

117

This leaves three possible sources of noise: pulse-to-pulse variation of the seed, the vibrations, and modal competition in the cavity. As noise has been observed as a result of each of these in various cases, it is likely that all three are contributing simultaneously to the variation in the laser's output.

In order to reduce the noise so the laser will consistently output the desired pulse shapes, each of the noise sources must be addressed individually. The most simply addressed is the pulse-to-pulse variation of the seed. This could be done by exchanging the existing seed for a low noise, single frequency diode. Then with one source of the noise eliminated, the remaining two can be assessed more easily in terms of their severity. The vibrational noise has a technically simple solution, which is to remove the TruDisk 1000 table from the case where the electronics and cooling system are housed. While the table is insulated for vibrations using various rubber pieces placed between it and the case (Figure 112), this is clearly not removing all the vibrational effects.

Figure 112: Rubber insulation between the TruDisk 1000 table and the case housing the electronics and cooling system, for damping of mechanical vibrations

The TruDisk 1000 was designed and intended to be used while the electronic vibrations are present. And this is something which is compensated for not only with the rubber insulation,

but also by the original opto-mechanical mounts for the laser mirrors. The mass and design of opto-mechanics used for the regenerative amplifier mirrors is significantly different. While high precision locking mirror mounts and 1" diameter posts were selected for the regenerative amplifier in order to bolster the mechanical stability of the system, the factory installed mirror mounts are engineered to an even higher degree of stability, especially in terms of mass (Figure 113). So rather than attempt to replace entirely all of the opto-mechanics in the cavity, it is much more practical to remove the table from the TruDisk 1000, and ideally co-locate it with the fiber seed and diagnostics all onto one table. While this will require some effort in terms of re-organizing the plumbing and electrical cabling for the pump diodes, there are no technical limitations which would prevent this from being done.
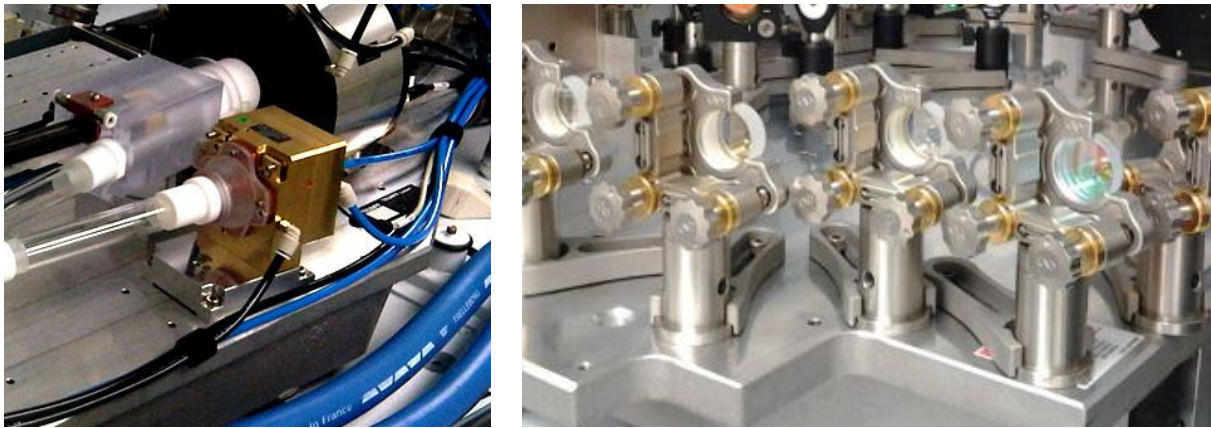
Figure 113: Mirror mount native to TruDisk 1000 (left) and mirror mounts used for the regenerative amplifier cavity (right)

Once these two sources of noise have been reduced or eliminated, the issue of modal competition in the cavity can be addressed. It is possible that the modal competition will be reduced along with the vibrational issues, or it may be necessary to modify the cavity, either by the insertion of more irises or by an exchange of some mirror curvatures in order to reduce the presence of higher order modes in the cavity. However, the exact solution cannot be determined until the other sources of noise have been separated or eliminated.

The output beam profile was examined in order to confirm that quality of the output beam. The behavior of the output beam can also reveal information regarding the modal content of the laser cavity. The same sort of fluctuation that was observed in the output power and pulse stability was also observed in the behavior of the beam, predominantly in terms of observed intensity, but also in beam shape to a small extent (Figure 114). However, the majority of the time the output beam profile is close to a perfect Gaussian (Figure 115).
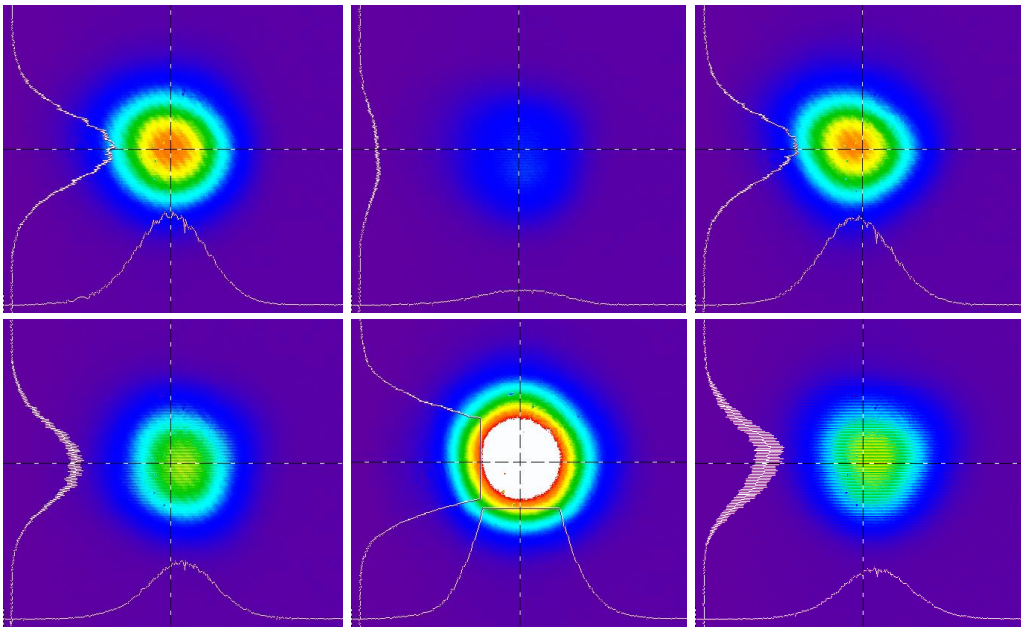
Figure 114: Variation in the intensity and shape of the output beam profile
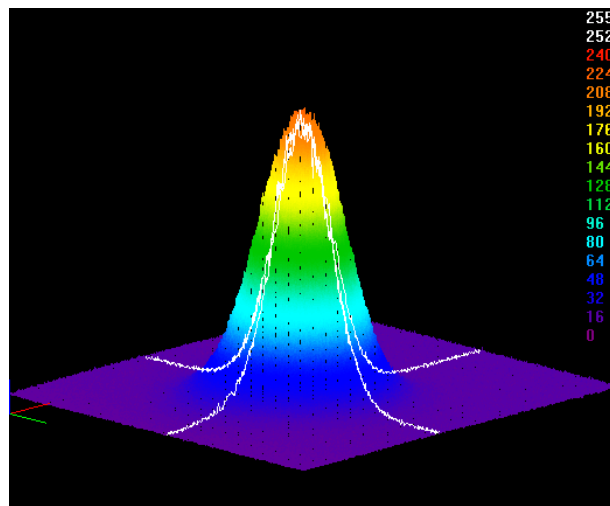
Figure 115: 3D representation of the output beam showing a Gaussian profile

The regenerative amplifier cavity M^2 was measured experimentally and projected using a LASCAD model. The M^2 measurement was performed by inserting a focusing lens into the beam path, and taking measurements of the beam radius at intervals before and after the focal plane of the lens using a filtered CCD camera. Values were taken by averaging 20 frames and using a Gaussian whole beam fitting for auto-computing the beam aperture.

The beam radii values collected in this fashion were plotted and fitted with the following expression:

$$W(z) = W_0 \{[1 + (z - z_0)^2 / z_R^2]\}^{1/2} \qquad (14)$$

In Equation 14, W is the beam radius, z is the distance from the lens to the camera, and by fitting this expression to the acquired data, values for the minimum beam waist, W_o, and the Rayleigh range of the beam, z_R, are found. These values in turn are used to calculate M^2 by using Equation 15, which is a ratio of the waist size of a perfect Gaussian to that of the calculated minimum beam waist.

$$M^2 = \frac{\pi W_o^2}{z_R \lambda} \qquad (15)$$

The LASCAD predicted beam quality for the regenerative amplifier is $M^2_x=1.5$ and $M^2_y=1.6$. Because of noise in the output beam, three fits were taken for the data as shown in Figure 116. These fits were taken for the measured averages, and for the maximum and minimum values within the measured error, the results of which are shown in Table 6. The best fits were $M^2_x \approx 1.4$ and $M^2_y \approx 2.0$ respectively. The various fits differ from the predicted M^2 by varying amounts, but all agree with the prediction the y-axis beam quality would be less than the x-axis quality. The noise and the fitted values of M^2 corroborate the presence of higher order

modes being present to varying extents, supporting the hypothesis that modal competition is contributing to the temporal noise in the system.
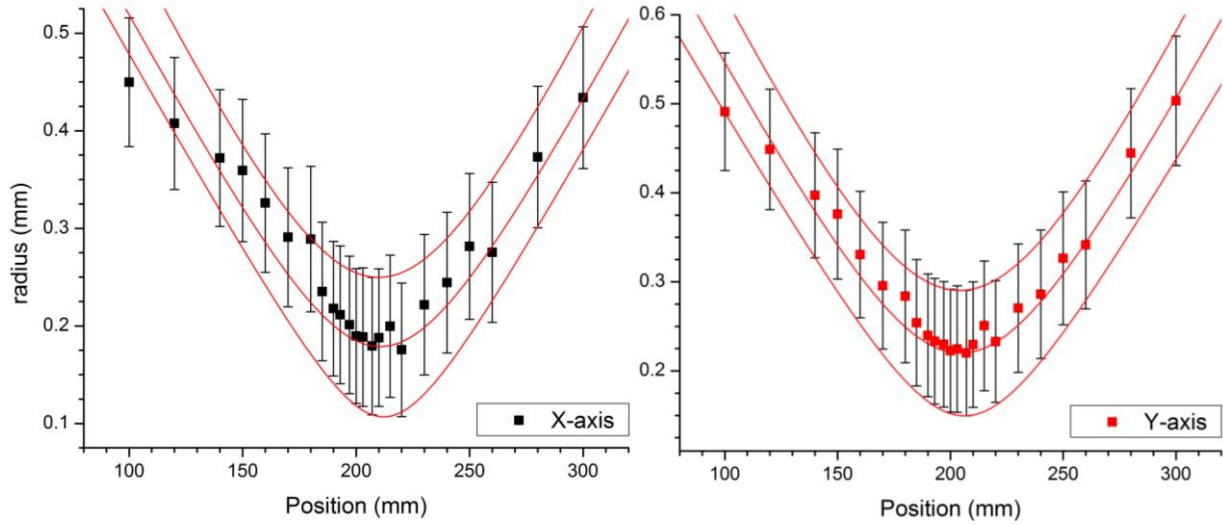
Figure 116: Fitted beam radii for the x and y axes of the beam profile

Table 6: Predicted and fitted values for M^2 in both axes

	M^2_x	M^2_y
Predicted	1.5	1.6
+Error	3.7	4.7
Average	2.4	3.2
-Error	1.4	2.0

Proceeding then with the existing noise, the output power of the system was examined at repetition rates of 250 Hz and 1 kHz, using the 20 ns square pulse described earlier. The repetition rate of 250 Hz was selected in order to cross-reference the power measurements with an energy meter which had a maximum pulse repetition rate of 400 Hz. The temporal pulse shape and energy values were measured using the oscilloscope, and both averages and envelopes were taken in order to assess the noise level and the range of pulse energies present (particular the maximum pulse energies).

Considering the output of the energy meter at 250 Hz, the signal appears to be a damped oscillation, going from positive to negative and back again (Figure 117). This behavior is

unexpected, and makes the results of the energy meter difficult to interpret and unreliable. Because it was therefore not possible to directly measure individual pulse energies with the energy meter, the maximum of the temporal averaged pulse was compared to the maximum found in the noise envelope (overlay of 512 pulses) is used to determine a rough estimate for the maximum pulse energies.
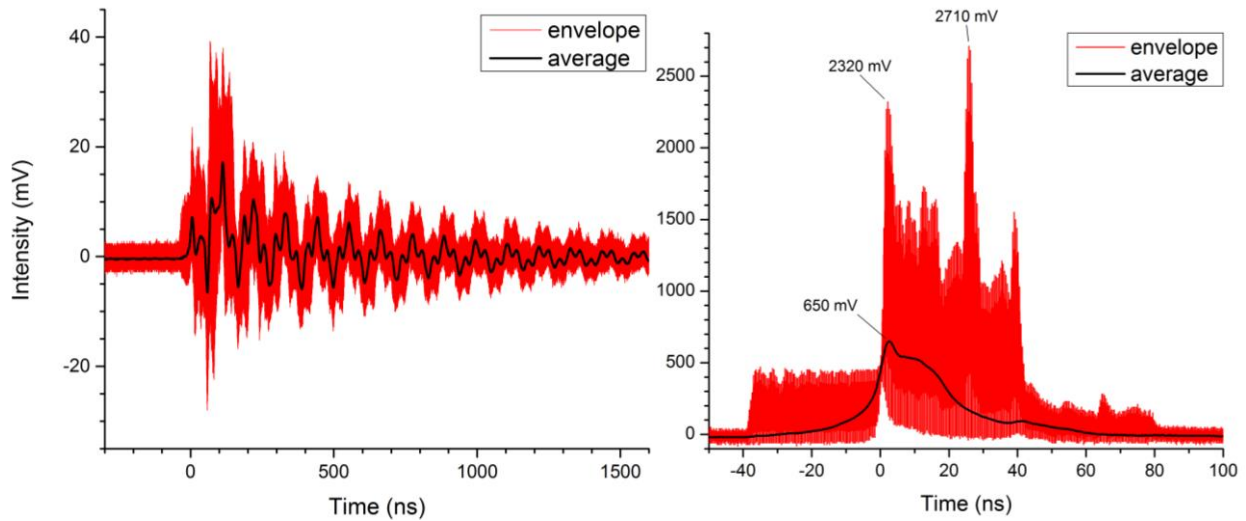
Figure 117: Energy meter (left) and photodiode (right) measurements of pulse average and envelope at 250 Hz with 218 W of pump power. The black line represents the average of 512 pulses, and the red represents the overlay of 512 pulses.
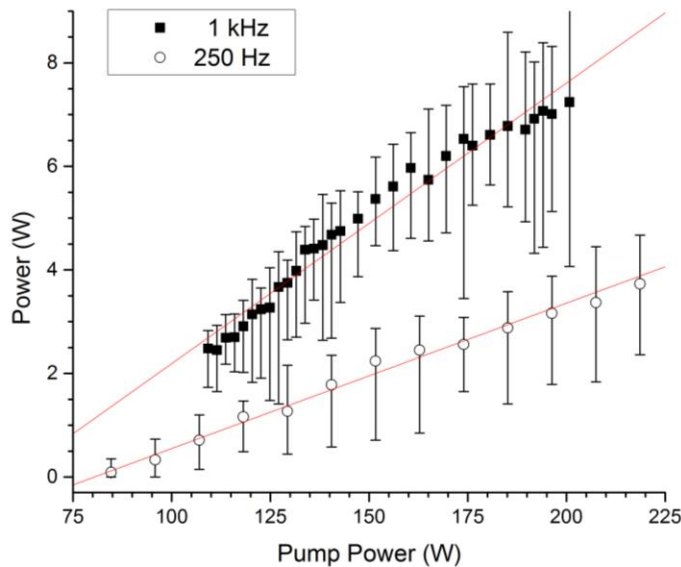
Figure 118: Average output power as a function of pump power for 250 Hz and 1 kHz repetition rates

123

Considering the photodiode measurement of the temporal pulse average and envelope, it appears that the maximum pulse energies output by the system are roughly a factor of 4 times the maximum of the average pulse shape. Taking the average power and the pulse repetition rate to determine the average pulse energy, and then scaling this by a factor 4.17, the maximum pulse energies are found for each repetition rate. The average measured powers at each repetition rate for various pump powers are shown in Figure 118.

The estimated pulse energies and the corresponding number of passes in the cavity is examined as a function of pump power applied to the disk. The number of passes in the cavity decays exponentially with the applied pump power in both cases, and the pulse energy increases linearly. The maximum estimated pulse energy of the system is 62 mJ at a pump power of 218 W for a 250 Hz repetition rate (Figure 119). For a repetition rate of 1 kHz the maximum estimated pulse energy of is 30 mJ with an applied pump power of 201 and 337 passes (Figure 120).
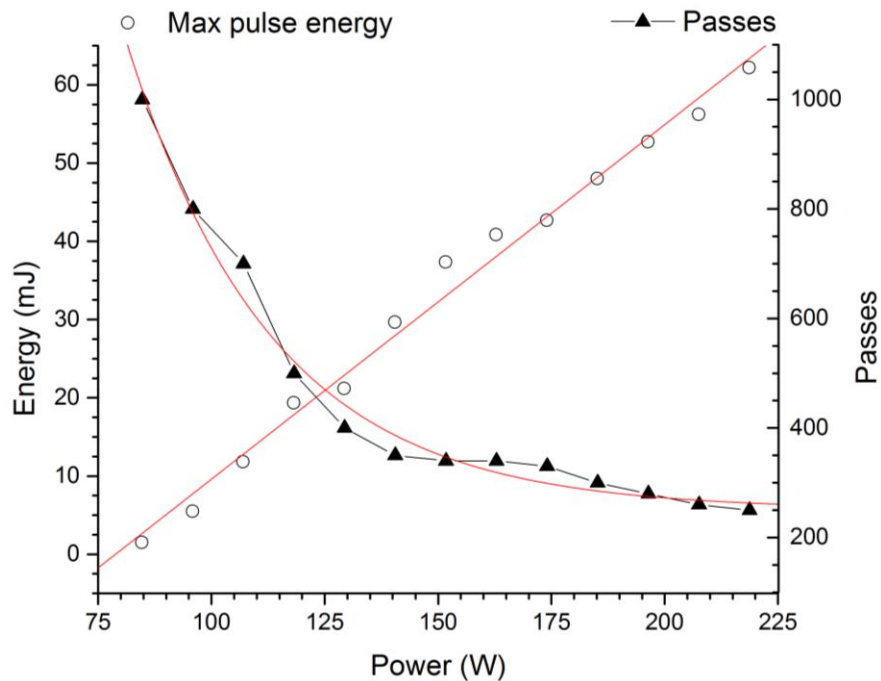
Figure 119: Pulse energies and the respective number of passes in the cavity at 250 Hz repetition rate, with a maximum estimated pulse energy of 62 mJ
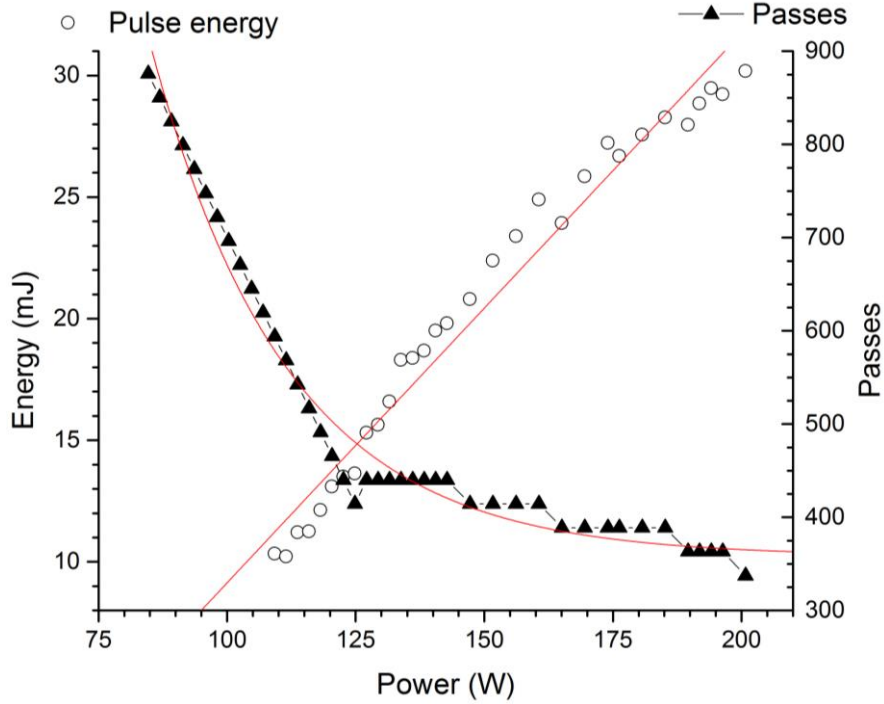
Figure 120: Pulse energy and respective number of passes for a repetition rate of 1 kHz
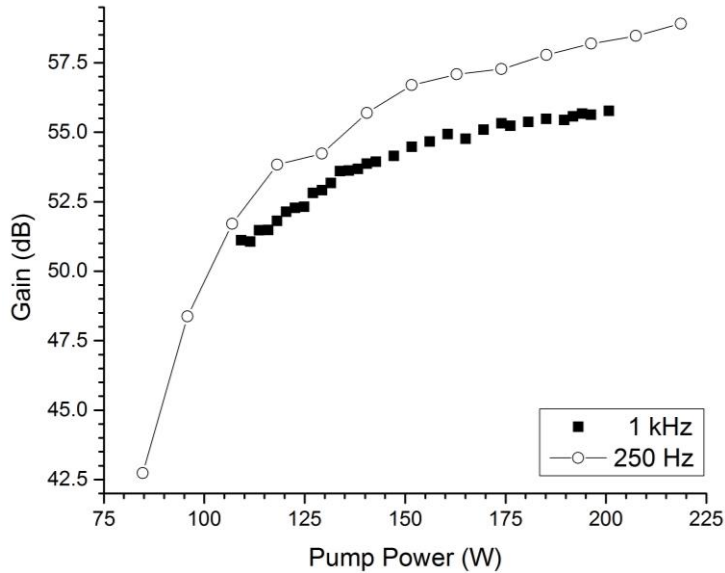
Figure 121: Gain of the system using a 80 nJ seed power for 250 Hz at 1 kHz repetitions rates

The gain of the system for these maximum pulse energies is calculated using an 80 nJ seed pulse (a 20% loss from the seed output of 100 nJ due to the optics including turning mirrors, periscope mirror, isolator optics, etc). The system gain as a function of pump power is shown in Figure 121. The maximum measured gain for the 250 Hz repetition rate is 58.9 dB, and for 1

kHz it is 55.8 dB. With improvements in temporal stability the system should reasonably scale

to 60 dB gain as there is a significant amount of pump power remaining.

A brief study was performed examining the relationship between the repetition rate of the

system and the average output powers and pulse energies. Repetition rates of 1, 2, 5 and 10 kHz

were examined at a fixed pump power of 89 W (Figure 122). The optimal number of passes

increased from ~825 at 1 kHz, to ~1184 at 10 kHz, and the same level of noise was present at

each repetition rate.
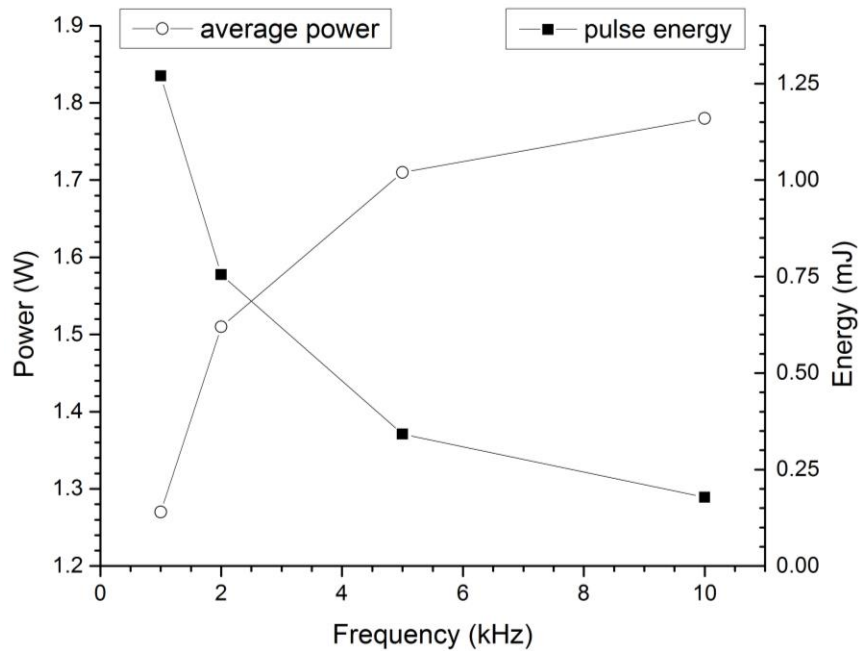
Figure 122: Average power and average pulse energy as a function of repetition rate

3.10. Applications and Future Developments

Before the system can be used to optimize the efficiency light/matter interaction for

various desirable applications, the noise sources in the system must be addressed. The effect of

vibrations in the system is the most likely source of noise, and once that has been eliminated

along with the pulse-to-pulse variation of the seed, the level of noise due to modal competition in

the cavity can be assessed. Once finalized, the cavity optimizer code can be used to redesign the

regenerative amplifier cavity by replacing certain mirror curvatures, and yield better output beam quality.

Once complete, the pulse-shaping capabilities of this system will useful for a variety of possible applications including materials processing and plasma generation including EUV generation. In the ns-regime thermal effects are present in the light-matter interaction, and the rate of heating and energy disposition is proportional to the shape and intensity of the incoming pulse. Depending on the desired effect, whether it is for plasma generation, cutting, marking, etcetera, the pulse shape can be optimized in order to produce a response optimized for that purpose.

Using a WFG with higher pulse shaping resolution will enable the creation of more detailed pulse shapes, and provide the flexibility necessary for gain-shaping compensation. Use of are higher bandwidth WFG requires on to connect the device to the modulator, but offers a dramatic improvement in potential performance. The highest bandwidth applicable would be 12 Ghz, which corresponds to the bandwidth of the modulator.

In its current state the laser system constitutes proof-of-concept for this method of generating high energy temporally tailored pulses. With the specified design improvements the system should be able to produce all the specified design requirements consistently and simultaneously.

CHAPTER 4:   THERMAL DISTORTIONS AND CERAMIC MATERIALS

The distortion of materials created by the accumulation of heat is a serious concern for high power and high energy lasers, as nearly any absorption can lead to high temperature gradients. As the temperature of the material increases it expands, which causes stresses and changes in index of refraction; thereby altering the way light is transmitted through the material, and in extreme cases, fracturing the material.

While there are a variety of ways to address thermally induced distortions, from novel materials to specialized cooling systems, the approach of primary importance for reducing thermal distortions is a thorough analysis of the behavior of materials under high temperature. By performing a detailed analysis, models can be developed along with a better understanding of the underlying mechanisms and behaviors. This knowledge is necessary to aid the development of more advanced techniques to reduce heating effects.

This chapter addresses the effects of heating in various optical materials, including passive oxide based materials, doped optical quality ceramics (Yb:YAG), and the crystalline Yb:YAG thin-disk used in the regenerative amplifier. The ultimate intent of this study is a progression towards the application of ceramic materials as thin-disk gain media, in order to improve overall performance.

4.1. Shack-Hartmann Wavefront Sensing

Using the Shack-Hartmann wavefront sensing technique, as described in the introduction, a diagnostic method is developed to measure thermal distortions in optical materials and assess material qualities. A SHWF sensor measures distortions by tracking the displacement of focal points created by a lenslet array. The measurement of the displacement is used to calculate the Zernike polynomials of the incident wavefront. For more details on the principles of SHWFS,

please refer to the introductory chapter. The distortions measured in these experiments are induced by pumping samples with an external heat source, and the measurement is taken by analyzing a probe beam which is transmitted through or reflected off of the material being analyzed.

The basic pump-probe experimental set up for transmission-based experiments is shown in Figure 123. A low power diode at 1080 nm (probe) is transmitted through the sample at normal incidence and onto the WFS, while a heating beam (pump) is incident on the sample at an angle off normal incidence. For both oxide and ceramic samples, probing is performed on transmission at normal incidence, with heating of the sample performed off-axis using either a 1 or 2 µm light.
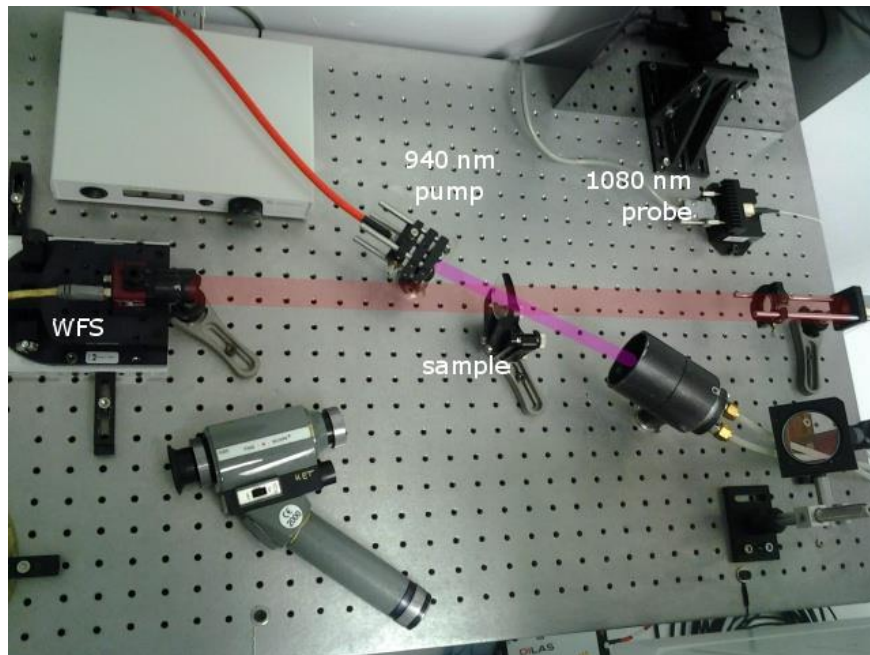
Figure 123: Example of transmission based SHWFS thermal lensing measurement set-up (WFS – wavefront sensor)

A variety of high-quality commercial SHWFS systems exist on the market, and are capable of producing measurements with both high repeatability and high sensitivity. For these experiments a SHWFS by Imagine Optic called the HASO First[TM]3 WFS is used, and is run with

HASOv3 software also by Imagine Optic (Figure 124). This camera has accuracy of $\lambda/200$, a sensitivity of $\lambda/100$, and a dynamic range of 400λ. The WFS is pictured here with a 2-axis mount for adjusting pitch and yaw of the camera, as the camera must be aligned to within $\pm3°$ to achieve full specified accuracy.
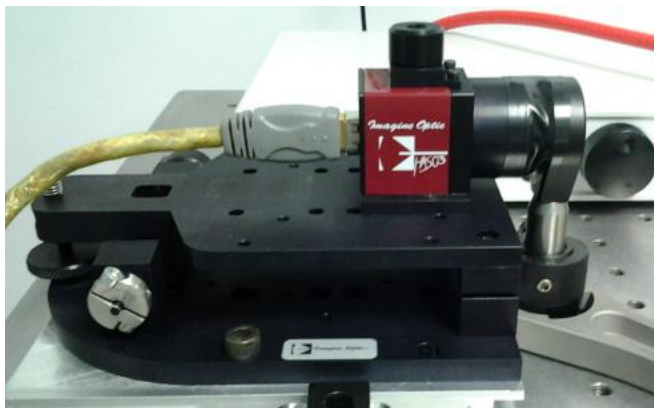
Figure 124: Imagine HASO First wavefront sensor shown with mount for pitch and yaw of the camera, and a notch-filter allowing passage of only the 1080 nm probe.

Shown with the camera is a transmission band pass filter (1064–1084 nm) situated over the aperture of the camera which lets through the probe light. Because the camera is sensitive to a broad range of wavelengths from ~900-1100 nm, the filter is especially important for the measurements of the ceramic samples because 940 nm pump light is used. This prevents any light other than the probe from entering the camera, which could otherwise produce focal spots in spurious locations and make the software's analysis of the wavefront meaningless.

The camera can be operated in either absolute or referenced mode. Operation in absolute mode results in an analysis of all the aberrations accumulated by the probe beam from its transmission or reflection through the various optical elements it encounters before reaching the camera. This analysis is done by comparing the location of the focal points to those of an ideal un-aberrated wavefront. In referenced mode the focal points created by the incoming wavefront are compared to those in a reference image, rather than an ideal wavefront. When reference

mode is used an image (reference) is taken of the focal points as created by the probe beam when no thermal distortion is applied, and the thermal distortions are then measured by tracking the change in location from the reference image. Measurements of the oxide and ceramic samples are performed in referenced mode, and the measurement of the thin-disk is performed in both absolute and referenced mode for reasons which will be discussed in more detail later.

In the pumping of the samples, a strong thermal lens is induced that dominates all other aberrations, and thus is taken as the primary metric for qualifying the materials. Measurements of the focal length are taken at increasing increments of incident pump power and at each step once thermal equilibrium is reached. Each data point for focal length is the mean of 1 minute of data collected, where each point taken towards the overall average is itself an average of 20 measured values. Averaging is used to compensate for noise in the measurement, caused primarily by airflow in the room.

In the following sections the results of the thermal investigations are described, with a subsection dedicated to each measurement of oxides and ceramics on transmission, and analysis of the thin-disk on reflection.

4.2. Thermal Lensing in Oxide Materials

Analysis of oxide materials is performed upon samples both with and without coatings. Five samples were examined: uncoated samples of BK7, fused silica, and Infrasil, and two mirrors, one high reflectivity (HR) and one high transmission (HT) at 2 μm, both with a fused silica substrate. Each sample analyzed was circularly symmetric with a 25.4 mm diameter and a 5 mm thickness. Because one of the mirrors measured was highly reflective of the heating beam, it was measured in two ways: with the light directly incident on the HR coating, and reversed

with the light incident on the opposite surface first, then passing through the sample before reflecting off of the HR coating (Figure 125).
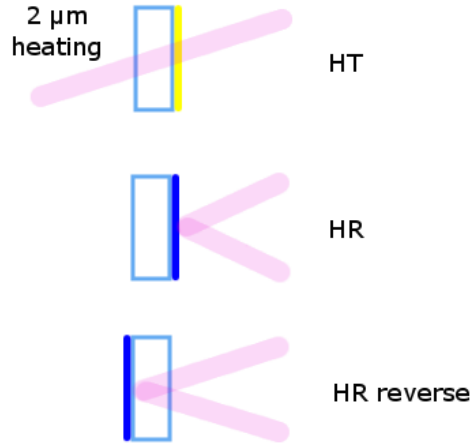
Figure 125: Different orientations used for the measurement of the coated samples

The pump source for these experiments was a CW 2 µm thulium fiber laser developed in-house. Much of current high power development occurs at 1 µm, at wavelength at which oxide materials have a very low absorption. However, absorption of oxide materials at 2 µm is roughly fifty times higher than at 1 µm, and so using 2 µm light as a pump source allows the simulation of even higher pump powers at 1 µm. By simulating high power 1 µm operation, valuable insights can be gained about the performance of various optical materials often used in high power systems. And by exploring samples which are both coated and uncoated, there is an opportunity to assess the effects of the coating on the distortion, another important aspect of high power operation.

The thulium fiber laser used as a pump source consisted of ~5 m of thulium dope LMA silica fiber (25 µm core, 400 µm cladding, Nufern) pumped by high power 780 nm fiber coupled diode sources (Figure 126). Feedback was provided by a high reflectivity mirror and Fresnel reflections from a flat cleave at one end of the fiber, which was used as an OC, allowing the

system to lase freely. The laser output was collimated, and had a diameter of ~4mm incident on the sample. Samples were examined with up to 45 W (un-polarized) of output power from the fiber laser, corresponding to a peak incident power of 2.6 kW/cm^2 (Figure 127).
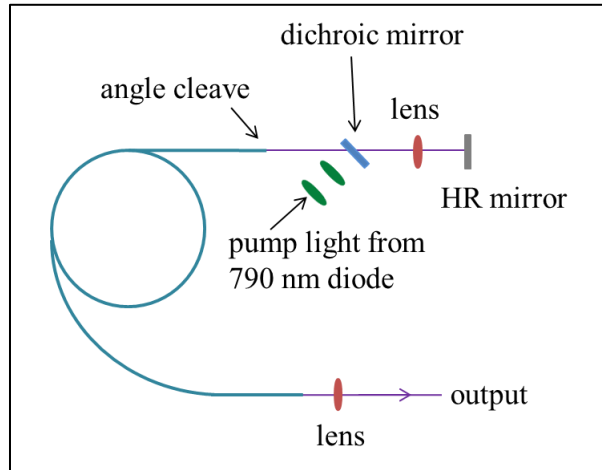
Figure 126: Schematic of the thulium fiber laser used as a pump source for the oxide samples
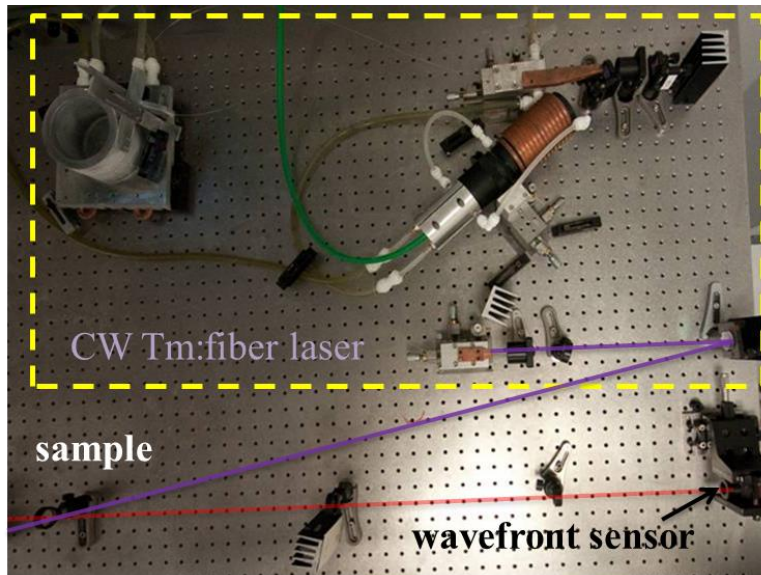
Figure 127: Photograph of thulium fiber laser pump source and experimental pump-probe set up

The resulting wavefront distortions are nearly circularly symmetric with the induced thermal lens dominating the resulting wavefront creating a focus. This can be seen in Figure 128 where three different incident powers create a growing level of phase delay at the center of the wavefront, creating a roughly conically shaped distortion. From these wavefronts, the focal

distance and power of the induced lens are measured, and examined as a function of incident power.
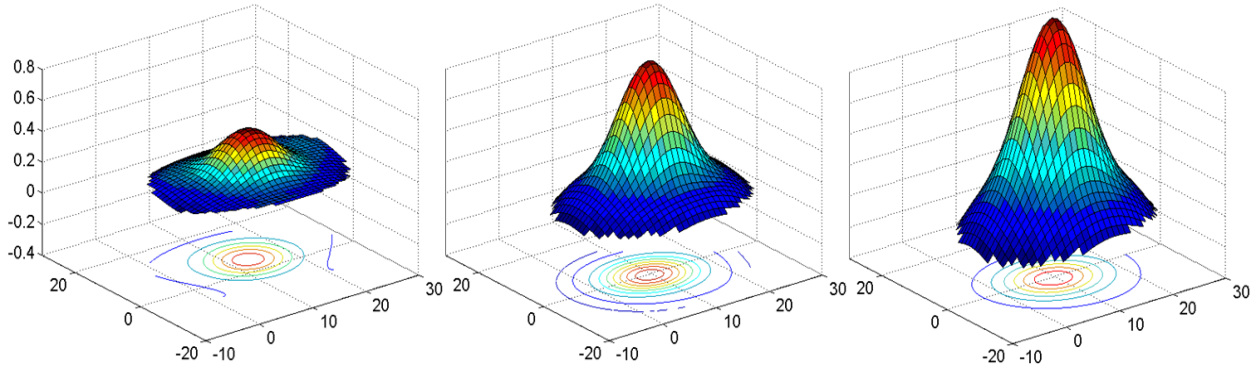
Figure 128: Thermal lensing in BK7 at 5, 15 and 25 W of incident pump power (left to right)
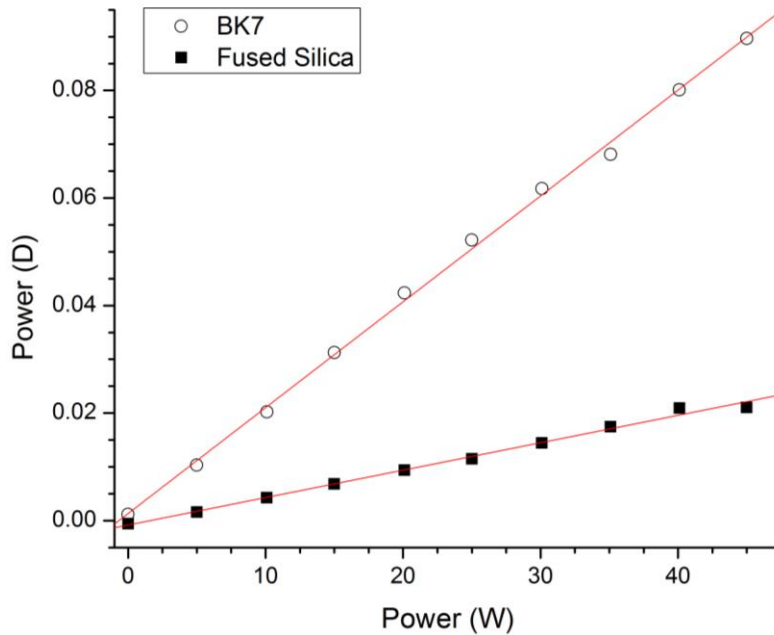
Figure 129: Thermal response in terms of the power of the induced thermal lens (in diopters) of BK7 and fused silica at increasing incident powers

For the measurements of BK7, Fused Silica and Infrasil, BK7 showed the strongest response and Infrasil showed no response for incident powers of up to 45 W, with Fused Silica falling in between. These results are shown in Figure 129. The thermal response of BK7 in terms of induced focal power as a function of incident pump power is $2 \cdot 10^{-3}$ D/W, and $0.5 \cdot 10^{-3}$ D/W for fused silica.
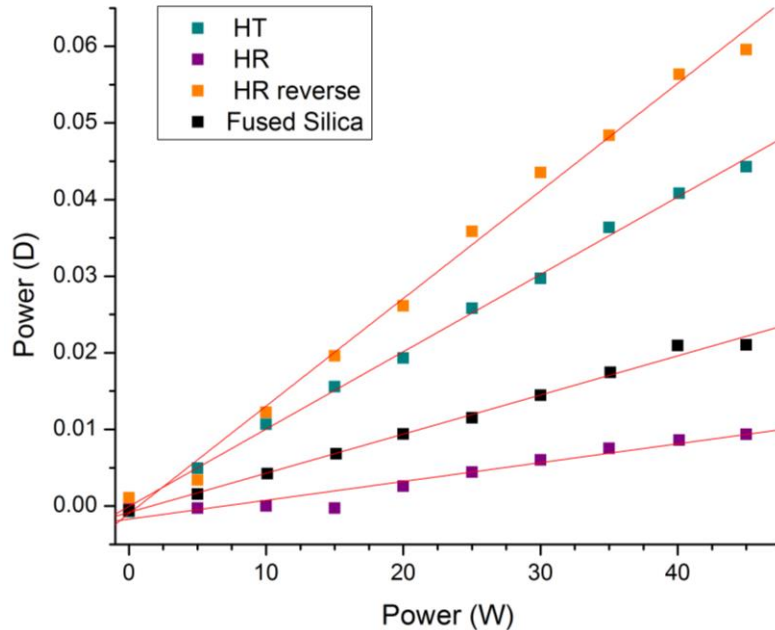
Figure 130: Thermal response of the fused silica sample (in terms of dioptric power) compared to the HR and HT mirrors with fused silica substrates, demonstrating the effect of the coating on thermal distortion

The measurement for the fused silica sample is compared against the results of the coated samples: the HT and HR mirror (Figure 130). The HT mirror shows a stronger response to the 2 µm light than the uncoated sample, indicating that the coating is either absorbing light to create additional heating, or that the presence of the coating is exaggerating the effect of the heating. The HT mirror had a thermal response of $1 \cdot 10^{-3}$ D/W, while the uncoated sample was half of that $(0.5 \cdot 10^{-3}$ D/W). The HR mirror gave either the strongest or the weakest thermal response depending on its orientation. When oriented such that the pump light was first incident upon the HR coating and did not pass through the material, it gave a response of $0.2 \cdot 10^{-3}$ D/W, and when oriented such that the pump beam passed through the material (the face opposite the HR coating is antireflection (AR) coated), and then was reflected back through the material by the coating, it gave a response of $1.4 \cdot 10^{-3}$ D/W. This follows logically in that in the reverse orientation light passes twice through the substrate, and in the forward orientation light does not pass through the substrate at all.

135

The result of the coating comparison indicates that the absorption of the coating alone is able to cause thermal lensing of the material. While the coatings of the mirrors analyzed are not designed for high power operation, this demonstrates the utility of analyzing the thermal responses of coating for mirrors which will operate in high-intensity systems.

The exact nature of the interaction between the effect of the coating and the substrate is no immediately apparent. In order to explore this effect, an attempt is made to separate the effects of each coating in a linear fashion. This is done through two routes. The first route takes the HT mirror, the HR mirror (reflection off coating) and the fused silica response values in an attempt to sum their responses to match that of the HR reverse configuration. The response of the AR coating on the back of the HR mirror is estimated as half the difference between the HT response (R_{HT}) and the uncoated fused silica response (R_{FS}), and this is then added to the fused silica response and the HR response (R_{HR}), shown in Equation (16, and plotted in Figure 131.

$$HRr_{est} = \frac{R_{HT} - R_{FS}}{2} + R_{FS} + R_{HR} \qquad (16)$$

The second route uses the response of the HR mirror, HR mirror reverse configuration, and the fused silica in order to linearly re-create the response of the HT mirror. This is done by subtracting the response of the HR mirror and the fused silica from the HR reverse response, presumably leaving only the effect of the AR coating on the backside of the mirror. The estimate for the HT mirror is then this value for the AR coating multiplied by two and added to the response of the fused silica (Equation (17). The results for this are plotted in Figure 132.

$$HT_{est} = 2 \cdot (R_{HRr} - R_{HR} - R_{FS}) + R_{FS} \qquad (17)$$
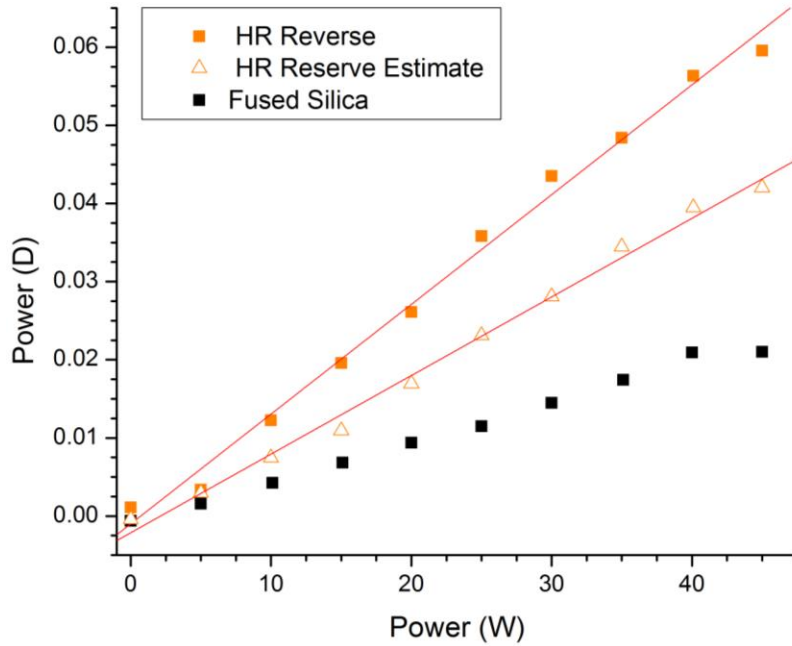
Figure 131: HR reverse response as a function of dioptric power vs. applied pump power, and the route 1 estimate from linear separation of effects
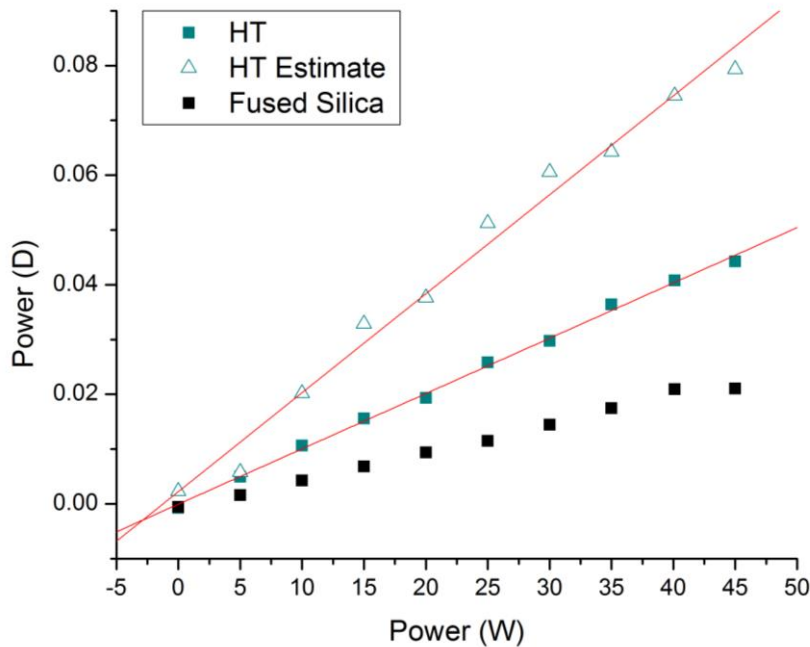
Figure 132: HT response and its estimate from linear estimate selection of effects

In both cases the estimated values produced by linear separation of the effects of the substrate and coatings differ significantly from the actual measurements of what they estimate, indicating a more complex relationship. This may result from additional heating by absorption

in the coating, from strain introduced by mechanical changes in the coating that result from that absorption or from thermal transfer at the boundary condition between coating and substrate. Thermal transfer at the coating/substrate interface may produce significantly different temperature profiles than present in the constituent tests. It is therefore not surprising the resulting distortions in the coated samples cannot be manifested as a simple sum of the constituent terms. A further parameter study would be needed to establish the exact effect of the coating and its interplay with the substrate.

Ultimately this pump-probe technique using SHWFS is able to measure and yield values for the responsiveness of the material, and by using a 2 μm pump source, where absorption in oxide material is higher, the relative levels of absorption can be used to estimate the responsiveness of the material at other wavelengths. Because the absorption of fused silica is ~50 times higher at 2 μm than at 1 μm, the maximum distortion that is achieved in fused silica at 45 W of 2 μm light, is equivalent to that which would be present for an incident power of >2 kW at 1 μm. Via this method estimates can be made for high power operation at 1 μm which would be technically challenging to achieve directly with a 1 μm heating source.

4.3. Thermal Analysis of Optical Yb:YAG Ceramic

The next set of thermal analysis experiments were performed on Yb:YAG ceramic and crystalline samples. Because ceramic Yb:YAG is of interest as laser gain medium it will be helpful to develop a metric which can be used to analyze and verify ceramic material performance. Processing of ceramic for use as laser gain media is both time and resource intensive and so a diagnostic which can eliminate ceramics a possible candidates for processing is highly desirable. By applying the pump-probe SHWFS analysis diagnostic to ceramic materials, it is possible to compare their performance relative to each other and to that of single-

crystal gain media of the same type. Relative performance is expected to be affected by both chemical and phase impurities that result from differing fabrication processes. Such a diagnostic technique can also be be used to optimize fabrication techniques and practices.

In order to demonstrate both the variation amongst materials from different sources (thus representing different fabrication routes) and the power of the diagnostic in detecting said variation, samples of Yb:YAG crystal and ceramic were procured from a variety of sources for analysis. All samples the examined are Yb^{3+}:YAG, circularly symmetric with equivalent surface polish (scratch-dig: 20-10, parallelism: $\leq$ 5 arcsec, surface quality: $\lambda/10$). The samples vary in diameter, thickness, and, to a small extent, dopant concentration ($\leq 0.2\%$).

For analysis of the ceramic samples, a special cooling mount was designed to hold the samples (Figure 133). The mount is water-cooled with a clear aperture of 40 mm. Samples are sandwiched between two plates with matched clear apertures of varying sizes. These plates are held in place in the water-cooled mount by 3 thumb screws, tightened only lightly so as not to induce stress in the sample. Such a mount is necessary due to the amount of heat generated during experimentation, as the samples are being pumped on resonance at an absorption feature of the Yb^{3+} dopant ion.

| (a) | (b) | (c) |
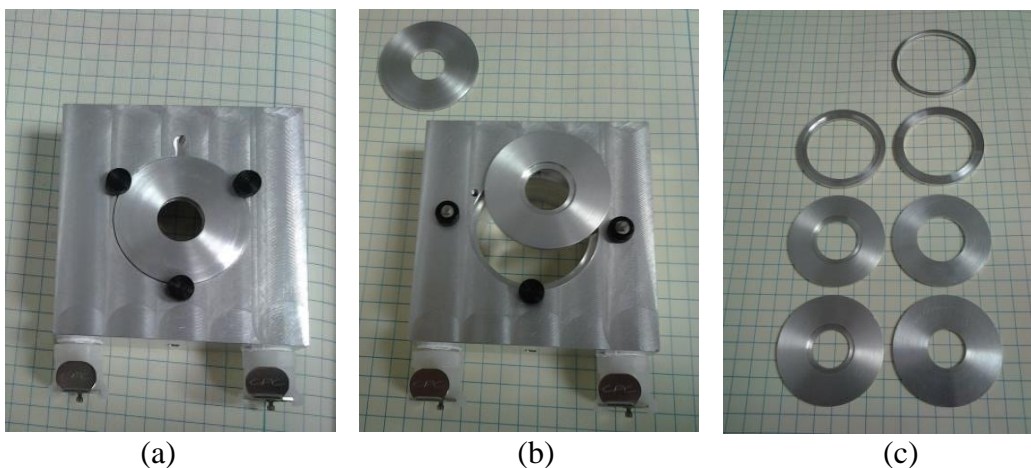
Figure 133: Water-cooled sample mount with a) holding rings in place, b) holding rings removed, and c) additional rings for varying sample sizes

139

Without such a mount the samples are capable of melting uncooled plastic mounts, and thermal transfer through a metal mount to the optical table prevents thermal equilibrium from being established. After a variety of configurations, this mount was developed in order to ensure thermal circular symmetry, more rapid establishment of thermal equilibrium, and prevention of heat damage to the mount.

Heating of the samples is performed off-axis using a 940 nm high power fiber coupled diode (Figure 134). Light from the output fiber is focused into the sample to a spot size of ~2 mm. Each sample is heated from 1 to 30 W of incident power in steps of 2 and 3 W.

(a)   (b)
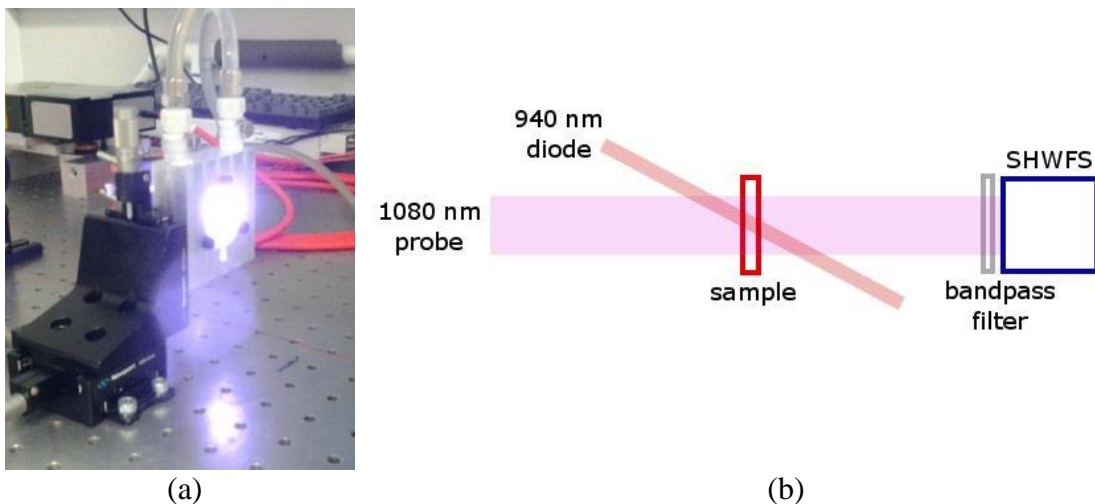
Figure 134: a) Image of a ceramic sample in the water cooled mount being while pump light is incident on the sample, which appears as purple light due to the camera's sensitivity to near IR light, and b) a diagram of the pump-probe measurement set up.

A total of 13 samples are examined (Table 7). The samples came from four different sources, and thus meet our goal to represent different fabrication routes. Additionally three of the samples are crystalline, which is useful for the purposes of comparison. As incident power increased so did the power of the thermal lens induced in the samples (Figure 136). The response of each sample was quantified by the slope of the linear change in power of the induced thermal lens as a function of incident pump power, referred to as its thermal response in diopters per watt. The lower the thermal response the sample, the less thermal distortion it exhibits.

Table 7: Complete list of Yb:YAG samples

Label	Source	Material	Dopant conc. (%)	Diameter (mm)	Thickness (mm)	Response (D/W)
Sample 1	1	ceramic	9.8	18.0	1.24	0.1455
Sample 2	1	ceramic	9.8	18.0	1.23	0.1444
Sample 3	1	ceramic	9.8	18.0	1.23	0.1367
Sample 4	1	ceramic	9.8	18.0	1.23	0.1491
Sample 5	1	crystal	9.8	17.9	1.31	0.1005
Sample 6	1	crystal	9.8	18.0	1.35	0.1012
Sample 7	2	ceramic	10	18.4	1.40	0.1382
Sample 8	2	ceramic	10	18.3	1.39	0.1342
Sample 9	2	ceramic	10	18.5	1.39	0.1349
Sample 10	3	ceramic	9.8	21.1	1.39	0.1155
Sample 11	3	ceramic	9.8	31.1	1.53	0.1159
Sample 12	3	crystal	9.8	20.0	1.59	0.0809
Sample 13	4	ceramic	10	41.1	2.16	0.1793
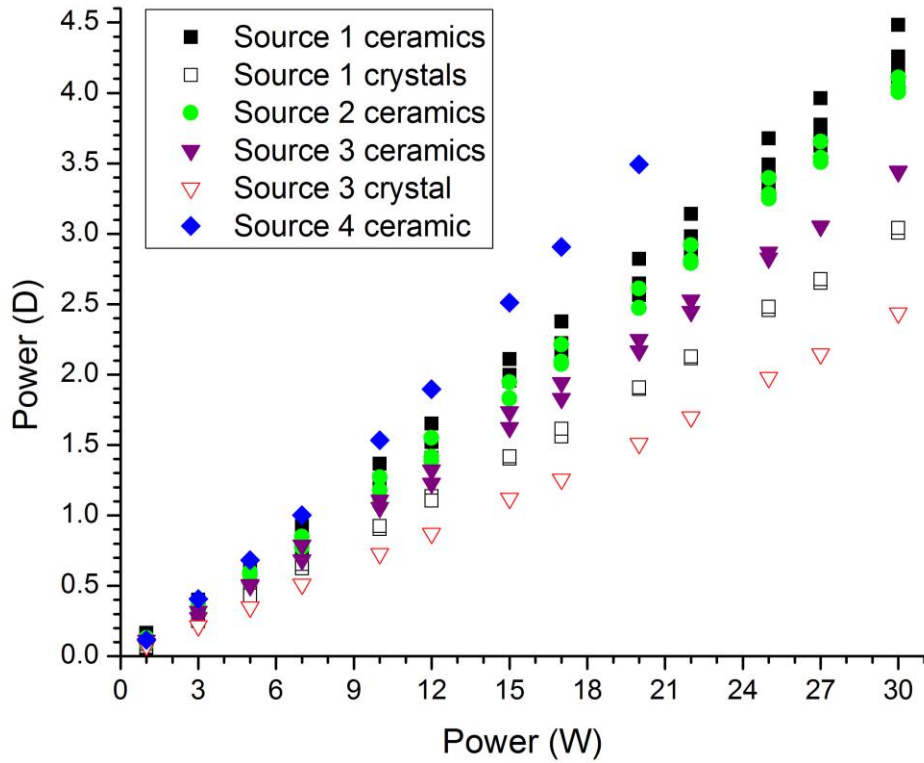
Figure 135: Power of induced focal lengths of all samples as a function of incident pump power as sorted by source and material type
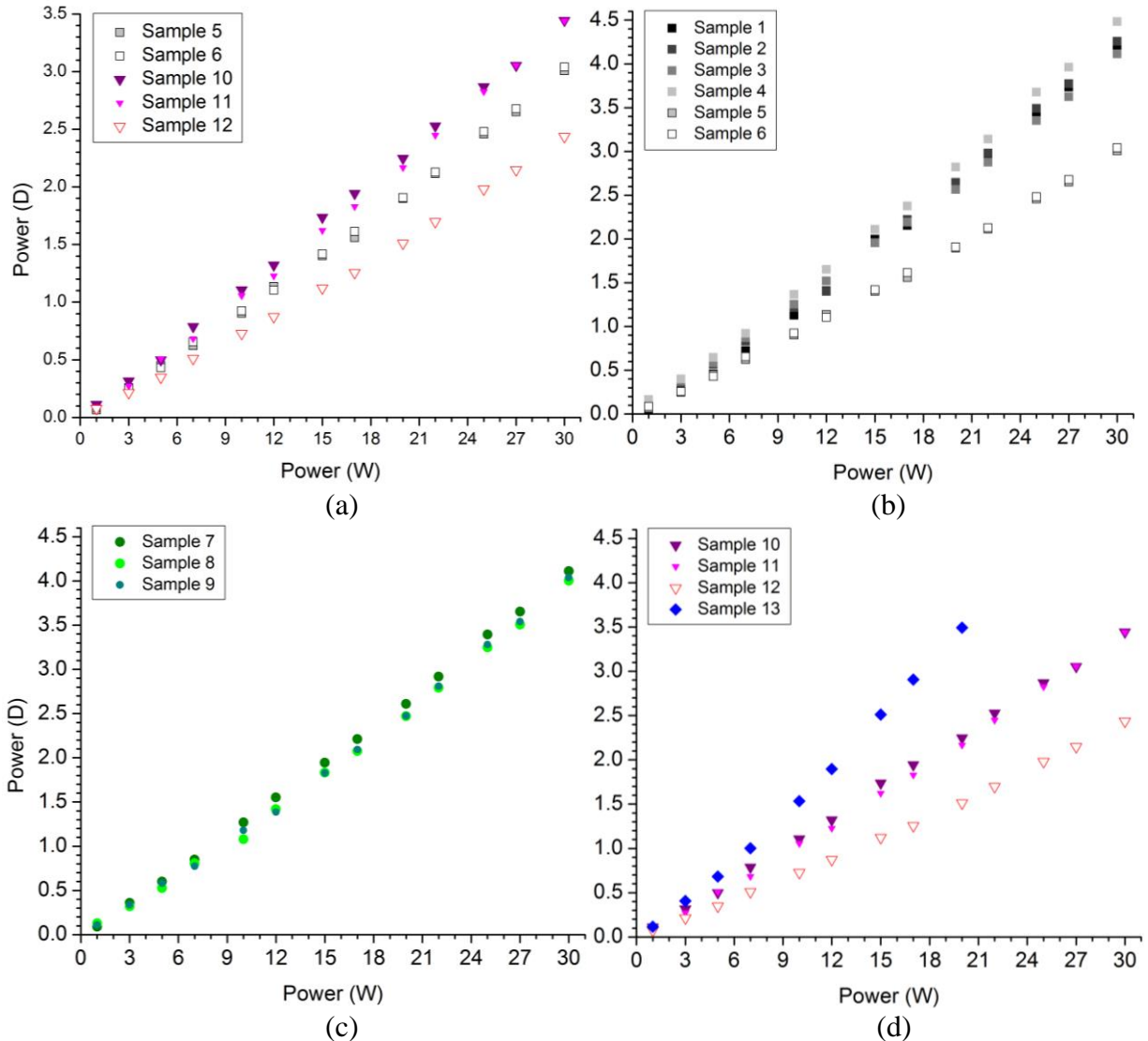
Figure 136: All samples as well as subdivisions of the data shown for clarity: a) shows all samples, b) shows samples from source 1, c) source 2 and d) sources 3 and 4

Considering Figure 135, where the set of the best responding samples is shown, and all samples are shown divided by source, several things become apparent. The sample from source 4 is an outlier with the greatest thermal response of the set (0.18 D/W). The performance of the ceramic samples from sources 1 and 2 are fairly tightly grouped with comparable responses ranging from 0.13 to 0.15 D/W for all 7 samples, showing a consistency in fabrication quality. The best performing samples were clearly the three crystals, numbered 5, 6 and 12. Of the ceramics the best performers were numbers 10 and 11. Notably, all three samples from source 3

(samples 10-12) are in the top 5 performers, indicating a superior fabrication quality. The performance of the two ceramics from source 3 are close in value, differing by only 0.0004 in their response, the smallest difference between any two samples, confirming again a consistency in fabrication.
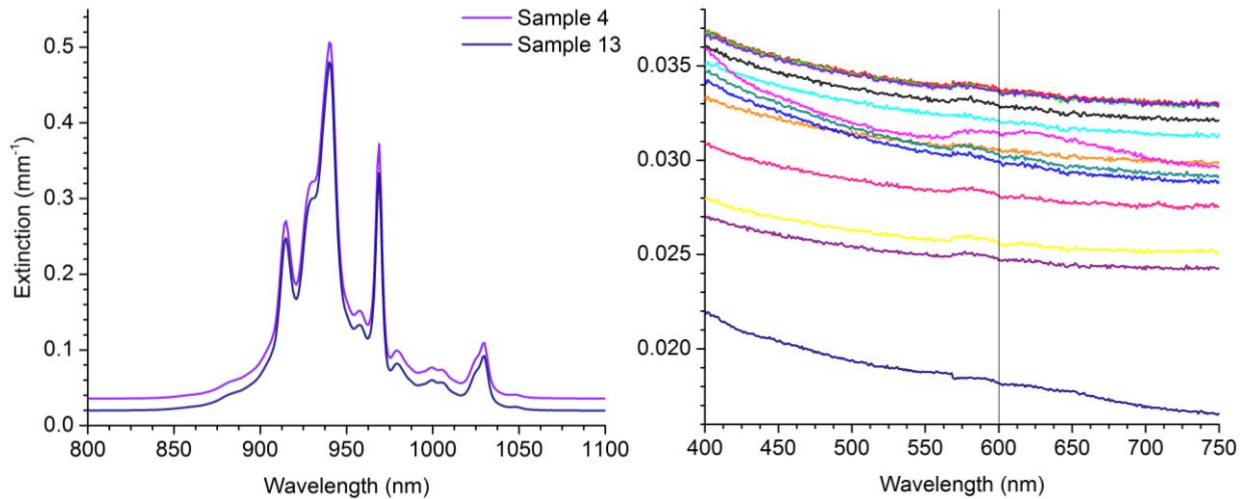
Figure 137: Representative extinction of samples showing features typical for Yb^{3+} absorption with samples 4 and 13 showing the top and bottom of the range for all samples (left) and extinction of all samples in the visible ranging, showing minor variation in this range (right)

The transmission of all samples was also measured with a spectrophotometer (Cary 500). After performing a baseline correction, extinction per unit length is calculated from the transmission of the samples from 200 to 3300 nm. The characteristic Yb^{3+} features from 800 to 1100 nm are present as expected (Figure 137), with all the samples tightly grouped in their response which confirms the expected low variation in dopant concentration. Extinction in the visible is also examined (Figure 137); with all samples being highly and almost uniformly transmissive in this range. The only notable spectral feature found which differentiates the samples occurs at 255 nm in some of the samples (Figure 138) and is most likely due to the presence of Fe^{3+} [170, 171], a material which is not uncommon as a component in fabrication equipment.
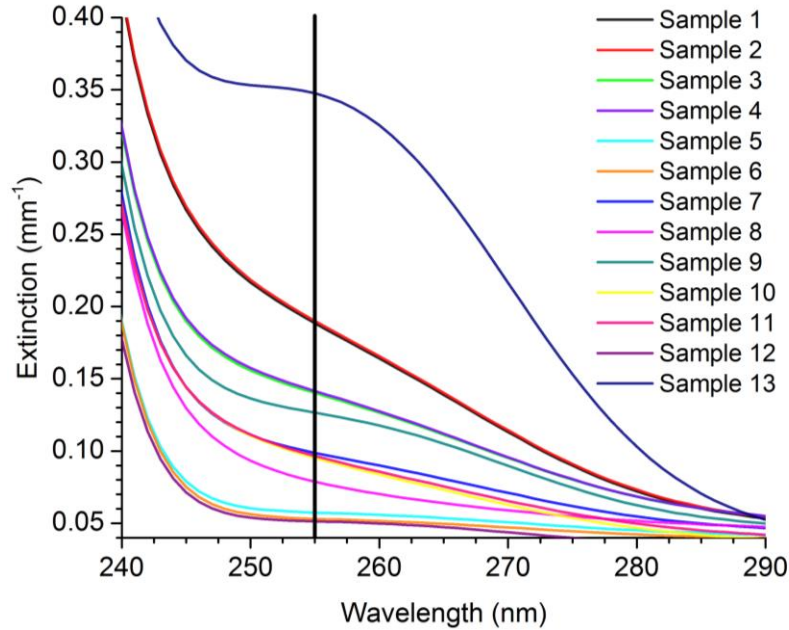
Figure 138: Extinction feature near 255 nm indicate the possible presence of an iron impurity

A ranking is done of the samples by two metrics, the strength of their thermal response (low to high), and their extinction (low to high) at the Fe^{3+} feature, the results of which is shown in Table 8. A correlation between the strength of the samples' thermal response and the absorption of the samples at 255 nm is readily apparent; no one sample changes rank by more than two places. This correlation indicates that the impurity causing the spectral feature at 255 nm has a direct effect on the sample quality and thermal response. However difference in the ranking of the samples indicates that there are additional factors, defects or impurities (possibly scatter), are also at play affecting the overall thermal response of the samples.

It was also of interest to develop a model which could predict or match the thermal response values of the materials. This was motivated in part by the geometric variations amongst the samples, which the current work does not entirely normalize out of the result. While length of propagation through the ceramic was normalized, there was no direct method to compensate for the varying diameters amongst the samples, which has the potential to change or alter the

final response values. Ultimately the model can also be used to determine discrepancy between a sample's performance and that of a theoretically perfect defect and impurity free sample.

Table 8: Ranking of samples

Ranking	Thermal Response	Transmission @ 250 nm
1	Sample 12	Sample 12
2	Sample 5	Sample 6
3	Sample 6	Sample 5
4	Sample 10	Sample 8
5	Sample 11	Sample 10
6	Sample 8	Sample 11
7	Sample 9	Sample 7
8	Sample 3	Sample 9
9	Sample 7	Sample 3
10	Sample 2	Sample 4
11	Sample 1	Sample 1
12	Sample 4	Sample 2
13	Sample 13	Sample 13

A standardized model for the focal length of an induced thermal lens is set forth in "Solid State Laser Engineering" by Walter Koechner [127], shown in Equation (18. This model accounts for end-face deformation, thermally induced changes in the refractive index, and strain induced refractive index change.

$$f = \frac{K\,A}{P_h}\left(\frac{1}{2}\frac{dn}{dt} + aC_{r,\phi}n_0^3 + \frac{ar_0(n_0 - 1)}{l}\right) \qquad (18)$$

In Equation 18, K is the thermal conductivity of the material, A is the sample cross-section, P_h is the total heat dissipated in the sample, dn/dt is the temperature coefficient of the refractive index, a is the thermal coefficient of expansion, $C_{r,\varphi}$ is a function of the material's elasto-optic coefficients, n_0 is the index of refraction at the center of the sample, r_0 is radius of the sample, and l is the sample length. The first term in the parenthesis accounts for the contribution of thermal index variation, the second the contribution of the strain induced index variation, and the third for the sample's end-face deformation.

However, this model makes the assumption that the lens is formed due to uniform heating of the sample, and as a result, that the radial change in refractive index is purely parabolic in nature. When the model is set up against our experimental results without modification, the resulting values differ greatly because our heat source is only a small point at the center of the sample. We therefore sought a method by which the existing model might be altered in order to produce more accurate results. Using the 13 ℃ boundary condition created by the cooling mount, the material parameters as found published in existing literature for Yb:YAG, and the applied pump values, the temperature distribution in the samples can be modeled using Comsol [172]. This shows a parabolic temperature distribution (and therefore refractive index distribution) at the center of the sample, with a logarithmic drop in temperature in the area between the heating region and the edge of the sample (Figure 139). By taking a parabolic fit of the center region, and substituting the values of that parabola into existing thermal lens model, we were able to calculate focal length values similar to those of the best performing samples.
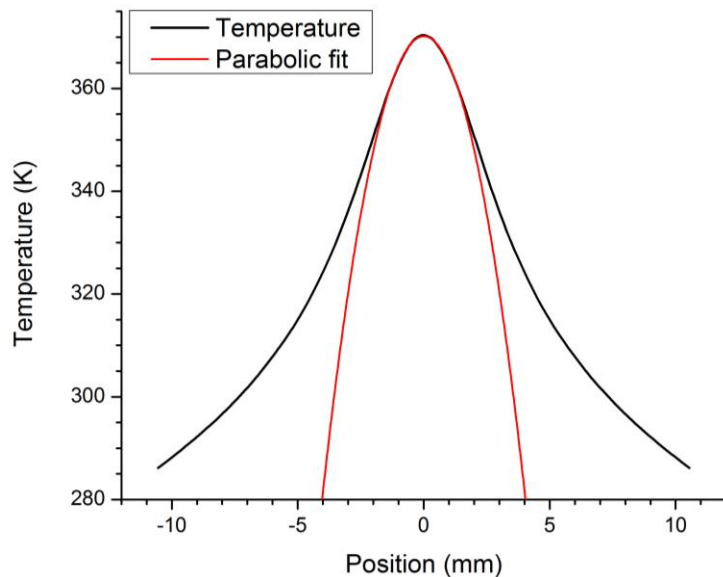
Figure 139: Example of the modeled radial temperature distribution in a sample, with parabolic fit of its central region

The fit was optimized, within the uncertainties in the material parameters and measurement values, for the best performing crystal sample, number 12 (Figure 140). The model was then applied to several other samples, including a ceramic and a crystal from source 1, sample numbers 3 and 5, the worst sample, number 13, and the best overall ceramic, number 10 (Figure 141).
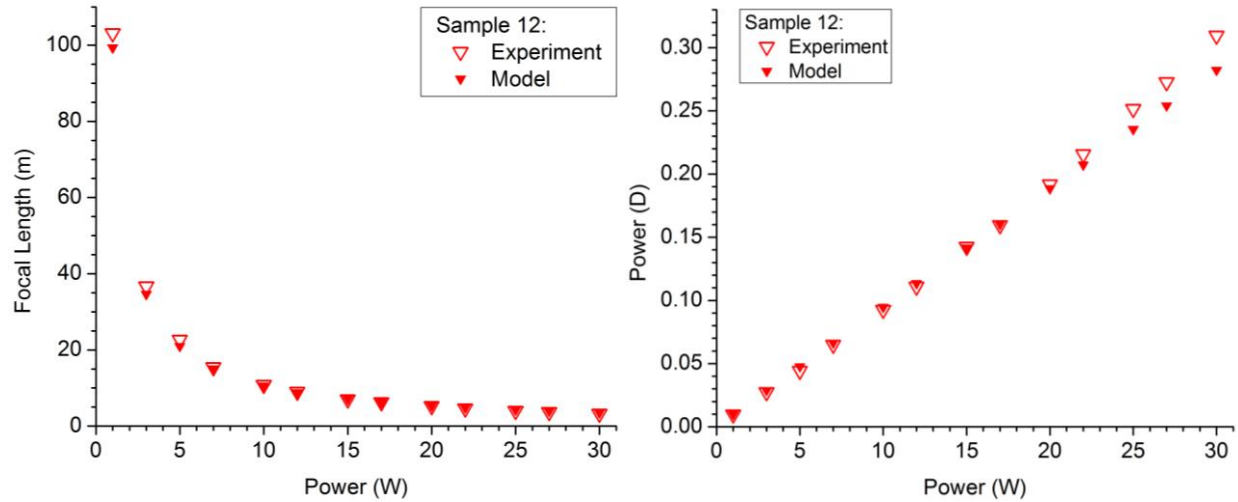
Figure 140: Fitting of the best performing sample, number 12, for which the fit was optimized, and shows close agreement between measured values and model predictions

As can be seen, the model prediction is best for the samples which have the best performance, with the greatest discrepancy occurring for the worst performing sample. This is the result of impurities and defects, which are not accounted for in the model, generating a heightened thermal response. The model effectively predicts for a theoretically pure and defect-less Yb:YAG sample, and the discrepancy between the sample and the model therefore represents the effect of the sum-total sample defects and impurities. The model can therefore be used to generate not just a relative quality assessment between samples, but an absolute comparison of one sample to a theoretically perfect sample. In order to assess samples, an application specific metric can be created which defines the maximum permissible level of imperfections in a sample, and samples can be assessed for use accordingly.

147
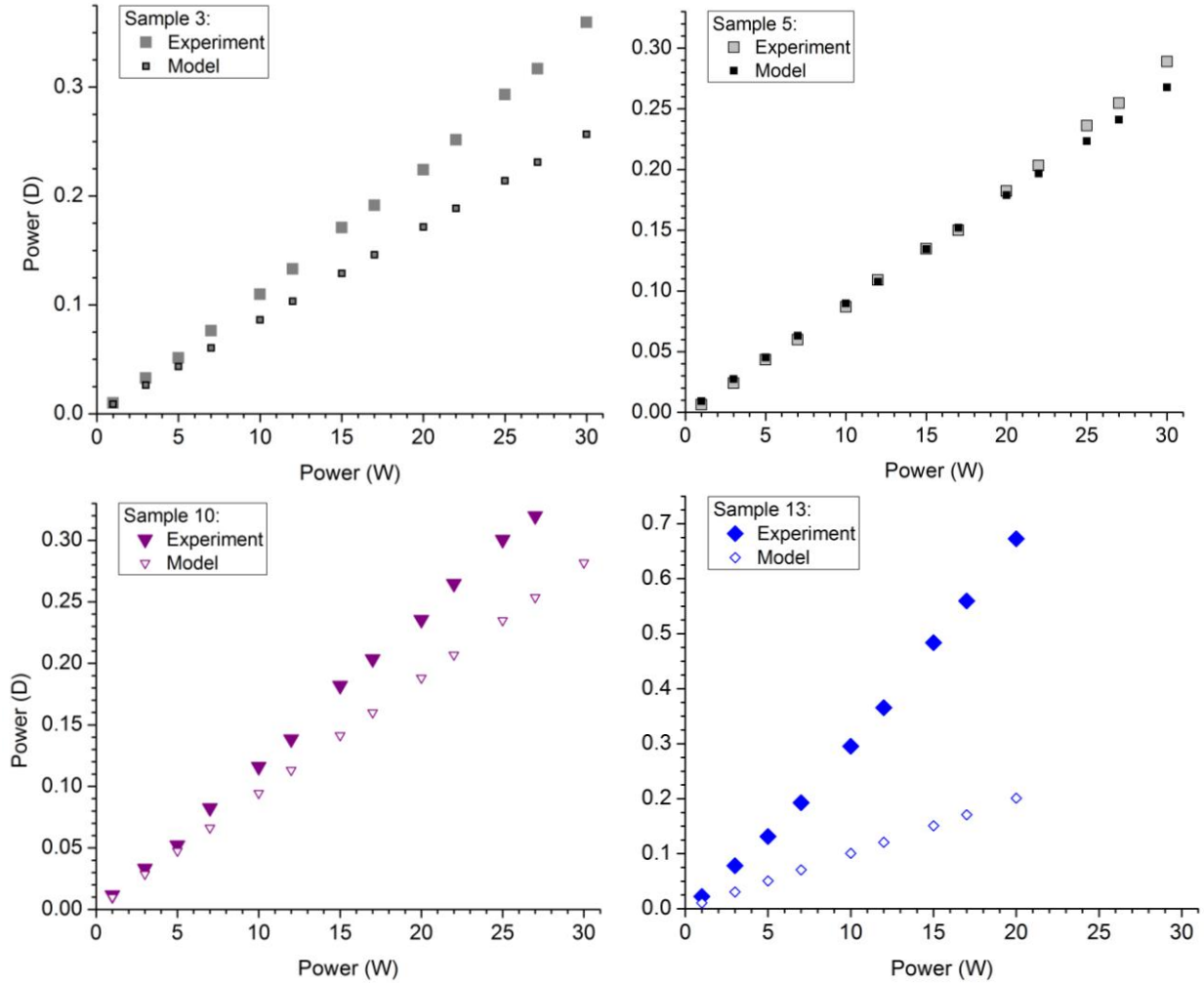
Figure 141: Comparison of the model predictions with the experimental measured focal powers

Overall this model and diagnostic provide a direct method to gauge relative sample quality in terms of the material thermal response. It showed that impurities, such as Fe^{3+}, can have negative effects on sample quality and result in a heightened thermal response. By supplying material parameters for an ideal sample, the discrepancy between the model prediction and the sample measurement offer a metric for absolute assessment of sample quality, even in the absence of an ideal sample. And as a result of this comparison, several ceramic candidates were selected for bonding by Trumpf as a thin-disk material, and were shipped to Trumpf for processing.

4.4. Thermal Analysis of the single crystal Yb:YAG Thin-Disk

Measurements of the thermal lensing effects in the thin-disk were taken under CW lasing conditions before any modifications were made to the original TruDisk 1000 cavity. As the measurements are taken under lasing conditions, the cavity mode could not be disturbed by the wavefront sensor or any of the directional optics for the probe beam. The configuration which satisfied these requirements is shown in Figure 142. In this case it is the laser's 940 nm pump light which acts as the pump and induces thermal distortions in the disk.
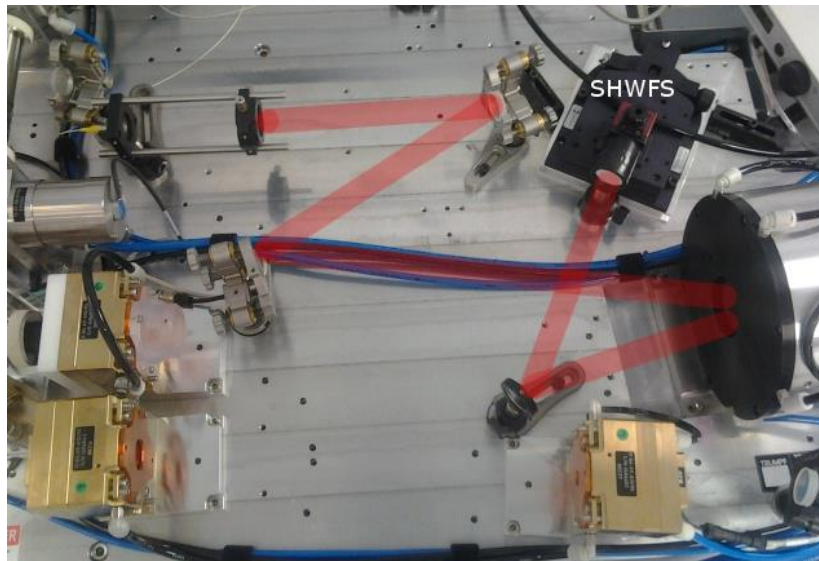
Figure 142: Experimental set-up for SHWFS the measurements of the thin-disk by reflection, with the path of the probe beam shown in red.

The disk measured is that of the TruDisk 1000 before any modification of the cavity was performed. The expected behavior is that the disk will flatten, or increase in ROC, as the pump and output power of the laser increase, a behavior which was observed experimentally. The manufacturer's specification is that the disk has a ROC of 2000 mm when no pump light is applied, which was used as a verification value for the measurements. However, in measuring the disk in referenced mode it was noted that ROC values seemed to deviate rather dramatically

as compared to what was expected, and so the same measurements were also taken in absolute mode to determine the best method for analysis for the disk (Figure 143).
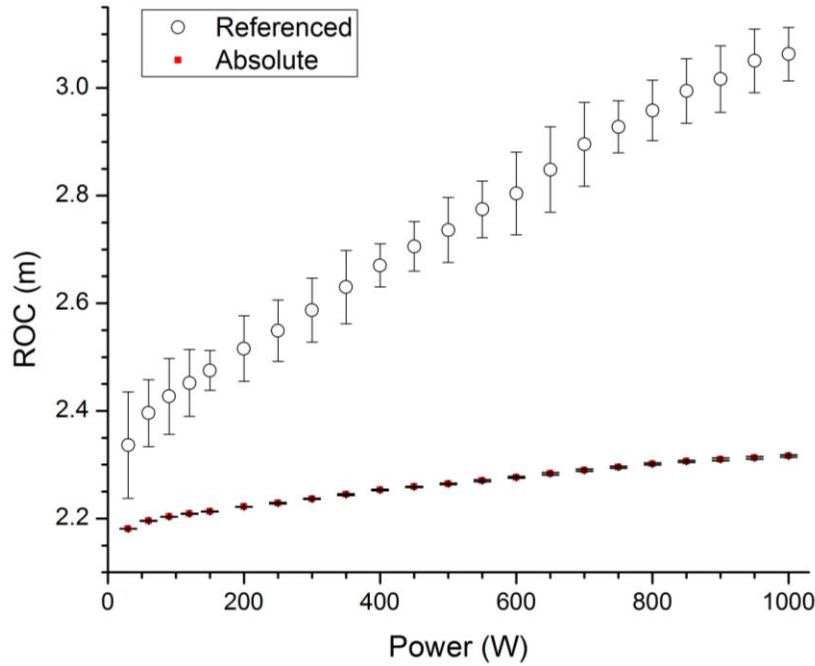
Figure 143: Radius of curvature of thin-disk measured by SHWFS in referenced and absolute modes over a range of output powers from 30 to 1000 W

In order to calculate the ROC values from the referenced measurement values, a Gaussian reduction of two lenses was used (Equation 19). This is because the quiescent state value of the disks ROC is referenced out of the measurement, so that the values given by the camera relate only to the change in the ROC, not its total curvature value. This is true in all cases of referenced measurement, but unlike the oxide and ceramic samples which are flat and parallel, the disk has an initial curvature making Gaussian reduction is necessary for finding the total curvature values.

$$\phi = \phi_{TD} + \phi_{\Delta} - \tau\phi_{TD}\phi_{\Delta} \qquad (19)$$

In Equation 19, ϕ is the combined power of the disk's state quiescent curvature and the thermally induced change in curvature, ϕ_{TD} is the quiescent state value of the disks ROC (2000

150

mm), ϕ_Δ is the thermally induced change in the disk's curvature, and τ is the distance between the two, which is zero. The ROC is then taken as shown in Equation 20.

$$ROC = \frac{2}{\phi} \qquad (20)$$

With zero pump power the measured absolute ROC of the disk was measured 2091 mm, which constitutes a 4.6% variation from the anticipated value (2000 mm). In referenced mode because of how ROC is calculated, with no applied pump power, the value is not meaningful as nothing but the change in curvature is measured.

Because the values measured in absolute mode appeared to have a smaller deviation from the expected values than was found via the referenced mode, the absolute mode values were used in the design of the cavity for the regenerative amplifier. However, as was mentioned in the section on design considerations, the models based on the absolute values proved inaccurate in terms of stability when assembled in the laboratory. For example, at 30 W of power, the absolute measured ROC was 2181 mm, and based on this value a regenerative amplifier cavity was created (Figure 144).

The cavity was assembled one mirror at a time, but with the addition of the 8th cavity mirror the cavity became unstable. Once the curvatures of all mirrors were checked using the SHWFS to ensure that they were the expected values, this left only the curvature of the disk remaining as an uncertainty. By determining the point at which the cavity became unstable, it was possible to use the model to determine empirically the value of the disk's ROC. This was done by finding a stable operating position for the 8th mirror, a position on the edge of stability, and a position at which the cavity was no longer stable (shown as positions a, b, and c respectively in Figure 145). By process of elimination the value found for the disk ROC was 2080 mm.
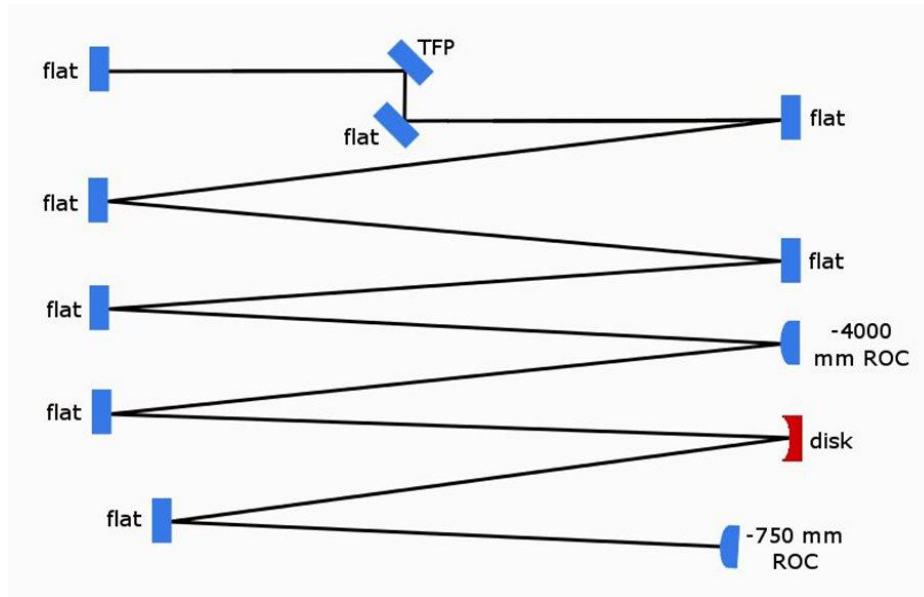
Figure 144: Early regenerative amplifier cavity design which was unstable due to an inaccurate ROC value of the disk
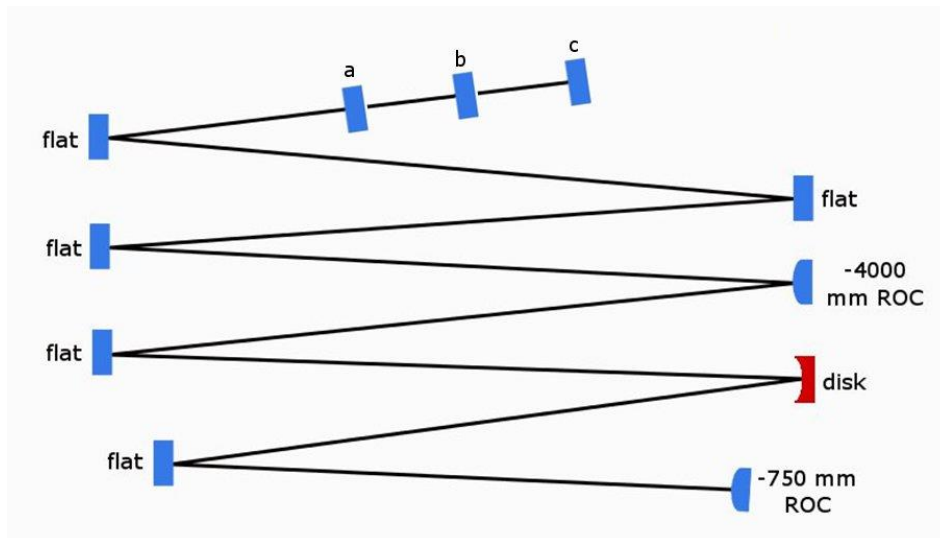
Figure 145: Early cavity design assembled with varying distances of the 8th mirror when it is added. Position (a) represents a distance at which the cavity was stable, position (b) where the cavity was on the edge of stability, and position (c) where the cavity had become unstable.

Next the curvature of the disk was re-measured to determine the source of the error. However, re-measuring the disk with the SHWFS only repeated previous measurements, representing a ~9% error between the SHWFS measured value of the disk (2180 mm ROC with zero pump power) and the value found via the experimental stability test (2080 mm ROC at low

pump powers). By comparison, when the curvatures of the cavity mirrors were checked with the SHWFS, the measured values were all within <1% error, indicating that the SHWFS is providing accurate values.

Exploring the source of this discrepancy, it was concluded that because light propagates through the disk itself twice in the process of being reflected, the curvature of both the front and back surfaces effects the point at which the light is focused, thus altering the value given by the SHWFS. A simplified model of this effect was created using ABCD matrices to examine what could cause the measurement of the camera to consistently over-estimate the disk curvature. The ABCD matrix for reflection off the disk (M_1 shown in Equation 21) was calculated by calculating the propagation of a collimated 3 mm beam (B) through free space (M_{FS1}), passing through the curved front surface of the disk (D_F) from air, propagating through the Yb:YAG (T), reflecting off the back surface of the disk (D_B), propagating back through the Yb:YAG, passing back through the front surface of the disk into air ($D_{F'}$), then traveling a given distance in free space again (M_{FS2}). For comparison, reflection off a mirror with the same curvature as the back surface of the disk is calculated as M_2 in Equation 22.

$$M_1 = M_{FS2} \cdot D_{F'} \cdot T \cdot D_B \cdot T \cdot D_F \cdot M_{FS1} \cdot B \qquad (21)$$

$$M_2 = M_{FS2} \cdot D_B \cdot M_{FS1} \cdot B \qquad (22)$$

Where:

$$B = \begin{bmatrix} r \\ \theta \end{bmatrix}$$

$$M_{FS1} = \begin{bmatrix} 1 & \dfrac{L}{n_{air}} \\ 0 & 1 \end{bmatrix}$$

$$D_F = \begin{bmatrix} 1 & 0 \\ \dfrac{n_{YAG} - n_{air}}{n_{YAG} \cdot R_f} & \dfrac{n_{air}}{n_{YAG}} \end{bmatrix}$$

$$T = \begin{bmatrix} 1 & \dfrac{t}{n_{YAG}} \\ 0 & 1 \end{bmatrix}$$

$$D_B = \begin{bmatrix} 1 & 0 \\ -\dfrac{2}{R_b} & 1 \end{bmatrix}$$

$$D_F = \begin{bmatrix} 1 & 0 \\ \dfrac{n_{air} - n_{YAG}}{n_{air} \cdot -R_f} & \dfrac{n_{YAG}}{n_{air}} \end{bmatrix}$$

For all these expressions, r is the incoming beam radius (1.5 mm)with θ its angle (0), L is the distance propagated to the disk (300 mm, arbitrary), n_{air} is the refractive index of air (1), n_{YAG} is the refractive index of 10% Yb:YAG (1.83), R_f is the ROC of the front surface of the disk (variable values used), t is the thickness of the disk (0.2 mm), and R_b is the ROC of the back surface of the disk (variable values used). The units used for all values are in mm. The value for the disk thickness (t) is only an estimate as the actual value is proprietary information, and the second free space matrix M_{FS2} represents a variable distance of propagation from the disk.

The result of this model shows that if the front surface of the disk has an ROC that is shorter than the ROC of the back surface, the incoming wavefront will converge at a distance that is greater than where focal plane of an equivalent mirror would like (ROC same as that of the rear surface of the disk). If the ROC of the front surface is greater than the ROC of the back surface, the point of convergence of the wavefront is closer to the disk than for the equivalent mirror. If the curvatures are exactly matched then the point of convergence is not offset from the focal plane of the rear surface. For a rear surface curvature of 2000 mm, the convergence of the wavefront for the three cases is shown in Figure 146, representing front surface curvatures of 1800, 2000 and 2200 nm.
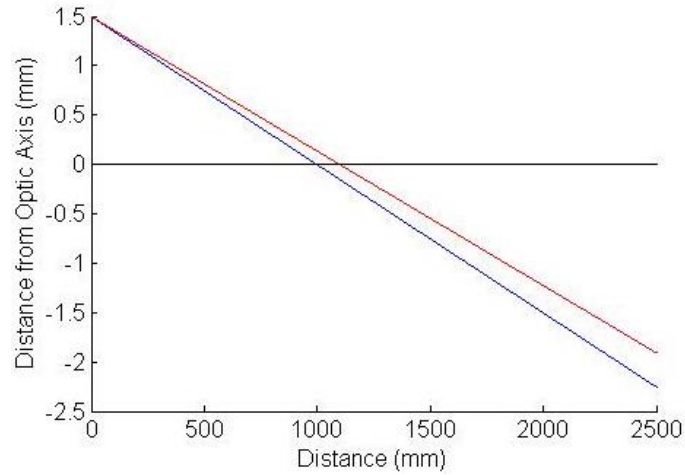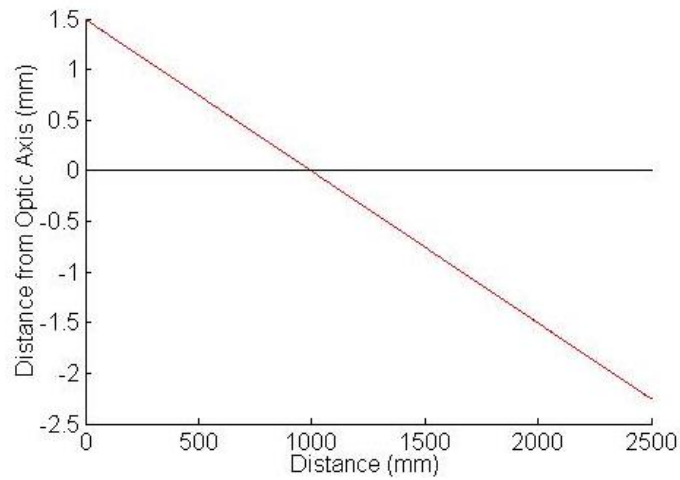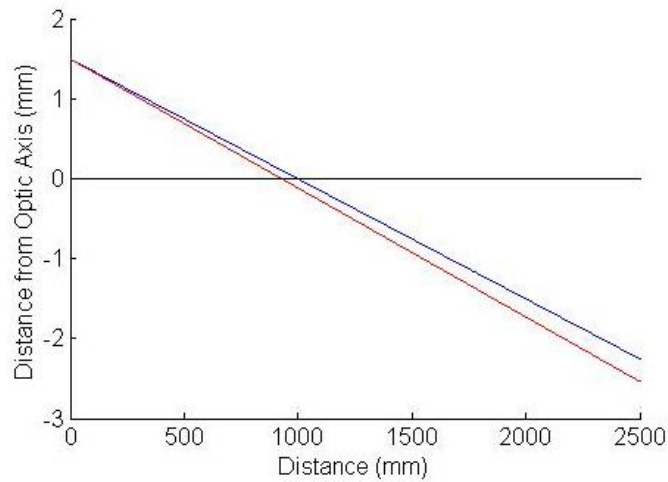
Figure 146: Calculated rays reflected from the disk (red) and comparison to an equivalent mirror (blue). In all cases the mirror and the rear ROC of the disk are set to 2000 mm. Each case represents a different curvature value for the front surface of the disk: a) 1800 mm, b) 2000 mm and c) 2200 mm.

Because the precise values for the curvature of the front and back surfaces of the disk, and its exact thickness, are unknown, the values produced by the model are only estimates. The stability conditions determined experimentally in the laboratory gave values which were smaller than those found by the SHWFS, indicating that the SHWFS is somehow over-predicting the ROC of the disk. The behavior of the model for different relative curvatures of the front and back surfaces of the disk offers one possible explanation for the discrepancy between these two assessment techniques. Over-prediction of the disk's ROC as found through the modeling of the disk (as described in this section) occurs when the ROC of the front surface of the disk is smaller than the ROC of the rear reflecting-surface of the disk.

CHAPTER 5:   CONCLUSIONS

The fiber-seeded thin-disk MOPA system which was designed and assembled as described in this work currently produces a maximum estimated pulse energy of 62 mJ, and offers a proof-of-concept demonstration of desired pulse shaping capabilities. With a reduction in noise through the methods outlined, the system has the potential to produce consistently temporally tailored output pulses of 10- 30 ns in duration with pulse energies of greater than 50 mJ, and meet all the originally specified design criteria simultaneously. By incorporating a higher bandwidth WFG to drive the modulator, control of the pulse shape down to ns resolution will enable the optimization of various light-matter interactions for materials processing and EUV generation. Expansion of the cavity modeling code will ultimately allow for a full optimization the full regenerative amplifier cavity.

Thermal analysis of various optical materials, including the thin-disk, Yb:YAG ceramics and crystals, and passive oxide materials has allowed the development of a diagnostic and model for analyzing thermal effects and determining ceramic material quality. This diagnostic can be used to analyze most optical materials for a variety of interests related to high power and high energy laser operation. Use of this technique during fabrication of ceramics can be used to refine the fabrication process and yield ceramics of higher quality. In this case, chemical impurities in ceramics were demonstrably correlated with the thermal response of the material. Finlly, the model that was created can be used to compare the performance of a ceramic to a theoretically perfect sample and thereby find an absolute assessment of the material quality.

Development of higher power lasers for a variety of applications continues at a rapid pace, with new designs and materials being analyzed and implemented in order improve laser performance through a variety of methods. The work described herein has addressed both the

development of a novel thin-disk laser system, and the future application of novel materials as thin-disk laser media.

REFERENCES

1. M. Sokolov, A. Salminen, M. Kuznetsov, and I. Tsibulskiy, "Laser welding and weld hardness analysis of thick section S355 structural steel," Mater Des **32,** 5127-5131 (2011).

2. L. Quintino, A. Costa, R. Miranda, D. Yapp, V. Kumar, and C. J. Kong, "Welding with high power fiber lasers – A preliminary study," Mater Des **28,** 1231-1237 (2007).

3. T. Han, S. S. PARK, K. KIM, C. KANG, I. WOO, and J. LEE, "CO_2 laser welding characteristics of 800 MPa class TRIP steel," ISIJ Int **45,** 60-65 (2005).

4. A. Matsunawa, N. Seto, J. Kim, M. Mizutani, and S. Katayama, "Dynamics of keyhole and molten pool in high power CO2 laser welding," in *Proc SPIE 3888* (2000), pp. 34-45.

5. W. W. Duley, "CO_2 lasers: effects and applications," NASA STI/Recon Technical Report A **77,** 15811 (1976).

6. C. Geddes, C. Toth, J. Van Tilborg, E. Esarey, C. Schroeder, D. Bruhwiler, C. Nieter, J. Cary, and W. Leemans, "High-quality electron beams from a laser wakefield accelerator using plasma-channel guiding," Nature **431,** 538-541 (2004).

7. J. Faure, Y. Glinec, A. Pukhov, S. Kiselev, S. Gordienko, E. Lefebvre, J. Rousseau, F. Burgy, and V. Malka, "A laser–plasma accelerator producing monoenergetic electron beams," Nature **431,** 541-544 (2004).

8. S. A. George, K. Hou, K. Takenoshita, A. Galvanauskas, and M. C. Richardson, "13.5 nm EUV generation from tin-doped droplets using a fiber laser," Opt. Express **15,** 16348-16356 (2007).

9. J. Vetrovec, "Solid-state laser high-energy laser," Laser and Beam Control Technologies (2002).

10. T. H. Weise, M. Jung, D. Langhans, and M. Gowin, "Overview of directed energy weapon developments," in *Electromagnetic Launch Technology, 2004. 2004 12th Symposium on,* (IEEE, 2005), pp. 483-489.

11. J. J. Wachs and G. T. Wilson, "United States army tactical high-energy laser program," Optical Engineering **52,** 021009-021009 (2012).

12. P. Thiagarajan, S. Smith, B. Caliva, J. Helmrich, S. Das, F. Lapinski, G. Pennington, R. Walker, and M. McElhinney, "Scalable Compact Laser diode Array Technology for High Energy Applications," in *CLEO: Applications and Technology,* (Optical Society of America, 2013).

13. G. H. Miller, E. I. Moses, and C. R. Wuest, "The national ignition facility," Optical Engineering **43,** 2841-2853 (2004).

14. M. Edwards, J. Lindl, B. Spears, S. Weber, L. Atherton, D. Bleuel, D. Bradley, D. Callahan, C. Cerjan, and D. Clark, "The experimental plan for cryogenic layered target implosions on the National Ignition Facility—the inertial confinement approach to fusion," Phys Plasmas **18,** 051003 (2011).

15. Lawrence Livermore National Laboratory, "Laser Inertial Fusion Energy (LIFE): Tackling the Global Energy Crisis," https://lasers.llnl.gov/about/missions/energy_for_the_future/life/.

16. G. Overton, T. Hausken, D. A. Belforte, and C. Holton, "ANNUAL REVIEW AND FORECAST: Economic aftershocks keep laser markets unsettled," Laser Focus World **48,** (2012).

17. T. H. Maiman, "Stimulated Optical Radiation in Ruby," Nature **187,** 493-494 (1960).

18. A. Javan, W. R. Bennett Jr, and D. R. Herriott, "Population inversion and continuous optical maser oscillation in a gas discharge containing a He-Ne mixture," Phys. Rev. Lett. **6,** 106-110 (1961).

19. E. Snitzer, "Optical Maser Action of Nd^{3+} in Barium Crown Glass," Physical Review Letters **7,** 444-446 (1961).

20. P. Sorokin, J. Lankard, V. Moruzzi, and E. Hammond, "Flashlamp-Pumped Organic-Dye Lasers," J. Chem. Phys. **48,** 4726-4741 (1968).

21. Z. I. Alferov, V. M. Andreev, E. L. Portnoi, and M. K. Trukan, "AlAs-GaAs heterojunction injection lasers with a low room-temperature threshold," Sov. Phys. Semicond. **3,** 1107 (1970).

22. D. A. Deacon, L. Elias, J. M. Madey, G. Ramian, H. Schwettman, and T. I. Smith, "First operation of a free-electron laser," Phys. Rev. Lett. **38,** 892-894 (1977).

23. H. Soda, K. Iga, C. Kitahara, and Y. Suematsu, "GaInAsP/InP surface emitting injection lasers," Japanese Journal of Applied Physics **18,** 2329 (1979).

24. A. Giesen, H. Hugel, A. Voss, K. Wittig, U. Brauch, and H. Opower, "Scalable concept for diode-pumped high-power solid-state lasers," Applied Physics B **58,** 365-372 (1994).

25. K. Thyagarajan, A. Ghatak, K. Thyagarajan, and A. Ghatak, "Doped Fiber Amplifiers and Lasers," in *Lasers: Fundamentals and Applications*, 291-321 (2010).

26. K. Du, N. Wu, J. Xu, J. Giesekus, P. Loosen, and R. Poprawe, "Partially end-pumped Nd: YAG slab laser with a hybrid resonator," Opt. Lett. **23,** 370-372 (1998).

27. S. Ruppik, F. Becker, F. Grundmann, W. Rath, and U. Hefter, "High-power disk and fiber lasers: a performance comparison," in *Proc SPIE 8235* (2012), pp. 8237-8225.

28. J. Li, S. Yang, A. Meissner, M. Hofer, and D. Hoffmann, "A 200 W INNOSLAB Tm: YLF laser," Laser Physics Letters **10,** 055002 (2013).

29. S. Tokita, J. Kawanaka, M. Fujita, T. Kawashima, and Y. Izawa, "Sapphire-conductive end-cooling of high power cryogenic Yb:YAG lasers," Applied Physics B **80,** 635-638 (2005).

30. N. Broderick, H. Offerhaus, D. Richardson, R. Sammut, J. Caplen, and L. Dong, "Large mode area fibers for high power applications," Optical Fiber Technology **5,** 185-196 (1999).

31. E. Locke, R. Hella, and L. Westra, "Performance of an unstable oscillator on a 30-kW CW gas dynamic laser," Quantum Electronics, IEEE Journal of **7,** 581-583 (1971).

32. P. Dunne, G. OSullivan, and D. OReilly, "Prepulse-enhanced narrow bandwidth soft x-ray emission from a low debris, subnanosecond, laser plasma source," Appl. Phys. Lett. **76,** 34-36 (2000).

33. S. Düsterer, H. Schwoerer, W. Ziegler, D. Salzmann, and R. Sauerbrey, "Effects of a prepulse on laser-induced EUV radiation conversion efficiency," Appl. Phy. B **76,** 17-21 (2003).

34. D. Gay, A. Cournoyer, P. Deladurantaye, M. Briand, V. Roy, B. Labranche, M. Levesque, and Y. Taillon, "Micro-milling process improvement using an agile pulse-shaping fiber laser," in *Photonics North 2009* (SPIE, 2009), pp. 73860R-73860R-12.

35. S. T. Hendow and S. A. Shakir, "Structuring materials with nanosecond laser pulses," Optics Express **18,** 10188-10199 (2010).

36. S. T. Hendow, R. Romero, S. A. Shakir, and P. T. Guerreiro, "Percussion drilling of metals using bursts of nanosecond pulses," Optics Express **19,** 10221-10231 (2011).

37. S. Eiselen, D. Wu, P. Galarneau, and M. Schmidt, "The role of temporal energy input in laser micro machining using nanosecond pulses," Physics Procedia **41,** 676-681 (2013).

38. A. Okishev, I. Begishev, R. Cuffney, S. Papernov, and J. Zuegel, "A highly energetic, multiwavelength, diode-pumped nanosecond laser system with flexible pulse-shaping capability," in *Photonics West LASE* (SPIE 2013), pp. 85990Q-85990Q-6.

39. M. Sparks, "Optical Distortion by Heated Windows in High-Power Laser Systems," J. Appl. Phys. **42,** 5029-5046 (1971).

40. R. Weber, B. Neuenschwander, M. Mac Donald, M. Roos, and H. P. Weber, "Cooling schemes for longitudinally diode laser-pumped Nd: YAG rods," Quantum Electronics, IEEE Journal of **34,** 1046-1053 (1998).

41. A. Ikesue and Y. L. Aung, "Ceramic Laser Materials," Nature Photonics **2,** 721-727 (2008).

42. R. L. Byer, "Progress in Engineering Ceramics for Advanced Solid State Lasers," in *3rd Laser Ceramics Symposium,* (2007).

43. R. L. Coble, "Sintering crystalline solids. II. Experimental test of diffusion models in powder compacts," Applied Physics **35,** 793-799 (1961).

44. S. E. Hatch, W. F. Parsons, and R. J. Weagley, "Hot-pressed polycrystalline $CaF_2:Dy^{2+}$ laser," Applied Physics Letters **5,** 153-154 (1964).

45. C. A. Handwerker, R. M. Cannon, and R. H. French, "Robert L. Coble: A Retrospective," J Am Ceram Soc **77,** 293-297 (1994).

46. K. A. Appiagyei, G. L. Messing, and J. Q. Dumm, "Aqueous slip casting of transparent yttrium aluminum garnet (YAG) ceramics," Ceramics International **34,** 1309-1313 (2008).

47. A. Ikesue, "Polycrystalline Nd:YAG ceramic lasers," Optical Materials **19,** 183-187 (2002).

48. A. Ikesue, Y. L. Aung, T. Yoda, S. Nakayama, and T. Kamimura, "Fabrication and laser performance of polycrystal and single crystal Nd:YAG by advanced ceramic processing," Optical Materials **29,** 1289-1294 (2007).

49. A. Ikesue and Y. L. Aung, "Synthesis and Performance of Advanced Ceramic Lasers," Journal of the American Ceramic Society **89,** 1936-1944 (2006).

50. G. A. Kumar, J. Lu, A. A. Kaminskii, K. Ueda, H. Yagi, T. Yanagitani, and N. V. Unnikrishnan, "Spectroscopic and Stimulated Emission Characteristics of Nd^{3+} in Transparent YAG Ceramics," IEEE Journal of Quantum Electronics **40,** 747-758 (2004).

51. T. Takunori, K. Sunao, S. Jiro, I. Akio, and Y. Kunio, "Highly trivalent neodymium ion doped YAG ceramic for microchip lasers," in *Advanced Solid State Lasers* (Optical Society of America, 1999), pp. TuB3.

52. H. Yagi, T. Yanagitani, K. Takaichi, K. Ueda, and A. A. Kaminskii, "Characterizations and laser performances of highly transparent $Nd^{3+}:Y_3Al_5O_{12}$ laser ceramics," Optical Materials **29,** 1258-1262 (2007).

53. J. Dong, A. Shirakawa, K. Ueda, H. Yagi, T. Yanagitani, and A. A. Kaminskii, "Laser-diode pumped heavy-doped Yb:YAG ceramic lasers," Optics Letters **32,** 1890-1892 (2007).

54. H. Cai, J. Zhou, H. Zhao, Y. Qi, Q. Lou, J. Dong, and Y. Wei, "Continuous-wave and Q-switched performance of an Yb:YAG/YAG composite thin disk ceramic laser pumped with 970-nm laser diode," Chin. Opt. Lett. **6,** 852-854 (2008).

55. H. Yoshioka, S. Nakamura, T. Ogawa, and S. Wada, "Diode-pumped mode-locked Yb:YAG ceramic laser," Optics Express **17,** 8919-8925 (2009).

56. H. Yoshioka, S. Nakamura, T. Ogawa, and a. S. Wada, "Dual-wavelength mode-locked Yb:YAG ceramic laser in single cavity," Optics Express **18,** 1479-1486 (2010).

57. W. Zhang, Y. Pan, J. Zhou, W. Liu, J. Li, B. Jiang, X. Cheng, and J. Xuz, "Diode-Pumped Tm:YAG Ceramic Laser," Journal of the American Ceramic Society **9,** 2434-2437 (2009).

58. V. Lupei, A. Lupei, C. Gheorghe, and A. Ikesue, "Spectroscopic characteristics of Tm^{3+} in Tm and Tm, Nd, Yb:Sc2O3 ceramic," Journal of Luminescence **128,** 901-904 (2008).

59. B. C. Platt and R. Shack, "History and Principles of Shack-Hartmann Wavefront Sensing," J. Refractive Surg. **17,** S573 (2001).

60. Imagine Optic, "HASO™v3 Shack-Hartmann wavefront analysis software," http://www.imagine-optic.com/iop_products_wavefront-analysis_HASOv3_wavefront-sensor-software_en.php.

61. C. J. Koester and E. Snitzer, "Amplification in a fiber laser," Applied Optics **3,** 1182-1186 (1964).

62. J. Canning, "Fibre lasers and related technologies," Optics and Lasers in Engineering **44,** 647-676 (2006).

63. V. Gapontsev and W. Krupke, "Fiber lasers grow in power," Laser Focus World **38,** (2002).

64. J. A. Alvarez-Chavez, de la Cruz May, L., A. Martinez-Rios, I. Torres-Gomez, and F. Martinez-Pinon, "High power Er3+/Yb3+-doped fiber laser suitable for medical applications," in *Electronics and Photonics, Multiconference on* (IEEE, 2006), pp. 279-281.

65. V. Dominic, S. MacCormack, R. Waarts, S. Sanders, S. Bicknese, R. Dohle, E. Wolak, P. S. Yeh, and E. Zucker, "110 W fibre laser," Electronics Letters **35,** 1158-1160 (1999).

66. J. Limpert, F. Roser, S. Klingebiel, T. Schreiber, C. Wirth, T. Peschel, R. Eberhardt, and A. Tiinnermann, "The Rising Power of Fiber Lasers and Amplifiers," Selected Topics in Quantum Electronics, IEEE Journal of **13,** 537-545 (2007).

67. Optics.org, "IPG tests first 10 kW singlemode production laser," http://optics.org/article/39511.

68. J. Nilsson, W. A. Clarkson, R. Selvas, J. K. Sahu, P. W. Turner, S. U. Alam, and A. B. Grundinin, "High-power wavelength-tunable cladding-pumped rare-earth silica fiber lasers," Optical Fiber Technology **10,** 5-30 (2004).

69. N. Peyghambrian and A. Schulzgen, "High-Power Devices in Compact Packages," Optics & Photonics News (2005).

70. Y. Jeong, S. Yoo, C. A. Coderaard, J. Nilsson, J. K. Sahu, D. N. Payne, R. Horley, P. W. Turner, L. Hickey, A. Harker, M. Lovelady, and A. Piper, "Erbium:Ytterbium Codoped Large-Core Fiber Laser With 297-W Continuous-Wave Output Power," IEEE J. Selected Topics in Quantum Electronics **13,** 573-579 (2007).

71. A. Tünnermann, T. Schreiber, and J. Limpert, "Fiber lasers and amplifiers: an ultrafast performance evolution," Appl. Opt. **49,** F71-F78 (2010).

72. J. W. Dawson, M. J. Messerly, R. J. Beach, M. Y. Shverdin, E. A. Stappaerts, A. K. Sridharan, P. H. Pax, J. E. Heebner, C. W. Siders, and C. Barty, "Analysis of the scalability of diffraction-limited fiber lasers and amplifiers to high average power," Optics Express **16,** 13240-13266 (2008).

73. Y. Jeong, J. Nilsson, J. K. Sahu, D. N. Payne, R. Horley, L. M. B. Hickey, and P. W. Turner, "Power scaling of single-frequency ytterbium-doped fiber master oscillator power amplifier sources up to 500 W," IEEE J. Selected Topics in Quantum Electronics **13,** 546-551 (2007).

74. G. P. Agrawal, *Non-linear Fiber Optics* (Elsevier Academic Press, 2007).

75. G. P. Agrawal, "9.2.1 Brillouin Threshold," in *Nonlinear Fiber Optics,* (Academic Press, Elsevier Inc., 2007).

76. R. G. Smith, "Optical power handling capacity of low loss optical fibers as determined by stimulated Raman and Brillouin scattering," Appl. Opt. **11,** 2489-2494 (1972).

77. J. Limpert, F. Roser, D. N. Schimpf, E. Seise, T. Eidam, S. Hadrich, J. Rothhardt, C. J. Misas, and A. Tunnermann, "High repetition rate gigawatt peak power fiber laser systems: challenges, design, and experiment," Selected Topics in Quantum Electronics, IEEE Journal of **15,** 159-169 (2009).

78. IPG Photonics, "YLR-SM Series: 100 W to 1.5 kW Single Mode CW Ytterbium Fiber Lasers," http://www.ipgphotonics.com/apps_mat_single_YLR_SM.htm (2010).

79. J. C. Almasi and W. S. Martin, "Face-pump, face-cooled laser device," US Patent 3631362 (1971).

80. K. Contag, M. Karszewski, C. Stewen, A. Giesen, and H. Hugel, "Theoretical modelling and experimental investigations of the diode-pumped thin-disk Yb:YAG laser," Quantum Electronics **29,** 697-703 (1999).

81. A. Giesen and J. Speiser, "Fifteen Years of Work on Thin-Disk Lasers: Results and Scaling Laws," IEEE J. Selected Topics in Quantum Electronics **13,** 598-609 (2007).

82. A. Giesen, "Results and scaling laws of thin disk lasers," in *Proceedings of SPIE,* Anonymous (SPIE, 2004), pp. 212-227.

83. J. Mende, E. Schmid, J. Speiser, G. Spindler, and A. Giesen, "Thin disk laser: power scaling to the kW regime in fundamental mode operation," 71931V-71931V (2009).

84. J. Spieser, "Scaling of thin-disk lasers-influence of amplified spontaneous emission," Journal of the Optical Society of America B **26,** 26-35 (2009).

85. C. Stewen, M. Larinov, and A. Giesen, "Yb:YAG thin disk laser with 1 kW output power," in *Advanced Solid State Lasers,* H. Injeyan, U. Keller, and C. Marshall, eds. (OSA, 2000), pp. 35-41.

86. W. T. Silfvast, *Laser Fundamentals* (Cambridge University Press, 2003).

87. A. Killi, I. Zawischa, D. Sutter, J. Kleinbauer, S. Schad, J. Neuhaus, and C. Shmitz, "Current Status and development trends of disk laser technology," in *Solid State Lasers XVII: Technology and Devices* (SPIE, 2008).

88. W. Koechner, "4.2 Regenerative Amplifiers," in *Solid-State Laser Engineering,* (Springer, 2006).

89. J. Vackaf, "Low-frequency regenerative amplifier," US Patent 2,991,423 (1961).

90. P. Lefferts, "Tansiently regenerative amplifier with A.C. and D.C. regeneration," US Patent 3,264,569 (1966).

91. A. Blume and K. Tittel, "Thermal effects in laser amplifiers and oscillators," Appl. Opt. **3,** 527-530 (1964).

92. J. Turner, E. Moses, and C. Tang, "Spectral narrowing and electro-optical tuning of a pulsed dye laser by injection locking to a cw dye laser," Appl. Phys. Lett. **27,** 441-443 (1975).

93. P. Bélanger and J. Boivin, "Gigawatt peak-power pulse generation by injection of a single short pulse in a regenerative amplifier above threshold (RAAT)," Can. J. Phys. **54,** 720-727 (1976).

94. D. Muller, A. Giesen, and H. Hugel, "Picosecond thin disk regenerative amplifier," in *International Symposium on Gas Flow, Chemical Lasers, and High-Power Lasers* (SPIE, 2003), pp. 281-286.

95. D. Nickel, C. Stolzenburg, A. Giesen, and F. Butze, "Ultrafast thin-disk $Yb:KY(WO_4)_2$ regenerative amplifier with a 200-kHz repetition rate," Optics Letters **29,** 2764-2766 (2004).

96. M. Larionov, F. Butze, D. Nickel, and A. Giesen, "High-repetition-rate regenerative thin-disk amplifier with 116 mJ pulse energy and 250 fs pulse duration," Optics Letters **32,** 494-496 (2007).

97. T. Metzger, A. Schwarz, C. Y. Teisset, D. Sutter, A. Killi, R. Kienberger, and F. Krausz, "High-repetition-rate picosecond pump laser based on a Yb:YAG disk amplifier for optical parametric amplification," Optics Letters **34,** 2123-2125 (2009).

98. J. Coey, "Rare-earth magnets," Endeavour **19,** 146-151 (1995).

99. W. Bailey, P. Kabos, F. Mancoff, and S. Russek, "Control of magnetization dynamics in Ni_{81} Fe_{19} thin films through the use of rare-earth dopants," Magnetics, IEEE Transactions on **37,** 1749-1754 (2001).

100. M. Humphries, *Rare earth elements: The global supply chain* (DIANE Publishing, 2010).

101. C. Hurst and the Institute for the Analysis of Global Security Washington DC, "China's Rare Earth Elements Industry: What Can the West Learn?" **ADA525378,** (2010).

102. M. Eichhorn, "Quasi-three-level solid-state lasers in the near and mid infrared based on trivalent rare earth ions," Applied Physics B269-316 (2008).

103. M. Eichhorn, "Thermal lens effects in an Er^{3+}:YAG laser with crystalline fiber geometry," Applied Physics B **94,** 451-457 (2009).

104. E. C. Honea, R. J. Beach, S. C. Mitchell, J. A. Skidmore, M. A. Emanuel, S. B. Sutton, and S. A. Payne, "High-power dual-rod Yb:YAG laser," Optics Letters **25,** 805-807 (2000).

105. F. Kallmeyer, X. Wang, M. Dziedzina, H. Rhee, and H. J. Eichler, "Nd:GSAG laser at 943 nm with high pulse energy," in *Advanced Solid-State Photonics,* Anonymous (OSA, 2008).

106. N. V. Kuleshov, A. A. Lagatsky, V. G. Shcherbitsky, V. P. Mickhailov, E. Heumann, T. Jensen, and A. Diening, "CW laser performance of Yb and Er, Yb doped tungstates," Applied Physics B409-413 (1997).

107. E. Lippert, S. Nicolas, G. Arisholm, K. Stenersen, and G. Rustad, "Midinfrared laser source with high power and beam quality," Applied Optics **45,** 3839-3845 (2006).

108. T. McComb, V. Sudesh, and M. Richardson, "Volume Bragg grating stabilized spectrally narrow Tm fiber laser," Optics Letters **33,** 881-883 (2008).

109. X. Peng, L. Xu, and A. Asundi, "Power scaling of diode-pumped Nd: YVO4 lasers," Quantum Electronics, IEEE Journal of **38,** 1291-1299 (2002).

110. I. V. Mochalov, "Laser and nonlinear properties of the potassium gadolinium tungstate laser crystal KGd $(WO_4)_2$:Nd^{3+}-(KGW:Nd)," Optical Engineering **36,** 1660-1669 (1997).

111. M. Stalder, M. Bass, and B. H. Chai, "Thermal quenching of fluorescence in chromium-doped fluoride laser crystals," JOSA B **9,** 2271-2273 (1992).

112. O. Svelto, *Principles of lasers* (Springer, 2009).

113. A. Vogel, P. Schweiger, A. Frieser, M. N. Asiyo, and R. Birngruber, "Intraocular Nd:YAG laser surgery: laser-tissue interaction, damage range, and reduction of collateral effects," Quantum Electronics, IEEE Journal of **26,** 2240-2260 (1990).

114. C. A. Nanni and T. S. Alster, "Laser-assisted hair removal: side effects of Q-switched Nd: YAG, long-pulsed ruby, and alexandrite lasers," J. Am. Acad. Dermatol. **41,** 165-171 (1999).

115. L. G. Hochman, "Laser treatment of onychomycosis using a novel 0.65-millisecond pulsed Nd:YAG 1064-nm laser," Journal of Cosmetic and Laser Therapy **13,** 2-5 (2011).

116. A. K. Dubey and V. Yadava, "Experimental study of Nd: YAG laser beam machining—an overview," J. Mater. Process. Technol. **195,** 15-26 (2008).

117. D. Fang, X. H. Wang, F. Wang, and S. Liu, "Highly efficient side-pumped solar laser," in *Optoelectronics and Microelectronics (ICOM), 2012 International Conference on,* (IEEE, 2012), pp. 95-98.

118. D. Fang, X. H. Wang, F. Wang, and S. N. Liu, "Solar pumped Nd:YAG laser," Optik-International Journal for Light and Electron Optics (2012).

119. B. Frei and J. Balmer, "1053-nm-wavelength selection in a diode-laser-pumped Nd: YLF laser," Appl. Opt. **33,** 6942-6946 (1994).

120. Y. Chen, "CW dual-wavelength operation of a diode-end-pumped Nd:YVO$_4$ laser," Applied Physics B **70,** 475-478 (2000).

121. T. Fan, "Heat generation in Nd:YAG and Yb:YAG," Quantum Electronics, IEEE Journal of **29,** 1457-1459 (1993).

122. A. Bellemare, M. Karbsek, C. Riviere, F. Babin, G. He, V. Roy, and G. W. Schinn, "A broadly tunable erbium-doped fiber ring laser: experimentation and modeling," Selected Topics in Quantum Electronics, IEEE Journal of **7,** 22-29 (2001).

123. R. Mears, L. Reekie, I. Jauncey, and D. Payne, "Low-noise erbium-doped fibre amplifier operating at 1.54 μm," Electron. Lett. **23,** 1026-1028 (1987).

124. S. Tokita, M. Murakami, S. Shimizu, M. Hashida, and S. Sakabe, "Liquid-cooled 24 W mid-infrared Er:ZBLAN fiber laser," Opt. Lett. **34,** 3062-3064 (2009).

125. J. B. Newman, J. L. Lord, K. Ash, and D. H. McDaniel, "Variable pulse erbium: YAG laser skin resurfacing of perioral rhytides and side-by-side comparison with carbon dioxide laser," Lasers Surg. Med. **26,** 208-214 (2000).

126. S. R. Visuri, J. T. Walsh, and H. A. Wigdor, "Erbium laser ablation of dental hard tissue: effect of water cooling," Lasers Surg. Med. **18,** 294-300 (1998).

127. W. Koechner, *Solid-State Laser Engineering* (Springer, 2006).

128. C. R. Giles and E. Desurvire, "Modeling erbium-doped fiber amplifiers," Lightwave Technology, Journal of **9,** 271-283 (1991).

129. E. Lim, S. Alam, and D. Richardson, "High energy in-band pumped erbium doped pulse fibre laser," in *Proc. SPIE 8237* (2012), pp. 82371V-1.

130. M. A. Jebali, J. Maran, S. LaRochelle, S. Chatigny, M. Lapointe, and E. Gagnon, "A 103W High Efficiency In-Band Cladding-Pumped 1593 nm All-Fiber Erbium-Doped Fiber Laser," in *CLEO: Science and Innovations,* Anonymous (Optical Society of America, 2012).

131. C. Ziolek, H. Ernst, G. Will, H. Lubatschowski, H. Welling, and W. Ertmer, "High-repetition-rate, high-average-power, diode-pumped 2.94-μm Er:YAG laser," Opt. Lett. **26,** 599-601 (2001).

132. F. Tong, W. P. Risk, R. M. Macfarlane, and W. Lenth, "551 nm diode-laser-pumped upconversion laser," Electronics Letters **25,** 1389-1391 (1989).

133. H. Tsao, S. Lin, C. Wang, H. Su, C. Huang, Y. Jhang, C. Hu, T. Tsai, and J. Sheu, "A Green Upconversion Laser with Erbium-Doped LiLuF4 Crystal by 976 nm Fiber Laser Pump," International Journal of Optics and Applications **2,** 72-75 (2012).

134. A. Godard, "Infrared (2–12 μm) solid-state laser sources: a review," Comptes Rendus Physique **8,** 1100-1128 (2007).

135. B. E. Knudsen, B. H. Chew, A. H. Tan, D. T. Beiko, J. D. Denstedt, and S. E. Pautler, "Assessment of hydrodissection, holmium: YAG laser vaporization of renal tissue, and both combined to facilitate laparoscopic partial nephrectomy in porcine model," Urology **75,** 1209-1212 (2010).

136. T. Lü, Q. Xiao, and Z. Li, "Influence of water environment on holmium laser ablation performance for hard tissues," Appl. Opt. **51,** 2505-2514 (2012).

137. N. M. Fried and B. R. Matlaga, "Laser/Light Applications in Urology," 561-571 (2012).

138. J. Nilsson, J. K. Sahu, Y. Jeong, V. N. Philippov, D. B. S. Soh, C. A. Codemard, P. Dupriez, J. Kim, D. J. Richardson, A. Malinowski, A. N. Piper, J. H. V. Price, K. Furusawa, W.

A. Clarkson, and D. N. Payne, "High power fiber lasers," in *Optical Fiber Communication Conference and Exposition* (OSA, 2005).

139. C. Gheorghe, A. Lupei, V. Lupei, L. Gheorghe, and A. Ikesue, "Spectroscopic properties of Ho^{3+} doped Sc_2O_3 transparent ceramic for laser materials," Journal of Applied Physics **105,** 123110-6 (2009).

140. W. A. Clarkson, L. Pearson, Z. Zhang, J. W. Kim, D. Shen, A. J. Boyland, J. K. Sahu, and M. Isben, "High Power Thulium Doped Fiber Lasers," in *Optical Fiber Communication Conference and Exposition* (OSA, 2009).

141. N. M. Fried and K. E. Murray, "High-power thulium fiber laser ablation of urinary tissues at 1.94 um," Journal of endourology **19,** 25-31 (2005).

142. N. S. Nishioka and Y. Domankevitz, "Comparison of tissue ablation with pulsed holmium and thulium lasers," Quantum Electronics, IEEE Journal of **26,** 2271-2275 (1990).

143. S. D. Jackson, "Cross relaxation and energy transfer upconversion processes relevant to the functioning of 2 mm Tm3+-doped silica fibre lasers," Opt. Com. **230,** 197-203 (2004).

144. S. D. Jackson and S. Mossman, "Efficiency dependence on the Tm^{3+} and Al^{3+} concentrations for Tm^{3+}-doped silica double-clad fiber lasers," Applied Optics **42,** 2702-2707 (2003).

145. J. Wu, Z. Yao, J. Zong, and S. Jiang, "Highly efficient high-power thulium-doped germanate glass fiber laser," Optics Letters **32,** 638-640 (2007).

146. M. Richardson, T. McComb, and V. Sudesh, "High Power Fiber Lasers and Applications to Manufacturing," in *AIP Conference Proceedings* (2008), pp. 12.

147. A. Tünnermann, T. Schreiber, F. Röser, A. Liem, S. Höfer, H. Zellmer, S. Nolte, and J. Limpert, "The renaissance and bright future of fibre lasers," Journal of Physics B: Atomic, Molecular and Optical Physics **38,** S681 (2005).

148. Y. Jeong, J. K. Sahu, D. N. Payne, and J. Nilsson, "Ytterbium-doped large-core fiber laser with 1.36 kW continuous-wave output power," Optics Express **12,** 6088-6092 (2004).

149. S. Christensen, G. Firth, and B. Samson, *Developments in thulium-doped fiber lasers offer higher powers* (SPIE Newsroom, 2008).

150. A. Tünnermann, A. Liem, M. Reich, F. Röser, T. Schreiber, S. Nolte, H. Zellmer, and J. Limpert, "Ultrafast Fiber Lasers and Amplifiers: Novel Light Sources for High Precision Micro Machining," in *Advanced Solid-State Photonics* (OSA, 2005).

151. A. Grigor'yants, A. Misyurov, A. Zaitsev, and N. Rodionov, "Investigation of thermal efficiency of treatment with the radiation of a high-power ytterbium-based fibre laser," Welding International **25,** 305-308 (2011).

152. J. Hernandez-Castaneda, H. K. Sezer, and L. Li, "Statistical analysis of ytterbium-doped fibre laser cutting of dry pine wood," Proc. Inst. Mech. Eng. Pt. B: J. Eng. Manuf. **223,** 775-789 (2009).

153. J. Petit, B. Viana, P. Goldner, D. Vivien, P. Lousieau, and B. Ferrand, "Laser oscillation with low quantum defect in $Yb:GdVO_4$, a crystal with high thermal conductivity," Optics Letters **29,** 833-835 (2004).

154. Y. Jeong, A. J. Boyland, J. K. Sahu, S. Chung, J. Nilsson, and D. N. Payne, "Mutli-kilowatt Single-mode Ytterbium-doped Large-core Fiber Laser," J. Optical Society of Korea **13,** 416-422 (2009).

155. E. Snitzer, "Glass lasers," Appl. Opt. **5,** 1487-1499 (1966).

156. H. Etzel, H. Gandy, and R. Ginther, "Stimulated emission of infrared radiation from ytterbium activated silicate glass," Appl.Optics **1,** (1962).

157. Optics.org, "IPG set to ship 100 kW laser," http://optics.org/news/3/10/44.

158. O. G. Okhotnikov, L. Gomes, N. Xiang, T. Jouhti, and A. B. Grudinin, "Mode-locked ytterbium fiber laser tunable in the 980-1070 nm spectral range," Opt. Lett. **28,** 1522-1524 (2003).

159. L. Goldberg, J. P. Koplow, R. P. Moeller, and D. A. Kliner, "High-power superfluorescent source with a side-pumped Yb-doped double-cladding fiber," Opt. Lett. **23,** 1037-1039 (1998).

160. S. Chernikov, Y. Zhu, J. Taylor, and V. Gapontsev, "Supercontinuum self-Q-switched ytterbium fiber laser," Opt. Lett. **22,** 298-300 (1997).

161. N. Berner, A. Diening, E. Heumann, G. Huber, A. Voss, M. Karszewski, and A. Giesen, "Tm:YAG: A Comparison between endpumped Laser-rods and the 'Thin-Disk'-Setup," in *Advanded Solid-State Lasers* (OSA, 1999).

162. M. Schellhorn, "Performance of a Ho:YAG thin-disc laser pumped by a diode-pumped 1.9 μm thulium laser," Applied Physics B **85,** 549-552 (2006).

163. U. Brauch, A. Giesen, M. Karszewski, C. Stewen, and A. Voss, "Multiwatt diode-pumped Yb:YAG thin disk laser continuously tunable between 1018 and 1053 nm," Optics Letters **20,** 713-715 (1995).

164. T. Metzger, "High-repetition-rate picosecond pump laser based on an Yb:YAG disk amplifier for optical parametric amplification," *Advanced Solid-State Photonics* (OSA, 2009).

165. Agilent Technologies, "33503A BenchLink Waveform Builder Pro Software," http://www.home.agilent.com/en/pd-1962285-pn-33503A/benchlink-waveform-builder-pro-software?&cc=US&lc=eng.

166. Gooch & Housego, "BBO LightGate Pockels Cells," http://www.goochandhousego.com/products/electro-optics/bbo-lightgate-pockels-cells/.

167. LAS-CAD GmbH, "LASCAD The unique combination of simulation tools for**LAS**er**C**avity**A**nalysis &**D**esign," http://www.las-cad.com/index.php.

168. The MathWorks Inc., "MATLAB - The Language of Technical Computing," http://www.mathworks.com/products/matlab/.

169. J. Campbell and L. DeShazer, "Near fields of truncated-Gaussian apertures," JOSA **59,** 1427-1429 (1969).

170. Y. Dong, J. Xu, G. Zhou, G. Zhao, L. Su, X. Xu, H. Li, and J. Si, "Gamma-ray induced color centers in Yb: YAG crystals grown by Czochralski method," Solid State Commun. **141,** 105-108 (2007).

171. C. Chen, G. Pogatshnik, Y. Chen, and M. Kokta, "Optical and electron paramagnetic resonance studies of Fe impurities in yttrium aluminum garnet crystals," Physical Review B **38,** 8555 (1988).

172. Comsol, "Comsol Multiphysics," http://www.comsol.com/.